ABSTRACT

Title of Document: ELECTROOSMOTIC SOFT ACTUATORS

Deepa Sritharan,

Doctor of Philosophy, 2017

Directed By: Professor Elisabeth Smela

Department of Mechanical Engineering

This dissertation details the research involved in creating the first paper-based soft actuator driven by electroosmosis. To accomplish this, research breakthroughs were made in the fields of electrokinetic pumping and device manufacturing using soft materials.

Electroosmosis is an electrically induced microfluidic flow phenomenon. When an electric field is applied to the fluid, across the microchannels, electroosmotic flow occurs in the direction of the applied electric field. In this work, liquid was electroosmotically displaced within a flexible microfluidic device to actuate an elastomeric membrane.

The goal of this work was to create a fully sealed fluidic actuator. It was therefore necessary to encapsulate the pumping fluid within the device, and to maximize pressure it was necessary to eliminate compliance caused by trapped gases. Electrolytic gas formation is well known to disrupt pumping in DC electroosmotic systems that use water

as the pumping liquid. In this work, electrolysis was eliminated by replacing water with propylene carbonate (PC): PC was determined to be electrochemically stable up to at least 10 kV, in the absence of moisture or salt contaminants. Bubble-free electroosmotic pumping with PC was achieved within sealed miniature actuators, which could be continuously operated for at least one hour.

Benchtop fabrication techniques were developed to build encapsulated fluidic actuators composed entirely of soft, flexible materials. Stretchable electrochemically stable electrodes were made using a conductive paint made by mixing carbon nanoparticles into a silicone base. High-density microchannel networks were incorporated by using paper and other flexible porous materials, instead of conventional planar replica-molded microchannels. The device was filled with pumping fluid without the use of external tubing, and then encapsulated by casting a film of elastomer over the filled reservoir to form the actuating membrane. The resulting actuators were flexible and stretchable, demonstrating significant membrane deformations (hundreds of μm) within seconds of applying the electric field and ability to lift large loads (tens of grams). These polymeric electroosmotic actuators are unique among electroactive polymer actuators because they are able to simultaneously generate high force as well as large stroke. It is envisioned that this research will pave the way for the creation of artificial muscles and smart shape-changing materials that can be actuated by electroosmosis.

ELECTROOSMOTIC SOFT ACTUATORS

By

Deepa Sritharan

Dissertation submitted to the Faculty of the Graduate School of the

University of Maryland, College Park, in partial fulfillment

of the requirements for the degree of

Doctor of Philosophy

2017

Advisory Committee

Professor Elisabeth Smela (Chair)

Professor Donald DeVoe

Professor Miao Yu

Associate Professor Sarah Bergbreiter

Professor Srinivasa Raghavan (Dean's Representative)

DEDICATION

To my parents.

ACKNOWLEDGEMENTS

This dissertation is a culmination of research that was made possible by the support and guidance of several people. Their encouragement was essential for reaching the finish line. First and foremost, I express my deepest gratitude to my adviser Dr. Elisabeth Smela for guiding my Ph.D. research. Thank you, Dr. Smela, for believing in my capabilities and providing every possible support required for successful completion of this Ph.D. I would like to thank the members of my committee Dr. Donald DeVoe, Dr. Srinivasa Raghavan, Dr. Sarah Bergbreiter, and Dr. Miao Yu, for their valuable time and consideration in evaluating my research.

I would like thank the members of my lab who have helped me in this work. I am most thankful to Jeffery Burke, Bavani Balakrisnan, Mark Kujawski, and Timir Datta-Chaudhuri for their guidance on several other aspects of my research. I would like to thank Justin Pierce, Robert Newby, Ying Chen, Im Deok Jung, Gradimir Georgevich, Daniel Gowetski, Disha Pant, Lei Young, Ephraim Zegeye, and Nehemiah Emaikwu, for the pleasure of working by their side during these years. I would also like to thank Marc Dandin for his help and moral support throughout my PhD. I have had the honor of mentoring several students who volunteered to work with me on my research. Their enthusiasm and fresh perspectives have motivated me, and working with them opened up exciting new avenues for my research. For this, I thank Abraham Simpson Chen, Prabhath Aluthgama, Matthew Bleakney, and Mylene Motsebo.

I am grateful to Professor Abhijit Dasgupta, and his student Elaine Lin, for their vital input in the mathematical modeling of the membrane deflection of my actuator. I would like to thank Professor Jong Soo Ko, visiting from Pusan National University in Korea, for his valuable guidance in microfabrication in the few days we were able to work together during his sabbatical at UMD. The thoughts he shared with me on maintaining mindfulness during research have had a deep impact on me. I would also like to thank Maria Bassil, visiting scholar from Lebanese University, and Professor Svetlana Tatic-Lucic for their generous advice. I cherish the comradeship of Prakruthi Hareesh while we both worked on our PhDs. We spent several evenings pondering over our research problems and findings, and she offered me many insights based on her microfabrication expertise.

My sincere acknowledgements to all FabLab staff members, John Abrahams, Tom Loughran, Mark Lecates, Jonathan Hummel, and James O'Connor, for their invaluable assistance with microfabrication. I am grateful to Karen Gaskell, Audaldo Ponce, Scott A. Taylor, and Karthik Sridhara for offering their expert insight and spending several hours with me to obtain and analyze spectroscopy data.

I am grateful to the Associate Director for Graduate Studies, Kerri Poplar James, and Amarildo DaMata who was the Graduate Coordinator for their kind advice and counseling during challenging periods during my graduate studies.

I would like to thank my mentors at the Division of Solid Mechanics at the FDA: Stephen Retta and Nandini Duraiswamy, as well as Luke Herbertson for their incredibly gracious support while I wrote this dissertation.

This journey would have been impossible without the support of my family. Side-by-side or miles apart we are always connected by the heart. This has been a period of intense learning for me, and it has had a profound impact on my friends and family who have lovingly and patiently stood by me throughout this journey. I am indebted to my parents Prof. Manjula Sritharan and Prof. Venkataraman Sritharan who motivated me by their example to pursue academic research. I have been ceaselessly inspired, since I was a child, by their unending enthusiasm for teaching and scientific research. Thank you for tirelessly cheering for me and counseling me while my courage waxed and waned during my studies. I am grateful to my husband, Srinivasan Rajaraman, whose steadfast love, astute critique, and encouragement were essential to finishing this work. I am thankful to my sister Nithya for being my confidante, providing sagacious conversation and laughter without end. I deeply appreciate my husband's family for their kindness and encouragement during this long journey. I would like to thank the friends who offered me much moral strength during this journey: Deepti Dutt, Lynette Arul, Geeta Negi, and Anupama Govindarajan. A special thanks to my amiable guinea pigs Yogini, Plumbum, Mercury, and Adele for being my constant companions; their unconditional love and boundless cheer has provided me comfort on many dark days.

TABLE OF CONTENTS

LIST OF TABLES

LIST OF FIGURES

1. Introduction

1.1 Motivation

Recently, there has been interest in making actuating devices that are small and composed of soft, flexible materials [1]. Such devices include robots, prostheses, wearable assistive technology, manipulators, interactive surfaces, and other active soft structures; these soft actuating devices have been summarized in review papers [2-4].

These devices must be capable of actuation, i.e. they must be able to respond to input energy by converting it into mechanical work. For creating portable and modular devices, it is preferred that actuators can be electrically controlled. Additionally, electrically-activated devices can often be operated in both actuation and sensing modes.

This dissertation describes the design and development of miniature soft actuators driven by fluid flow induced by an applied electric field. In this introduction, a brief historical perspective is presented to describe the need for soft actuation technologies, followed by a classification of these technologies based on the driving principles employed to induce motion. Next, an overview of the physics responsible for the flow is presented. Finally, the design approach used in this work to create the soft electrohydraulic actuators is described.

1.2 Historical Background

Engineers are constantly striving to miniaturize existing devices for increasing portability, decreasing material costs, and enabling system integration [5]. Miniaturization allows multiple devices to be mounted on a single system platform in limited spaces [5]. An integrated multi-device system can perform various tasks, and redundant device units can be incorporated for improved system safety. Miniature devices are efficient and have fast response times because they have low mass and volume and are able to achieve fast transport processes (like transport of heat, chemical species, or electrical charge) [6].

Miniaturization has thus far been accomplished by microelectromechanical systems (MEMS) technology, and the robots are driven by physical phenomena that are dominant at the microscale [5] [7]. It is desirable for robots to be able to exhibit three-dimensional motions, and for this non-planar device layouts are often required. The microfabrication techniques commonly used in MEMS manufacturing are planar processes, and it is often challenging (and time consuming) to create high-aspect-ratio microstructures in which vertical dimensions are larger than the lateral dimensions. MEMS processes are best suited for machining thin layers of hard materials like silicon and metal, with few processes suitable for 3D polymer MEMS [8]. Meanwhile, digital additive/subtractive processes are being actively developed to facilitate rapid prototyping of meso-scale devices in “makerspaces” around the world [9,10]; techniques like 3D printing and laser machining enable facile device design iteration without the high costs and skills involved

in MEMS fabrication [11]. However, presently, these additive/subtractive processes are only able to pattern a few elastomeric materials, which are often proprietary, and the processes are not readily amenable to directly pattern elastomers like PDMS [12,13] that are commonly patterned by replica-molding. Ingenious fabrication processes have been developed for machining soft materials to create actuators at various size scales [14-16].

Miniature robots are valuable for a variety of applications. In medical research, small robots are used for cellular and sub-cellular operations [17-20], and large robots are used to assist doctors during medical procedures and minimize invasive procedures [21,22]. Micromanipulators attached to robots enable access to internal organs, and are used to grip and manipulate delicate tissue, nerves, and blood capillaries [22]. Incorporating soft materials into medical robots minimizes the risks of injury during various procedures [23,24]. This is particularly useful in handling delicate samples like brain tissue that is so soft that neurosurgeons often excise tissue sections using vacuum instead of a cutting tool [25]. Surgical cutting tools, staplers, and needles are composed of hard materials because they must be able to exert high pressures accurately without becoming deformed [26]. However, tasks like occluding, dilating, grasping, stretching, probing, and positioning soft tissue structures benefit from using tools composed of compliant materials that can be collapsed for safer tool delivery and retrieval [27]. Soft active prostheses have even been used to support failing organs by dynamically adjusting force distribution [28].

Researchers have developed robots using soft and deformable materials and these technologies have been reviewed in several publications [4,29-31]. A wide variety of

driving principles have been demonstrated to generate and transmit forces within soft structures. Technological advancements in soft robotics involve expertise in multi-disciplinary engineering, soft-matter physics, and biomimetic design. Soft-bodied machines are envisioned to complement or replace existing technologies, particularly in complex environments which require the robot to vary its shape and form in order to complete tasks. These robots have the ability to squeeze through small openings, conform to irregular objects, handle small or delicate payloads, and to demonstrate multi-functional and multi-gait abilities. Soft robots are typically lighter in weight compared to conventional hard robots, have a collapsible design with few stress concentrations, are quiet during operation, and have high mechanical compliance and damage tolerance. Researchers envision that soft robots will be able to adapt dynamically to situations in field applications, navigate complex environments, perform with high dexterity in tight spaces, handle and transport irregular and unknown objects, and interact with people without causing injury [32]. Thin devices made of materials that are as compliant as skin or clothing, which can be electrically controlled, would enable the development of wearable robotics technology [33,34].

Soft robot design is often inspired by biological actuation systems composed entirely of soft tissues that enable motion and dexterity in plants and animals, such as the Venus fly trap and the octopus tentacle [4,35]. Just as muscles and plant organs have developed into various types to meet specific needs, each soft actuator technology has features that make it suited for specific application areas. The design of robust soft actuators must take into consideration the trade-off between material compliance, force generation,

speed, and stroke; stiff materials can provide higher forces, whereas soft materials can undergo large displacements. Other considerations can be compatibility of the soft robot with associated components of a system and scalability of the driving principles and manufacturing processes.

Today's soft actuators can be broadly classified into two categories: a) where motion is achieved by activating the actuator material itself and b) where the actuator material is deformed by pumping fluids within the body of the actuator. Each category is briefly described in the subsections below.

1.2.1 Actuation Using Stimulus-Active Polymers

Certain polymeric materials are able to change their morphology in response to an input energy stimulus (electrical, magnetic, thermal, optical, or chemical) and produce mechanical work [36]. Electroactive polymers (EAPs) respond to electrical stimulation. Combining the features of structural flexibility, actuation and sensing functions within the same material makes EAPs suited for developing artificial muscles and soft robots [37-39].

In electronic EAPs, charge transfer from the electrodes through the polymer is through electrons. There are several methods of transduction of this electrical energy to produce mechanical strain such as piezoelectricity [40,41], electrostriction [42], ferroelectricity

[43,44], and electrostatics [45]. In some polymers, the applied electric field can cause phase change which results in overall material deformation as seen in shape memory polymers and liquid crystalline polymers. In ionic EAPs, where the charge transfer from electrode to polymer is through ions of an electrolyte, conductive liquid is required for operation [46,47]. On the other hand, electronic EAPs are typically operated in dry environments. Examples of ionic EAPs include polymer gels [48,49], ionic polymer-metal composites (IPMC) [50], and conjugated conducting polymers [51-53].

1.2.2 Actuation Using Fluidic Power

A fluid is broadly defined to be a state of matter in which the constituent particles or molecules can freely move past one another when a force is applied to it. Fluids include both liquids and gases. Although all fluids freely yield to shear, they are distinguished by the speed with which they can deform in response to the force [54]. Gases deform much faster than liquids because their loose molecular bonds enable them to change both shape and size, whereas liquids are able to change only their shape but not their size. Fluidic power (using pressurized fluids) can be employed to generate high force densities in actuators [55]. This offers practical advantages for soft robotics because of the high compliance of fluids, the ability to transmit forces without gears, links or pulleys.

In a soft fluidic actuator, the force can be transmitted either pneumatically (using gases) or hydraulically (using liquids). The performance metrics of the actuator varies when the

fluid is changed from gas to liquid because of the difference in their compressibility. When the actuator fluid is a gas (i.e. it is operated pneumatically) it is capable of achieving large, rapid, displacements because gases have low viscosity and can quickly undergo large volumetric changes. However, because gases are compressible, the load capacity of the actuator is low, and it can be overly sensitive to load changes. On the other hand, when the actuator fluid is a liquid (i.e. it is operated hydraulically) then the actuator can lift much heavier loads because liquids are denser and nearly incompressible. (For example, when a balloon is filled with water instead of air it exerts a force one thousand times greater on its surroundings.) Liquids are more viscous than gases, therefore the actuator deformation would be slower but steadier (due to viscous damping of overshoots in pressure) than when it is pneumatically actuated.

An interesting actuator technology that combines the speed of pneumatics with the strength of hydraulics uses "jamming" [56] [57], a physical process in which a granular medium of solid particles (micron-sized or larger) behaves like a fluid at the macroscale when loosely packed and transforms into a solid-like material when packed or "jammed" into a smaller volume. This is akin to liquid-like behavior of free-flowing salt or the gas-like behavior of styrofoam beads. In jamming actuators, pneumatic pressure is applied to pack and unpack the granular medium.

Fluidic actuation is usually achieved by connecting the actuator, via tubing, to an external source of pressurized fluid [55,56,58,59]. In pneumatics, this source is often a cylinder of compressed gas, and in hydraulics the liquid is supplied by a displacement pump. The

flow of fluids to both pneumatic and hydraulic devices is generally controlled using mechanical valves. To create free-standing robots it would be advantageous to eliminate tethers to external equipment, and devise technology that would enable pressure generation to be directly mounted on the actuator. Autonomous fluidic actuators can be driven by generating flows by mechanisms such as phase change and electrofluidics (electrically induced flows).

1.2.2.1 Fluidics Driven by Phase Change

Pneumatic pressure can be created by liquid-gas or solid-gas phase transitions, typically achieved by applying heat or by chemical reaction [60]. Thermal phase transitions (usually reversible) in miniature devices can be realized by mounting Peltier elements that can heat and cool the device about the phase transition point of the fluid. Pneumatic pumping by thermal phase change has been demonstrated using volatile liquids such as diethyl ether [61], Fluorinert coolant liquids [62], Freons [63] and ethanol [64]. These liquids are vaporized by applying heat to form gases that expand and cause shape-change of compliant structures.

Phase change can also be induced by chemically reacting liquids to cause release of gases. This approach has been used to create a rolling soft robot [65] and an octopus-like soft robot [66]. The robots have discrete chambers of reactant liquids inside a microfluidic actuator, which are released and mixed by means of microvalves and micromixers to create gaseous reaction products. The flow of reactants, their mixing, and

the amount of gas contained in the actuating structure are controlled by sophisticated soft microfluidic machinery driven by fluidic pressure. Liquid-gas transformation can also be induced by electrochemical reactions. Electrolytic gases are released when an electric field is applied to a volume of liquid, which can be used to deform soft structures [67-69]. Chemical and electrochemical actuators, especially in small-scale devices, have a short device lifespan because of the limited volume of liquid reactants that can be contained within the device; most reactions cannot be easily reversed to re-form the liquid, because the reverse reaction is thermodynamically less favorable without the addition of a recombination catalyst in the gas phase. The volatility, flammability and/or toxicity of these fluids make it necessary to carefully design devices that are hermetically sealed to prevent loss of fluid, and to prevent potential safety hazards. Silicone elastomers have high gas permeability [70-72] and are therefore ill-suited for forming autonomous miniature pneumatic soft robots. Miniature robots operate on small amounts of fluid contained within the device, so if the actuator material cannot fully contain the gases the pumping fluid will quickly become depleted. Such actuators would require encapsulation with a flexible impermeable material that can serve as a gas barrier.

Hydraulic pumping by thermal phase change has been achieved using materials than can undergo smooth solid-liquid transitions within a short operating temperature range. For example, waxes undergo smooth phase transitions and can expand significantly in volume when melted. Wax-based pumping has been successfully demonstrated for miniature devices [73-75].

1.2.2.2 Fluidics Driven by Electric Fields

Fluids can be induced to flow by an applied electric field. A wide variety of electrokinetic flow phenomena can occur in heterogeneous (multiphase) fluidic systems; each type occurs under specific physical and chemical conditions [76-80]. These flows are caused by forces exerted by the applied electric field on the fluidic interfaces. Some of these phenomena can be employed to generate bulk motion for electrohydraulic actuation/propulsion. Electro-pneumatic actuation has been demonstrated by electrohydrodynamic corona discharge [81,82]. When a large electric field is applied to a gas through a sharp conductor, ionization of the gas occurs and the charged ions are pushed away from the sharp tip due to electrostatic forces resulting in "ion winds". This phenomenon has been used to create MEMS actuators [83-85]. However, due to the complex electrode geometry required to create ion winds, it may be challenging to embed these structures within a miniature soft actuator.

Bulk motion in liquids in response to an electric field can occur due to electrohydrodynamic and electrokinetic flow phenomena [86]. Electrohydrodynamic flows [87-89] are usually caused by forces originating at the electrode-liquid interface. For directional flow, this purportedly requires asymmetric electrode geometries which can add complexity to fabricating miniature soft actuators. Flow can also be induced by electrical forces applied to the interface of the liquid and the channel walls. The surface charge (wettability) of the channel wall can be modified by applying an electric field across the solid-liquid interface. The resulting liquid movement is known as

electrowetting, which has been used extensively for electronic displays, and has been demonstrated in pumping applications [90,91]. Liquid motion by electrowetting is localized to the electrode area. Using a single pair of electrodes, forces on the order of hundreds of μN can be achieved [92]. Using electrode arrays it is possible to laterally displace a liquid droplet from one electrode to the next adjacent electrode. However, it is not possible to achieve continuous bulk flow by electrowetting. In contrast, electroosmosis and electrohydrodynamic flow techniques are able to produce continuous fluid flow using only a single pair of electrodes. A summary table of the capabilities various electrohydraulic flow effects is presented in the book "Electrokinetics and Electrohydrodynamics in Microsystems" by Antonio Ramos. [79]

In this work, fluid flow due to **electroosmosis** was used to generate actuator force. Electroosmosis is the movement of bulk liquid relative to a stationary charged surface, when an applied electric field is applied to the liquid. Electroosmotic flows are enhanced by increasing the interfacial contact area between the liquid and the channel wall; micro/nano-fluidic channels have large surface-to-volume ratios [93] and therefore electroosmosis can be used to drive liquids more effectively than pressure-driven flows that can be hindered by surface tension effects at these scales. Also, unlike electrohydrodynamic flows, electroosmosis does not require specialized electrode geometries to focus the electric field for directional flow. These features make electroosmotic pumping highly suited for driving microfluidic soft robots. Several researchers have reported considerable force generation by means of electroosmotic flow (EOF) (reviewed by [94]). However, electroosmosis is yet to be applied as a robust

driving mechanism for miniature actuators. Water has been the choice of pumping fluid for electroosmotic applications. However, water splits to form electrolytic gases when a current passes through the pumping liquid, even at low voltages (> 1 volt) which causes device failure. This dissertation details the efforts to achieve bubble-free electroosmotic actuation to produce high forces and large strains in elastomeric devices.

1.3 Electroosmotic Soft Actuators

The objective of this doctoral research was to employ electroosmotic pumping inside a flexible substrate to create an actuator that will quickly undergo large deformations and lift substantial loads. This work was guided by the following hypotheses.

- Electroosmosis can be used for actuation because in microchannels it generates fast bulk flows and large pressures. Liquids are minimally compressible, so electroosmotic actuators will be able to transmit high forces.
- The liquid is pressurized by application of electric fields instead of mechanical force, therefore eliminating the need for external pumps.
- Flexible electrodes can be integrated into the actuator.
- It is possible to minimize the build-up of electrolytic byproducts inside the actuator by finding optimal designs, materials, and/or operating conditions.
- Using available resources fabrication processes can be developed for building compact modular soft actuators amenable to system integration.

1.3.1 Design Overview

The actuator design is inspired by the plant cell which is able to deform in response to a chemical gradient across its cell wall. When plant cells in an organ undergo deformation, this causes macroscale shape change of the organ. Plants exhibit a variety of reversible movements that occur in response to environmental stimuli known as "nastic" movements driven entirely by osmosis. Therefore, the actuators that use EOF for motion are dubbed here as "electro-nastic" actuators.

The electro-nastic actuators (Figure 1) include microscale channels connecting two reservoirs that are filled with a pumping liquid. Electrodes are positioned at either end of the microchannels and placed in contact with the liquid. Application of an electric field causes directional fluid flow to occur between the reservoirs that causes bulging and contraction of the surrounding elastomer, thereby causing overall change in the shape of the material. The direction of flow can be reversed by switching the polarity of the electric field.

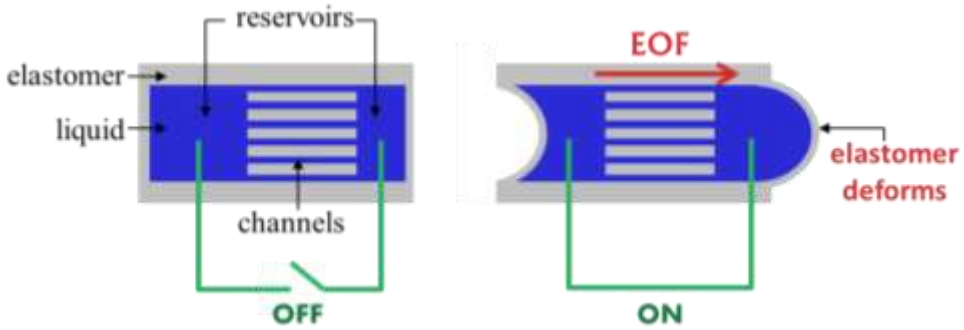

Figure 1. Schematic of the electro-nastic actuator. Deformation occurs upon applying an electric field due to electroosmotic flow.

1.3.2 Physics of Electroosmosis

Electroosmosis is the first electrokinetic effect that was discovered [78]. In 1808, Reuss observed that when an electric field was applied to wet clay soil (i.e. solid phase is the stationary phase) it caused directional flow of water (electroosmosis), and conversely when the electric field was applied to a suspension of clay particles (i.e. solid phase is the moving phase) in water, it caused directional flow of the clay particles (electrophoresis).

Electroosmosis is understood to be a surface effect; its magnitude and direction is defined by the charge distribution in the electrical double layer at the liquid / channel interface. The electric double layer (EDL) is a thin neutrally charged region that forms along the surface of the channel wall when in contact with the liquid; ions on the solid surface attract a cloud of counterions from the liquid by Coulomb forces to maintain electroneutrality. Thus, one side of the EDL is positively charged and the other is negatively charged resulting in an electrical potential across the EDL known as the zeta potential. The structure of the ion distribution in the EDL is described by theoretical

models, with the Gouy-Chapman-Stern model being the most standard model [95]. According to this model, the zeta potential decreases exponentially with distance from the channel wall [96]. The velocity and pressure of electroosmotic flow are directly proportional to the zeta potential. Large zeta potentials are achieved by employing highly charged surfaces and liquids with low ion concentrations [93].

In this work, the channels were formed of either PDMS or paper. In native PDMS the wall charge is attributed to ionizable silanol groups of the silica fillers in the PDMS mixture [97,98]. In paper, the surface charge is due to ionizable carboxyl, sulfonic acid, phenolic, and/or hydroxyl groups in cellulose [99]. A polar liquid with high dielectric constant is required to ionize the aforementioned chemical groups on the wall. In polar solvents the formation of counterions in the liquid (that are attracted towards the channel wall to neutralize the surface charge and form the electric double layer) occurs by phenomena such as autoprotolysis or auto-ionization, in which there is spontaneous transfer of electrons or protons between neighboring liquid molecules or the channel wall and the liquid [100].

When an electric field is applied along the channel, the outermost diffuse layer of charges that are loosely bound in the EDL is displaced, dragging the adjacent fluid by viscous forces, thereby generating electroosmotic flow. Electroosmotic flow in microchannels is assumed to have a plug flow profile (uniform velocity across the width of the channel) because the no slip-region (a thin layer of fluid that remains stationary because the liquid molecules are bound by Coulomb force within the EDL, also known as the Stern-Layer)

is minuscule in comparison to the channel size [93] [101]. If E is the applied electric field, ε is the permittivity of the liquid, ζ is the zeta potential of the channel/liquid interface, and η is its dynamic viscosity, then electroosmotic flow velocity (V) is given by [93],

$$V = \mu E; \text{ where } \mu = \frac{\varepsilon\zeta}{\eta} \text{ is the electroosmotic (EO) mobility.}$$

In nano-channels (< 100 nm), the Debye length (thickness of the mobile diffuse charge layer) is comparable to the channel width. Consequently, electroosmotic flow in nano-scale systems is found to have a parabolic profile EO flow, similar to Poiseuille flow, because no-slip boundary conditions apply at this size scale.

1.3.3 Actuator Performance

The standard metrics that are used to evaluate actuator performance are stroke, speed, and force, which determine actuator work and power. The stroke is determined by the volume of liquid that can be displaced and the compliance of the actuating structure. The speed is determined by how quickly the expansion chamber can be filled and therefore described by the flow rate (see Equation 1). The deformation force provided by the hydraulic pressure due to electroosmotic flow is given by Equation 2.

Equation 1 EO flow rate = $Nwd\,\frac{\varepsilon\zeta}{\eta}E$

Equation 2 EO pressure= $\frac{12\varepsilon\zeta L}{d^2}E$

Here, N is the number of channels of length L, width w, and depth d; ε is the dielectric constant of the pumping liquid of viscosity η. These equations apply when the thickness of the Debye layer is at least one order of magnitude smaller than the distance between the channel walls, so that EOF has a uniform flow profile [102]. The equations are invalid when the Debye layers at the channel walls overlap; in these cases the boundary layer effects will cause the flow to have a parabolic profile [102,103]. This can occur in nanoscale channels (usually << 100 nm), and also larger channels with liquid of low ion concentration resulting in thick Debye layers [104]. Equation 2 applies to shallow channels of rectangular cross section ($d << w$). Both flow rate and pressure depend linearly on the E, ζ, and ε. E can be increased by increasing the voltage and/or decreasing the spacing between electrodes. ζ can be increased by using channels with high surface charge.

In order to apply these theoretical design concepts in a soft actuator there are various research topics to be considered.

1.3.3.1 Pumping Liquid

Typically polar liquids are known to have high dielectric constants, and are hence best suited for EOF [105]. For actuator applications, the liquids should amenable to encapsulation in an elastomer and have low volatility. They should also be able to withstand large electric fields and not release electrolytic products that impede actuation, such as electrolytic gases or precipitates that can block the channels. The electrodes should also be composed of a corrosion-resistant inert material.

1.3.3.2 Channel Design

Increasing the channel width and depth increases the flow rate. In contrast, the pressure increases sharply as the depth of the individual channels are reduced. Therefore, to maintain a large pumping area for fast flows and simultaneously maximize force it is optimal to employ a dense network of micro/nanochannels. This will enhance the surface forces (like electroosmosis and capillary forces) and inhibit the bulk volume forces (like pressure driven flows, which can occur when loads are applied on the device). Employing numerous channels in parallel also ensures redundancy of design so that the actuator will continue to function even if some of the channels get clogged.

1.3.3.3 Deformable Materials

The ideal device must be able to quickly displace a large volume of fluid when subjected to an electric field and cause large deformations. The extent to which EOF can deform

the device material is limited by the material's elastic restoring force, or by other applied forces. So the actuating structure should be composed of a stretchable material that can be expanded and contracted with minimal effort to produce large actuator stroke, and the material must also be able to resist damage from external forces. The pump stroke can be improved by increasing the amount of liquid displaced by EOF. For this, the reservoir dimensions must be optimized to maximize holding capacity without causing significant backpressures.

1.3.4 Prior Work

This thesis builds on the first prototype device (see Figure 2) that was developed to demonstrate that electroosmosis could be used as a driving force for actuators [106]. The device was composed of polydimethylsiloxane (PDMS) and formed by replica molding using a microfabricated SU-8 mold to create planar reservoirs and connecting microchannels. A thin film of PDMS was formed on a smooth wafer by spin-coating. The cured film was plasma-bonded to the replica molded PDMS surface to form the actuating membranes atop the reservoirs. The pumping fluid in this work was de-ionized (DI) water. Salt was not added to the pumping liquid because water is known to undergo auto-ionization. The device was filled using silicone tubing, which was then plugged off to seal the device for actuation. The electrodes, spaced 3 cm apart, were platinum wires inserted through the tubing. Membrane deflections of hundreds of micrometers were achieved within seconds of applying a high voltage (kV).

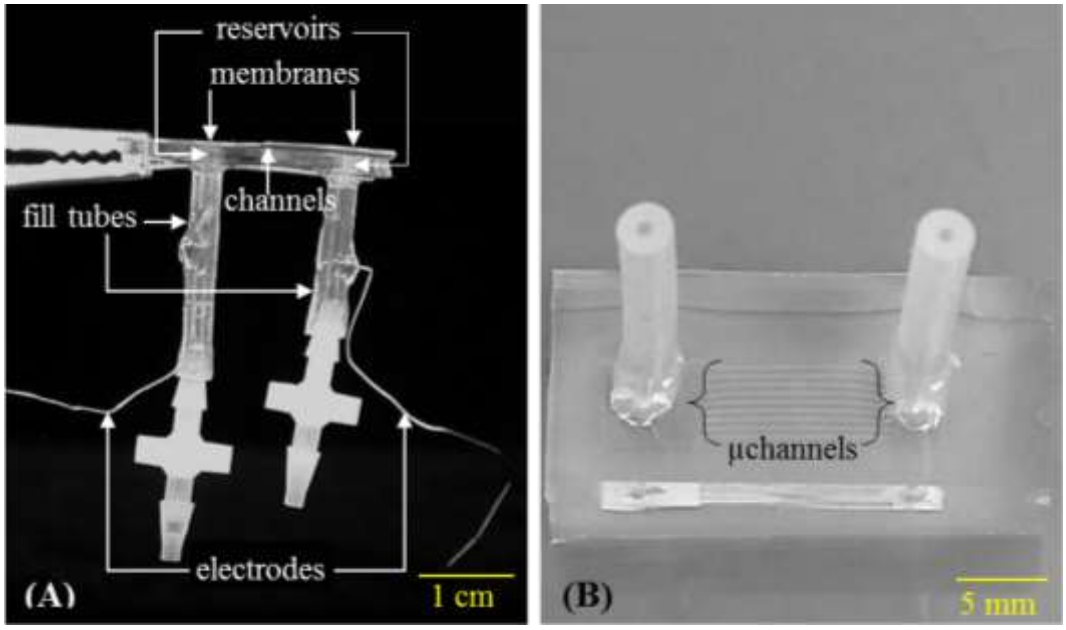

Figure 2. Photographs of original electro-nastic prototype actuator. (A) Side view of original actuator prototype showing protruding tubing and electrode wires. (B) Overhead view of the device showing two reservoirs connected by nine microfluidic channels. The reservoirs and channels were filled using the attached tubing. The actuating membranes covered the reservoirs. EOF caused liquid to flow from one reservoir to the other, causing the membrane to collapse at the reservoir supplying liquid and bulge at the receiving reservoir.

However, it was found that the device operation was limited to only a few minutes because electrolysis of the DI water occurred within seconds. This released bubbles into the device, resulting in the channel conductivity being cut off by the trapped gases. Based on visual observation of gases which collected at the top of the membrane, it is also likely that the pressures and deflections recorded were a combination of both EOF as

well as electrolytic gas pressure. PDMS is permeable to gases [70-72], so this possibly allowed some venting of the gases generated by electrolysis. However, this venting was inadequate as many of the gas bubbles remained trapped within the microfluidic channels. Additionally, the fluid had to be refilled frequently (due to the small volume capacity of the reservoirs) for continued operation of the device. These limitations made this prototype impractical for high-speed applications systems that require sealed actuators.

1.3.5 Actuator Fabrication and Operation

The original prototype was a useful proof-of-concept device to demonstrate that electroosmosis can be used to deform a flexible structure. However, the device design was unsuitable for actuator applications because of the large fluidic and electrical appendages, and relatively small pumping area. New multiscale, non-planar, manufacturing paradigms were required to tailor the design of the soft electro-nastic actuators for applications that require three-dimensional deformability. Drawing on the insights gained from the prior work, the following focus areas were proposed to create a modular, fully flexible, actuator that maximizes the space dedicated to the pumping channels, while minimizing the real-estate occupied by bulky components that limit actuator motion.

The microchannels are the most important components of an electroosmotic device because their surface properties, size, and number dictate the force, stroke, and speed of the device at a given voltage (refer Equation 1 and Equation 2). To simultaneously improve actuation stress and flow rate the surface-to-volume ratio of the channels must be maximized by increasing their number while decreasing their size. Depending on the form-factor required for the target application, the fabrication process should enable facile design iterations of the channels and reservoirs configuration/orientation (e.g. for displacing structures vertically/horizontally/diagonally), so that sizable volumes of fluid can be pumped without causing large backpressures. Standard PDMS soft lithography, using a microfabricated mold is suited for the creation of planar lab-on-chip type devices. But it is challenging to use this technique, or allied techniques such as photolithography, dry or wet etching, and microCNC machining, for creating features with aspect ratio greater than 10:1. Also, the overall thickness of devices made by soft lithography is typically several millimeters thick, because thin films of PDMS are difficult to peel off the mold. Thus, the active pumping region forms only a small portion of the device volume in conventionally fabricated PDMS devices.

The fluid filling tubes in the original prototype can considerably impede movement in miniature actuators, so an alternate tube-free method to fill and encapsulate the pumping liquid must be devise (while eliminating any trapped air.). For the same reason, the protruding metal wire electrodes must be replaced with embedded corrosion-resistant flexible electrodes. Electroosmosis is driven by the applied electric field (Equation 1), so

the required voltage for operation could be reduced while maintaining the electric field by placing the electrodes closer to each other.

2. **Limiting Electrolysis in Electroosmotic Systems**

Electroosmosis requires the application of large electric fields to generate fast bulk fluid transport. Applying high voltages to the liquids could result in electrochemical redox reactions that decompose the liquid to form gases or precipitate, or cause electrode corrosion. Electrolysis will degrade device performance and result in loss of pumping fluid if the gases diffuse through the elastomer. The most significant challenge in realizing this technology has been the mitigation of electrochemical reactions in the pumping fluid, at voltages higher than its redox potential.

Electrolysis has long beset electrohydraulic microsystems making it difficult to employ them for robust pumping applications. Several approaches were taken in the past to manage electrolysis in electroosmotic pumps by research groups including, like using AC instead of DC electric fields, chemically recombining the electrolytic gases to form liquid, or using functionalized electrodes that can trap the gases. Early in my PhD work I attended the 2011 Gordon Conference on Microfluidics where I had the invaluable opportunity to meet with Professors Juan Santiago (Stanford University), Martin Bazant (Massachusetts Institute of Technology), and Antonio Ramos (Universidad de Sevilla) and gain insight for applying these methods my electro-nastic devices. They unanimously held the view that electroosmosis is highly effective for driving fast flows in microchannels, but the methods employed thus far for managing electrolysis have been impracticable for sealed miniature elastomeric actuators.

The following sections describe my efforts to apply these strategies cited in the literature in the PDMS microchannel devices. EOF was monitored by monitoring the liquid meniscus rise, monitoring tracer beads, and/or looking at bubble movement.

2.1 Low DC Voltage

EOF has been described in the literature [93] to be dependent on the electric field. So it is expected that the operating voltage can be reduced by decreasing the electrode spacing. Electroosmosis has been demonstrated by applying low voltages [107,108] using closely spaced electrodes. As expected, based on the governing equations for EOF (refer Equation 1 and Equation 2), at low voltages these devices produce slow flows (nL/min) and low pressures. However it has been demonstrated that flow and pressure can be increased by using a series of pumping regions. Takamura et al were able to achieve 25 kPa at 10 V [108] with such a cascaded pumping EO device.

Based on the findings in the literature, I hypothesized that by using an array of closely spaced electrodes, the EOF caused by each electrode pair would cumulate and be able to overcome backpressure to propagate over a 1 cm distance. The electrodes were comprised of platinum with a titanium adhesion layer patterned on a silicon dioxide wafer. Gold electrodes using with chromium adhesion layer were found to be unsuitable for EOF testing with DI water because the underlying chromium experienced corrosion

and delamination when subject to an electric field. Ti (20nm)/Pt (200 nm) was deposited by e-beam. The metal-coated wafer was dehydrated for 10 min at 120 ^{o}C. It was then spin coated with hexamethyldisilazane (HMDS) adhesion promoter at 4000 rpm for 40 sec, followed by Shipley 1813 photoresist spin coated at 4000 rpm for 60 sec. The photoresist was soft baked by placing the wafer on a hotplate at 95 ^{o}C for 1 min. The photoresist was patterned by UV exposure (8 mW/cm^2, Karl Suss MJB-3 mask aligner), for 11 seconds through a mylar photomask. Photoresist was developed using Microposit CD-352 solution, and hard baked at 120 ^{o}C for 1 min. The electrodes were patterned by wet etching; the platinum was etched using hot (90 ^{o}C) aquaregia (3:1 mixture of hydrochloric acid and nitric acid), and the titanium was etched with hydrofluoric acid.

Five pairs of closely spaced Ti/Pt electrodes (see Figure 3) were patterned on a silicon oxide wafers. The electrode gap was varied from 25 μm to 200 μm. The spacing between the electrode pairs was kept constant. The width of the electrode trace was changed to fit the electrodes in the same space. The PDMS microfluidic device was bonded to the wafer with patterned electrode traces by oxygen plasma bonding (the PDMS device design, fabrication, and bonding conditions are described in Section 3.6.1.).

An electric field of 4000 V/cm was applied; so for a gap of 25 μm the applied voltage was 10 V. Two devices were tested for each electrode gap. Voltage was first applied to each electrode pair, one at time, to observe if flow may be observed using a single pair of electrodes by optimally positioning the electrodes with respect to the microchannels.

Then, the number of active electrode pairs was increased to two, three, and finally all electrode pairs.

First, the meniscus level in the capillaries inserted in the tubing was monitored. No change in the liquid levels was observed. Then, 10 μm polystyrene beads were added to the water to observe their motion under the applied field using a microscope. The beads moved in response to the electric field but they did not move beyond the electrodes, implying that their motion was due to electrophoresis and not due to fluid flow. Finally, a small bubble was introduced (while viewing the device through a microscope) with an air-filled 30 gauge syringe; the bubble was able to float freely in the channel. However, no bubble displacement occurred when voltage was applied. Noticeable EOF did not occur at tens of volts, while electrolytic bubbles continued to form at the electrodes.

Figure 3. Closely spaced electrodes for low-voltage EOF testing. Device with 5 pairs of electrodes. These electrodes are spaced by a 100 μm gap, and each pair is spaced by 1 mm.

The device was modified as shown in Figure 4 to prevent possible backpressures due to fluid in the tubing, the receiving reservoir end of the devices was cut off so that the device had only one reservoir and filling tube. The cut device was bonded to Ti/Pt electrodes formed on glass coverslips, with the electrodes aligned along the length of the channels. The electrode gap was 25 μm. Each electrode pair was spaced by 100 μm to minimize EOF in the reverse direction. The channels were partially filled with a small amount of DI water so that it covered the electrodes but the air-water meniscus was visible past the electrodes, so that displacement of the meniscus can be monitored to measure EOF. The filling tube was plugged. Four devices were tested at 10 V as previously described addressing some or all of the electrodes. The meniscus was observed through an optical microscope. No movement of the meniscus was observed.

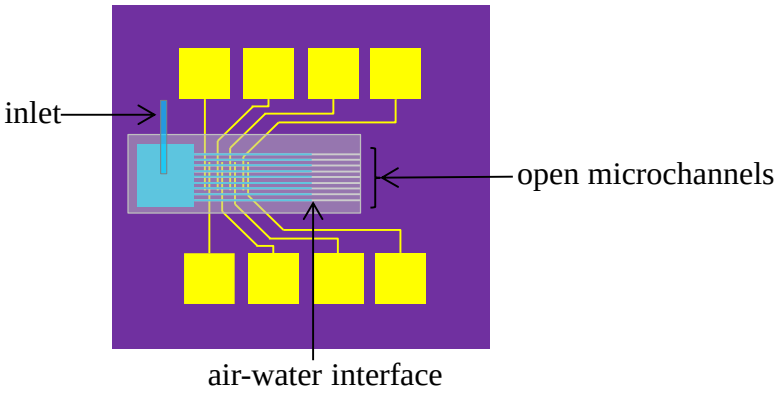

Figure 4. Device layout for low-voltage DC EOF. The electrode array is depicted in yellow. A microfluidic device with a single inlet tube and open channels was bonded to the electrodes. The flow was monitored by observing the air-water interface in the open microchannels.

In summary, although fast EOF was observed at high voltages (kV), EOF was not observed at lower voltages. At tens of volts considerable bubble formation due to electrolysis continued to occur. Further optimization of electrode geometry and the spacing between each pair of electrodes would be required. The operating voltage would need to be reduced below 1 V to prevent the electrolytic splitting of water while achieving appreciable EOF for actuation purposes.

2.2 Modified Input Signal

2.2.1 Delay Bubbles Using Square Wave

When a DC potential greater than the redox potential is applied to a solution, electrolysis occurs. When water undergoes electrolysis, hydrogen and oxygen gas molecules are formed at the cathode and anode respectively. Bubble nucleation occurs as the concentration of gas molecules increases on the electrode. Higher surface roughness increases bubble nucleation. The bubbles grow in size when the gas concentration is higher than its solubility in water, and may coalesce with other bubbles, until buoyant or convective forces cause the bubbles to detach and float in the channel.

With a continuous DC potential, this can occur within seconds depending on the current, ion concentration, pH, temperature, and electrode properties. If the current passed through the electrode is interrupted within this time period, and/or the applied voltage can be maintained below the redox potential of water, then the reactions at the electrodes and bubble generation can be prevented. I sought to answer whether Faradaic electrolysis reactions could be delayed and/or reversed by periodically turning off the applied field, and further if it might be possible to identify a duty cycle and frequency at which bubble growth can be stemmed, while generating fluid flow comparable to that achieved using continuous DC fields while.

The setup used for these tests is shown in Figure 5. Platinum electrodes patterned with a gap of 50 μm were used. The wafer was attached to an acrylic block stage using double-sided tape. A window was cut out of a sheet of transparency and adhered to the stage using electrical tape to create a reservoir (1cm×1cm) for the electrolyte. A 0.5 mL drop of electrolyte was dispensed into the reservoir window using a syringe. A glass coverslip was used to cover the drop to minimize the loss of electrolytic gases produced during the experiment flatten it, and to flatten the liquid drop to enable observation using a microscope.

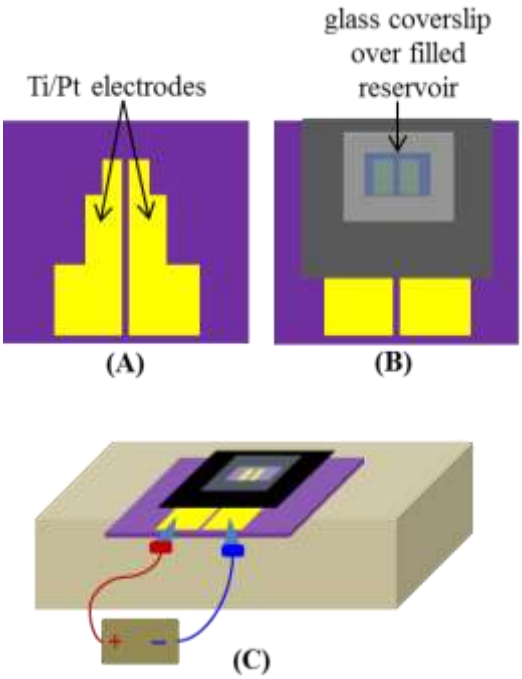

Figure 5. Test setup to study the influence of input signal on bubble formation. (A) Ti/Pt electrode layout. (B) The reservoir was taped over the electrodes, filled with the electrolyte, and sealed using a glass cover slip. (C) Experimental setup for bubble testing.

Voltage signals were applied using the Autolab Eco-Chemie PGStat. A 10 V on-off DC signal was applied to the electrodes; a 10 V AC square input from a function generator was superimposed with 10 V DC signal. Frequencies of 200 kHz, 100 kHz, 50 kHz, 25 kHz, 4, kHz, 1 kHz, 0.4 kHz, 40 Hz, 4 Hz. Four electrode samples were tested, samples A and B were tested in ascending of signal frequency, and samples C and D were tested in descending order, once each. Then voltage was stepped up to 10 V at 50 Hz for different duty cycles; three runs were conducted in a single device.

The results obtained for the frequency tests are shown in Figure 6A. In Samples A and B, bubble formation occurred within a few seconds under a pure DC signal, and as the frequency was increased although there was a marginal delay in bubble generation. However, the bubble generation rate at high frequencies was much faster than in samples C and D. This implied that the electrochemical reactions that occurred during the DC cycle had irreversibly affected the system. Upon closer inspection it was observed that electrode pitting had occurred at some of the sites of bubble generation. Based on the results from samples C and D it may be inferred that a small increase in the frequency of the applied DC voltage can delay bubble formation by several minutes.

The plot in Figure 6B shows the time taken to see bubbles at each duty cycle for a 50 Hz square wave stepped to 10 V. The results implied that bubble formation could be delayed by several seconds by turning off the voltage for short durations. With pure DC bubbles were seen within 5 seconds. When voltage was turned off for 10% no bubbles were observed for at least 2 minutes.

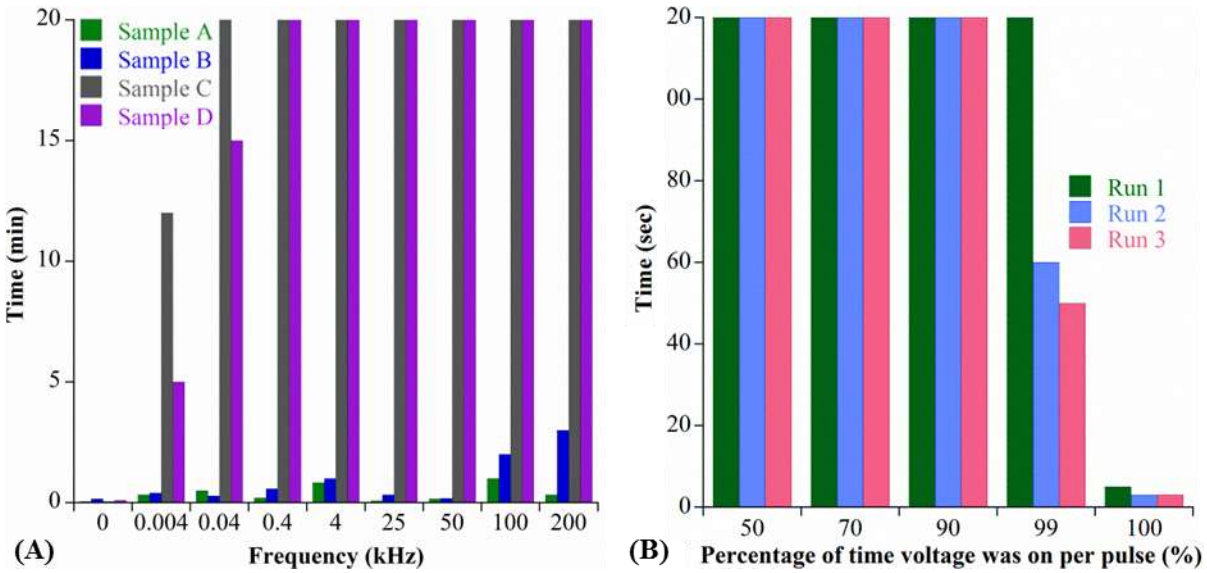

Figure 6. (A) Bubble generation rate when voltage is stepped up to 10 V at different frequencies. The frequency of the signal was increased from 0 Hz to 200 kHz for samples A and B, and for samples C and D the frequency was decreased from 200 kHz to 0 Hz. (B) Bubble generation rate vs duty cycle for a 10 V on-off input with 50 Hz frequency.

2.2.2 ACEOF

Several papers have been published on employing methods to induce EOF with applying DC fields [80,109] [110] [79,111-113] [114] [115] [116,117]. Applying a low-voltage alternating-current (AC) electric field, to generate electroosmotic flow would ensure that a net-zero current passes through the electrolyte solution, thus avoiding the occurrence of faradaic reactions at the electrodes. A symmetric AC field cannot produce net flow as forward and reverse flows are equal and opposite in each AC cycle. Unidirectional fluid

motion using AC fields may be generated by two methods: using asymmetric electrodes or by applying an asymmetric input signal.

When an AC field is applied to the electrodes, capacitive charging occurs and polarizes the electrode surface. A Debye double layer is formed between the electrolyte and electrode to screen the external electric field [111], [117], [80], [79]. The AC field induces a current that charges the Debye layer like a capacitor. The charging process can be described using an RC circuit analogy [111], [117], [118]. The time constant for charging is given by $\tau_o = R_o C_o$ where R_o is the resistance of the bulk electrolyte, and C_o is the Debye layer capacitance; the time constant for discharging (charge transfer by Faradaic reactions) is given by $\tau_{ct} = R_{ct} C_o$ where R_{ct} is the charge-transfer resistance between the solid electrode and liquid electrolyte [118]. The pumping velocity is optimal when the frequency of the AC input, $\omega \approx \tau_o^{-1}$ [118].

Unidirectional flow may be achieved by creating an asymmetry in the electrodes, either by tuning surface electrochemical properties or the shape of the electrode surface [117]. The flow is directed from the electrode of higher surface charge to that with a lower surface charge. In DC electroosmosis the electric field is constant throughout the system; in AC electroosmosis the field is non-uniform and more concentrated at the corners of the electrodes. The tangential component of the electric field causes an electrostatic torque which results in convective rolls which sets the liquid in motion [79]. The net fluid flow scales quadratically with the applied field and can be modulated by varying the electrode capacitance or design [117].

For this approach to be incorporated into soft robot design, electrodes with asymmetric geometry must be microfabricated (which can be challenging), that are also compliant and stretchable. To transmit forces over distances that would be significant for actuation, large arrays of these asymmetric electrodes would be required. To minimize the complexity of design and fabrication of my device I decided to instead attempt to generate ACEOF using asymmetric input signals that have been described in the literature [119,120].

2.2.2.1 DC-Biased AC Signal

Background

AC-EOF was demonstrated by applying a DC bias to the AC field by Wu, et al [119]. The applied AC signal with DC bias of magnitude V_0 is of the form $V_{applied} = V_0$ (1+cos $2\pi wt$), where f is the input AC frequency in Hertz. At low voltages, capacitive charging occurs, when counterions form a double layer to screen the electric field. At higher voltages, Faradaic charging occurs, by the formation of co-ions due to electrochemical reactions at the electrodes. At the negatively charge electrode the charging mechanism is capacitive, whereas at the positive electrodes charges are produced mostly due to Faradaic reactions. When the applied DC biasing voltage is sufficiently high, the symmetry in the surface charge at the electrodes is broken and directional flow from positive to negative potential occurs.

The experimental setup described by Wu et al [119] consisted of microfabricated arrays of Au/Ti electrode pairs patterned on a silicon substrate, Ti being the adhesion layer and Au being in contact with electrolyte. The electrodes were 80μm wide and 40μm apart. A PDMS microchannel (cross-sectional area 100 × 500 μm^2, 2 mm long) was bonded to the silicone substrate containing the electrodes. DI water was used as testing solution and EOF was monitored by tracking the motion of 3μm diameter polystyrene spheres suspended in the water. V_0 was varied from 0 to 4 V; the frequency was varied between 25 and 500 Hz. It was observed that up to 2.2 V particle motion was localized and caused due to capacitive vortices. Beyond 3.4 V, directional particle flow was observed. The flow rate increased exponentially with voltage. Bubbles were observed at $V_0 = 6$ V. Bulk fluid flow was also claimed to have been observed by observing the movement of the air-water interface in a partially filled microchannel; a flow of 100 μm/sec was observed at 3-4 min for 30 min.

Testing DC-Biased AC Signal for Electro-Nastics

First, I tested the described approach to observe bubble formation. The test set up described previously in Figure 5 was used, with DI water as electrolyte. Using the Eco-Chemie, an input 11 V/100 kHz square wave was offset by -1 V DC (i.e., the positive cycle was 4.5 V and the negative cycle was -5.5 V). The DC bias was then increased to -2 V (i.e., the positive cycle was 3.5 V and the negative cycle was -6.5 V). Two sample electrodes were tested for each signal, and two trials were conducted per sample. It was observed that no bubbles were formed for at least 10 min, for both signals. To test if flow

could be generated using these signals, I bonded a PDMS microfluidic device to the electrodes by oxygen plasma treatment as shown in Figure 7. The device was filled with DI water.

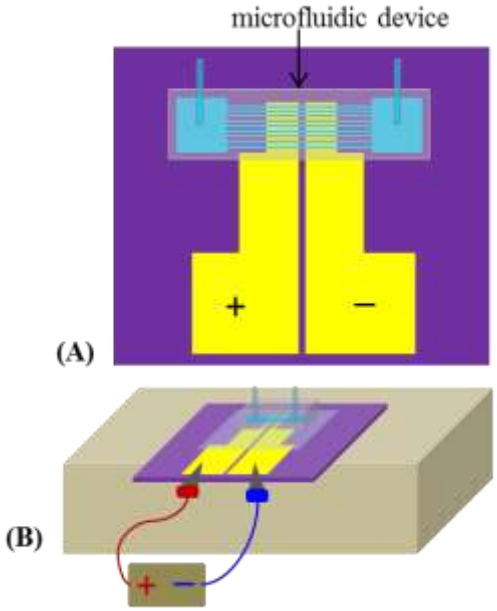

Figure 7. (A) A PDMS microfluidic device was bonded to a wafer with patterned platinum electrodes. (B) Experimental setup to apply various electrical signals to test for bubble-free EOF.

When voltage was applied no displacement of the liquid was seen at the inlet and outlet tubes. So, polystyrene beads (10 μm) were introduced into the channels. Two devices were tested for each signal, and two trials were conducted per device. When the DC-biased AC signal was applied, the particles were observed to oscillate about their initial positions but no net directional movement was observed for the -1 V or -2 V DC-biased AC inputs. Two devices were tested. Thus, this was ruled out as a viable approach to control EOF for my actuators.

2.2.2.2 AC-EOF Using Zero-Average Current Input

Background

In addition to applying a biased AC field, ACEO has also been reported by applying an asymmetric signal (shown in Figure 8): the positive and negative portions of each cycle are of different magnitude and duration, but the time-averaged input for the cycle remains zero, thus avoiding gas generation [120].

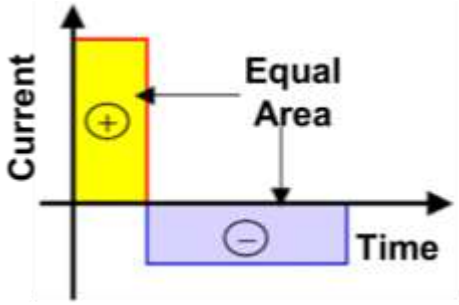

Figure 8. Zero time-averaged asymmetric AC signal input [120].

The test device described by Selvaganapathy et al [120] contained 16 parallel microchannels (each 50 μm long, 3 μm tall, and 3 μm wide) connecting two reservoirs. Two gold (no adhesion layer was mentioned between the gold and parylene) electrode pads (200 μm long, 20 μm wide, and 200 nm thick), were patterned to flank each end of the microchannels, therefore electrode spacing was 50 μm. The pumping liquid used was 10 μM NaCl. EOF was monitored by tracking the motion of 1μm diameter polycarbonate spheres suspended in the liquid. A 1 Hz current input with the waveform shown below was applied. In each pulse cycle, 1 nA was applied for 1/3 sec and -0.5 nA

was applied for 2/3 sec. The peak voltages when applying this input varied between 7 and 10 V. The beads were observed to exhibit pulsatile motion, moving back and forth in keeping with the applied field, but with net movement towards the downstream reservoir. The net particle velocity was 20 μm/sec at 1 Hz; the highest frequency at which movement was visible was 10 Hz. Bubble formation was observed at frequencies below 0.5 Hz. EOF was also recorded by tracking the motion of a bubble, formed intentionally by electrolysis, in a glass microchannel bonded to silicon; the velocity of the bubble was about 30 μm/sec at 1 Hz. The operation time for the device was claimed to be 15-20 sec after which backpressure overwhelmed the EOF. However, there was no mention about how long the device is able to operate without bubble formation.

To reduce backpressure, a porous monolith was introduced to increase the hydraulic resistance [121]. The microchannels were replaced with a polymeric microporous plug of 300 nm pore size, and the pumping liquid was replaced with DI water. EOF was monitored by observing the water-air interface downstream. The maximum velocity was 1.8 μm/sec at 0.8 Hz. The velocity was increased to 14 μm/sec by decreasing the width of the downstream region from 200 μm to 20 μm. The device consisted of a vent hole positioned at the upstream edge of the porous plug to vent air bubbles formed during filling or due to electrolysis.

Testing AC-EOF Using Zero-Average Current Input for Electro-Nastics

I tested the zero-averaged current signal approach for bubble generation. The test set up described previously in Figure 5 was used, with DI water as electrolyte. Signal inputs were applied using the Eco-Chemie. Zero-averaged current input at 2 Hz frequency were applied; positive and negative current were applied for 30% and 70% of the time, respectively, for each cycle. Two electrode samples were used for the tests. In each sample the current magnitude was decreased until bubble generation ceased; this was repeated twice per sample.

Table 1. Time taken for bubble-formation using 2 Hz zero-averaged current inputs.

Current (A)		Time (sec)		Observations
0.7	-0.3	0.15	0.35	copious bubble formation ≥ 5sec
0.07	-0.03	0.15	0.35	copious bubble formation ≥ 5sec
0.007	-0.003	0.15	0.35	copious bubble formation ≥ 5sec
0.0007	-0.0003	0.15	0.35	slow bubble formation ≥ 10 sec
0.00007	-0.00003	0.15	0.35	slow bubble formation ≥ 10 min
0.000063	-0.000027	0.15	0.35	no bubbles ≤ 20 min
0.000056	-0.000024	0.15	0.35	no bubbles ≤ 20 min

The results are shown in Table 1. Although the net current per cycle was zero, at this low frequency, it was observed that bubble formation could not be prevented unless the current values were less than 70 μA in the positive/negative portions of the cycle.

Flow was tested using a PDMS microfluidic device bonded to the electrodes using the set up shown in Figure 7. No movement of liquid was seen at the outlet tubing, so the motion of polystyrene beads (10 μm) device in DI water was tracked. A current input signal of 2 Hz was applied: 63 μA for 0.15 sec and -27 μA for 0.35 sec per pulse. Two devices were tested, and two runs were conducted per device. When the zero-averaged

current signal was applied, the particles were observed to exhibit net motion from the positive to the negative electrode. The forward displacement during the positive portion of the pulse was faster and larger than the slower, smaller backward motion during the negative portion giving a net positive particle velocity of 1 mm/sec.

It was however observed that particle motion did not continue beyond the location of the electrode. To test for bulk fluid flow, glass capillaries were attached to the device outlet. Upon application of the signal, no movement of the meniscus was observed. A device with larger microchannels (2 cm long, 1 mm tall, and 1 mm wide) was fabricated using a laser machined Delrin mold. The device was filled with DI water and the tracking beads were introduced. When the current signal was applied, similar particle motion was observed as in the smaller microchannels. A small air bubble was introduced into the channel using a syringe. Upon application of the signal, no displacement of the bubble was observed.

The tests were repeated in two other device designs shown in Figure 9 to confirm the absence of EOF. Syringe needles (30 gauge) were used as the electrodes. In the design shown Figure 9A multiple pumping zones were created so that the flow could be propogated over a longer distance and overcome backpressures. Single and multiple electrode pairs were employed. Figure 9B shows another design that was created to observe if particles motion occurred beyond the electrodes. Two large reservoirs were created in PDMS using a tape molds. The ends of the reservoirs formed were cut off to open them to atmosphere. Holes were punched at the top of the reservoirs in line with the

nastic device tubing. The PDMS nastic device was then plasma bonded over the reservoirs.

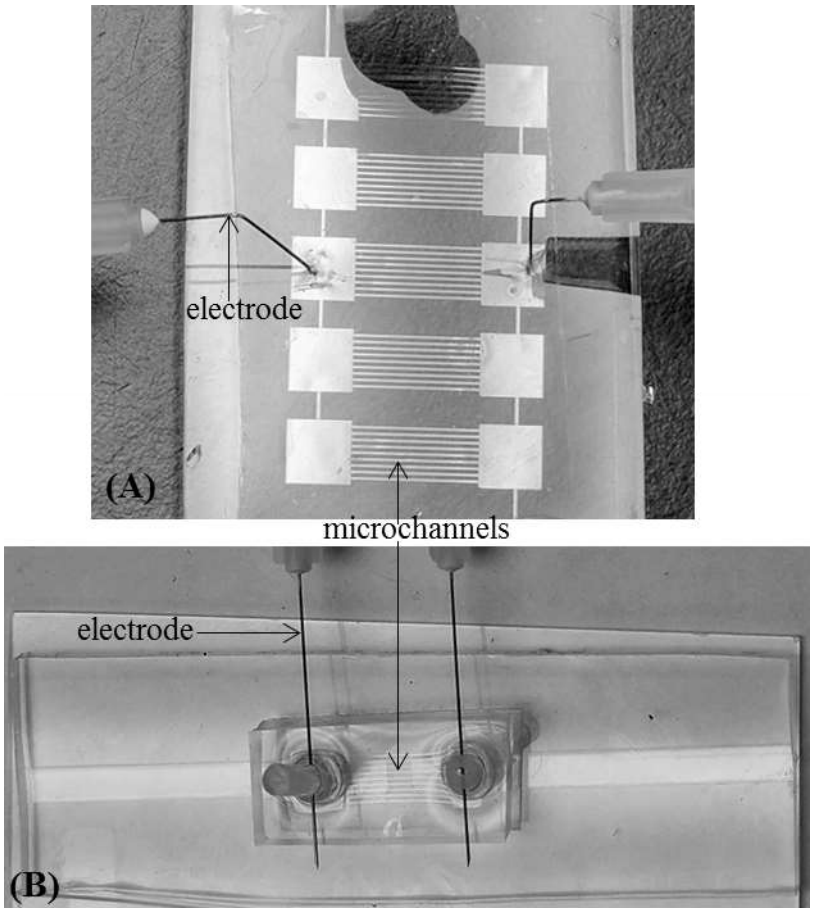

Figure 9. (A) Device with multiple pumping zones. (B) Microfluidic device mounted over large channels.

As observed in the previous test, no fluid motion was seen, and the particles only electrophoresed and did not flow past the electrodes. No movement was observed with introduced bubbles. In conclusion, although particle motion was seen, no liquid movement was detected when tracking an air bubble or a liquid meniscus. Thus the conclusion was that particle motion was predominantly due to electrophoresis not

electroosmosis. Even if imperceptible EOF did occur, the liquid displacement was likely too small to be applicable for actuator development.

2.2.2.3 FlowFET

Background

EOF has been demonstrated using low driving voltages by a technique known as flowFET [122,123]. This involves amplifying EO mobility by enhancing the surface charge of the microchannel, during EOF, by applying a perpendicular potential field (Figure 10). This setup is analogous to a field-effect transistor (FET) where electric current is manipulated by a perpendicular field generated by a gate electrode. When a positive gate voltage is applied externally to the microchannel then an equal and opposite negative charge is induced on the inner surface of the microchannel wall to maintain electroneutrality. This technique allows dynamic control of the direction and magnitude of EOF velocity. I expected that using this approach it may be possible to reduce the required driving voltage to minimize electrolysis by increasing the zeta potential at the channel wall.

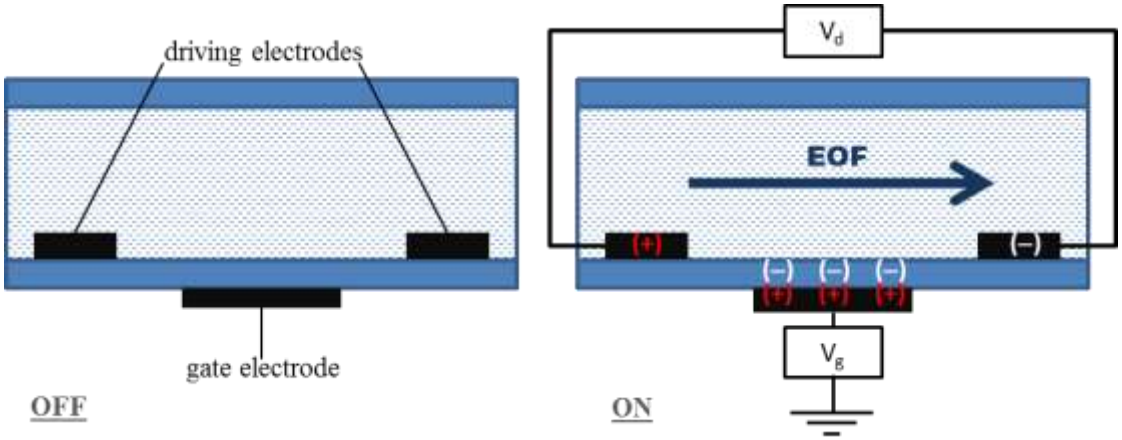

Figure 10. Illustration of flowFET concept.

In the work by Schasfoort et al [122], DC fields were applied to the electrolyte (buffered 2 mM NaH_2PO_4/H_3PO_4 solution of pH of 3.6). EOF was tracked by observing the movement of a dye front; red rhodamine B dye was added to the pumping liquid at one end of the microchannel. Fluid motion was slow when only the 25 V driving voltage (30 V/cm) was applied. The flow was accelerated when the gate voltage was applied; gate voltages between -35 V and 20 V were tested. A gate voltage of -35 V resulted in a flow velocity of 50 μm/sec.

Wu et al [124] demonstrated that bubble-free flowFET EOF could be generated by applying AC voltages instead of pure DC. The driving voltage was applied as an AC symmetric square voltage waveform along the axis of the microchannel. The gate voltage to modulate zeta potential was also applied as an AC symmetric square waveform perpendicular to the microchannel, and phase synchronized with the drive voltage. The phase synchronization allowed the surface charge to change with driving field resulting in

rectified EOF, so that flow direction remained constant for both positive and negative AC cycles.

Gold (200 nm) (with 20nm chromium adhesion layer) was deposited on a glass substrate to form the gate electrode. PDMS was spin coated on the metal to form the dielectric layer. A PDMS device with microchannels (20 mm × 2 mm × 3 mm) and reservoirs on either end was bonded to the dielectric layer. The device was open to the atmosphere. Platinum wires were threaded into the reservoirs to serve as driving electrodes. A function generator equipped with two channels was used to apply the 10 Hz square waveform to the gate and driving electrodes. The function generator was connected to an amplifier to modulate the voltage amplitudes. For a driving field of 5 V/mm and gate voltage of 300 V, EOF velocity of DI water was 42 μm/s, observed by tracking 8 μm polystyrene beads.

Testing FlowFET for Electro-Nastics

These two flowFET approaches were investigated with the experimental set up shown in Figure 11. A silicon wafer was coated with Cr (20 nm)/Au (200 nm), by thermal evaporation, to form the gate electrode. PDMS was spin coated over the gold electrode and cured to form a 20 μm layer. A second 20 μm layer was spin coated to cover any pinholes in the first layer.

A PDMS microfluidic device (fabricated as described in 3.6.1.1) was bonded to the PDMS film. Platinum electrodes were threaded through the inlet and outlet tubing. The device was filled with DI water. Glass capillaries were inserted into the tubing.

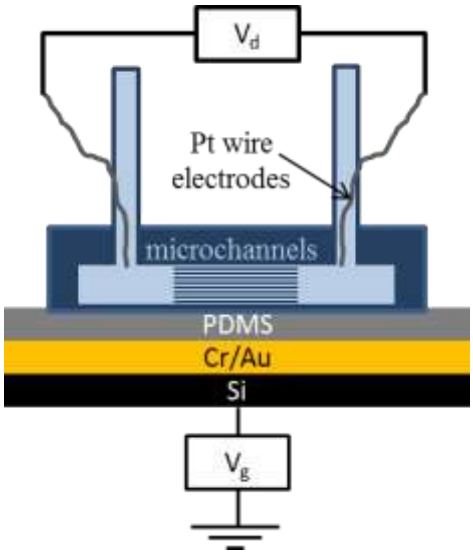

Figure 11. Schematic of experimental setup for testing EOF by flowFET.

Driving voltage between 25 V and 500 V was applied across the channel (electrode spacing 1 cm). Gate voltages between 25 V and 4000 V were applied. No fluid flow was observed until the driving voltage was increased to 500 V and the gate voltage was increased to 4000 V. At these conditions, flow was observed to occur from the negative electrode towards the positive. This was surprising as the negative zeta potential induced by the gate voltage was expected to cause flow towards the negative electrode. Upon closer inspection it was observed that a small burn hole had formed in the PDMS indicating that dielectric breakdown of the PDMS had occurred, resulting in DC EOF that was driven by the potential difference between the gate electrode and the positive driving

electrode. This occurred in three other devices that were tested in a similar manner. This approach was not pursued further as EOF based on DC flowFET was not achieved.

The AC flowFET approach was tested by applying a 10 V, 10 Hz symmetrical AC square wave to both the gate and driving electrodes. Due to unavailability of the amplifier discussed in the literature, it was presumed that EOF may not be observable by capillary rise, so bead movement was tracked under a microscope. The beads were observed to oscillate symmetrically about their initial position, but no net directional movement was observed in the two devices tested.

ACEOF Conclusions

I concluded that the results achieved in the literature could not be reproduced because of dissimilarities in the experimental setup and the capabilities of the powers sources used. It is likely that the flows generated by ACEOF can be transmitted only across small distances, and to achieve bulk flow in long channels using ACEOF more careful electrode array design would be required. I also realized that in order to override the electrophoretic forces on the beads it would be necessary to pre-treat the beads to remove their surface charge [125].

2.3 Catalytic Recombination of the Electrolytic Gases

Based on the various signal inputs that were tested, it became apparent that pure DC EOF was the most effective method of generating flow, and that alternate methods of mitigating the electrochemical degradation needed to be researched.

It has been demonstrated that hydrogen and oxygen can be recombined over a Pt catalyst [126], and recombination has been demonstrated in a closed microfluidic apparatus [67,127,128]. However, in these systems the recombination occurs in the gas phase in an allocated headspace, not within the liquid. Nevertheless, I attempted to see if it may be possible to achieve recombination of the electrolytic gases by using closely spaced platinum electrodes with ample surface area for catalyst action. The electrodes were 3 mm wide and were separated by 25 μm (this was the smallest size that could be microfabricated using a mylar photolithography mask). The data collected from the first experiment in shown below. Using the Eco-Chemie, a field of 4000V/cm was applied to each electrode sample. The experimental setup was similar to that described in previous bubble monitoring tests. Ten runs were conducted in three devices. Fresh DI water was used for each run.

Figure 13 shows the deterioration of the current output recorded when 10 V was applied continuously for 1 min, in ten successive runs. Figure 12 shows bubble patterns in two runs over 1 min. It shows the difference in bubble patterns in earlier runs where bubble formation is slow and recombination may be occurring, as the bubbles can be seen to

dissolve. After run 6, bubble dissolution no longer occurred; Figure 13 shows an increased number of peaks indicating redox reactions. The images show that electrode deterioration occurs near the site of bubble formation; the Ti layer was observed to be intact, but delamination of the Pt layer occurred near the electrode edges. It was concluded that applying a low DC voltage across closely spaced platinum electrodes may be useful to increase the operation time of a device by a few minutes, but was not a feasible solution for long term operation.

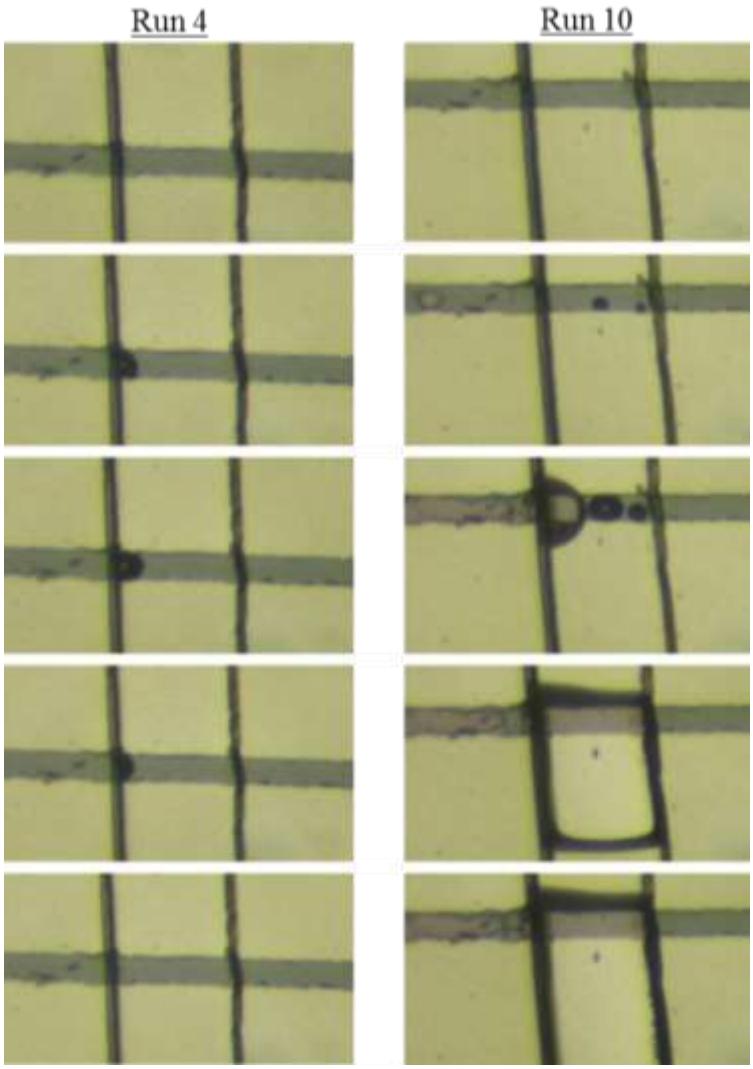

Figure 12. Time lapse of bubble formation over 10 sec in DI water at 10 V, applied across platinum electrodes spaced by 25 μm.

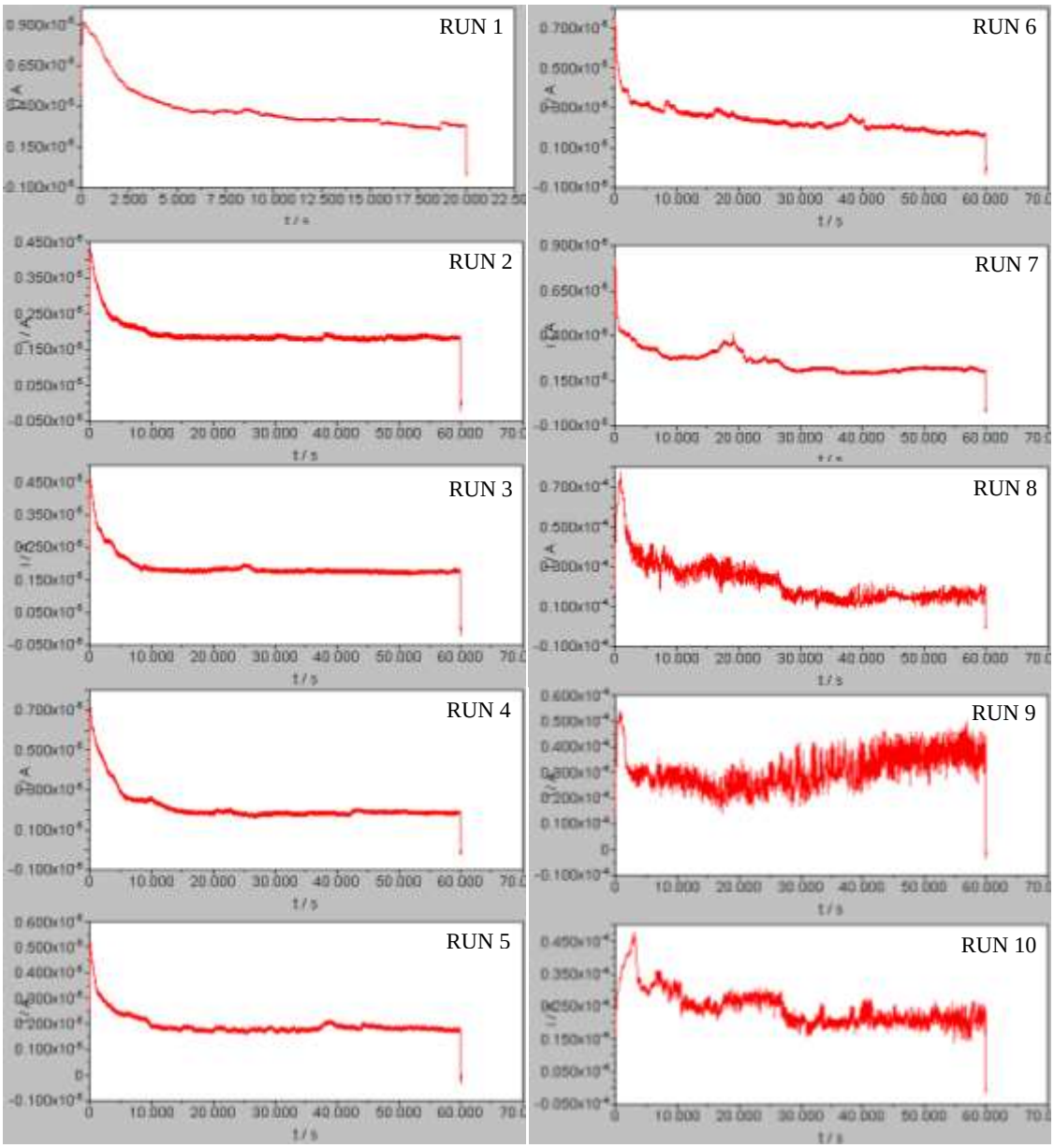

Figure 13. Variation in current as an indicator of electrochemical activity.

2.4 Active Electrode Materials

Electrolytic gases have been reduced in electrochemical systems by using active electrodes that either that are able to undergo chemical reactions instead of the liquid electrolyte, or by physically capturing the gases.

It has been observed that palladium has a high affinity for hydrogen and has been used for absorption in electrolytic systems [129]. Coating the electrode with organic conducting polymers has been reported to physically isolate the electrode and electrolyte while permitting charge transfer. Charge transfer occurs by ion transport from the redox reactions of the polymer material at the electrolyte interface [130]. EOF has been demonstrated at less than 2 V using poly(3,4-ethylenedioxythiophene) electrodes, and the electrodes were shown to be stable for potentials of at least 100 V. [107]. Another approach was to incorporate a salt bridge between the electrodes; Ag/AgCl salt bridges have been patterned by photolithography in microdevices to achieve stable EOF at 10 V [108].

However, relying on the electrodes to eliminate the gases seems likely to have a low lifetime due to the finite extent to which the electrode material will be able to adsorb or react with the electrolytic gases before being mass-transport limited, especially in miniature devices that can accommodate only small amounts of electrode material.

Polypyrrole (PPy) is a conjugated polymer that has been used to protect electrodes against corrosion in electrochemical systems [131]. Coating the electrodes was expected to increase the lifetime of the devices, as long as the PPy was able to under redox changes..

The PPy(DBS) layer was deposited on stainless steel wires and platinum wires potentiostatically (Eco-Chemie AutoLab) to a thickness of 30 nm at 0.46 V vs. Ag/AgCl in 100 mL of an aqueous mixture of 0.1 M pyrrole monomer and 0.1 M NaDBS (sodium dodecyl benzene sulfonic acid). The PPy-coated electrodes were rinsed thoroughly with DI water, and placed in a glass vial filled with 10 mL DI water spaced by 1 cm.

A DC voltage of 15 V was applied to the electrodes. Bubble formation was observed within 5 sec using the steel electrodes and within 10 sec using the Pt electrodes. Thus, it appeared that the polypyrrole coating was not effective at reducing or delaying bubble generation at the operating voltages required for EO actuators.

2.5 EOF testing with Other Pumping Liquids

It has been reported that adding hydroquinone to water can prevent it from forming electrolytic gases in electrochemical systems that use kilovolts and microamperes [132]. The explanation is that the oxidation of water is replaced with the oxidation of more hydroquinone a shown in the equations below. The product, p-benzoquinone, is water-

soluble and replaces the formation of gaseous oxygen gas, thereby eliminating bubble formation [132].

$2H_2O(l) \leftrightarrow O_2(g) + 4H^+ + 4e^-$; $E°_{red} = 1.229$ V

hydroquinone $\leftrightarrow$ p-benzoquinone $+ 2H^+ + 2e^-$; $E°_{red} = 0.699$ V

I tested concentrations of 50 mM and 100 mM hydroquinone (Sigma Aldrich) in unbuffered DI water. I applied 10 V signals using platinum electrodes in the set up shown in Figure 5. With 50 mM and 100 mM hydroquinone bubble suppression was achieved for 45 sec and 2 min respectively. In comparing my results to the literature, I concluded that hydroquinone reduces but does not eliminate bubble formation. This is helpful for high-flow open electrochemical systems where the bubbles can be expelled, but not for closed actuator systems.

My subsequent efforts involved replacing the water with a polar, organic pumping fluid with a wider electrochemical window. The fluid must be compatible with the PDMS elastomer used to make the device. Organic solvents can swell PDMS and pumping fluid can be lost due to evaporation and leakage; making it necessary to modify the PDMS surface to seal in the liquid. PDMS was the chosen material for device fabrication due to its chemical resistance, and ease of processing for creating flexible microfluidics. The liquids that were chosen for testing were ethanol, isopropanol, methanol, N-methyl formamide, acetonitrile, 3M Fluorinert electronic liquid FC72, and propylene carbonate. They were chosen due to their high ratio of dielectric constant to viscosity which should

produce fast electroosmotic flows. Dimethyl sulfoxide (DMSO) have been cited for bubble-free EO but it was not tested due to its toxicity [133].

Each of the liquids was tested for bubble formation. Two platinum wires (28 gauge) were placed, 1 cm apart, in 10 mL of solvent taken in a glass vial. A DC voltage of 15 V was applied to the electrodes. Bubble formation was observed within 10 sec in ethanol, isopropanol, and methanol. Bubbles were seen after 1min in acetonitrile and 2 min in N-methyl formamide. No bubbles were seen in FC72 and propylene carbonate over 5 min.

Flow testing was conducted using the set up used in Section 3.2.2. The microfluidic devices were filled with the test solvent. A voltage of 5000 V was applied, and the movement of the meniscus in the glass capillary was observed. Liquid movement was observed using ethanol, isopropanol, and methanol, N-methyl formamide, acetonitrile, and propylene carbonate. However, with acetonitrile it was observed that the solvent was oozing out of the PDMS, this would impractical for development of a robust actuator. The FC72 was too volatile to conduct a flow experiment successfully, the liquid in the device evaporated with seconds of filling the device.

In conclusion, the most promising of these solvents for extending the EO device operation time was propylene carbonate. This finding led to the study on EOF using propylene carbonate presented in the earlier sections.

3. **Bubble-Free Electrokinetic Flow with Propylene Carbonate**

Author Contributions: Elisabeth Smela conceived the idea of testing propylene carbonate for EOF. Deepa Sritharan and Elisabeth Smela designed the devices and the experiments. Deepa Sritharan fabricated the microfluidic PDMS devices and designed the test experiments. Abraham Simpson Chen and Deepa Sritharan performed the experiments. The data from these experiments were analyzed by Abraham Simpson Chen, Deepa Sritharan, and Elisabeth Smela. The flow experiments in the large channels were designed by Deepa Sritharan. Prabhath Aluthgama performed the flow experiments under the supervision of Deepa Sritharan. The data were analyzed by Prabhath Aluthgama, Deepa Sritharan, and Elisabeth Smela. The experiments to understand propylene carbonate electrochemistry were designed by Deepa Sritharan and Elisabeth Smela. Bilal Naved performed the current monitoring experiments at high DC voltages in PC and water and recorded the data described in Section 3.3.1.1 of the paper. Deepa Sritharan and Elisabeth Smela wrote the paper.

Abstract

For electroosmotic pumping, a large direct-current electric field (10+ V/cm) is applied across a liquid, typically an aqueous electrolyte. At these high voltages, water undergoes electrolysis to form hydrogen and oxygen, generating bubbles that can block the electrodes, cause pressure fluctuations, and lead to pump failure. The requirement to manage these gases constrains system designs. This paper presents an alternative polar liquid for DC electrokinetic pumping, propylene carbonate (PC), which remains free of bubbles up to at least 10 kV/cm. This offers the opportunity to create electrokinetic devices in closed configurations, which we demonstrate with a fully sealed microfluidic hydraulic actuator. Furthermore, the electroosmotic velocity of PC is similar to that of water in polydimethylsiloxane (PDMS) microchannels. Thus, water could be substituted by PC in existing electroosmotic pumps.

3.1 Introduction

Various electrokinetic phenomena contribute to the motion of a fluid under an electric field, including electrohydrodynamic flow [76] (also known as electroconjugate flow [89]) and electroosmotic flow; in microchannels the latter typically dominates. Electroosmosis (EO) is the motion of a liquid along a charged surface under an applied electric field: a layer of mobile ions in the liquid shields the surface charge, and when this layer migrates under the field it drags the adjacent fluid with it by viscous forces. This effect becomes significant in micro-channels because of their high surface-to-volume ratios, and it can create substantial forces [127,135]. Electroosmotic flow (EOF) is pulseless and the flow profile is uniform. In contrast to pressure-driven pumps, electroosmotic pumps have no moving parts, so they can easily be miniaturized for applications such as chip cooling [136], fuel cell evacuation [137], lab-on-a-chip assays, and high-resolution chemical separations with minimal dispersion. Applications of EO pumps in microfluidics were reviewed in [94].

The EO flow generated by a DC electric field E in a rectangular microchannel of length L, depth d, and width w is described by the following equations [106,138,139] for channels that have dimensions that are significantly larger than thickness of the electric double layer [140].

$$\text{velocity} = \frac{\varepsilon\zeta}{\eta} E = \mu E \tag{1}$$

Flow scales linearly with the electric field. Fast electroosmotic flow occurs when the liquid has a high permittivity (ε) and low viscosity (η) in a channel with a high zeta potential (ζ), where ζ is a measure of the charge at the solid-liquid interface. These properties of the fluid and the surface are typically combined into a single parameter, the mobility (μ) [141].

The ion flow along the walls, an ionic current, is sustained by an electronic current in the external circuit. Electrons are transferred between the electrodes and species in the liquid or on the electrode surfaces by reduction and oxidation (redox) reactions. Which electrochemical reactions occur in a given system depends on the chemical constituents and available energy (voltage).

EOF is well suited for integration into microdevices, but the problems caused by electrolysis, as discussed in [94,107,135,142-146], have limited the demand for EO pumps. In most applications water is utilized as the pumping liquid because it has a high electric permittivity and because biomolecular separations typically require aqueous solutions. However, water undergoes electrolytic decomposition at 1.2 V, generating O_2 and H^+ (H_3O^+) at the anode, and H_2 and OH^- at the cathode [147]. This leads to pH gradients, depletion of the pumping liquid, electrode corrosion [148], and gas bubbles, all of which are detrimental to the functioning of the device. Gas bubbles adhere to the channel walls and block the electrodes, interrupting current flow and causing device failure [135]. Since the bubbles are compressible, they also reduce the overall pressure that can be generated by the pump.

Several approaches addressing electrolysis have been reported. Most commonly, the electrodes are placed in open reservoirs to allow release of the gases [94,146]. In closed systems, techniques to mitigate electrolysis include pressurizing the system to dissolve the gases [135], adding semipermeable membranes to vent the gases [149], using electrodes that eliminate the gases by adsorption or chemical reaction [150], coating the electrodes with redox active materials [107], separating the electrodes from the pumping fluid with ionic bridges [108], and recombining the gases [151]. However, these approaches can be challenging to implement in a microfluidic system. Other proposed approaches include performing EOF using asymmetric AC fields [109,112,113,119,152,153] or zero-averaged currents [120], but flows in pumps using AC EOF are localized near the electrodes and not suited for bulk fluid transport [109].

Another approach is to replace the water with another polar liquid that does not produce electrolytic gases. In this paper we present salt-free propylene carbonate (PC), a polar organic liquid, as a bubble-free pumping fluid to replace water in closed electroosmotic systems. PC-based electrolytes (i.e. PC + salt) are used in lithium ion batteries due to their wide electrochemical windows (on the order of 5 V) [154]. PC has a dielectric constant of 64, comparable to water's 80 [155], but its viscosity is greater (η_{DI} = 1 cp, η_{PC} = 2.5 cp [155]). It is nonvolatile [155], having an evaporation rate of less than 0.005, compared to 0.3 for water (evaporation rate is measured with respect to n-butyl acetate, which has a value of 1) [155]. Electroosmosis using PC as a carrier fluid has been mentioned in the context of capillary electrophoresis [156]: the EO flow rate decreased with salt concentration, as expected by the reduction in the size of the electric double

layer [157]. High electric fields were used in that study, but the test system was open to the atmosphere and the paper did not discuss electrochemical effects. Also reported has been an EO pump for evolving small amounts of H_2 by using PC or ethylene carbonate with various lithium salts [148]. Therefore, in this paper we assume that pumping is due to EO, and the data are not inconsistent with such an interpretation. We demonstrate that the flow velocities of PC are comparable to those of water. In our polydimethylsiloxane (PDMS) channels the mobility of salt-free PC was 2.5×10^{-8} m^2/V-sec, and for DI water it was 3×10^{-8} m^2/V-sec. A significant outcome of this work is that the operation time before device failure of a sealed microfluidic system at 5 kV was extended from 5-10 seconds using water to at least one hour using PC. However, PC is sensitive to moisture, from which it must be shielded.

One long-term objective of the present work is to actuate bio-inspired soft robots by electric-field driven fluid pumping. Liquid-filled cavities that swell or shrink in response to changes in hydrostatic pressure are found in plants and animals [4]. Because high forces and large strokes can be achieved by hydraulic actuation, microfluidics-based compliant actuators can potentially enable the creation of shape-changing elastomer structures.

3.2 Materials and Methods

3.2.1 Electrochemical Stability

In order to evaluate PC (anhydrous 99.7%, Sigma-Aldrich, 310328) as a pumping liquid, its stability under electric fields was investigated. Anhydrous ("dry") PC was used; problems due to moisture in PC are described below and in the Supporting Information (SI). The PC was aliquoted into 20 mL glass vials in an argon atmosphere, capped, and stored in a glove box. All experiments in this paper were, however, performed under atmospheric conditions, not in a glove box. Glass tubes (10 mL) were filled with PC (6 mL), and two electrodes were inserted into the liquid, spaced 5 mm apart. As electrodes, platinum wire (99%, 28 gauge, uGems, model # 14242) or steel pins (600 μm diameter, Singer, 00349) were used, allowing comparison of inert and reactive electrode materials.

Electrolysis was evaluated using cyclic voltammetry, performed with a potentiostat-galvanostat (Autolab Eco-Chemie PGStat). The reference electrode was Ag/AgCl (BAS, MF-2052). The salt tetra-n-butylammonium tetrafluoroborate (TBTF) (Alfa Aesar) was added to the PC in some experiments. The potentiostat recorded current as a function of voltage.

In order to determine whether reactions occurred outside the 10 V range of the potentiostat, the electrodes were connected to a high voltage power supply (HV Rack, Ultravolt) and a voltage scan was performed up to 1500 V by manually ramping the

voltage. To measure the small currents, a 100 kΩ resistor was connected in parallel with the electrochemical cell, and the voltage across the resistor was measured using a multimeter (Fluke 179); the current was determined by applying Ohm's law. The vials were monitored visually for bubble formation and changes in color.

3.2.2 Measurement of Electroosmotic Velocity

Microfluidic devices for measuring pumping velocity were fabricated in PDMS by soft lithography from an SU-8 mold. Masks were drawn using AutoCAD (Autodesk) and printed commercially (FineLine Imaging) at high resolution (20,000 dpi). Molds were formed from 60 μm thick SU8-2025 (Microchem) on Si wafers by photolithography, following the manufacturer's instructions. Thicknesses were measured by mechanical profilometry (Tencor AlphaStep 200).

The PDMS replica comprised a 5.0 mm × 2.5 mm supply reservoir, a 5.0 mm × 5.0 mm expansion reservoir, and nine channels connecting the two reservoirs, each 1 cm × 150 μm. The features were 41± 1 μm deep using an SU-8 mold of depth 43± 1 μm, as determined by mechanical profilometry (Tencor AlphaStep 200). Inlet and outlet silicone tubes (2.5 cm long, 0.89 mm I.D., Cole Palmer) were cured in position within the reservoirs.

To fabricate these devices, the silicone tubes were placed upright onto the mold and a steel pin was inserted into the center of each; the pins were held upright and in position by rare earth magnets beneath the mold. PDMS pre-polymer was mixed with the curing agent (Sylgard 184, Dow Corning) in a 10:1 w/w ratio. The mixture was degassed in a vacuum desiccator for 30 minutes, poured onto the mold around the tubes to a height of 2 mm, and baked at 60 °C for 1 hour in an oven. The elastomer was peeled from the mold and the pins were removed. It was bonded to a glass slide by activating both surfaces in oxygen plasma (10 seconds, 600 mTorr, 50 W, March Jupiter III O_2 plasma system), contacting the two surfaces face-to-face, and baking at 60 °C for 1 hour in an oven.

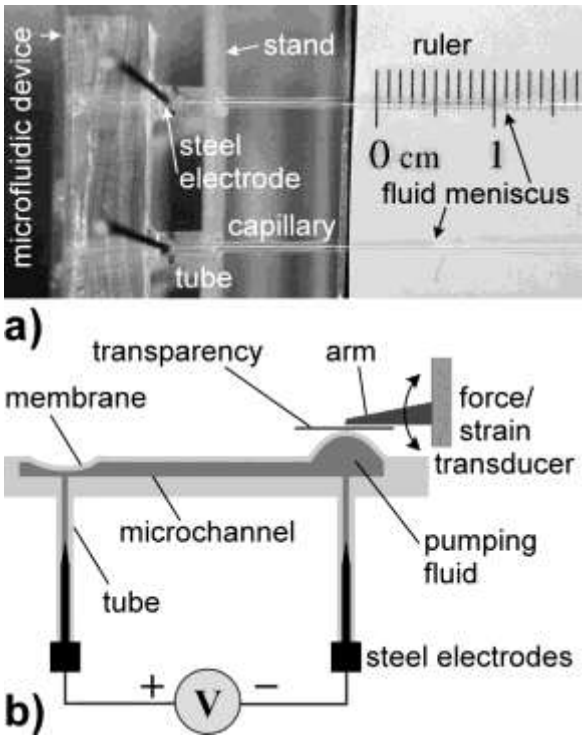

Figure 14. a) Test setup for measuring flow velocity. A PDMS device with microchannels is oriented perpendicular to the page, as are the steel electrodes pierced through the horizontal inlet and outlet tubes. Capillaries, parallel to the page, are press-fit into the silicone tubes for measuring the fluid meniscus position vs. time. b) Cross-sectional schematic of the closed-system device to measure actuation. Pumping fluid through the microchannels caused upward deflection of one membrane and collapse of the other; the height of the former was measured with a force-strain transducer at constant load (isotonic mode).

The microchannels were filled with pumping fluid via the inlet tube by applying positive pressure using a syringe. Glass capillaries (inner diameter 400 μm) were press-fit into

each tube, and steel pin electrodes were pierced through the sides of the tubes. (See the Supporting Information, SI-1 for further detail.)

Flow rates were obtained by measuring the rate of displacement of the meniscus in the glass capillary (Figure 14a). The device was placed on its side to eliminate the effect of gravity on liquid movement. The capillaries were affixed to a ruler to facilitate measurement of the position of the meniscus. The time taken for the meniscus to reach the 10 mm mark was measured with a stopwatch. The meniscus was reset to the same starting position before each run by using a rubber capillary bulb to apply negative pressure.

3.2.3 Measurement of Electroosmotic Actuation

Closed systems were prepared for measuring pressure. The microchannels and reservoirs were molded as described above, but instead of bonding the molded PDMS to glass, it was bonded to a 25 μm thick PDMS membrane layer. The membrane was formed by spin-coating a degassed 10:1 PDMS prepolymer:curing agent mixture onto a glass slide coated with a mold-release layer (Mann Ease Release 200, Smooth-On) at 2500 rpm for 60 seconds (ramped from rest at 500 rpm/sec). The membrane was cured on a hot plate at 95 °C for 15 minutes. The two PDMS layers were bonded by oxygen plasma treatment as described above. The bonded device was peeled off the glass slide and filled with

pumping liquid through the tubing. Steel pins were inserted into the tubes (Figure 14b) to seal the device and contain the fluid within. The pins also functioned as electrodes.

The device was fixed membrane-side-up. To uniformly distribute the force applied by the lever arm, a 5 x 5 mm^2 piece of transparency film was placed on the upward-deflecting membrane surmounting the expansion reservoir (Figure 14b). The lever arm of a force/strain transducer (Aurora 300B) was positioned to rest on the center of the film. These two manual steps led to inter-experiment variation, as shown in section 3.3.2.2; the causes are described in SI-6). When voltage was applied to the electrodes, the membrane bulged due to liquid displacement. The bulging of the membrane lifted the lever arm, and this deflection was measured using the force/strain transducer in isotonic mode (constant force). Images of the membrane were taken through a stereo zoom microscope (Leica GZ6) using a digital camera (Nikon Coolpix 4500). The transducer was interfaced to a computer via a data acquisition card (National Instruments), and data were recorded using a custom LabVIEW program.

3.3 Results

The electrochemical stability of PC is presented first: the rates of bubble formation in PC and water are compared, as are the voltammograms. The velocity and pressure in the microfluidic devices are presented next.

Buffering agents are typically added to maintain the pH of an aqueous pumping liquid, since changes in pH can affect the zeta potential. The zeta potential is also affected by the electrolyte concentration: salt decreases the Debye layer thickness, thereby reducing the pumping efficiency [157,158]. In this work we present electrokinetic pumping using PC without added salt, and as a direct comparison, de-ionized water without salt.

3.3.1 Electrochemical Stability

3.3.1.1 High DC Voltage

High electric fields (tens to thousands of V/cm) are typically applied to achieve useful electroosmotic velocities and pressures, but electrochemical reactions occur readily at those voltages, interfering with stable flow. As discussed previously, water splits to create bubbles of hydrogen and oxygen that disrupt device function. As shown in Figure 15a, upon applying 3 kV (6 kV/cm) to Pt electrodes immersed in deionized (DI) water, bubbles appeared within 10-20 seconds. On steel electrodes (Figure 15b) bubbles became visible even sooner, within 5-10 seconds; furthermore, the water turned yellow (see SI-2 for a color figure) and a brown deposit formed on the anode. Currents were on the order of several mA for both steel and platinum electrodes.

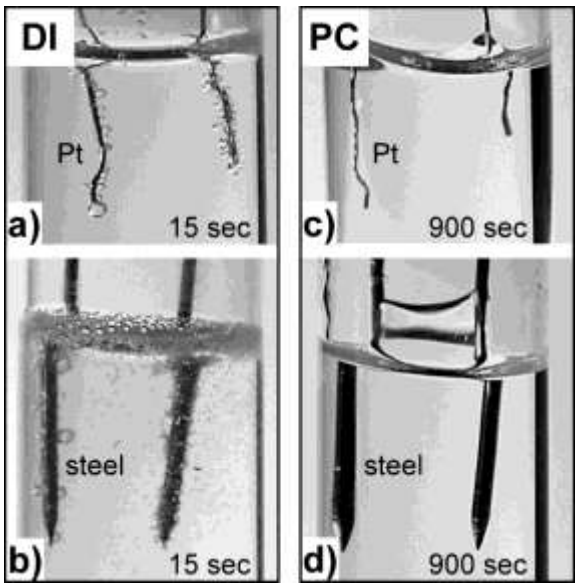

Figure 15. Comparison of DI water (a,b) and PC (c,d) upon the application of 3 kV with two types of electrodes, Pt (a,c) and steel (b,d).

In contrast, no bubbles were seen in dry PC without salt upon applying the same voltage across either the Pt or steel electrodes for at least 30 min., and no surface deposit was observed on the steel (Figure 15c,d). (The PC between the electrodes above the meniscus in Figure 15d is likely due to the formation of a dielectric liquid bridge [159].) The current was three orders of magnitude smaller than in water: 1-3 μA. The absence of bubbles and deposits was an unexpected and favorable finding: the electrochemical window of PC was expected to be near 5 V based on the battery literature, yet the fluid showed no visible reaction even at kV.

3.3.1.2 Voltammetry

Cyclic voltammetry was conducted to probe the onset of redox reactions in the pumping liquids at low voltage. The electrochemical responses of DI water, PC, and PC with added TBTF are compared in Figure 16.

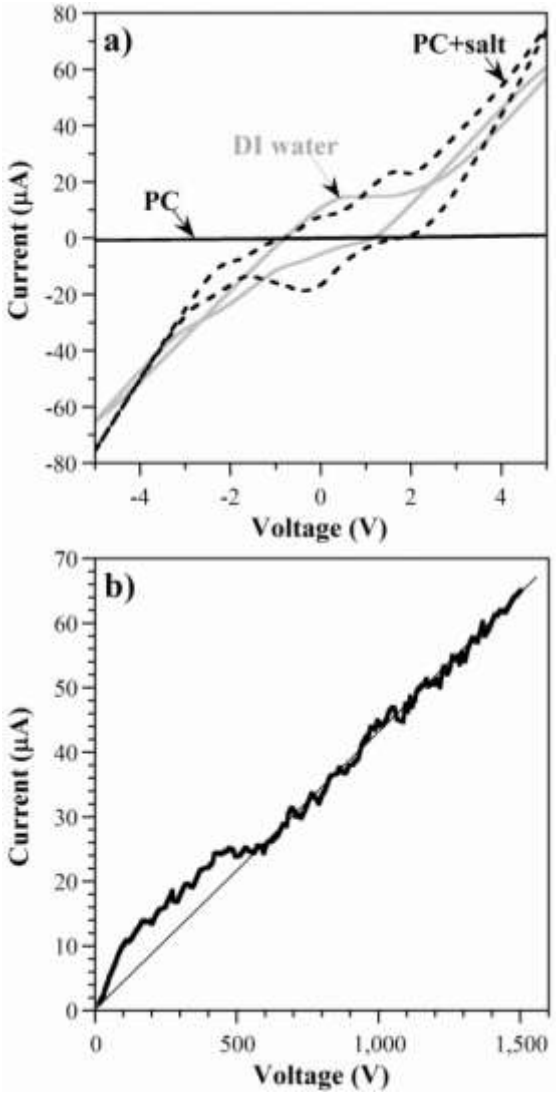

Figure 16. a) Cyclic voltammograms on Pt electrodes in de-ionized water, PC, and PC with 1 mM TBTF salt (vs. Ag/AgCl, 200 mV/sec). b) High voltage voltammogram of PC.

DI water reacted at the Pt electrodes at the expected $\pm$1.2 V [160], giving currents of tens of μA at $\pm$2 V. On the other hand, in dry PC without salt there were no peaks, with a maximum current of only 0.6 μA at 5 V (3 μW). This result was unexpected because

propylene carbonate has been reported to undergo reactions at 5 V [154,161]. It was, however, consistent with the absence of reactions leading to bubbles and surface deposits.

When 1 mM TBTF was added to the PC, the current increased to tens of μA, comparable to the magnitude in water. Thus, the electrochemical window of PC without salt is significantly wider than that of the PC-based electrolytes used in battery applications [154,161]. (Voltammograms taken with steel electrodes also showed smaller currents in PC than in water, shown in SI-2).

To explore the behavior at even higher voltages, the current was measured while the voltage was linearly ramped to 1500 V using a high voltage power supply. As seen in the scan in Figure 16b, the current increased, essentially, linearly with voltage, with no distinct reaction peaks, reaching a maximum of 65 μA. The PC behaved as a linear resistive element with constant conductivity, suggesting that PC is electrochemically stable and can therefore be used in high voltage applications.

3.3.2 Electroosmotic Performance

Having established the stability of the PC at the voltages typically used for electroosmosis, we turn to whether it can be used for pumping and whether useful velocities, pressures, and actuation speeds can be achieved. Some of the experiments

were performed only with PC because of the difficulty of making measurements with water due to the profuse generation of bubbles.

3.3.2.1 Flow Rate

The flow velocities of PC and DI water were measured separately in nominally identical microfluidic devices (i.e., made using the same molds and methods). As described in the Materials and Methods section, the devices had nine parallel PDMS microchannels, and glass capillaries were affixed to the inlet and outlet tubes. The uncertainty of the meniscus position (estimated using a ruler) was estimated to be < 0.5 mm, and the uncertainty in timing (using a stopwatch), 0.2 sec. The percent relative standard deviation (%RSD) in the flow rate was therefore 6% at 1 kV and 13% at 6 kV.

When high voltage (1-6 kV) was applied, the pumping liquid was transported out of one capillary and into the other, consistent with EOF. (In channels with mm-scale diameters, additional electrokinetic forces [89] contributed significantly to the flow, as discussed in SI-5.) For both DI water and PC, the meniscus of the liquid in the capillary on the anode (+) side moved towards the device and on the cathode (-) side it moved away from the device. Movement towards the cathode indicates that the charge moving along the walls is positive, so the zeta potential is negative, as previously reported for water in PDMS [162]. Flow began at 1 kV, at which the current was 10 μA (10 mW).

Figure 17 compares the flow rates for DI water and dry PC in two devices. (Bubble formation was not observed for the duration of these experiments (≤10 seconds), but bubbles did begin to appear in water 12-20 seconds after applying the electric field.) The key finding is that the velocity of PC was similar to that of water. (Data from additional devices are shown in SI-4. Results were similar, with device-to-device variations of approximately 30%, presumably due to variations in fabrication and device age, as well as other surface and history-related factors [162].)

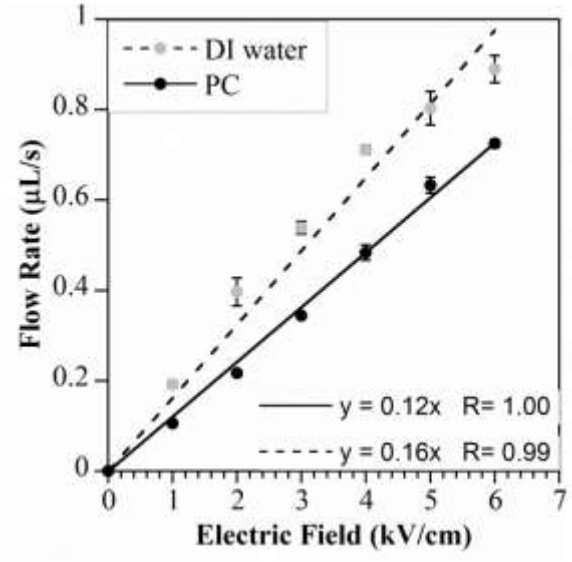

Figure 17. Fluid flow rates in glass capillaries at the inlets and outlets of the microfluidic devices as a function of applied electric field for DI water in one device and PC in another device. Error bars represent standard deviations of three repeated measurements; in some cases they cannot be seen because the variation is smaller than the size of the data point.

The flow rates for both PC and DI water increased linearly with voltage, as expected from Equation (1). The electroosmotic mobility of a pumping liquid is defined as the ratio of the velocity to the applied electric field and can be found from the slope of the flow rate-voltage curve, dividing the slope by the cross-sectional area of the capillary. The mobility of the PC from the data in Figure 17 was $2.5*10^{-8}$ m^2/V-sec, and for DI water it was $3*10^{-8}$ m^2/V-sec. From these mobilities a calculation of the effective zeta potential for PC in PDMS gave ζ_{PC} = -97 mV and for water ζ_{DI}= -41 mV. There are no previously published values for the mobility of DI water in plasma-treated PDMS, but a 10 mM, pH 7 aqueous electrolyte was reported to have a similar value of $3.8*10^{-8}$ m^2/V-sec [163]. Zeta potentials for water in PDMS vary greatly, depending on a number factors [162], including pH [164], Joule heating [162], the age of the SU-8 mold [165], and time elapsed after plasma exposure [166] [163]. The ζ_{PC} is larger than the ζ_{DI} and larger than expected: zeta potentials for polar liquids are typically ≤ 100 mV [167]. This may indicate that there are additional electrokinetic forces contributing to the fluid flow. (See Discussion and SI-5.)

In this system, the mobility of PC was as good as that of DI water. The benefit of electrochemical stability may therefore make PC a better pumping fluid than DI water for some EOF applications, and switching the fluid in existing devices would not require significant, if any, changes to either device design or fabrication.

3.3.2.2 Pressure and Speed

In this work, the pressure and speed in PC-filled closed devices were evaluated indirectly by measuring the deflection of a PDMS membrane above the outlet of the microchannels. Because of bubble formation, actuation with water was not done for comparison. Membrane deflection was measured at intervals between 1 and 10 kV; the voltage was turned on and off five times at each level (Figure 18a). Figure 18(b) shows a close-up of the deflection upon stepping to 7 kV. The applied load was the minimum 1 g.

As expected, deflection increased with voltage. Inflation took longer during the first actuation cycle but thereafter times were 2.5 ± 0.5 seconds for both rise and fall to reach 90% of the final value. (Additional data for another device and a more detailed description of the variability are included in SI-6.) For each voltage, the final amplitude of deflection in a given device were similar in successive cycles: variation was ± 0.9 μm at most. The measurements were highly sensitive to the positioning of the lever arm and force distribution plate, however (SI-6): membrane deflections among three nominally identical devices varied from 42 to 158 μm at 8 kV.

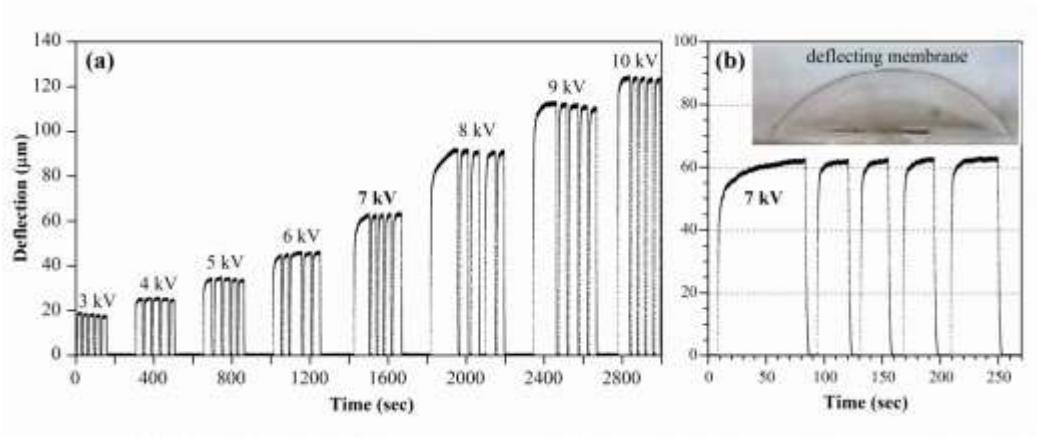

Figure 18. (a) Membrane deflection vs. time in a sealed, PC-filled device with steel electrodes under a load of 1 g upon stepping the voltage on and off, 5 times each, at voltages between 3 and 10 kV. (b) A close-up for 7 kV and a side view of a deflecting membrane.

To determine the pressure generated by the actuator, a series of increasing loads were applied on the membrane by the force-strain transducer until no measurable deflection was obtained. Three measurements were made at each load, stepping the voltage to 7 kV. Figure 19 shows the results for one device (see SI-6 for the others). Membrane deflection was blocked above 15 g in all three devices. Assuming this weight was uniformly distributed over the entire membrane area of 5x5 mm^2, the generated electroosmotic pressure was 6 kPa. The load curves with data from three devices are shown in the inset of Figure 19. The load curve is nonlinear below 5 g, possibly due to a lower area for adhesion between the membrane and the force distribution plate as membrane deflection increases.

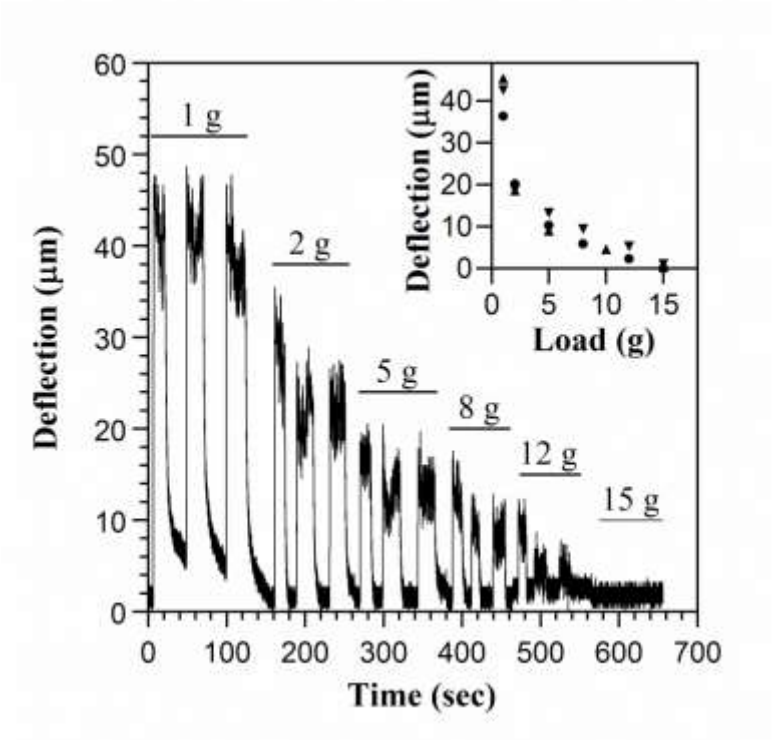

Figure 19. Deflection under increasing loads over time for one sample, each load applied for three step cycles. The loads at each time interval are indicated. Inset: deflection versus load for three samples, each point representing the average of the three cycles at each load.

To determine the theoretically expected pressure based on the membrane deflection and flow rate data, analytical and finite element modeling were used. These methods, however, underestimated the pressure in the system (SI-6).

3.3.2.3 Reaction Products

Stability of pumping is another important consideration, and given that electrochemical reactions of some kind must take place on the electrodes to support the ionic current, some change in performance should be expected. This is a topic for future work. However, over the course of experiments lasting up to 50 minutes, based on visual observation no gases or deposits were formed and there were no changes in electrolyte color.

Previously, we reported [168] that pumping performance drops after PC is exposed to air: the current rises and the velocity decreases. This occurs after even a brief exposure to room air and is irreversible. Furthermore, in PC that has been exposed to moisture sporadic small bubbles and a deposit form on the anode, even when the electrode is Pt. These results are similar to reactions that have been reported in battery applications [154]. The PC must therefore be protected from moisture and kept anhydrous.

To gain insight into the degradation in performance of wet PC, PC was exposed to moisture for a week and then 3000 V for 5 hours, during which time a translucent deposit formed on the anode; on steel the deposit was yellow, and on platinum it was white. The fluid and the deposit were examined spectroscopically (SI-7). No changes could be seen in the fluid at infrared frequencies, but the deposit on both steel and Pt electrodes showed absorption peaks consistent with various carbonaceous species. X-ray photoelectron spectroscopy (XPS) confirmed the presence of carbon-containing compounds.

3.4 Discussion

Understanding of electrokinetic flows is still largely based on experimental data [141], to which our findings contribute. The flow rates for DI water and PC within PDMS were comparable (Figure 17). Since the two fluids have a similar ε but PC has a 2.5x higher η, this would suggest, referring to equation (1), that ζ is higher for PC. The zeta potential, which depends on surface reactions and shielding, is complex on polymer surfaces and is a function of pH, of ion size, valence, and concentration, and of surface modifications [141].

Based on the large flow rates seen with widely spaced (1 cm) electrodes, it is reasonable to conclude that the fluid flow in our system is due primarily to electroosmosis. There are other means of moving liquids using electric fields such as electrohydrodynamic (EHD) flow [76,89,169] and electrocapillary flows (liquid dielectrophoresis [170] and electrowetting [171]). Both are driven by the action of the electric field on the double layer at the electrode/electrolyte interface [172]. Electrocapillary flows require closely spaced electrodes (μm distances). For widely spaced electrodes, EOF can co-exist with EHD flow. Since it scales linearly with electric field, the flow in these micro-channels is predominantly driven by EO; for EHD, the flow scales quadratically [173]. In larger, mm-diameter channels, flow is possibly driven by EHD (SI-5). For confirmation, future work should study the roles of channel diameter and surface charge and compare with theoretical predictions.

One question raised by these results is: what are the cationic species responsible for EOF in the two fluids to which no salts were added? In DI water at neutral pH it is presumably the H_3O^+, for which there is no equivalent in PC. We therefore assume that the pumping in PC is due to trace impurities. Future work should more closely examine the role of added salt. Based on Figure 16, however, this may serve only to increase the current and render the PC less stable. There have been reports that salt in PC accelerates electrochemical breakdown [154].

The current in PC was three orders of magnitude lower than in water (Figure 16), without significantly affecting the flow rate (Figure 17), so the pumping efficiency in PC is higher. The additional current in water reflects "unnecessary" electrochemical reactions that do not contribute to EOF.

With water as the pumping fluid, it is necessary to employ inert electrodes such as platinum [174]. With anhydrous PC, on the other hand, even steel electrodes can be used for EOF.

In conclusion, bubble-free pumping is required in sealed devices. In this work we have presented salt-free, anhydrous propylene carbonate as a pumping liquid, eliminating two issues associated with electrolysis: bubble formation and electrode corrosion. Furthermore, the flow velocity of PC is comparable to that of DI water, while the currents are orders of magnitude smaller. Thus, it may be possible to exchange water for PC in many electroosmotic pumping applications.

3.5 Acknowledgements

This work was funded by the AFOSR under contract # FA95500910125 and by NSF under contract CNS 0931878. We thank Santa Fe Science and Technology, Inc. for the generous donation of their force/strain transducer software. We are grateful to Dr. Karen Gaskell for her expert insight on the interpretation of the spectroscopy data and Karthik Sridhara for assisting with the XPS and Raman spectroscopy. We thank Dr. Aldo Ponce and Scott Taylor for their help with the FTIR measurements, and Dr. John Kinyanjui at Shimadzu Corp. for analyzing samples by FTIR microscopy. We thank Dr. Abhijit Dasgupta and Elaine Lin for their guidance in modeling the membrane behavior under pressure. Finally, we acknowledge the support of the Maryland NanoCenter and its FabLab.

3.6 Supporting Information

Electronic online information includes additional information about device fabrication, cyclic voltammetry, flow speeds, and actuation, as well as a discussion of the evidence in support of electroosmosis as the pumping mechanism. Also included is FTIR, SERS, Raman, and XPS characterization of PC degradation in the presence of moisture.

3.6.1 Device Fabrication

3.6.1.1 Devices for Flow Rate Measurement

Figure 20 illustrates the procedure used to fabricate the microfluidic devices for measuring EO flow rates. A photograph of the final device is shown in Figure 21. These were fabricated in polydimethylsiloxane (PDMS) by soft lithography using an SU-8 mold.

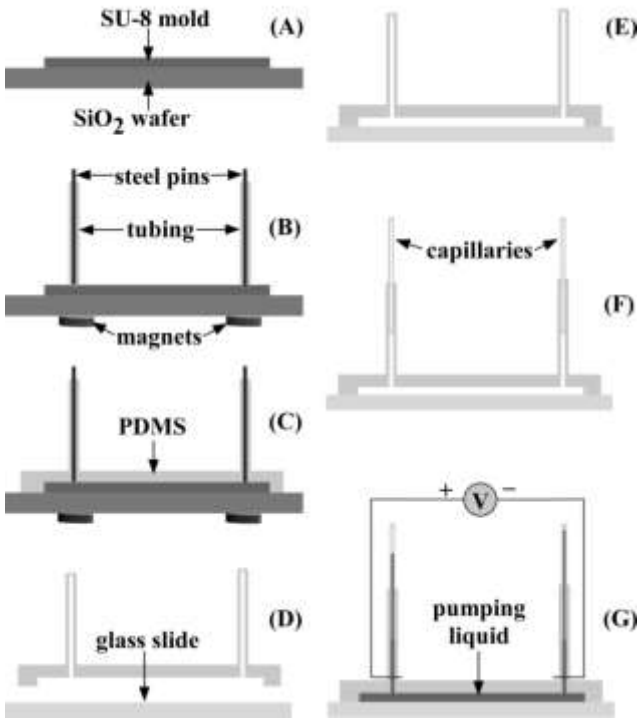

Figure 20. Fabrication of devices for measuring velocity of electroosmotic flow. (A) The SU-8 mold was fabricated by photolithography. (B) Two magnets were fixed under the wafer using PDMS, one positioned beneath each reservoir. To make the inlet and outlet, a piece of silicone tubing was placed on each reservoir. A steel pin were inserted into each tube and aligned with the magnets to hold the tubes upright. (C) The PDMS mixture was poured over the SU-8 mold around the tubes. The PDMS was cured at 60 ^{o}C on a hotplate oven for 45 minutes. (D) The resulting replica consisted of molded microchannels with attached inlet and outlet tubing. (E) The replica was oxygen plasma bonded to a glass borosilicate slide. (F) Glass capillaries were inserted into the inlet and outlet tubes. (G) Electrodes were pierced through the side of the tubing and connected to a high voltage power supply.

The SU-8 was spin-coated onto a silicon wafer at 500 rpm for 5 sec with 100 rpm/s acceleration and then at 2000 rpm for 1 min with 100 rpm/s acceleration. The edge bead was removed from around the wafer, and the device was allowed to rest for 30 minutes at room temperature. The wafer was pre-baked at 65 ^{o}C for 5 min and then at 95 ^{o}C for 15 min. The sample was cooled to room temperature over 10 min. The SU-8 was exposed to UV light (9 mJ/cm^2) for 20 sec through the mask, then post-baked at 65 ^{o}C for 5 min and then at 95 ^{o}C for 15 min. The pattern was developed in SU-8 developer (Microchem, Newton, MA) to produce the mold. Thicknesses were measured by mechanical profilometry (Tencor AlphaStep 200). The final mold had an average height of 60 µm.

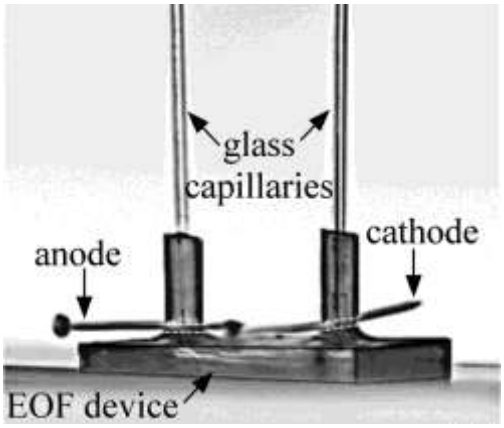

Figure 21. Photograph of a microfluidic device fabricated for measuring electroosmotic flow rate.

3.6.1.2 Devices for Measurement of Electroosmotic Actuation

In order to measure pressure generated by EOF, closed systems were prepared as shown in the photograph of the assembled device in Figure 22 and delineated in the schematic shown in Figure 23.

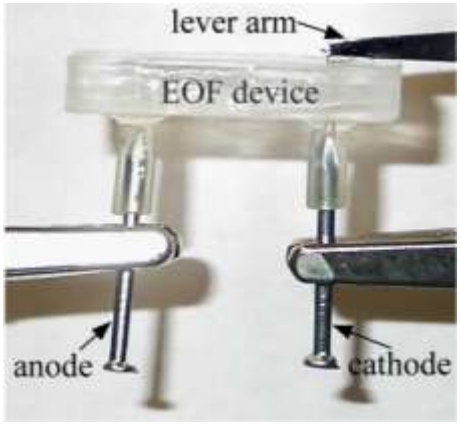

Figure 22. Photograph of a microfluidic device fabricated for measuring actuation of a PDMS membrane by electroosmotic flow.

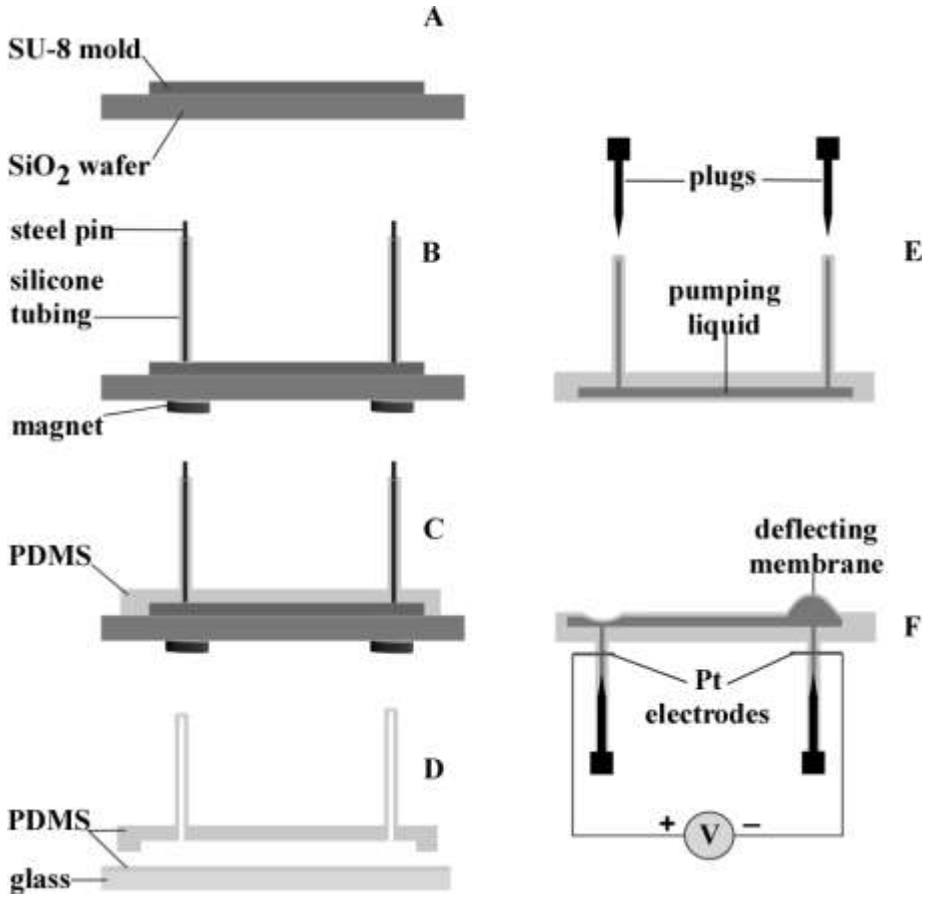

Figure 23. Fabrication of devices for measuring pressure. (A-C) Steps were the same as (A-C) in Figure 20. (D) A thin layer of PDMS was spin-coated onto a glass slide. The replica molded PDMS layer was plasma-bonded to the spincoated PDMS. (E) The device was filled with liquid and sealed by inserting steel pins to plug the tubing. (F) High voltage was applied across the steel electrodes.

3.6.2 Voltammetry

Steel electrodes were used for flow rate and actuation measurements. To assess the reactivity of the steel electrodes with the PC, we performed cyclic voltammetry (Figure 24) in DI water, PC, and PC with 1 mM TBTF.

The voltammograms on steel in DI and PC + TBTF differed from those on Pt, due to reactions with the water and the salt. It is interesting to note, however, that the current with anhydrous PC without salt was still small (the maximum current was 1.8 μA) and increased linearly with voltage. Currents on steel electrodes were approximately 3 times higher than currents on Pt in all three solutions.

For PC with salt on the platinum electrodes, Faradaic reactions started at 2.2 V, and multiple peaks were observed. On the steel electrodes, a sharp increase in current occurred at 1.3 V. The current increased steadily, with no peaks.

The shape of the DI water curve on steel was also different from that on platinum. On platinum currents became appreciable at 1.2 V, as expected from the literature. On steel, the curve looked Ohmic, as seen for PC without salt, but with a higher slope. There are no published voltammograms on steel available for comparison with our data.

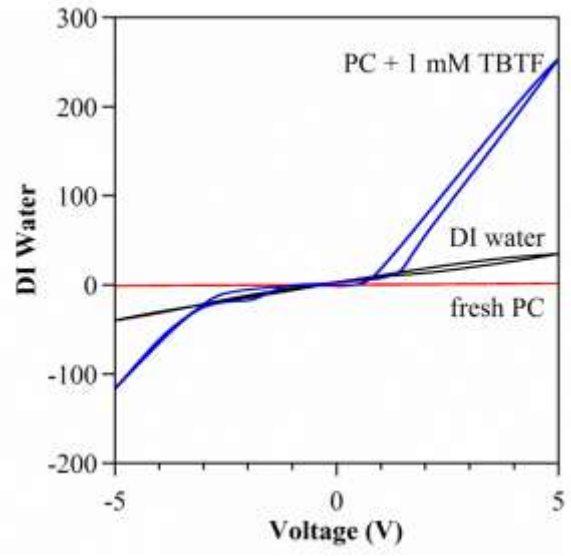

Figure 24. Cyclic voltammograms on steel electrodes in deionized water, PC, and PC with 1 mM TBTF salt (vs. Ag/AgCl, 200 mV/sec).

3.6.3 Color Version of Figure 2

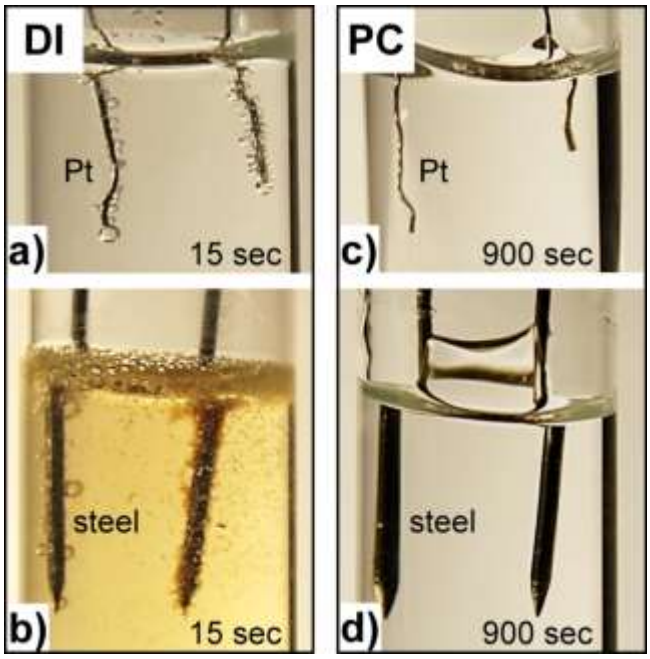

Figure 25. Color version of Figure 2 in the main text showing the water turning yellow with steel electrodes.

3.6.4 EOF Velocity

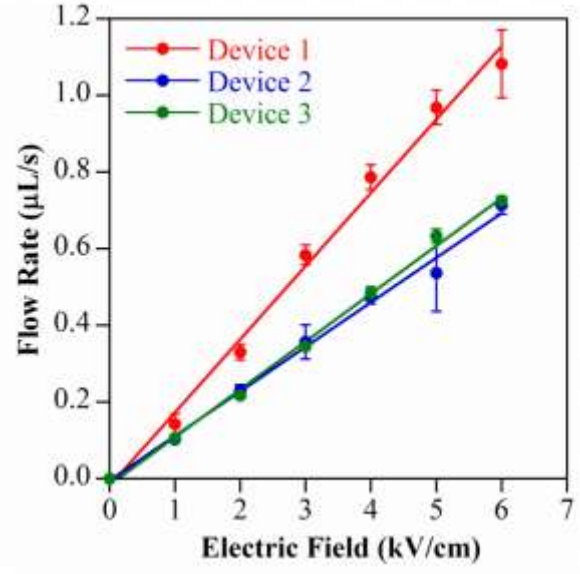

Figure 26. Repeatability of electroosmotic flow rates illustrated by measurements in three nominally identical devices.

In this section we present additional flow measurement data. The electroosmotic velocity of propylene carbonate was measured in three separate devices. Three velocity measurements were made at each voltage. The initial wetted length was 1 cm. After each cycle (turning the voltage on and off once) the voltage was left off for 10 seconds to allow the liquid to come to rest at the starting position to avoid back-pressure effects. The applied voltage was systematically increased for Device 1 (data shown in the paper) and Device 3, and the three repeats at each voltage being made one after the other. The voltages were randomized for Device 2. The data in Figure 26 were obtained by multiplying the measured velocity (mm/sec) by the cross-sectional area of the glass capillary (400 µm inner diameter).

Uncertainty Analysis

The uncertainty in velocity (v) can be determined by the propagation of errors in meniscus position (x) over time (t) [175]:

$$v = \frac{x}{t}$$

$$\Delta v = \sqrt{\left(\frac{\partial v}{\partial x}\Delta x\right)^2 + \left(\frac{\partial v}{\partial t}\Delta t\right)^2}$$

$$\Delta v = \sqrt{\left(\frac{1}{t}\Delta x\right)^2 + \left(\frac{-x}{t^2}\Delta t\right)^2}$$

The uncertainty in flow rate (f) is then $\Delta f = (\pi r^2)\Delta v$ where r is the inner radius of the glass capillary (200 μm). The uncertainty in the measurement was < 13% as shown in Table 2.

Table 2. Uncertainty analysis of flow rate for device 3, shown in Figure 4 of main paper.

Voltage (kV)	Meniscus Position 'X' (mm)	Mean of X	Standard Deviation of X	Ruler Uncertainty	Net Error ΔX	TIME 't' (sec)	Mean of t	Standard Deviation of t	Stopwatch Uncertainty	Net Error Δt	Net Error in Velocity Δv (mm/sec)	Net Error in Flow Rate ΔF (μL/s)	Mean Flow Rate F	% Relative Error 100*ΔF/F
1	10	10	0	0.5	0.5	11.9	11.8	0.30665	0.2	0.37	0.04968835	0.03122011	0.530973	5.87979
1	10					11.5								
1	10					12.1								
2	10	10	0	0.5	0.5	5.78	5.79	0.03215	0.2	0.2	0.10531589	0.06617193	1.084554	6.1013
2	10					5.83								
2	10					5.77								
3	10	10	0	0.5	0.5	3.69	3.65	0.04509	0.2	0.21	0.20632134	0.12963552	1.722994	7.52385
3	10					3.65								
3	10					3.6								
4	10	10	0	0.5	0.5	2.5	2.6	0.08888	0.2	0.22	0.37656574	0.23660323	2.41661	9.79071
4	10					2.63								
4	10					2.67								
5	10	10	0	0.5	0.5	1.93	1.99	0.05508	0.2	0.21	0.58274647	0.3661504	3.162677	11.5772
5	10					2.04								
5	10					1.99								
6	10	10	0	0.5	0.5	1.71	1.73	0.02082	0.2	0.2	0.7287943	0.45791496	3.624915	12.6324
6	10					1.75								
6	10					1.74								

3.6.5 Evidence for EO Flow

It can be difficult to determine the pumping mechanism for fluid flow under an electric field in a channel. Fast flow of PC also occurs in channels with diameters of 3 - 7 mm under fields of 1.5 to 3.5 kV/cm. Figure 27 shows a set-up that allows variation of the channel material and diameter. Tubes 2 cm long made of glass, polyethylene, or PDMS-coated glass were placed between the tips of two polyethylene pipettes. Needles (BD PrecisionGlide), serving as electrodes, were pierced through the pipettes (Samco Scientific 263-1S polyethylene transfer pipettes) just at the edges of the tubes, on either side. Openings were cut into the pipette bulbs to form open reservoirs for the PC.

With 30 gauge needles, the direction of flow was from the positive to the negative electrode. However, for larger sizes (23, 22, and 18 gauge) flow was in the opposite direction. The switch in direction was consistent when the experiments were replicated. The reversed flow using the 18 gauge needles was 50% faster than the forward flow using the 30 gauge needles at 3, 5, and 7 kV. This effect has previously been observed in electroconjugate flow experiments [89]. The flow rate depended on the tube material, suggesting that electroosmosis also contributed.

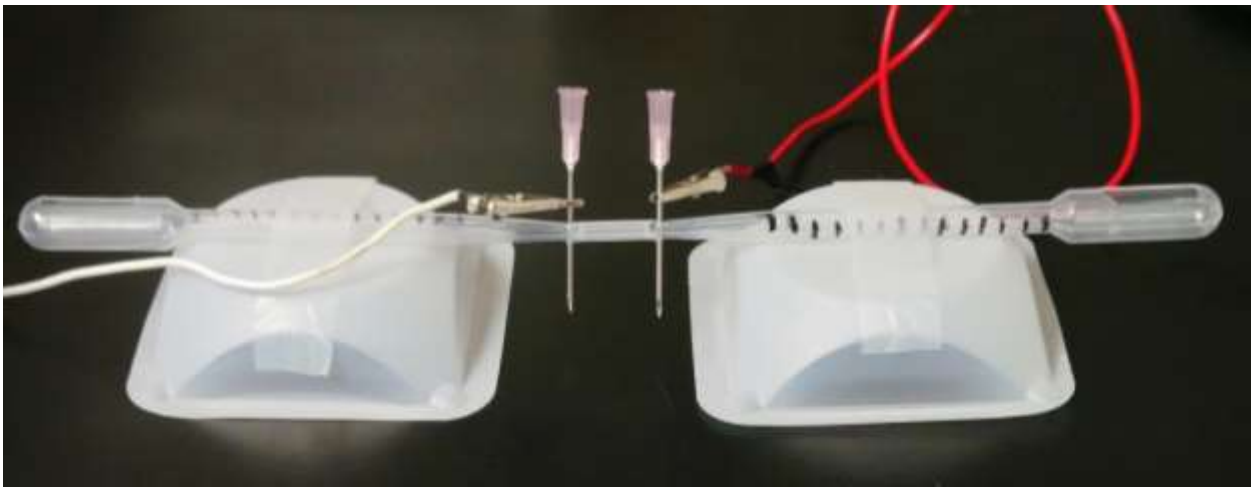

Figure 27. Experimental set-up for flow studies in meso-scale channels filled with PC. Syringe needles are used as electrodes on either side of a tube of varying material. The reservoirs in the pipette bulbs are open to the atmosphere.

When this experiment was conducted with the PDMS microchannels described in the main text, flow always occurred from the positive to the negative electrode, for both 18 and 30 gauge needles. (The device consisted of 9 microchannels connecting two open reservoirs, Figure 28, with the same 2 cm spacing between electrodes.) There was also

no difference in flow rate between the two electrode sizes. These results are consistent with flow dominated by EO (wall effects) rather than electrode effects.

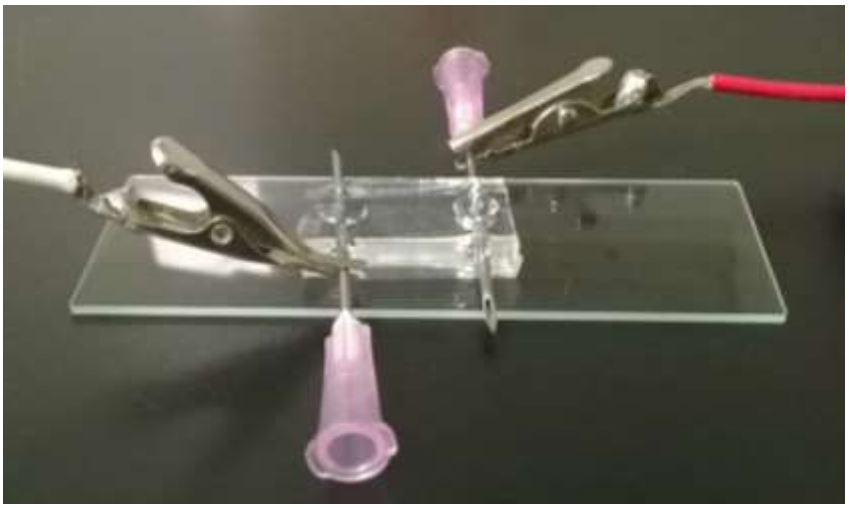

Figure 28. Experimental setup for flow studies in micro-channels.

3.6.6 Deflection at Increasing Voltage

The actuation behavior was similar in the three device that were tested. Deflections for a second device are shown in Figure 29.

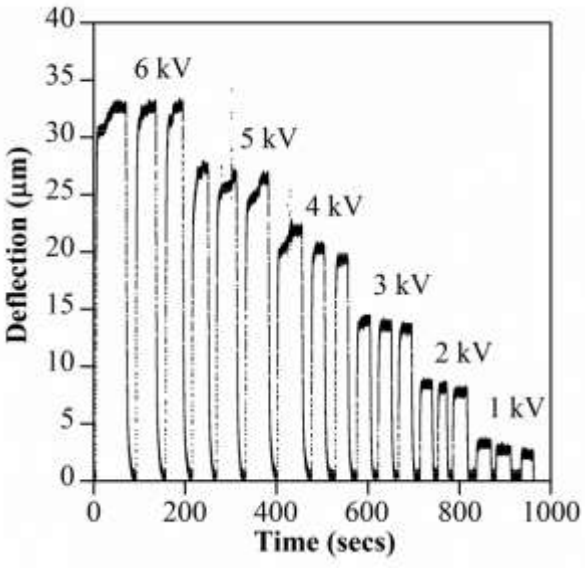

Figure 29. Membrane deflection in Device C versus time upon turning the voltage on and off 3 times each at voltages between 6 kV and 1 kV.

We took several precautions to prevent inconsistency.

- During fabrication, the same spin speeds were used to try to achieve the same membrane thickness (25 μm). The cast channel layers were made thick (3 mm) to prevent deformation during actuation, so that all the deformation occurred at the membrane. The filling tubes were placed exactly below the center of the membrane, determined visually. Devices were used at least one day after fabrication to allow surface charge induced during plasma bonding to dissipate.
- The device was filled with the same volume of liquid for each run, and trapped air bubbles were eliminated. If insufficient fluid was added, the membrane could stick to the bottom of the device.

- During fluid filling, the device was placed membrane-side down on a petri dish (to which it did not adhere) to prevent the required high filling pressures from bursting the membrane. The device was then flipped over for actuation.
- A constant electrode separation (1 cm) was maintained by visually ensuring the electrodes were inserted into the tubing to the same depth after filling the device.
- The force applied by the transducer to the membrane was calibrated before beginning each set of measurements.
- As described in the main text, in order to uniformly distribute the force applied by the transducer lever over the surface of the membrane, a small piece of transparency film was placed on the membrane.
- The transparency and lever arm were gently positioned over the membrane to minimize the possibility of the membrane sticking to the transparency. If the membrane adhered to the transparency, the shape of the bulged membrane changed, resulting in dissimilarities between readings and sudden jumps in lever position.
- Care was taken to position the lever tip precisely at the center of membrane.
- The lever was brought into contact with the transparency using a labjack by visually observing the reflection of the lever in the transparency.
- Before turning on the voltage we waited 10 seconds for the liquid to stop moving to avoid back-pressure effects.

Nevertheless, deflections and speeds varied between devices. Figure 30 shows a comparison of membrane deflection measurements in three devices, A (the device in

Figure 6 of the main paper), B and C (the device in Figure 29), at voltages between 1 kV and 10 kV. Device B had more than twice the deflection of Device C.

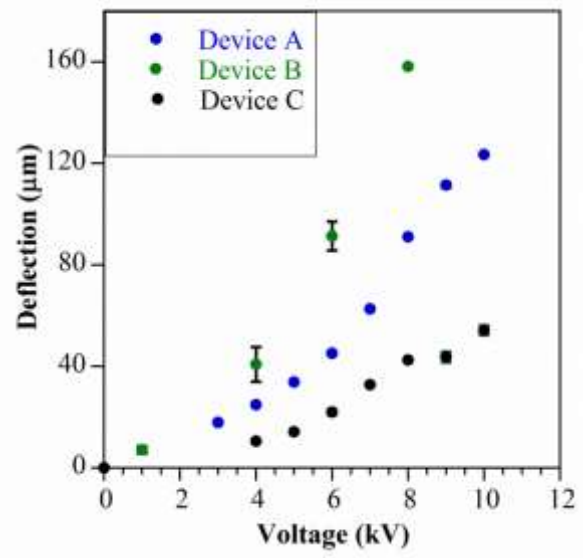

Figure 30. Repeatability of membrane actuation in different devices. Error bars indicate the standard deviation of five runs on the same device. In most cases, they cannot be seen because the variation is smaller than the size of the data point.

As shown in Figure 6 in the main paper, upon applying the voltage the membrane deflection initially increased rapidly and later plateaued. Similarly, when the voltage was turned off the membrane rapidly deflated and then slowly tapered off. At first glance, it appeared that the actuator displayed a first order response to the change in applied voltage. However, upon analysis it became apparent that multiple unknown processes with different time dependence were affecting the inflation/deflation. Future work will focus on understanding the causes of these variations. In addition, in future work the commercially available steel nail electrodes will be replaced with a more

electrochemically inert and homogenous material, such as platinum or carbon, to eliminate the possibility of undesired electrochemistry.

Figure 31 is a close-up of the last inflation step in Figure 6 in the main paper, showing small oscillations at steady voltage. This effect may be due to the force-strain transducer. In isotonic mode, a constant lever force is applied and the displacement recorded. In our experiments this lever force deviated from the set value of 1 gram by $\pm$ 0.1 grams due to subtraction errors in the internal PID force control. One gram is close to the lower limit of the measurement capability of the transducer. Future research to increase the force generated by the actuator will allow greater lever forces to be applied, and thus more accurate readings. Future experiments will also be performed on a vibration-free platform to mitigate external disturbances.

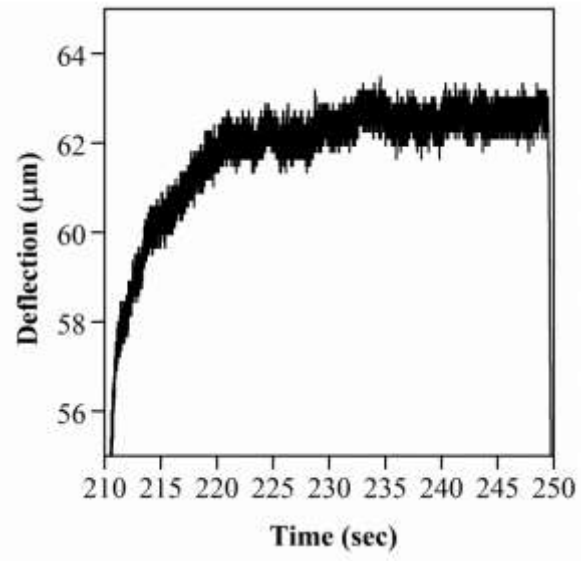

Figure 31. Close-up of the final membrane deflection in Figure 6 in the main paper. (7 kV).

3.6.7 Force Generation

The force generated by the actuator was determined experimentally by applying a constant force on the deflecting membrane via the force-strain transducer arm. The voltage was stepped on and off to 7 kV three times at each loading value, with loads increasing from 1 g to 15 g. The deflection decreased with load, as shown in Figure 32. The load curve was nonlinear, although deflection decreased almost linearly for loads greater than 5 g. The nonlinearity is most likely due to a decrease in contact area between the force distribution plate and the membrane at higher deflections.

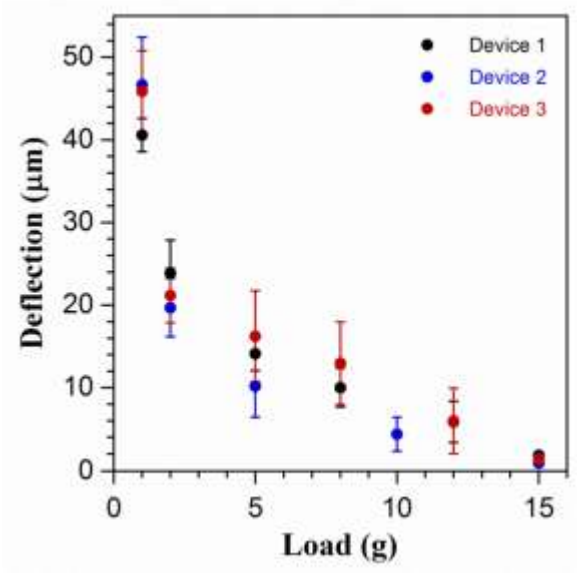

Figure 32. Load curve for three actuator devices. The load on the membrane was increased from 1 g to 15 g until no deflection was discernable.

The volumetric flow rate in the closed devices was determined by approximating the shape of the inflated membrane as a spherical cap with a base of diameter 5 mm and height equal to the deflection. (The base of the membrane was a 5x5 mm^2 square.) The average time for membrane inflation was 2.5 seconds. At 7 kV, for a deflection of 45 μm the calculated flow rate was 0.8 μL/sec. The flow rate in the closed actuator devices was comparable to the flow rate in the open configuration (SI Section 3.6.4). From Figure 26, the average flow rate for the three devices with the open configuration can be extrapolated to 0.85 μL/sec at 7 kV.

A pump curve is a graphical representation of a pump's ability to produce flow against a given pressure head. The pump curve was obtained by plotting the calculated flow rates

for membrane filling against the applied pressure (load over the membrane surface area) (Figure 33).

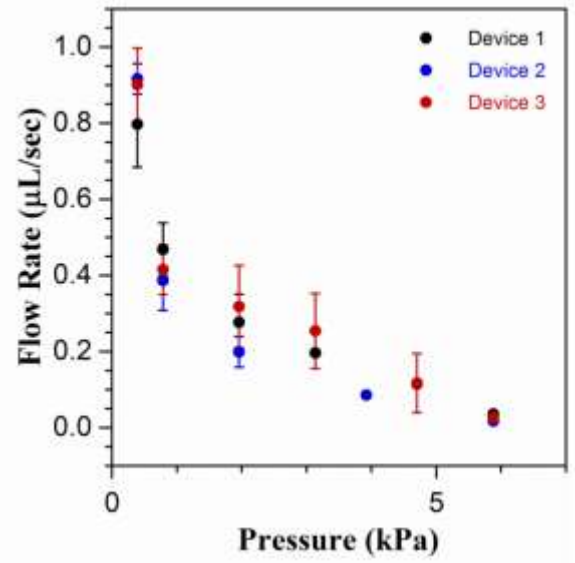

Figure 33. Pump curves for the three devices of Figure 32.

Deflection was blocked when a load of 15 grams was applied. This corresponds to a pressure of 6 kPa. At steady state, the EO flow rate is equal and opposite to the pressure-driven restorative flow rate, Q_p. Pressure-driven flow in the open device configuration is described by the Hagen-Poiseuille equation for flow in rectangular channels (Equation 3)[139].

Equation 3: $$Q_p = \Delta P \frac{n\left(d_c^3 w_c\right)}{12\mu L_c}\left[1 - 0.63\frac{d_c}{w_c}\right]$$

Here ΔP is the pressure drop across the channels, n is the number of channels, d_c is the channel depth (41 μm), w_c is channel width (150 μm), L_c is channel length (1 cm), and μ is viscosity of PC (2.5 cp). For a pressure drop of 6 kPa the expected flow rate is

1.5 μL/sec, which is in reasonable agreement with the open system flow rate of 0.85 μL/sec at 7 kV when the minimum load of 1 g was applied.

The flow rates in the open configuration were obtained by observing the meniscus in cylindrical glass capillaries attached to the microchannel devices. The flow rate in the capillary must be equal to the flow rate within the device, so it would be expected that the pressure drops would also be equal. Equation 4 describes pressure driven flow in a cylindrical channel.

Equation 4: $$Q_p = \Delta P \frac{\pi d_c^4}{128 \mu L_c}$$

When the pressure drop required for a flow rate of 0.85 μL/sec was estimated based on capillary dimensions (length 1 cm, inner diameter 400 μm), the value obtained was much smaller (34 Pa instead of 6000 Pa). This may be due to pressure losses due to surface tension forces, or because the effective inner diameter was smaller: the pressure drops match if 100 μm is used instead of 400 μm. The flow rate is highly sensitive to the radius (r^4).

We also modeled the membrane as a thin homogeneous membrane stretched by a uniform load over an opening in a rigid base [176] (Figure 34). At equilibrium, balancing the forces results in Equation 5, subject to the boundary condition $z = 0$ along the edge of the membrane.

Equation 5: $$\frac{\partial^2 z}{\partial x^2}+\frac{\partial^2 z}{\partial y^2}=-\frac{p}{T}$$

Here, p is the applied load and T is the tension in the membrane.

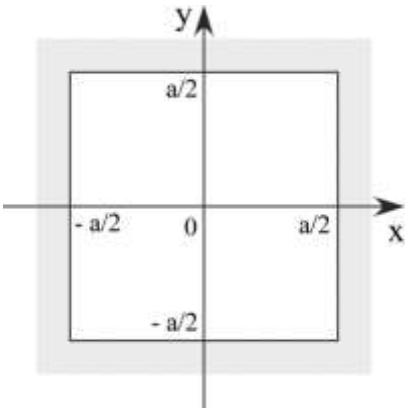

Figure 34. The undeflected membrane has a square surface of side a = 5 mm and is fixed along all edges to the surrounding PDMS base.

To non-dimensionalize the equation, we made the substitution $z=\frac{p}{2T}\varphi$. Equation 5 then becomes:

Equation 6: $$\frac{\partial^2 \phi}{\partial x^2}+\frac{\partial^2 \phi}{\partial y^2}=-2$$

subject to the boundary condition φ = 0 along the edge of the membrane. The solution to this equation is

Equation 7: $$\phi(x,y)=\frac{a^2}{4}+\frac{1}{2}(y^2-x^2)-\frac{8a^2}{\pi^3}/\sum_{n=0}^{\infty}\frac{(-1)^n}{(2n+1)^3}\frac{coshk_n y}{cosh(k_n a/2)}coshk_n x$$

Maximum deflection occurs at the center of the membrane (x, y) = (0,0). From Equation 7, for a = 5 mm,

Equation 8: $$\varphi(0,0) = 6.32 = \varphi_{max} = \frac{2T}{p} z_{max}$$

Hooke's law for isotropic materials in two-dimensional compliance matrix form, in the absence of shear forces, is given by [177]

Equation 9: $$\begin{bmatrix} \varepsilon_x \\ \varepsilon_y \end{bmatrix} = \frac{1}{E} \begin{bmatrix} 1 & -\nu \\ -\nu & 1 \end{bmatrix} \begin{bmatrix} T_x / t \\ T_y / t \end{bmatrix}$$

The strain ε and tension T were assumed to be equal in the x and y directions; this was verified in the Abaqus simulation. Stress in the thin membrane is given by T/t.

Equation 10: $$\varepsilon = \frac{1}{E}(1-\nu)\frac{T}{t}$$

In our case the membrane thickness t was 25 μm, and the Poisson's ratio ν for PDMS was assumed to be 0.5 [178]. Tension in the membrane at maximum deflection is then:

Equation 11: $$T_{\max} = \frac{Et\varepsilon_{z_{\max}}}{1-\nu}$$

Based on a deflection of 45 μm, the strain $\varepsilon_{z_{\max}}$ was calculated as shown below.

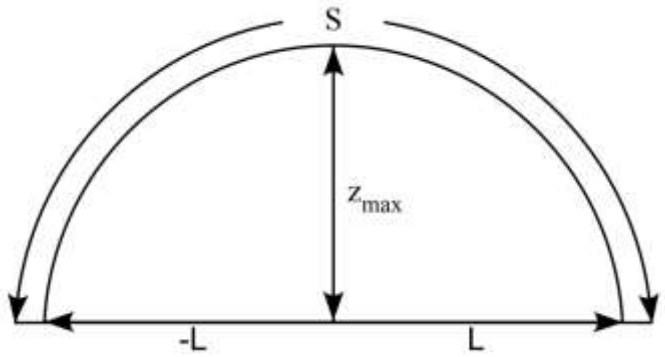

Figure 35. Cross-sectional view of the inflated membrane. The uninflated membrane has an initial length of a= 2L = 5 mm. At maximum deflection z_{max} the membrane assumes a parabolic profile of arc length *S*.

Equation 12: $$\varepsilon_{z_{\max}} = \frac{S - 2L}{2L}$$

where the arclength S is given by:

Equation 13: $$S = \int_{-L}^{L} \sqrt{1 + \left(\frac{dz}{dx}\right)^2}\, dx = 2\int_{0}^{L} \sqrt{1 + \left(\frac{dz}{dx}\right)^2}\, dx$$

Substituting,

Equation 14: $$\varepsilon_{z_{\max}} = \frac{2\int_{0}^{L} \sqrt{1 + \left(\frac{dz}{dx}\right)^2}\, dx - L}{L}$$

For a parabolic segment,

Equation 15: $$z = z_{\max}\left(1 - \frac{x^2}{L^2}\right)$$

Differentiating Equation 15:

Equation 16: $$\frac{dz}{dx} = \frac{-2z_{\max}x}{L^2}$$

Substituting Equation 16 into Equation 13 and integrating between L = 0 mm and L = 2.5 mm, a deflection value of z_{max} = 45 μm gives a strain $\epsilon_{z_{max}}$= 0.054%. Using Equation 8 and Equation 11, the calculated modulus is 1.8 GPa. The modulus of PDMS has been reported to be 4 MPa [179]. Thus the deflection was greatly overestimated by this model:

using a modulus of 4 MPa predicted a deflection of 1.5 mm, 30 times larger than the experimentally observed value. This leads us to conclude that the deflection cannot be described exclusively by a membrane stretching model and that additional factors must be considered in the force balance.

3.6.8 Results

3.6.8.1 FTIR Analysis of PC

Freshly aliquoted PC ("fresh PC"), from a new, previously unonopened bottle was used as a control. This was compared with PC exposed to humid air ("moisture-exposed PC") and the PC exposed to humid air followed by electrolysis using steel electrodes ("electrolyzed PC").

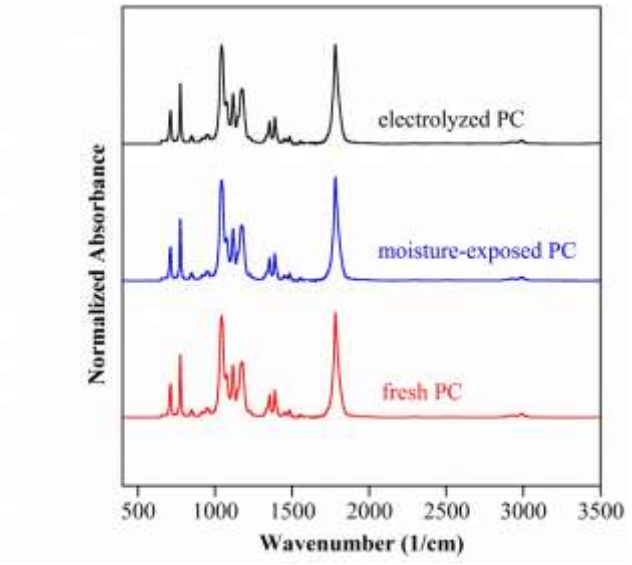

Figure 36. FTIR spectra of fresh PC (from a just-opened bottle), moisture-exposed PC (stored in a high humidity (85-90%) environment for 1 week), and electrolyzed PC (subjected to 5 hours of current flow at 1 kV after exposure to 85-90% humidity over a period of one week).

The FTIR spectra from the three liquids are shown in Figure 36. The spectrum for the fresh PC matched that in the literature [180,181]. However, we were surprised to find that even after the PC was exposed to moisture and high electric fields (kV) the spectra remained unchanged. Upon electrolysis using the steel electrodes the initially colorless PC turned yellow (presumably due to formation of iron oxide, and gas bubbles and a deposit were produced. We had anticipated peaks suggesting oxidative decomposition products, such as acetone [182]. PC electrolyzed using platinum electrodes had the same spectrum. Our conclusion is therefore that the reaction products are present in too low a quantity to contribute to the spectra.

3.6.8.2 FTIR Analysis of Electrodes

Using the NEXUS 670, there were no peaks in any of the IR spectra (normalized to the pristine surfaces) from the anodes, despite the presence of the visible deposits. There were also no peaks from the deposits placed in the KBr pellets.

From the Shimadzu IRPrestige-21, peaks were obtained only from the steel anode. Spectra were recorded at multiple positions on the anode; the one shown in Figure 37 was obtained where the deposit was thick. The peak heights and positions varied appreciably at the different positions, suggesting that the deposit was inhomogeneous in thickness and composition. The main peaks are listed in Table 3 together with the corresponding bonds, based on IR reference tables [183-185]. These peaks suggest the formation of alcohol, ether, and amorphous carbon species.

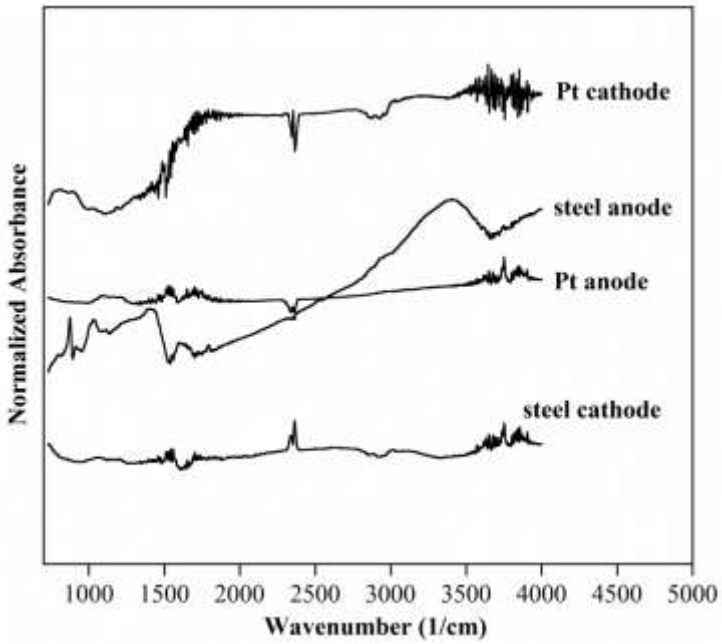

Figure 37. IR spectra of the surfaces of the steel and platinum electrodes after electrolysis of PC. The spectrum was obtained by FTIR reflectance microscopy from Shimadzu Inc.

Table 3. IR peaks from the deposit on the steel anode and the corresponding molecular bonds and possible functional groups.

Wavenumber, cm^{-1}	Molecular Bond [183-185]
3375	O–H stretch, H–bonded
2932	C–H stretch
1790	C=O stretch
1597	C–C stretch (in-ring)
1034	C–O stretch
872	C–H bend
389	C–H bend

3.6.8.3 Raman Analysis of PC

Raman spectra were obtained for fresh PC, moisture-exposed PC, and electrolyzed PC (Figure 38). There was no change after moisture exposure or degradation by electrolysis. This implies that the species formed by electrolysis were not detectable by SERS, either due to their low concentrations or because they contained bonds that were not Raman active.

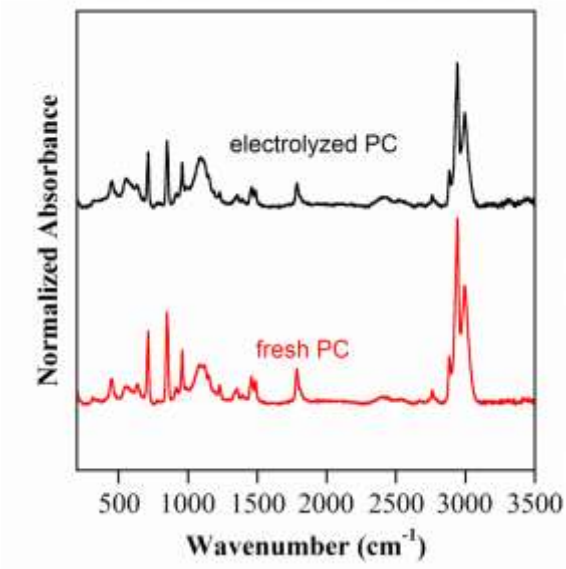

Figure 38. Comparison of Raman spectra of fresh PC and electrolyzed PC. The spectra had identical peaks.

3.6.8.4 Raman Analysis of Electrodes

No peaks were observed on the cathodes of either steel or platinum, but there were peaks on the anodes (Figure 39). The Raman spectra suggest that amorphous carbon and ether moieties constituted a significant portion of the deposit. The main peaks are listed in Table 4, together with the corresponding bonds.

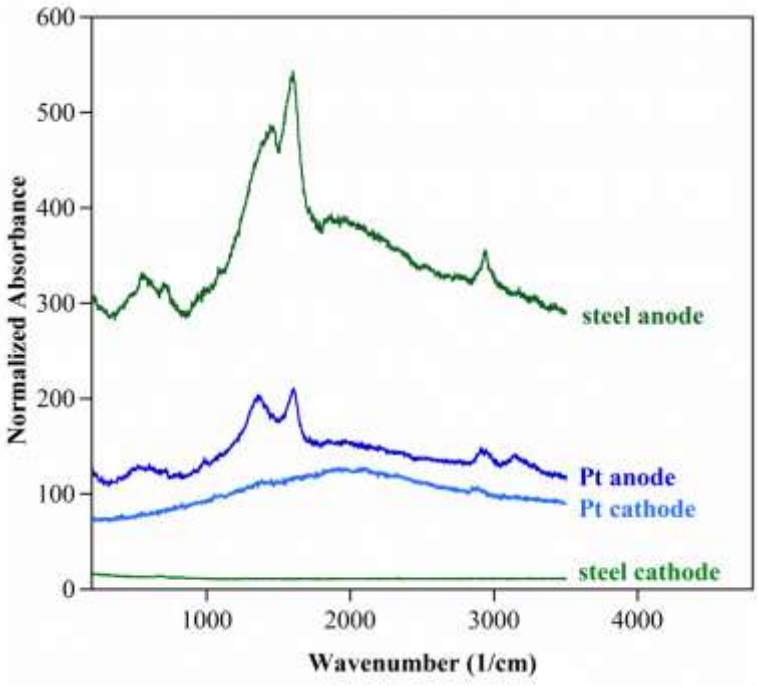

Figure 39. Raman spectra of deposits on steel and Pt anodes.

Table 4. Raman peaks and assignments for deposits on steel and platinum anodes.

Wavenumber, cm^{-1}	Molecular Bond [183-185]
≥ 3100 (steel, Pt)	O–H stretch
2932 (steel) 2909 (Pt)	C–H stretch
1864 (steel) 1843 (Pt)	C=O stretch
1606 (Pt)	C–C
1355 (steel)	C–C
935 (steel)	C–O–C stretch

809, 909, 982 (Pt)	
695 (steel) 716 (Pt)	C–H bend
550 (steel) 597 (Pt)	C–C

3.6.8.5 XPS Analysis of Steel Electrodes

Apart from iron, carbon, and oxygen, the steel control contained chromium, zinc, nickel, sodium (the most abundant, and persistent impurity), lithium, calcium, fluorine, nitrogen, and silicon. Some of these elements are likely to be involved in the reactions that occur at the electrodes [154]. The peak sizes of iron, carbon, oxygen, and sodium upon electrolysis are given in Table 5.

Table 5. Surface composition of steel electrodes from XPS survey scans.

Element Detected	Steel Control (atom%)	Steel Anode (atom%)	Steel Cathode (atom%)
Na (1s)	0.61%	0%	0%
Fe (2p)	12.96%	3.38%	9.51%
C (1s)	44.78%	63.36%	50.97%
O (1s)	40.12%.	32.62%	37.09%

The percentage of metallic iron decreased on the surfaces of both the anode and the cathode, accompanied by an increase in the percentage of carbon, consistent with the formation of a carbonaceous deposit. While sodium was present in the control sample, there was no sodium on either cathode or anode, suggesting that it had been dissolved into the electrolyte. (In order to test this hypothesis, the liquid was inspected by FTIR and Raman, but no sodium was seen; at these low concentrations, that is not surprising.)

When the electrolyte used with steel was subjected to electrolysis a second time, now using clean platinum electrodes), sodium (Na (1s) 0%) reappeared on the cathode (Na (1s) 7.11%), as verified by XPS spectroscopy. In the literature [186] this has been seen previously and attributed to electroplating from the solution. The presence of sodium as an impurity in steel could reduce the EO pumping efficiency by increasing the ionic strength of the PC and thereby lowering the zeta potential [157]. Sodium can also can trigger carbonaceous deposit formation and degrade PC [154].

While it was expected that metal oxidation occurred at the anode, it was not possible to quantify the increase in iron oxides based on the high resolution scans for iron, or by comparison of the atomic percentage compositions from survey scans of the control and the anode. This is likely due to the presence of a large amount of native iron oxide species on the control.

However, the high resolution scan for carbon did confirm, by peak fitting, that on the anode carbonaceous products having carboxylic acid, alcohol, and ether groups were

deposited (Figure 40a). At the cathode, carbonaceous deposits were formed having alcohol, ether, and polyether groups (Figure 40b).

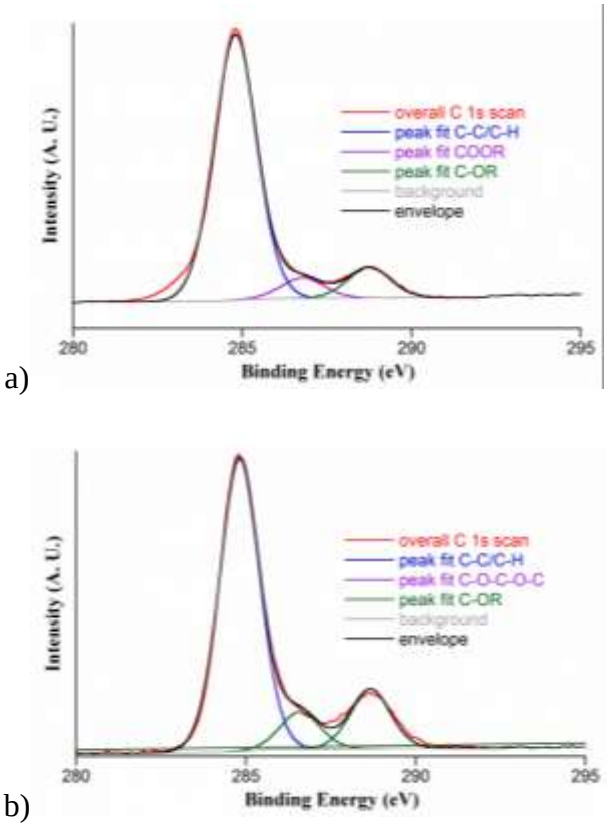

Figure 40. High resolution scan of steel a) anode and b) cathode for carbon species.

3.6.8.6 XPS Analysis of Platinum Electrodes

The surfaces of the platinum electrodes after electrolysis were compared to the surface of a control sample of platinum (800 nm Pt on a 200 nm Ti adhesion layer on an oxidized silicon wafer). The results are summarized in

Table 6.

Table 6. Surface composition (atom%) of platinum control from XPS survey scan.

Element	Platinum Control	Platinum Anode	Platinum Cathode	Platinum Passive
Na (1s)	0%	0%	13.18%	0%
Pt (4f)	48.19%	24.85%	8.46%	40.14%
C (1s)	43.90%	34.78%	30.39%	44.44%
O (1s)	7.91%.	37.12%.	45.44%	15.42%

The percentage of metallic platinum decreased on both anode and cathode, accompanied by an increase in the percentage of carbon and oxygen, indicating the formation of carbonaceous deposits. While no sodium was present on the control sample or anode, it appeared on the cathode, suggesting that it deposited as a contaminant from the electrolyte as suggested by [186]. The clips used to make electrical contact were a possible source of contamination. The sodium was difficult to eliminate despite careful experimental set up. Prior to electrolysis, all components that came in contact with the PC were cleaned of organics: the steel and platinum electrodes, the handling tweezers, and the steel clips used to make electrical contact were rinsed sequentially with acetone, methanol, isopropanol, and DI water. It has been reported that moisture, sodium, and other electropositive elements can trigger the formation of deposits through reductive electrochemical decomposition of PC [154]. Based on these data, to avoid deposit formation the solution must be maintained free of contaminants.

High resolution scans for platinum (Figure 41a) revealed Pt oxide on the anode, showing that the platinum anode had oxidized. The platinum electrodes therefore cannot be assumed to be completely inert, since they are affected when used with degraded PC. There was no change in the oxidation state of the platinum used as a cathode (Figure 41b).

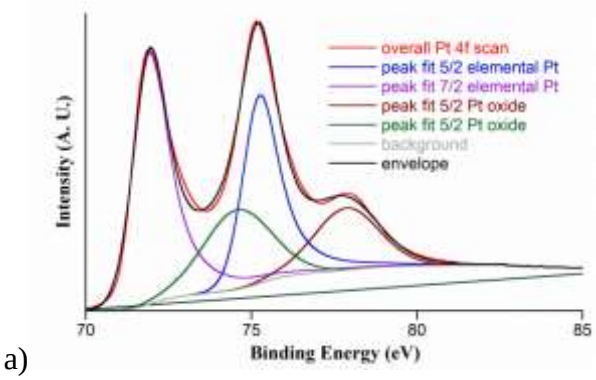

a)

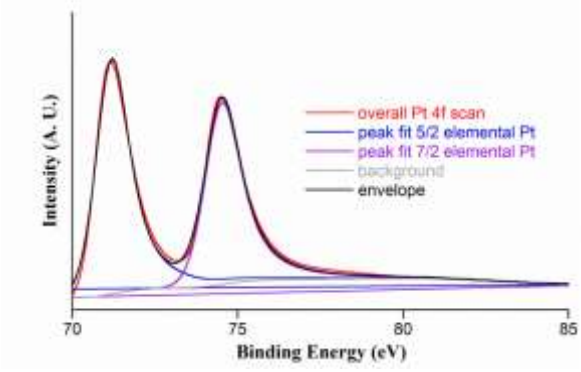

b)

Figure 41. High resolution scan of platinum a) anode and b) cathode for platinum species.

The high-resolution scan of the platinum anode for carbon confirmed that carbonaceous products with carboxylic acid, alcohol, and ether groups were deposited (Figure 42a). At

the cathode, carbonaceous deposits with alcohol, ether, and polyether groups were seen (Figure 42b). These results indicate that the products formed on steel and platinum were similar.

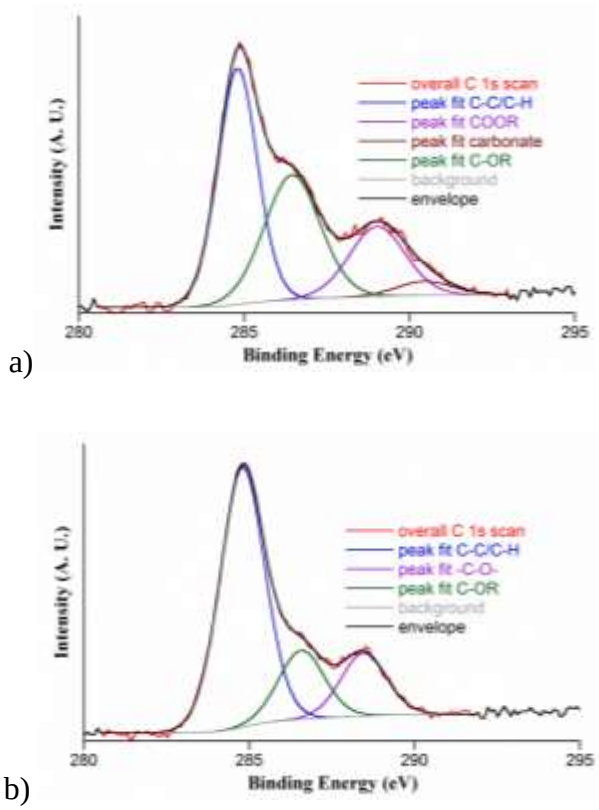

Figure 42. High resolution scan of the platinum a) anode and b) cathode for carbon species.

In order to verify that deposit was formed only on the electrodes used to apply the electric field, a platinum sample was placed in the electrolyte (electrically disconnected) to observe whether a deposit/precipitate formed (Platinum Passive in Table 6). The

composition of the surface of this sample was similar to that of the control, confirming that deposits formed only when the platinum was connected to the voltage source.

3.6.8.7 Summary of Spectroscopy Results

PC was subjected to a humid environment and then to electrolysis. When electrolysis was performed with steel, the PC turned yellow. When electrolysis was performed with platinum, the PC remained colorless. FTIR and Raman did not have the sensitivity required to reveal the new species.

When electrolysis was performed with steel, a thick (~50 μm based on visual inspection) yellow deposit was formed on the anode. A much thinner white deposit was formed on the platinum anode. For both metals, spectroscopy revealed that the deposits contained alcohol, ether, and carboxylic acid groups. While neither steel nor Pt cathodes had a visible deposits, spectroscopy showed that alcohol, ether, and polyether groups were present. These findings are consistent with a prior study [154].

3.7 Additional Data

The following data were not presented in the journal publication.

The voltage was ramped up to 1500 V and then ramped down by manually turning the knob of the high voltage power source as described in Section 3.2.1. The voltage scans were performed in the same sample as Figure 16. In the first scan higher currents in the voltage was observed up to 500 V. On the reverse cycle this deviation was not observed. The response continued to be linear in the following cycle. The red line shown is a linear curve fit of the data. These additional curves were provided to emphasize that redox reaction peaks were not observed in pure PC.

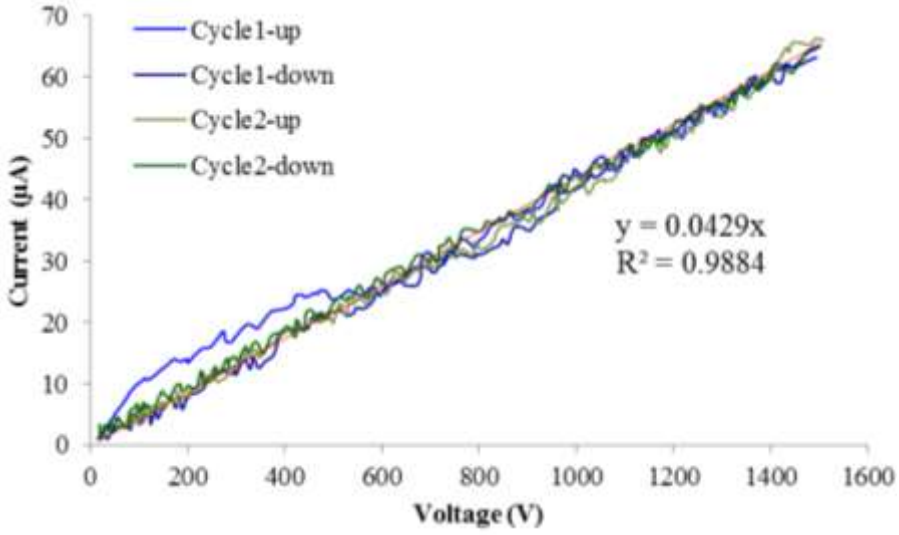

Figure 43. High voltage voltammetry of PC. The voltage was ramped linearly up to 1500 V and then down to 15 V. The cycle was repeated twice; cycle 1 is shown in blue and cycle 2 is shown in green. As shown in the plot the current response was linear, and there were no noticeable redox peaks.

4. **Porous Acrylate Monoliths in PDMS Microchannels**

4.1 Introduction

Porous polymer monoliths can be employed in microfluidic channels in a manner similar to packed beds in chromatography columns. Monoliths consist of a cross-linked polymer filled with interconnected micropores. Monoliths can be fabricated in situ in microfluidic channels and they can chemically functionalized, which enables a wide variety of lab-on-chip applications: for chromatography [187-192], separations [193-195], cell trapping and lysis [196], immunosensing [197]. They have also been reported to be useful for electroosmotic pumping [146,198]. Takamura et al [108] created a monolith-based electroosmotic pump for lab-on-chip applications. To avoid electrolytic bubbles an Ag/AgCl salt bridge gel was photopolymerized around the monolith. This pump was able to achieve a pressure of 800 Pa at 10 V with a single monolith and one pair of electrodes, and 25 kPa using 10 monoliths and 10 pairs of electrodes. An advantage of monolith-based EO devices is that the small pores restrict pressure-driven backflows, while maximizing EO flow.

Various methods have been developed to prepare the walls of PDMS microchannels for attachment of different types of polymer monoliths [192, Zhou, 2010 #174]. Embedding monoliths in PDMS is particularly challenging because PDMS is highly permeable to solvents and gases; this markedly inhibits proper monolith formation due to migration of the monolith molecules into the PDMS. Dr. Jeffrey Burke guided me in this effort, to

embed charged photopatternable acrylate-based monoliths within PDMS microchannels [196] using two different approaches for PDMS surface modification. These monoliths were well anchored to the channel walls and could withstand high pressure (at least 40 psi).

4.2 Materials and Methods

The microfluidic devices were fabricated using PDMS (Sylgard 184, Dow Corning) as described in Section 3.6.1. Monolith formation was tested within three PDMS channel sizes of width 2 mm, 150 μm, and 50 μm; they all had a depth of 40 μm. (The 2 mm channels were formed by PDMS replica molding using a tape mold instead of an SU-8 mold. The reservoirs and channel were cut out of 3M Scotch Magic Tape using an X-Acto knife; the dimensions of the reservoir were the same as in the SU-8 mold, the channel was 1 cm long and 2 mm wide.) The monomer solutions used were ethylene diacrylate (EDA), methyl methacrylate (MMA), butyl methacrylate (BuMA), methyl methacrylate (MMA), ethylene dimethacrylate (EDMA), and 3-trimethoxy silyl propyl methacrylate (TSPA). The photoinitiators used were 2,2-dimethoxy-2-phenyl-acetophenone (DMPAP), benzophenone. The solvents used were chloroform, methanol, ethanol, decanol, tert-butanol. These chemicals were purchased from Sigma-Aldrich. An activated alumina column (Brockmann I, 150 mesh) was used to remove the inhibitors from the monomer solutions. All the monomer solutions were stored in a refrigerator in opaque vials to minimize photo-crosslinking and exposure to oxygen.

4.2.1 PDMS Surface Modification

In order to fabricate embedded monoliths, the inner walls of the PDMS microchannels must have functional groups that can crosslink with the monolith. The PDMS can be prepared for embedding monoliths by coating it with a surface modifying polymer layer. The surface modification bonds to the monolith and anchors it, so that it does not dislodge under applied pressure. The surface modification also limits the absorption of the monolith monomers into the PDMS [187], and the diffusion of oxygen into the channel [199]. Two different surface modification protocols were tested. The first approach involves photographting [196], and the second approach uses silanization to create this polymer layer.

4.2.1.1 Surface Modification by Photopolymerization

The solutions used for surface modification were degassed and purged to eliminate oxygen, which inhibits monomer crosslinking. The photoinitiator solution (0.25 M DMPAP in chloroform), surface modification solution (50% MMA and 50% EDA monomers by weight), and DI water were degassed by sonication (the caps were loosened and the vials placed in the Branson 1510 sonicator, frequency 40 kHz, iced bath) for 10 minutes. In addition, the DI water and surface modification solution were purged with nitrogen (nitrogen was gently bubbled through the liquids) for 10 minutes. The photoinitiator solution was not purged to avoid evaporation of chloroform, which is highly volatile. The PDMS devices were degassed in a vacuum chamber for 1 hour.

The area of surface modification (desired location for monolith formation) was defined using a tape photomask during UV exposure. Black electrical tape was adhered over the entire PDMS device, except for the area of irradiation. Then, the channels were flushed with the photoinitiator solution for 90 sec, followed by a DI water flush for 60 sec. This was repeated twice to enhance the swelling of the PDMS by chloroform which facilitates absorption of the photoinitiator, DMPAP, into the PDMS channel walls. A syringe-full of air was used to purge unabsorbed photoinitiator solution, to prevent the polymer from crosslinking within the inlet and outlet tubings. Next, the channels were filled with the surface modification monomer mixture. Then, the inlet and outlet tubes were plugged and the solution was incubated in the device for 1 minute. The device was exposed to long wave UV light (wavelength 365 nm, 100 W, Blak-ray B-100A from UVP LLC.) for 30 seconds to form the surface coating. The unpolymerized monomers were then flushed out with methanol. The black tape mask was removed, and devices were left to dry overnight at atmospheric conditions.

4.2.1.2 Surface Modification by Silanization

The surface modification solution was prepared a couple minutes before oxygen plasma bonding: 0.254 g of TSPA was mixed into 1.01 g of pH 4.5 ethanol (set using glacial acetic acid), in a dark glass vial. Immediately (within 30 sec) after bonding, the surface modifying silane was injected at the rate of 0.1 mL/s for 1 min using a syringe pump; the device was filled and incubated for 20 min. The monomer flush and incubation was repeated thrice. Ethanol was then injected to rinse out the excess silane. Then, the

devices were baked for 1 hour at 60 ^{o}C in an oven. The devices were left to dry overnight at atmospheric conditions.

4.2.2 Monolith Formation

The monolith solution (0.28 g EDMA, 0.12 g BuMA, 0.75 g decanol, 0.04 g DMPAP) was sonicated for 15 minutes followed by purging with nitrogen gas for 10 minutes to remove dissolved oxygen. EDMA and BuMA are the photo-sensitive monomers, decanol is the porogen, and DMPAP is the photoinitiator. The PDMS devices were degassed in a vacuum chamber for 1 hour. The black electrical tape photomask was adhered to the device. The device was placed on a cold stage (a metal block chilled in a -70 ^{o}C freezer) to minimize polymerization due to heat produced by the UV lamp. The monolith solution was introduced into the channels, and the inlet and outlet were sealed. The solution was irradiated through the photomask for 15 min using the long wave UV lamp. Typically short exposure using a higher intensity light source is recommended to minimize solvent loss. After exposure, the channels were flushed with methanol followed by DI water. The devices were stored submerged in DI water to ensure that the monoliths do not shrink or crack.

4.2.3 Monolith Functionalization

Three methods were tested for attachment of functional groups to the monoliths in order to increase their surface charge. In the first attempt, we tried to form the monolith and functionalize it in a single step. Prior to UV cross-linking, the monolith solution was mixed with 2-acrylamido-2-methylpropane sulfonic acid (AMPS) (Sigma Aldrich), a reactive, hydrophilic, sulfonic acid acrylic monomer used to alter the chemical properties of wide variety of anionic polymers. AMPS was first dissolved in DI water (1.5 g AMPS/ml water). The AMPS-water solution was then mixed with decanol to form the porogen mixture. The monolith was formed as described in Section 4.2.2 using the mixture 0.28 g EDMA, 0.12 g BuMA, 0.75 g porogen mix, 0.04 g DMPAP. To determine the optimal amount of AMPS required for functionalization, monolith mixtures were made containing 1.2%, 0.6%, and 0.3% by weight of EDMA and BuMA monomers. The amount used in the reference literature was 0.6% [200].

In the second approach the functionalization was done after the monoliths were formed. Photoinitiator solution was made by adding 0.025 g of benzophenone to 2 g of solvent (a mixture of tert-butanol and water, in 3:1 volume ratio). To make the grafting solution, 0.1 g AMPS was mixed with 0.1167 g of the photoinitiator solution, and 0.45 g of the solvent mixture. The grafting solution was injected into the channels containing pre-formed monoliths. The tubing was plugged and the device was exposed for 5 min to short wave UV light (wavelength 254 nm, 6 W, UVG-54 Mineralight from UVP LLC.). The channels were then rinsed with methanol followed by water.

In the final approach, the AMPS-grafted monoliths (made in the second approach) were further treated with polyelectrolytes. I learned the process of layer-by-layer polyelectrolyte deposition for increasing surface charge [201] by Jason Benkoski at JHU APL and adapted the recipe for monoliths embedded in microchannels. A polycation polydiallyldimethylammonium chloride (polyDADMAC) (Aldrich 409022), and a polyanion poly (sodium 4-styrenesulfonate) (PSS) (Aldrich 561967) were used. PolyDADMAC is a quaternary amine polycation, and PSS is a sulfonated polyanion. These polyelectrolytes were chosen because they are not pH sensitive, and operate close to neutral pH. Stock solutions were diluted in DI water to yield a 20% (weight) polycation solution, and 30% (weight) polyanion solution. The polycation and polyanion solutions were further diluted to 2% (weight) using a solution of 100 mM NaCl in DI water. The polycation solution was injected into the device via inlet tubing using a syringe, and incubated at room temperature for 10 min. This was followed by a rinse with DI water for 10 min at 1 mL/min using a syringe pump. A syringe full of air was injected to purge the channels. Then, the polyanion solution was injected into the device and incubated at room temperature for 10 min, followed by a rinse with the 100mM NaCl/DI water solution for 10 min at 1 mL/min using a syringe pump. A syringe full of air was injected to purge the channels. The incubations with the polyelectrolyte solutions and subsequent rinse steps were repeated twice so that a total of four electrolyte layers may be adsorbed on the channel walls. Depositing more layers was not expected to provide any further improvement, according to Jason Benkowski.

4.2.4 Elemental Analysis of Functionalized Monoliths

Energy dispersive X-ray spectroscopy (EDS) elemental analysis was performed on the monoliths. Samples were prepared for scanning electron microscopy (SEM) by cutting vertically through the monolith-filled portion of the PDMS channels, followed by sputter-coating with carbon. Samples were probed (using the Hitachi SU-70) at an acceleration voltage of 10 kV. The line scan mode was used to detect the presence of sulfur atoms. I was assisted in the SEM analysis by Dr. Li-Chung Lai. These samples were also examined by an electron probe microanalyzer (JEOL JXA-8900 Superprobe) by Dr. Philip Piccoli.

4.2.5 Electroosmotic Pressure Measurement

The effect of including the monoliths on electroosmosis was studied by measuring the pressure exerted by the pumping fluid (DI water) with and without monoliths. The devices with 150□m channels were used for this experiment. The monoliths embedded in these test devices were not functionalized.

The devices were fixed to the glass substrate through the experiment (i.e., mold release was not applied to the glass surface) in order to prevent membrane inflation and device delamination under EO pressure. Two 1.5 mL Eppendorf microcentrifuge tubes were used as open reservoirs to allow venting of electrolytic gases. Fluidic connectors were inserted into the base of the Eppendorfs, to connect them to the EO device. Without the

large reservoirs, in prior attempts to measure EO pressure with monoliths, the gas bubbles formed due to water electrolysis clogged the monoliths. In order to circumvent this issue, I relocated the electrodes into large reservoirs in order to isolate the electrolysis from the device performance using a set up as shown below in Figure 44. DI water was filled in the EO device, the Eppendorfs were connected and then filled as shown in Figure 44, making sure to eliminate any trapped air at the connectors. While making these connections care was taken to make "wet" connections to avoid trapping air bubbles.

Platinum wire (99%, 28 gauge, uGems, model # 14242) electrodes were inserted in the reservoirs and connected to the power supply (HV Rack, Ultravolt). A pressure gauge was attached to the connector on the side of negative electrode, because flow was expected to occur from the positive electrode towards negative electrode in PDMS microchannels.

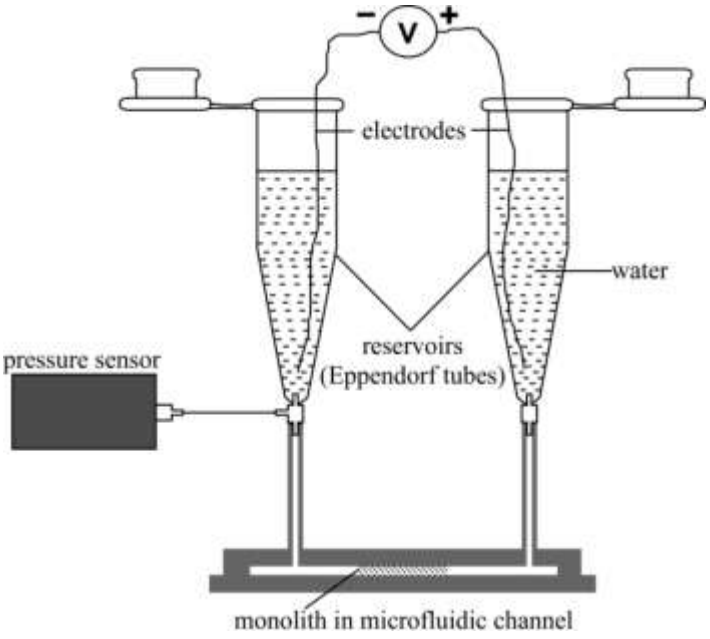

Figure 44. Test setup for measuring electroosmotic flow.

4.3 Results

4.3.1 Monolith Formation

In the 2 mm wide channels, the edges were well defined, and the monolith adhered to the channel walls. However, hollow pockets were observed in the monolith, implying that longer exposure times (> 10 min) may be required for the larger monolith structures. In the 50 μm wide channels, high backpressures were experienced in the presence of monoliths, and the devices could not be filled without applying excessive pressure resulting in monolith being dislodged and/or broken. Monolith formation was most successful in the 150 μm wide channels (Figure 45) ; the monoliths were well anchored

to the walls, had homogeneous porosity with no gaps, and offered moderate resistance when filling the device.

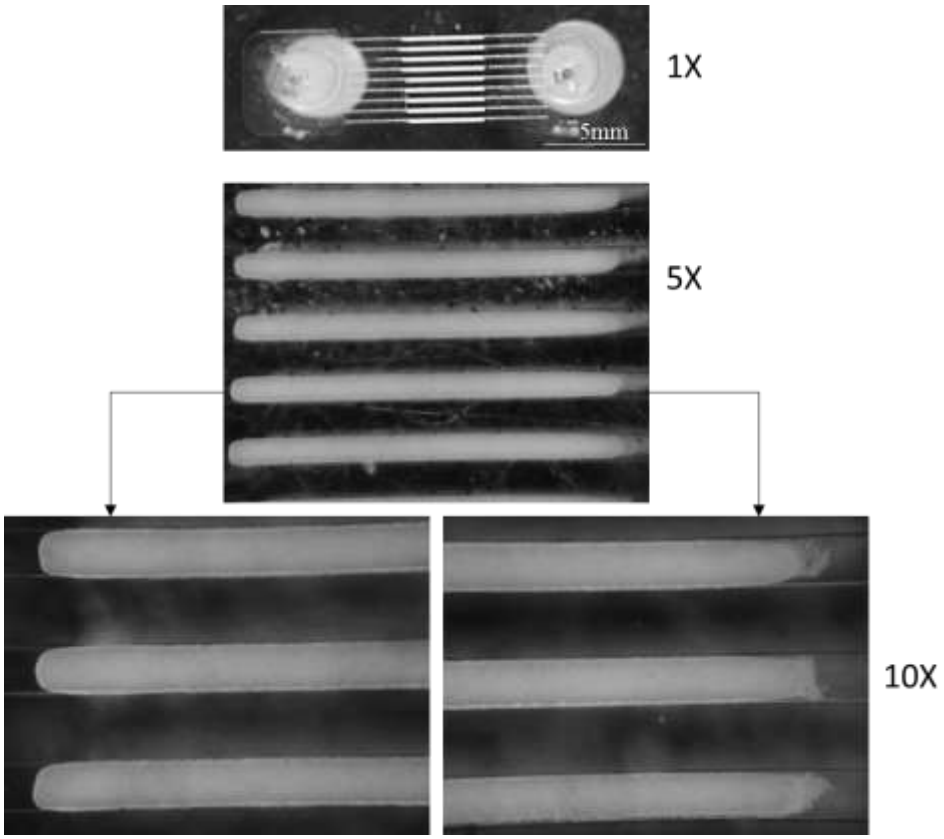

Figure 45. Monoliths formed in 150 μm wide PDMS microchannels. The monoliths were rounded and more sharply defined towards the inlet side, where solutions were injected (bottom left image), as compared to the outflow end (bottom right image).

It is to be noted that the monoliths were formed in PDMS devices still attached to the glass substrate in order to prevent deformation and rupture of the 25 μm PDMS membrane during the process. Device release after monolith formation was enabled by treating the glass with mold release (Mann Ease Release 200) before spin-coating the

membrane. In the absence of mold release it was observed that the monolith often bonded to the underlying glass, resulting in membrane rupture during release. It was noted that only a minimal amount of mold release must be applied (wiped off multiple times after spray coating), otherwise the device peeled off too easily from the glass during the injection of monolith solutions.

4.3.2 Elemental Analysis of Monoliths

Elemental analysis of the samples functionalized by the three methods was conducted by electron microscopy. Figure 46 shows the cross-section of the monolith embedded inside the PDMS microchannel that was analyzed. EDS was unable to detect sulfur atoms on any of the samples. This was probably because the concentration of sulfur in the monoliths was lower than the limit of detection by the EDS equipment (0.1% atomic weight). Using the electron probe microanalyzer sulfur was detected only in the monoliths samples coated with both AMPS and polyelectrolytes, at 0.0334 % atomic weight, indicating that this protocol could potentially increase the zeta potential for EO pumping.

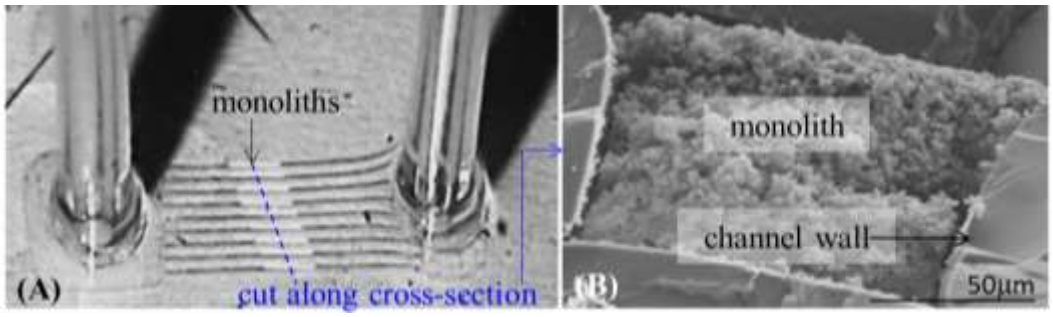

Figure 46. (A) Device with embedded monoliths. (B) SEM image of channel cross-section.

4.3.3 Electroosmotic Pressure Measurement

The pressure produced by EOF flow, with and without monoliths were integrated within the device, was measured using a commercial sensor. In the presence of monoliths, the pressure was significantly higher, but not by the expected orders of magnitude that have already been demonstrated by other groups [135,198,202]. Also, larger fluctuations and variability in pressure was observed in devices containing embedded monoliths. Electrolytic gases (seen within 10-15 sec of application of the electric field) can get trapped within the monoliths and are the most likely cause for the loss of pressure and the fluctuations, due to the compressibility of the gases.

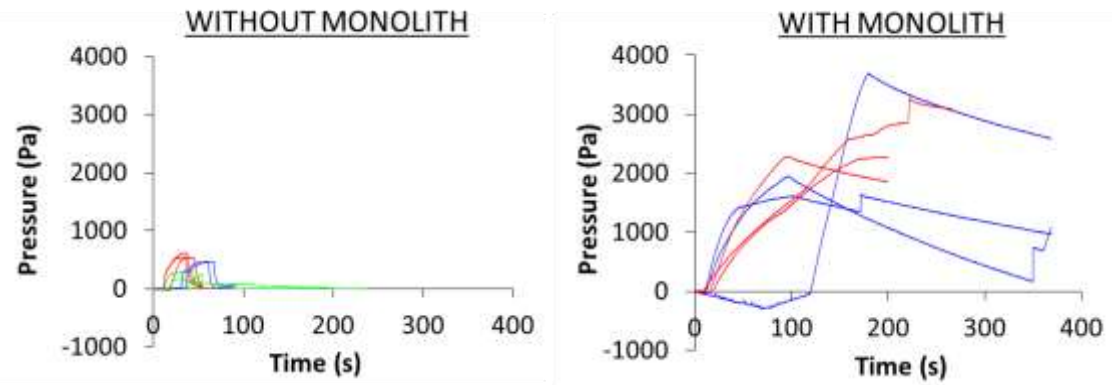

Figure 47. Measured EO pressure using DI water (A) without monolith and (B) with monolith. (Note: (A) and (B) have different scale bars). Pressure output with monoliths was higher but large fluctuations were caused by electrolytic gases.

In order to confirm that monoliths can improve the performance, it is required to eliminate these gases. Thus, future work on monoliths for EO, would involve replacing DI water with PC as the pumping liquid to eliminate the gases, and then conducting tests using the functionalized monoliths to determine if the additional surface charge enabled higher pressures.

5. **Microporous PDMS for EOF**

Author Contributions: Deepa Sritharan conceived the idea of testing microporous PDMS for EOF. Deepa Sritharan designed the devices and the experiments. Mylene Motsebo Deepa Sritharan fabricated the microporous PDMS devices and performed the EOF experiments. Julia Tumbic, Deepa Sritharan tested propylene carbonate degradation. Deepa Sritharan and Elisabeth Smela designed experiments. Deepa Sritharan and Elisabeth Smela wrote the paper.

Abstract

We have previously presented "nastic" actuators based on electroosmotic (EO) pumping of fluid in microchannels using high electric fields for potential application in soft robotics. In this work we address two challenges facing this technology: applying EO to meso-scale devices and the stability of the pumping fluid. The hydraulic pressure achieved by EO increases with as 1/d2, where d is the depth of the microchannel, but the flow rate (which determines the stroke and the speed) is proportional to nd, where n is the

number of channels. Therefore to get high force and high stroke the device requires a large number of narrow channels, which is not readily achievable using standard microfabrication techniques. Furthermore, for soft robotics the structure must be soft. In this work we present a method of fabricating a three-dimensional porous elastomer to serve as the array of channels based on a sacrificial sugar scaffold. We demonstrate the concept by fabricating small pumps. The flexible devices were made from polydimethylsiloxane (PDMS) and comprise the 3D porous elastomer flanked on either side by reservoirs containing electrodes. The second issue addressed here involves the pumping fluid. Typically, water is used for EO, but water undergoes electrolysis even at low voltages. Since EO takes place at kV, these systems must be open to release the gases. We have recently reported that propylene carbonate (PC) is pumped at a comparable rate as water and is also stable for over 30 min at 8 kV. Here we show that PC is, however, degraded by moisture, so future EO systems must prevent water from reaching the PC.

Keywords: electroosmosis, actuator, microchannels, electrolysis, bubble-free

5.1 Introduction

Electroosmosis is the motion of a liquid along a charged surface under an applied electric field. Electroosmosis has been employed as a method of fluidic pumping in micro-scale devices for applications such as chip cooling [136], fuel cell evacuation [137], lab-on-chip assays [94], and electrokinetic separations [94]. The high surface-to-volume ratios

in micro-channels mean that surface effects, such as those involved in electroosmosis (EO), dominate over bulk effects and can create large forces [127,135]. In contrast to pressure-driven pumps, electroosmotic pumps have no moving parts, being actuated by an electric field, and so can be easily miniaturized for integration with micro-systems. Because of the high forces that can be achieved by hydraulic actuation, EO can potentially enable the creation of polymer structures capable of changing their size or shape.

Electroosmotic pumping has previously been used to produce mechanical work in valving [202-205] and in nastic actuators [106,206]. Nastic actuators were inspired by biological structures such as muscular hydrostats [207] and bulliform plant cells [208] in which force transmission is provided by hydraulic pressure. Nastic actuators use electroosmosis within a closed, compliant system to deform the structure. In our initial proof of concept, a membrane surmounting a fluid reservoir was deflected, and weights placed on top of the membrane were lifted. Those devices were fabricated from polydimethylsiloxane (PDMS) and had embedded microchannels and reservoirs filled with water; when an electric field was applied across the microchannels, the water was pumped from one reservoir to the other. One of our long-term goals is to create modular soft robots from arrays of nastic actuators.

In a rectangular microchannel, the flow generated by a DC electric field can be described by the following equations [106].

Equation 17 $$\text{Flow rate} = nwd\frac{\varepsilon\zeta}{\eta}E$$

Equation 18 $$\text{Pressure} = \frac{12\varepsilon\zeta}{d^2\left[1-0.63d/w\right]}E$$

Thus, to achieve fast electroosmotic flow (EOF) the pumping liquid should have a high permittivity (ε) and low viscosity (η), and the solid-liquid interface should have a high zeta potential (ζ). In addition, because both the velocity and the pressure scale linearly with the electric field (E), the applied voltage must be high. Lastly, the channel dimensions must be small to achieve high pressure, since the actuation pressure is inversely proportional to the square of the smallest channel dimension, *d*. (In Equation 18, the channel depth (d) is smaller than width (w); if w were smaller, then d and w should be interchanged.) As seen from Equation 17 and Equation 18, a device containing small microchannels can give rise to large electroosmotic pressures, and increasing the number (n) of channels will increase the flow rate.

In this paper we describe a nastic device with an embedded elastomeric three-dimensional network of channels. The porous structure was fabricated using a sacrificial sugar scaffold. The advantage of this porous material with its interconnected network of channels is that enables the creation of a meso-scale electroosmotic pump that can handle larger volumes of liquid. Meso-scale EOF systems have thus far been difficult to create because standard microfabrication techniques are not well suited to creating large 3D

microchannel arrays. Using a porous sacrificial structure enables the creation of a network of micro-scale channels without the need for patterning each channel individually. This approach may be amenable to use in to roll-to-roll manufacturing, and thus may enable large-scale production of meso-scale actuator modules.

In this work we also address a second issue in the practical application of EO: preventing breakdown of the pumping fluid. While electroosmosis is convenient, in practice it can be difficult to apply reliably [135,143,145,146]. This is primarily because water has been used as the pumping liquid due to its high electric permittivity and because of its importance in chemistry and biology. However, in DC electrokinetic systems, water undergoes electrolytic decomposition into oxygen and hydrogen gas at just 1.2 V [209], but EOF typically requires several thousand volts. Apart from depleting the pumping liquid, the evolved gases form bubbles, which adhere to the channel walls and block the electrodes, interrupting current flow and causing pump failure. We have recently demonstrated [134] that EO can be performed with an electrochemically stable polar organic liquid [154], propylene carbonate (PC), as the pumping fluid to replace water for bubble-free electroosmosis. PC is nonvolatile [210] and has a high dielectric constant of 64 [210]. Unfortunately, we show here that while it is an excellent pumping fluid for electroosmosis, it is also susceptibile to degradation in the presence of moisture which increases its conductivity. Thus, in order to minimize Faradaic currents and maintain high EOF, steps must be taken to minimize exposure to moisture.

5.2 Part I: Electroosmotic Pumping

5.2.1 Methods

5.2.1.1 Pumping Fluid

Propylene carbonate was used as received (Sigma-Aldrich, 99.7% anhydrous). It was stored and aliquoted for use in a positive-pressure argon-filled glove box to prevent exposure to moisture (see Part II). Experiments were conducted in atmospheric conditions.

5.2.1.2 Fabrication of Porous 3D Elastomer

Electroosmotic pumps were fabricated from polydimethylsiloxane (PDMS). The pumps consisted of a two reservoirs and a porous channel layer sandwiched between them. The channel layer was a PDMS "sponge" formed around sugar cubes (Domino Dots Sugar Cubes). The PDMS was prepared by mixing the pre-polymer and curing agent (Sylgard 184, Dow Corning) in a 10:1 w/w ratio. The mixture was poured into plastic petri dishes to a height of 4 mm and degassed in a vacuum desiccator for 30 minutes or until the PDMS was observed to be free of bubbles. At this point, the PDMS mixture was still fluid. A sugar cube was placed into the mixture, in the middle of the petri dish, and the dish was returned to the dessicator for a further 60 minutes. Under the low vacuum, the PDMS filled the sugar cube. The petri dish was then placed in an oven and baked at 60 °C for 1 hour to cure the PDMS. After curing, the sugar was removed by immersing the

petri dish containing the PDMS-sugar cube in a beaker filled with a 1:1 (by volume) mixture of ethanol and DI water and sonicated for 90 minutes. The ethanol swells the PDMS and enables the water to quickly dissolve the sugar. Because PDMS is hydrophobic, it takes much longer to dissolve the embedded sugar using water alone. The solution was replaced with fresh ethanol-DI water mixtures 5-6 times, and the sonication was repeated until the liquid-filled sponge appeared translucent and no white sugar crystals were visible. The sample was then removed from the beaker and the sponge was trimmed using a sharp razor to the level of the solid PDMS surrounding the sponge. The trimming was done while the sponge was still wet in order to ensure that the pores were not damaged by the pressure applied while cutting. The final structure was a three-dimensional (3D) PDMS sponge surrounded by a flat, solid PDMS frame (Figure 49). Using optical microscopy, the pores were determined to be 150-500 μm in diameter.

5.2.1.3 Fabrication of Electroosmotic Pump

Reservoirs were formed by PDMS replica molding as described Figure 48. The molds consisted of a laser-cut square of Delran of sides 3 cm and height 2 mm fixed in the center of a 100 mm diameter plastic petri dish using cyanoacrylate (Instant Krazy Glue). PDMS (prepared by mixing the pre-polymer and curing agent in a 10:1 w/w ratio and degassing) was poured into the mold to a height of 3 mm and degassed to remove any air bubbles trapped around the square mold. The PDMS was cured for 30-60 min at 65 °C, and the replica was peeled off the mold. Silicone tubing was used for the inlet and outlet.

A silicone tube (1 cm long, 0.89 mm I.D., Cole Parmer) was bonded to the top of each reservoir by applying uncured 10:1 PDMS around the tube and baking at 65 °C in an oven. A steel pin was inserted into the tubing and pierced into the reservoir to hold the tubing in place while the surrounding PDMS cured.

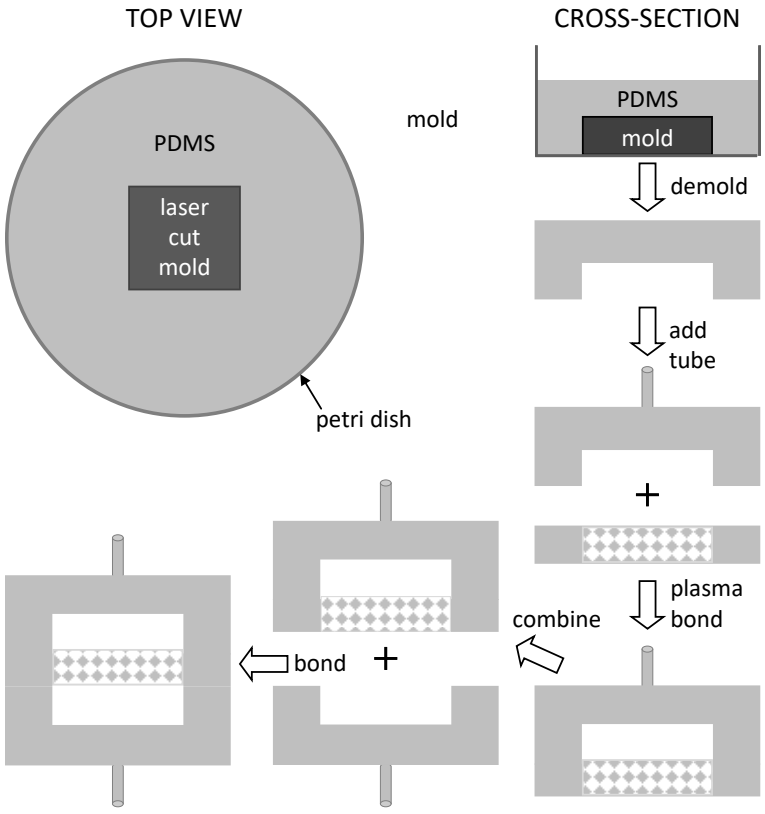

Figure 48. Fabrication of a meso-scale electroosmotic pump. Reservoirs, of 2 mm depth, were molded in PDMS using a square-shaped mold. Tubing was fixed on top of the reservoirs. The reservoirs were plasma bonded to either side of the porous PDMS layer.

The reservoirs were attached on either side of the PDMS sponge by oxygen plasma treatment (10 seconds, 600 mTorr, 50 W, March Jupiter III O2 plasma system). The

device was placed in an oven and baked at 80 °C overnight to ensure complete bonding. Devices were stored in the oven at 80 °C until use to minimize moisture absorption. This was done to alleviate the degradation of the propylene carbonate pumping liquid, which will be discussed in Part II.

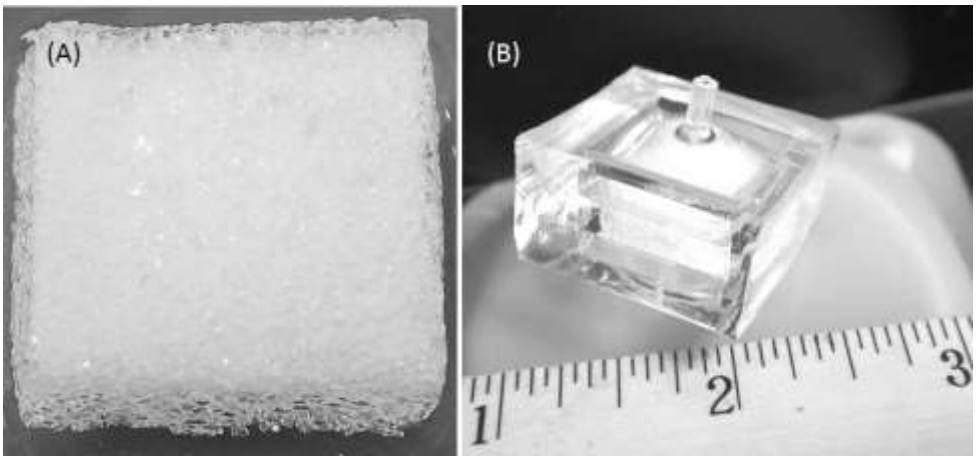

Figure 49. A) The PDMS sponge after removal of the sugar. B) Pump containing reservoirs flanking the embedded sponge.

To fill the device, the device was placed under vacuum for 30 minutes. It was removed and PC was manually introduced through one of the tubes using a 10 ml syringe with an 18 gauge needle. In order to eliminate trapped air pockets, the filled device was immersed in a beaker filled with propylene carbonate so that the tubes to both reservoirs were fully submerged. The beaker was placed in a dessicator and degassed until no bubbles were seen escaping the device, approximately 60 minutes, and the porous sponge became transparent, indicating it was fully filled. Although the device can be filled

without the first two steps, by simply immersing it in PC and then dessicating, this can cause PDMS to swell with PC, resulting in shorting when voltage is applied. The first two steps minimize the swelling of the PDMS by PC. It is important to ensure that the sponge is filled completely with liquid, with no air entrapped, and that the electrodes are completely immersed in the liquid in order to avoid sparking and electrode reactions with the oxygen, which burn the PDMS and oxidize the electrodes.

Steel wire was used for the electrodes: a length of 0.1 mm steel wire was threaded through a 0.4 mm inner diameter, 75 mm long glass capillary (Drummon Scientific Co., PA). The PC-filled pump was removed from the dessicator, maintaining the silicone tubes horizontal to prevent air from entering the device. The capillaries were press-fit into the tubes, taking care to ensure that the electrodes were inside the reservoirs close to the porous PDMS layer.

The assembly was fixed to a lab jack to allow height adjustment, and the capillary was aligned against a graduated scale (Figure 50). The electrodes were connected to a high voltage supply (HV Rack, Ultravolt, Ronkonkoma, NY). The level of liquid in the capillaries was equilibrated before each run, i.e. we ensured the liquid was at rest in both capillaries. The electroosmotic velocity was measured by timing the movement of the fluid meniscus in the glass capillaries.

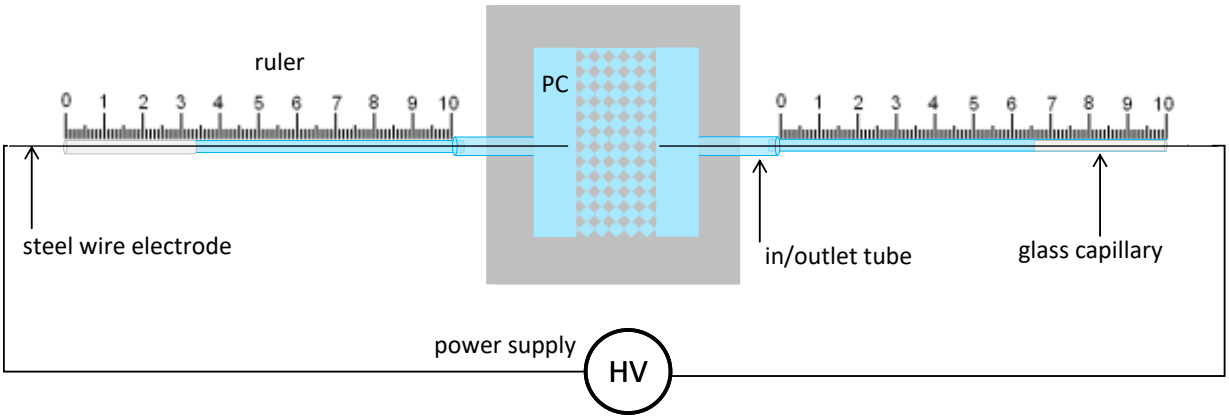

Figure 50. Device to measure electroomostic flow rate. The filled device was positioned so that the inlet and outlet tubing were held horizontally. Glass capillary tubes were inserted into the inlet and outlet. Steel wire electrodes were threaded through the capillary into the device so that they were on either side of the porous channel layer.

5.2.1.4 Fabrication of Unfurling Structure

As a demonstration of high flow rate actuation, the electroosmotic pump was used to unfurl a 10 cm long rolled-up PDMS "balloon". This structure was fabricated using a glass vial as a mold (12 mm × 75 mm borosilicate culture tubes, Fisherbrand). The vial was fixed to a plastic petri dish using double-sided tape with the mouth of the vial facing downwards. The PDMS precursor mixture (10:1) was poured over the vial and allowed to flow down the sides, resulting in a uniform, bubble-free coating. The PDMS skin was cured in an oven at 65 °C for 2 hours. The PDMS was then gently pulled off the vial, resulting in a balloon-like structure attached to a base of PDMS. Using uncured 10:1

PDMS mixture as an adhesive, this base was bonded to a block of PDMS with a silicone tube, fabricated as described above.

The PDMS balloon was evacuated by placing it in a desiccator for 10 minutes, and then it was rolled up from the closed end towards the end with the silicone tube. The silicone tube was attached to the outlet silicone tube of an EO pump using an 18 gauge needle as the connector. This needle also served as the cathode. The inlet tube of the pump was connected to a 20 ml glass vial containing PC, serving as a large reservoir of pumping fluid, using an 18 gauge needle that also served as the anode. The anode and cathode were contacted with alligator clips and connected to the high voltage supply. The assembled actuator is shown in Figure 51.

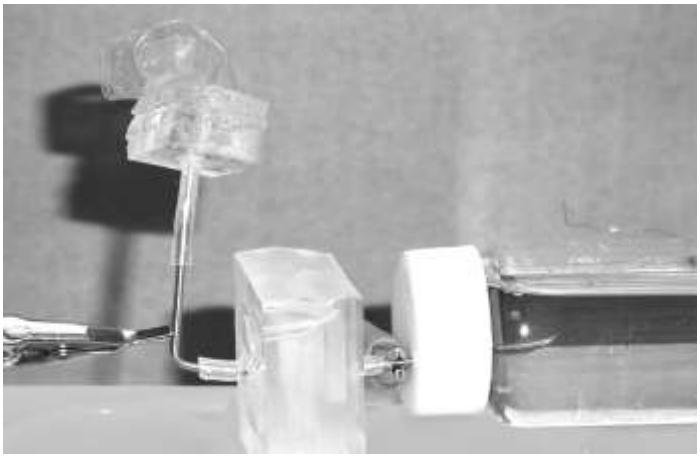

Figure 51. Device setup for electroosmotic actuation of a hollow rolled-up balloon structure. The pump is at the bottom of the image, in the center. The unfurling balloon is at the top right. The large external fluid reservoir is on the left.

5.2.2 Results and Discussion

5.2.2.1 Electroosmotic Pumping by the Porous Elastomer: Flow Rate

The efficacy of the porous 3D elastomer for EO pumping was evaluated by measuring the flow rate produced by the pump. The experimental set-up is shown in Figure 52A, and a video is shown in Figure 52B.

Care was taken to ensure that there were no trapped air bubbles in the channels and tubes, and the capillaries were positioned horizontally to eliminate the gravitational forces on the liquid. The voltage was applied, and six velocity measurements were made. After each measurement, the voltage was turned off and the liquid was allowed to come to rest to minimize pressure-driven flow. Data were collected from two devices.

EOF occurred from the anode toward the cathode, showing that the zeta potential was negative. At 4000 V, the first device gave a velocity of 25±13 mm/s and the second 22±5 mm/s. Device-to-device variation were expected because the porous layer was hand cut and each device individually hand-made, giving small differences in the positions of the electrodes with respect to the microchannel structure (which affects the electric field strength), microbubbles were trapped during filling at the capillary joint, etc. It was also difficult to measure the speed accurately because of the fast fluid flow, which filled the 10 cm capillary within 2-3 seconds.

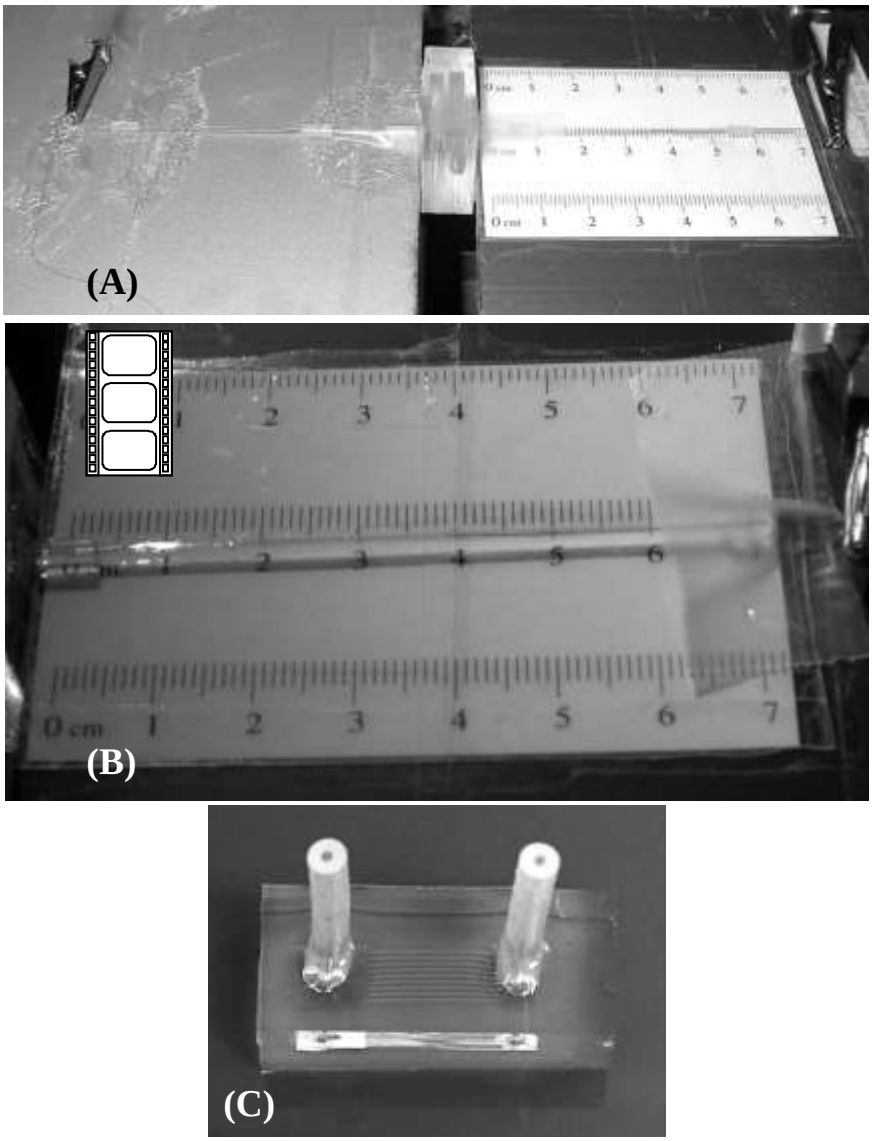

Figure 52. A) Experimental set-up for measuring flow rate. The pump is in the center. The anode is threaded into the capillary on the left side and the cathode is in the capillary on the right. As fluid was pumped from the left to the right upon the application of a voltage, the position of the meniscus was measured against the ruler. B) Video showing electroosmotic pumping of PC through a glass capillary. mesopump velocity.wmv C) Micro-channel pumps tested for comparison.

In comparison to our previous microchannel-type nastic device (Figure 52C) [106], the velocity achieved using the meso-scale device was significantly higher. The microchannel devices were tested in a similar setup as the meso-scale device. The capillaries were fixed horizontally to eliminate the effect of gravity on the fluid movement in the capillary. The EOF velocity of PC pumped by the microchannel-type nastic device, in a capillary of the same dimensions as used with the meso-scale pump, was 5.3±1.3 mm/s at 4000 V. To compare the performance with the porous elastomer pump, we assume that the work/area, given by the pressure times the flow rate, should be similar since the material is the same. The microchannel devices comprised 9 channels of 25 μm x 150 μm, giving a total cross-sectional area of 0.04 mm^2. The porous PDMS layer was 1 x 1 in^2; taking the porosity as 50% the cross sectional area was approximately 323 mm^2, a factor of 8064 times larger. In the porous 3D PDMS, the channels were larger, 150-500 μm. Comparing the factor $d^2[1-0.63d/w]$ in the expression for pressure, the porous elastomer would be expected to produce a pressure that was lower by a factor of 90-1000. The 5 times increase in flow rate is therefore not unreasonable and encouraging.

Two commercially available EOF devices are the Osmotex Nanopump and the Electroosmotic Pump by Dolomite Microfluidics. The pump by Dolomite achieves a maximum flow rate of 150 μL/min, and the Osmotex Nanopump achieves up to 0.57 μL/min [211]. In comparison, we have been able to achieve an average of 188 μl/min using our meso-scale electroosmotic pump.

The flow rate of 20 mm/sec-V demonstrates that useful electroosmosis can be achieved in a meso-scale device. Devices on this scale have not been developed until now because large flow channels experience pressure-driven backflows that are greater than the flows produced by electroomosis. By employing a porous 3D pumping layer, the dominant electroosmosis effects seen at the microscale are combined with a large number of channels to produce high flow rate electroosmotic flow.

5.2.2.2 Electroosmotic Pumping by the Porous Elastomer: Application

We have been able to demonstrate the potential application of electroosmosis for soft robotics by using the meso-scale EO pump to unfurl a rolled-up flexible structure. The experimental set-up is shown in Figure 51, and a series of photographs of the unfurling PDMS balloon as the device filled with fluid is shown in Figure 53.

Care was taken to ensure that there were no trapped air bubbles in the PDMS sponge and the tubes. The balloon was rolled as tightly as possible by hand and positioned on top of the inlet. There was a small amount of air at the interface of the balloon inlet and the cathode (18 gauge needle seen in Figure 51) that was difficult to eliminate. This caused a small amount of air to be pushed into the balloon before it filled with PC. When 10 kV was applied, fluid filled the device in approximately 6 minutes.

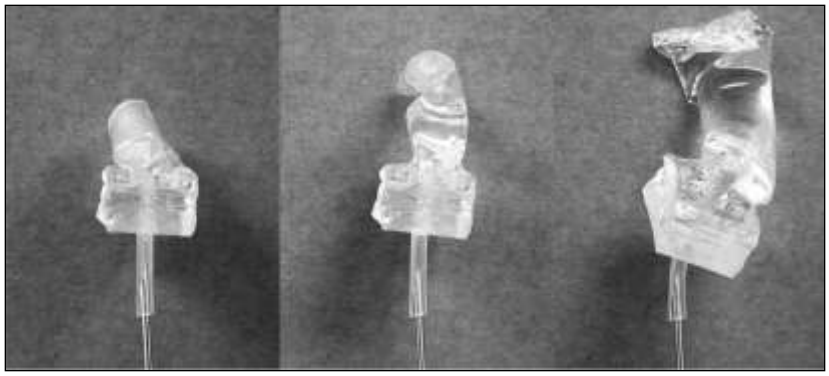

Figure 53. Unfurling of a PDMS balloon by electroosmostic actuation. The structure unrolled as fluid filled the balloon and expanded. As the balloon filled it caused the structure to bend due to the weight of the fluid. The final frame shows the filled balloon. unfurling.pptx

5.3 Part II: Propylene Carbonate Degradation

5.3.1 Methods

5.3.1.1 Electrical Testing of PC

The electrical stability of PC was characterized by chronoamperometry, monitoring changes in current over time at constant applied voltage. Two steel pins (length 1 inch, diameter 600 μm) were used as electrodes. They were held in parallel by a rubber stopper and immersed to a depth of 1 cm into a glass vial (12 mm × 75 mm borosilicate culture tubes, Fisherbrand) containing 6 mL PC (Figure 54). The current was measured

until it reached steady state. After the chronoamperometric measurements, the pins were examined by optical light microscopy.

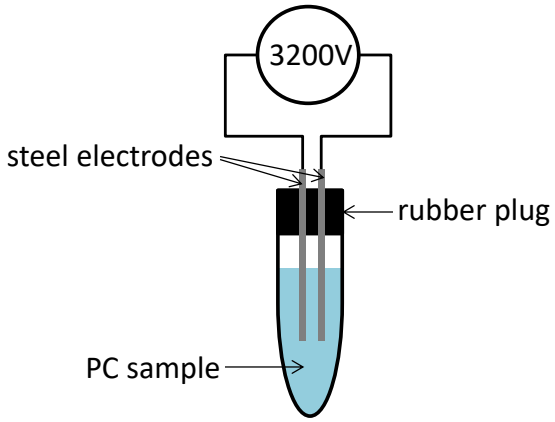

Figure 54. Set-up for chronoamperometry in PC.

5.3.1.2 Exposure to Moisture and UV Light

Five 20 mL glass test tubes were filled with 10 mL of PC. Two vials were placed uncapped inside a container that maintained a relative humidity of 94-99% for 4 hours. One vial was capped and wrapped with aluminum foil to hold the PC in darkness. Three vials were capped and exposed to UV light of 364 nm (Blak-Ray, UVP, Upland CA, Model B-100 A) for 15, 30, or 105 minutes.

5.3.2 Results and Discussion

In testing the PC as a pumping fluid in microchannel-type membrane actuator devices as described in [106], we observed that when using fresh PC from a previously unopened container the current was less than 5 μA throughout the duration (15-20 min) of the experiments. However, the pumping behavior progressively changed, and with PC that had been exposed to the atmosphere for 8+ hours the current was two orders of magnitude higher (> 0.3 mA). Furthermore, the velocities for fresh PC were higher than those for exposed PC. When using steel pins as electrodes with exposed PC, but not fresh PC, a deposit formed on the anode (Figure 55). This motivated a study of the effects of moisture and UV light, both alone and in combination.

Figure 55. Top: fresh steel pin. Bottom: steel pin used as cathode covered with sticky deposit upon high voltage (3.2 kV) application to degraded PC.

Given the difference in current between the two solutions, we performed chronoamperometry at high voltage in order to determine the environmental factor responsible for the degradation in the performance of the PC. Fresh PC was exposed to moisture and UV light, and the current examined for changes compared to the current in fresh PC. Steel electrodes were used because of their reactivity.

Typical chronoamperograms are shown in Figure 56. In fresh PC the current decayed exponentially, following the behavior of an RC circuit where R is the resistance of the PC and C is the capacitance of the electric double layer at the PC-electrode interface [174]. No gas was evolved, by visual inspection, and no deposits were created on the surface. PC that had been exposed only to UV light had the same behavior.

The current in samples that had been exposed to moisture (alone and in combination with UV) had larger currents that persisted for longer before decaying to zero, suggesting that Faradaic reactions were occurring. The time course of the decay varied significantly, as

shown by two examples in Figure 56, in nominally identical trials. A pale yellow deposit formed on the pin that served as the cathode, and the anode darkened in color (Figure 55). Moisture can thus be concluded to be the problem. The effect of moisture on the behavior of the PC is irreversible and cannot be eliminated by heating the PC to drive off the moisture.

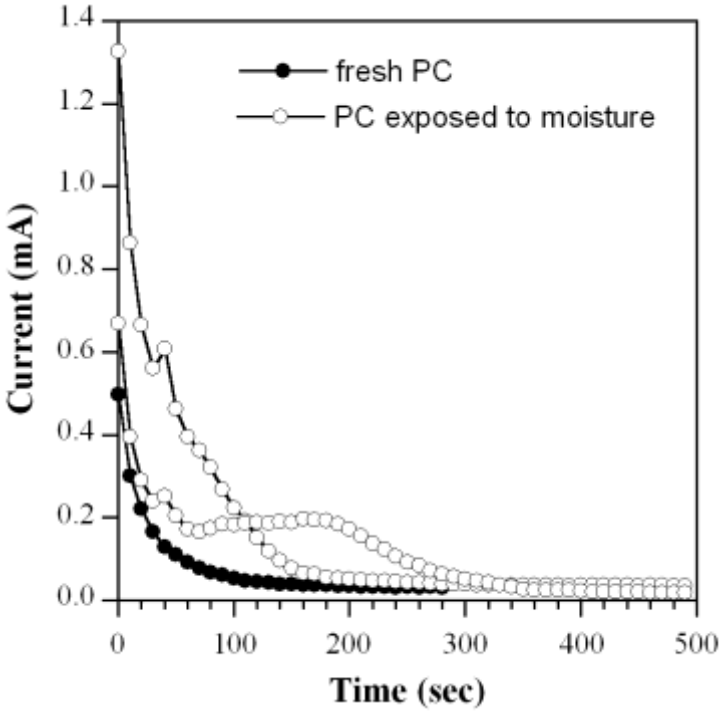

Figure 56. Chronoamperometry of fresh PC versus PC exposed to moisture.

Because most polymers are permeable to moisture, particularly elastomers, these data reveal a challenge to developing soft robots based on nastic actuators. While PC can be stably pumped at high voltage, unlike water, which hydrolyzes, it must be rigorously protected from water. Future work must take this finding into account, either by protocol

(filling the device immediately before use and limiting the time of use) or by design (materials).

Sections 5.4 and 5.5 have not been previously published.

5.4 More on Forming Porous PDMS

To obtain connected channels it is required to pre-form a continuous network of the porogen material. The previous chapter describes using sugar cubes to form microchannels. Conventional sugar cubes are formed by adding trace amounts of water to granular sugar particles and packing the moistened sugar tightly into cube-shaped molds. The water holds the grains of sugar together by surface tension forces, and the sugar grains remain in this position even after drying resulting in a sugar matrix with many open pores.

The pores formed using a standard sugar cube were large (150-500 μm). To reduce the pore size I worked with freshman student Ruth Baldwin on finding other porogens to form sacrificial structures. First water-soluble porogens were tested. The granular porogens tested were iodized salt (Giant Food, Landover, MD) and sweeteners: Equal (Merisant Co., Chicago IL), Splenda (McNeil Nutritionals, Fort Washington PA), Sweet'n Low (Cumberland Packing Corp., Brooklyn, NY), white sugar (Domino Foods,

Inc. Yonkers, NY). Then, camphor was tested as a porogen that dissolves in organic solvents. Powdered samples of the above porogens were also prepared by grinding them with a glass mortar and pestle.

Vial caps (screw caps of 20 mL scintillation vials from Wheaton Industries, Millville NJ) were used as molds to form the porogen matrices, samples were prepared.using porogens in both their granular and powdered forms. In each mold 1 gram of porogen was placed and moistened with 1 mL of water, by adding 20 µL at a time and thoroughly stirring to avoid dissolving the porogen yet uniformly distribute the water amongst the porogen grains. The moistened porogens were firmly pressed into the molds using a spatula. The samples were placed in the oven at 50 ^{o}C overnight to dry. 2.5 grams of PDMS (prepolymer and curing agent were mixed in 10:1 weight ratio) was slowly added to the porogen matrix allowing time for the PDMS to seep into the interstitial gaps. Samples were also prepared by directly mixing the 1 gram of the porogen (both granular and powder forms) and 2.5 grams of PDMS and packing the mixture into the molds with a spatula. In addition to the above described samples a third sample was prepared using water droplets as a porogen. A surfactant, 1% (v/v) Triton X-100 was added to water keep the water droplets uniformly dispersed and emulsified with PDMS. Immediately after mixing in the porogens (to minimize settling or phase separation) all samples were cured in an oven at 70 ^{o}C overnight.

The samples were removed from the molds, and the thin skin of PDMS encapsulating the porogen matrix was scraped off using a razor blade to expose the outermost layer of

porogen grains. The samples were placed in a large beaker filled with a 20% ethanol (remaining 80% was DI water). (The ethanol enables better permeation of the DI water into the hydrophobic PDMS matrix.). The camphor sample was rinsed in undiluted acetone. The beaker was placed in a heated ultrasonic bath (Branson 1510 sonicator, frequency 40 kHz, maintained at 60 ^{o}C for twenty to forty minutes. The beaker was then emptied and replenished with fresh solvent (20% ethanol) to maintain a high concentration gradient between the porogen and the solvent, and thus increase the rate of dissolution. This rinsing process was repeated about ten times. The samples were then dried in an oven overnight at 65 ^{o}C.

Cross sections of the porous PDMS samples were inspected under a microscope. Table salt produced pores that 25-50 μm were seen. Using white sugar large pores of 50-150 μm were seen. Samples using ground salt the PDMS did not cure fully remained tacky. Samples formed with ground sugar had visible remnants of sugar that could not be eliminated despite extensive soaking and rinsing. Camphor as a porogen created huge mm-scale pores. Samples using water droplets had no visible pores.

The porosity of the samples was tested by placing dispensing drops of water, dyed with red food coloring, on the samples until it formed a liquid film covering the top surface. The liquid was allowed to seep into the samples overnight. For all porogen types, other than the pre-formed commercial sugar cube, it was observed that only a thin layer at the top had absorbed the red liquid. Next, the samples were pressed into a dish filled with the colored water, to displace the air and soak up the liquid. Similar results were

obtained despite the higher pressure applied for filling liquid. Scanning electron microscopy showed that continuous pores were not formed by mixing solute particles into PDMS (Figure 57).

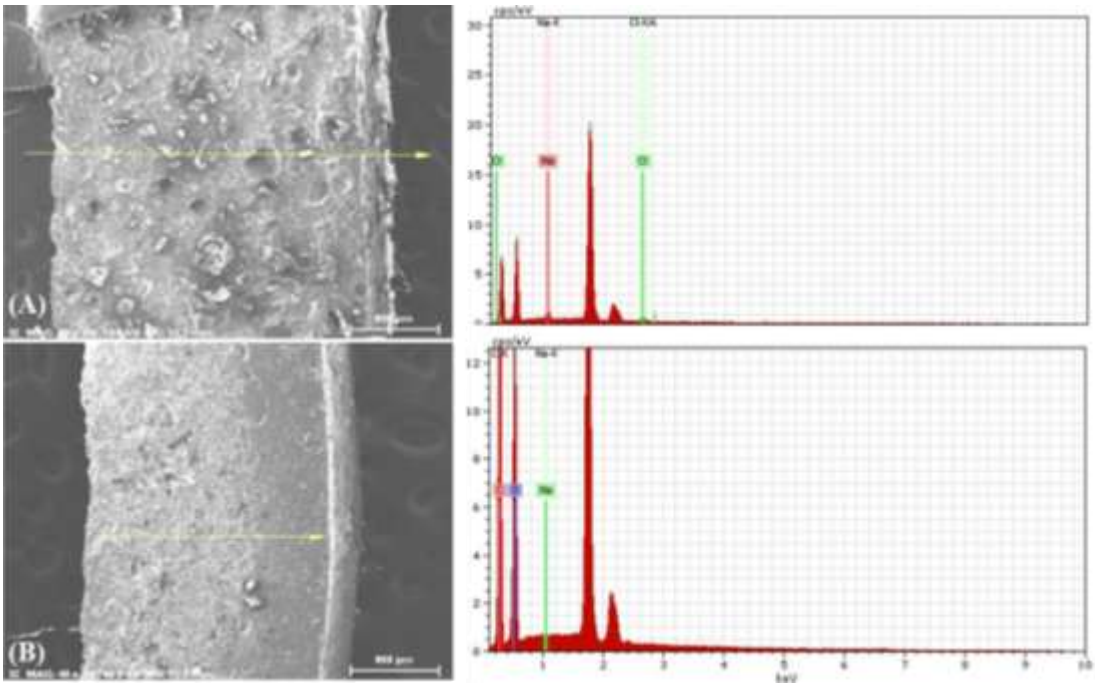

Figure 57. Scanning electron microscopy images of the cross-section of a sample formed by mixing porogens into uncured PDMS before curing. The images show that pores formed by this method were not interconnected. The corresponding elemental analysis on the right shows remnants of Na and Cl atoms in the sample indicating incomplete salt dissolution. (B) SEM of cross-section of sample formed by mixing powdered white sugar as porogen into uncured PDMS before curing. The corresponding elemental analysis on the right shows remnants of C and O atoms in the sample indicating incomplete sugar dissolution.

For forming PDMS that has better wettability, not only on the surface but throughout the bulk of the polymer, I mixed the surfactant 1% (w/w) Silwet I-77 (Momentive Performance Materials Inc.) with uncured PDMS mixture [212,213] and formed test sponges using Domino sugar cubes. The resulting sponges showed excellent wettability with water and instantly absorbed dispensed drops of liquid. However, there was no improvement in wettability with PC.

I then tried forming microchannels by using microspun sugar, commonly known as "cotton candy". Spun sugar was prepared using a benchtop cotton-candy machine (West Bend Back to Basics Old Fashioned Cotton Candy Maker, West Bend, Wisconsin). The spun sugar was packed into the plastic vial cap (screw caps of 20 mL scintillation vials from Wheaton Industries, Millville NJ) and PDMS was poured over the sugar. The PDMS was heavier than the spun sugar, so caused it to become compressed during casting. The PDMS was allowed to cure for 24 hours at room temperature; heat was not applied to avoid melting the sugar. The PDMS skin was scraped off the top and bottom of the cured material so that the sugar became exposed to the ambient. The sugar was dissolved out of the PDMS by rinsing it in a mixture of ethanol water using heated ultrasonic bath, as described in the preceding paragraphs.

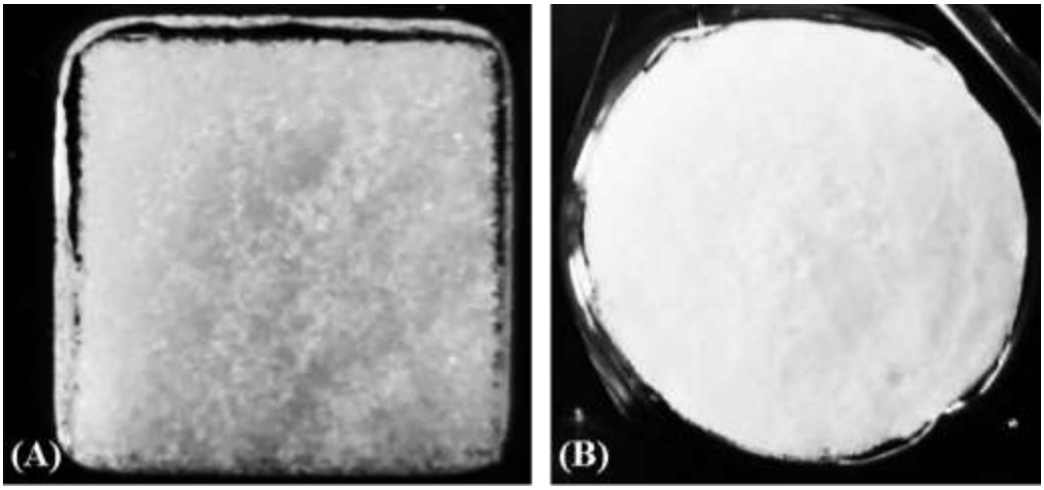

Figure 58. (A) Porous PDMS formed using Domino sugar cube. (B) Porous PDM formed using microspun sugar.

The electroosmotic device was then formed using the same process described in Chapter 5. The pores formed by this method were significantly smaller than those formed using the Domino sugar cube (Figure 58). Due to this, it was difficult to fill the device and vacuum filling was required for at least 2 hours to remove trapped air. On the other hand, this device was able to demonstrate EO pumping at 120 mL/min as compared to 1 mL/min obtained using the Domino sugar cube device. I obtained this result using only a single device, because it was difficult to successfully fill the other test devices; the trapped air caused the devices to spark and burn holes through the porous PDMS. This method may be useful if the PDMS can be chemical modified to make it more PC-philic.

5.5 Fabrication with Sugar

In addition to using sugar for making PDMS sponges I also tried to form larger channels and reservoirs using melted sugar. I poured PDMS over the sodied sugar structures and allowed the PDMS to cure at room temperature. I later dissolved the sugar to create a PDMS slab with embedded multi-level channels and reservoirs. I found that it was possible to create rounded dome structures and channels with rounded edges and connections (see Figure 59), unlike traditional photolithography.

Sugar has been used to form intricate structures in the culinary world for several years. When melted it behaves similar to glass and it can be pulled, blown, or spun. Sculpting with sugar has been considered a sophisticated art that requires years of practice and the products have low reproducibility when handmade. For sugar-based sacrificial fabrication to be amenable to rapid prototyping of fluidic devices it would be useful to employ 3D printing for forming the features because the equipment has built-in temperature control and a fine nozzle that can extrude the sugar filaments [214].

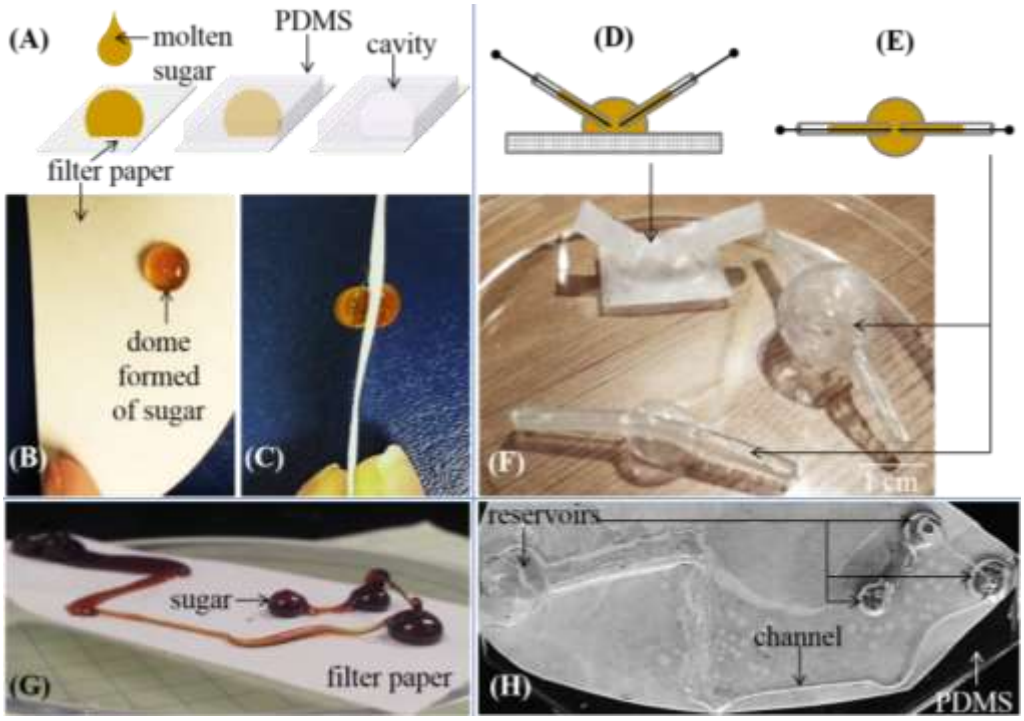

Figure 59. Sugar structures made by manual fabrication. (A) Molten (≥ 180 ^{o}C) sugar is applied onto filter paper using a glass pipette. The drop of sugar permeates the paper pores until it cools and solidifies at room temperature to form a solid dome that is adhered to the paper. PDMS is poured over the solidified dome. The sugar dissolved with water to yield a dome-shaped cavity that could later be filled with pumping liquid for EOF. (B) Photograph of a sugar dome formed as described in (A). (C) Domes can be formed on either side of a sheet of filter paper and then be encapsulated in PDMS. When the sugar is dissolved it results in two reservoirs connected by a paper microchannel layer (that can function as EOF channels) embedded inside the PDMS matrix. (D) Molten sugar can be drawn into a variety of shapes by controlling the speed of the pipette to form multi-planar structures. (E) PDMS poured over these features results in a device with embedded reservoirs and channels with rounded edges.

6. **EO Pumping in Paper**

Author Contributions: Elisabeth Smela conceived the idea of testing paper microchannels for EOF. Deepa Sritharan designed the devices and the experiments. Deepa Sritharan fabricated the devices and performed the experiments. Deepa Sritharan and Elisabeth Smela analyzed the data. Deepa Sritharan and Elisabeth Smela wrote the paper.

Abstract

A voltage-controlled hydraulic actuator is presented that employs electroosmotic fluid flow (EOF) in paper microchannels within an elastomeric structure. The microfluidic device was fabricated using a new benchtop lamination process. Flexible embedded electrodes were formed from a conductive carbon-silicone composite. The pores in the layer of paper placed between the electrodes served as the microchannels for EOF, and the pumping fluid was propylene carbonate. A sealed fluid-filled chamber was formed by film-casting silicone to lay an actuating membrane over the pumping liquid. Hydraulic force generated by EOF caused the membrane to bulge by hundreds of

micrometers within fractions of a second. Potential applications of these actuators include soft robots and biomedical devices.

6.1 Introduction

Soft actuators are able to stretch, twist, squeeze through tight spaces, and gently grip fragile objects (see reviews [4,29]) because they are constructed using deformable materials. Motors are not used for actuation. Instead, force generation is achieved by mechanisms such electrostatics, shape memory actuation, and fluidics, among others.

Fluidic actuators [216] employ pressurized fluids, either gases (pneumatic) or liquids (hydraulic) [55], to generate motion by causing inflatable or deformable fluid-filled chambers to change shape. Fluidic actuators are capable of large movements and can achieve high work densities [216]. The earliest and most extensively studied pneumatic soft actuators are McKibben muscles [217], which are composed of an elastic tube surrounded by a sleeve, and which contract with pressure [218,219]. Recently, soft robots have been demonstrated that contain multiple fluidic channels embedded within an elastomer [220] to provide more complex motions such as limb-like motion [66], crawling [58], and grasping [59]. Curving, for example, can be achieved with fluidic channels separated by a bendable, but not stretchable, layer [59], which is often made of fabric, paper, or a stiffer polymer. Both pneumatics [221-223] and hydraulics [224] have been used to realize soft robots. Pneumatic actuators are capable of rapid movements,

enabling motions such as jumping [225]. Hydraulic actuators are suitable for larger loads because liquids are incompressible, resulting in a higher strength-to-weight ratio, lower pressure losses, and good power transmission. There are relatively few miniature hydraulic actuators due, at least in part, to the difficulty of constructing leak-proof devices at cm-scales [226].

Fluidic actuators are usually operating with pressure-driven flow by connecting them, via tubing, to a compressed gas tank (pneumatic) or an external pump (pneumatic or hydraulic), limiting the system's motion. Eliminating tethers would be advantageous to achieving stand-alone robots, and would facilitate miniaturization and integration with other systems. Untethered force delivery in pneumatic systems has been achieved by generating gases within the actuator by decomposition of the liquid propellant via peroxide reactions [65,66], combustion [227], thermal liquid-vapor phase change [62,228], or electrolysis [67,68]. Regrettably, these devices have short lifetimes (seconds to minutes) because of reactant depletion. Untethered hydraulic actuation has not been demonstrated, but applying an electric potential to generate electrokinetic flow [76] provides a possible means for that. This would theoretically allow fine control of actuator motion using electronic circuits, while achieving longer device operation because no decomposition occurs.

Here we describe a fabrication process to create fully-sealed actuators via layer-by-layer assembly of flexible materials: silicone and paper. The paper is sandwiched between elastomeric electrodes, and the pores in the paper serve as the fluidic channels. The

process includes a tubing-free method to fill the device with the pumping liquid and then encapsulate it. Electrohydraulic fluid flow occurs upon applying an electric field, which inflates the membrane. Actuator characterization shows that large displacement, reasonable force, and good speed can be achieved by electrohydraulic force transmission.

6.2 Materials and Methods

6.2.1 Materials

The microchannel layer consisted of Whatman cellulose filter paper (No. 2, qualitative, pore size 8 μm, particle retention efficiency 98%, thickness 190 μm).

The pumping liquid for electroosmosis was propylene carbonate (PC)(anhydrous 99.7%, Sigma-Aldrich, 310328). The PC was stored in a glove box with an argon atmosphere because exposure to ambient moisture causes irreversible chemical degradation [134]. The device fabrication and experiments were, however, performed under atmospheric conditions, not in a glove box.

Three platinum-cure silicone elastomers were used: polydimethylsiloxane (PDMS, Dow Corning Sylgard 184, 10:1 base:curing agent) and Ecoflex 00-50 and 00-30 (Smooth-On Inc., 1:1 parts A:B). PDMS is transparent, has a durometer hardness of 43 Shore A (at 10:1), and has an ultimate strain of 150% [229]. Ecoflex 00-50 is translucent, has a

durometer hardness of Shore 00-50, and has an ultimate strain of 980% [230]. All three were cured at 65 °C in an oven for 1-2 hrs, depending on thickness. Spin-coated layers of PDMS (200 rpm, 60 sec, 50 rpm/sec ramp) were allowed to rest at room temperature for at least one hour to allow air bubbles to escape before curing.

Mold release (Mann Ease Release 200) was applied to glass substrates (slides 5×7.5 cm^2) to allow removal of the elastomers. Mold release was not required when using transparency sheet substrates because the silicones readily peeled from the plastic. In fact, when patterning the elastomers with a cutting machine mold release treatment of the transparency caused the films to delaminate and get damaged by the blade.

6.2.2 Patterning

Filter paper was patterned using a computer-controlled electronic plotter cutter (Cricut Explorer, paper setting). The paper was adhered to a cutting mat. To prevent damage to the paper during release after cutting, the tackiness of the mat adhesive was reduced by dabbing it lightly with cotton fabric. The final shapes were released by sliding a razor blade beneath them; this avoided paper curling, which occurred if the paper was peeled off the mat.

Electrodes were patterned either by cutting (manually with a razor blade or with the Cricut Explorer, pressure 129, “aluminum foil” setting), punching (Harris Unicore tissue

coring tool), or printing through stencils. Stencils were formed by cutting (Cricut Explorer, cardstock setting) multiple layers of tape (3M Scotch blue masking #2080EL, thickness t = 0.0038" = 90 μm): 5 for the device layer (t = 483 μm) and 4 for the reservoir. The cut pressure was adjusted so that the blade did not score the underlying substrate; score marks were replicated as ridges when the electrodes were embedded in PDMS, lowering the quality of plasma bonding and leading to leaks during operation.

Film roughness was determined with a mechanical profilometer (Tencor AlphaStep 200). Thickness was measured with calipers or a ruler.

6.2.3 Electrode Materials

Electrodes were composed of 14 wt% carbon black (40 nm, Alfa Aesar 39724) mixed into the silicone elastomer (PDMS or Ecoflex), prior to curing. Suspensions were prepared in a 20 mL glass vial, starting with adding 0.07 mg of carbon black to the pre-polymer (4.5 g of PDMS base or 2.5 g of Ecoflex part A). After manual stirring, the suspension was vortex mixed (Fisher Scientific digital vortex mixer, 60 sec, 3000 rpm) and sonicated in a water bath (40 kHz, 20 min) at room temperature. Curing agent was added to the suspension (0.45 g for PDMS or 2.5 g for Ecoflex B), which was again stirred, vortexed, and sonicated (1 min).

In addition, a faster mixing technique was tested (5 min total preparation time vs. 25 min) in which carbon black, pre-polymer, and curing agent were added all at once to the mixing container of a planetary centrifugal mixer (Thinky Mixer ARE-310) used in standard mode (30 sec. mixing at 2000 rpm, 30 sec. de-foaming at 2200 rpm). The mixture was scraped off the sides of the container, stirred with a dowel, and placed back into the mixer again. This was repeated four times, for a total time of 4 min. in the mixer. Both mixing methods resulted in smooth pastes with similar spreadability.

PDMS/carbon (C-PDMS) paste was applied to cover the stencil and doctor bladed (6 passes with a razor blade) to ensure a uniform layer with a thickness determined by the stencil height. The stencil was peeled off, and the C-PDMS cured. Doctor-blading yielded a top surface with high roughness (≥ 130 μm, exceeding what could be measured by profilometry), and a bottom surface, facing the glass, that was smooth (roughness ≤ 2 μm) and glossy.

6.2.4 Plasma Bonding

Plasma bonding was used to adhere the device layers. Surfaces were treated in oxygen plasma (Branson 3000 Barrel Resist Stripper, 20 sec, 50 W, 1 Torr) and immediately brought into contact. The process required surfaces to be clean, flat, minimally rough, and free of defects such as holes, scratches, and particulates. Fingerprints, dust, moisture, and impressions formed from scratches impaired the bonding.

6.2.5 Actuator Performance Testing

Membrane deflections and forces were measured using a force/strain transducer (Aurora 300B), the former in isotonic mode (constant force) and the latter in isometric mode (constant position). The transducer was interfaced to a computer via a data acquisition card (National Instruments), and data were recorded using a custom LabVIEW program.

The actuator was fixed to a glass slide, membrane-side-up. The carbon-elastomer electrodes were connected to the power supply (HV Rack, Ultravolt) with toothless alligator clips. A pressure-distribution plate, consisting of a piece of transparency film (5 x 5 mm^2), was manually centered on top of the membrane, and the lever arm of the transducer was positioned to rest in the middle of it (
Figure 61). The plate was coated with mold release to minimize stiction to the membrane.

6.3 Device Design

The goal of the present work was to create miniature hydraulic soft actuators: self-contained, untethered, high-force devices that are voltage controlled. The design of the actuators was inspired by plant motion. Although plants lack muscles, they can generate a variety of movements, both slow and fast, by pumping water in and out of their cells via osmosis [231]. Mimicking the plant cell design, our actuators comprised an elastomer with embedded fluid-filled reservoirs connected by microchannels. Application of an

electric field across the microchannels induced electroosmotic flow of the liquid from one reservoir to another, causing deformation of the surrounding elastomer.

6.3.1 Pumping Mechanism

A variety of flow effects occur when an electric field is applied to a liquid, but the electrokinetic effects that have been used for generating bulk flow are electroconjugate flow, electrowetting, and electroosmosis. In electroconjugate flow, fluid jets are generated with dielectric liquids [89,232-235]. Electrowetting actuators employ flow driven by applying a voltage to the channel wall [90]. Our research focused on employing electroosmosis, also a surface phenomenon like electrowetting but distinguished by the fact that flow is initiated by an electric potential applied over the liquid, instead of the contacting solid.

The surfaces of solid objects in contact with a fluid have a net charge [236]. Mobile counter-ions (ions in the fluid with opposite charge to the surface) are attracted to the surface to maintain electrical neutrality, resulting in a so-called electric double layer, one side of which is positive and the other of which is negative; the potential difference is called the zeta potential. The bulk of the fluid remains charge neutral. When an external electric field is applied along a fluid-filled channel, the mobile charges in the double layer are induced to move. The direction of fluid flow depends on the sign of the surface charge. This counter-ion motion along the walls transfers momentum to the remaining

fluid, resulting in bulk flow with a nearly flat velocity profile. Microfluidic devices employ electroosmosis to achieve fast, pulseless pumping at high forces [94,135,137,143-146,149,158,170,237,238].

Electroosmotic flow in N channels of length L, cross-sectional area A, and depth d, filled with a liquid having permittivity ε and viscosity η, and employing a channel material giving a zeta potential ζ is believed to be described by [138]:

(2) $\text{EO flow rate} = NA\frac{\varepsilon\zeta E}{\eta}$

(3) $\text{EO pressure} = \frac{12\varepsilon\zeta EL}{d^2}$, in rectangular channels (depth << width)

For high force and fast EOF, the device requires: (a) a large number of small channels with high surface charge, and (b) a low viscosity and a liquid with high permittivity.

In addition, the liquid must exhibit electrochemical stability. Typically, water is used in EO pumps due to its high polarity, but in water electrolysis causes depletion of the pumping liquid, changes in pH, and evolution of gas bubbles, resulting in irreproducible pumping, low actuation pressure, and device failure. In this paper we used propylene carbonate (PC) as the pumping liquid because it exhibits bubble-free operation up to kV [134,168]. The zeta potential for both water and PC in PDMS is negative [134]: fluid moves from the positive electrode toward the negative electrode, indicating that the mobile charges at the walls are positive (cations).

6.3.2 Paper Microchannels

The first electroosmotic actuators we reported [106,134] were fabricated entirely from PDMS by soft lithography using a microfabricated SU-8 mold. They contained 9 rectangular channels each 1 cm long, 150 μm wide, and 25 [106] or 40 μm deep [134].

While forming microchannels by soft lithography is well suited for the creation of lab-on-a-chip devices, for EO a large number of small microchannels is needed to produce a significant flow rate. Equation (2) shows that flow rate depends on the total cross-sectional area *NA*, and equation (3) that force depends inversely on the square of the channel depth *d*. One approach to increasing the number of pumping channels and reducing their diameter is to pack conventional microfluidic channels with beads [135] or porous monoliths [135,136,142,146,196,239]. Another approach is to employ pre-formed microporous structures, such as mullite [137], porous glass frits [94], or porous elastomeric sponges [168].

Here we employ the second approach, with paper as the microchannel layer, since it is highly porous and readily absorbs liquid between the cellulose fibers. Figure 60 shows the microstructure of the filter paper used in this work. It consists of interwoven cellulose fibers, touching in places and separated by a range of relatively large gaps in others.

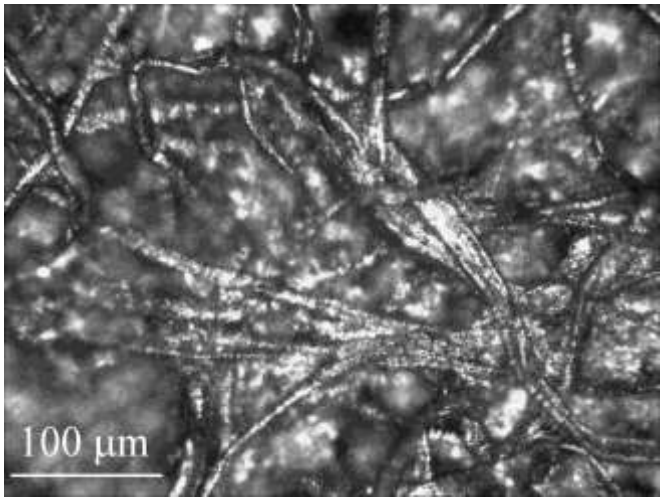

Figure 60. Micrograph of the surface of Whatman 2 filter paper, coated with platinum for enhanced contrast to permit visualization of the fiber structure.

There is extensive literature on paper-based microfluidics, as reviewed in [240,241], and electroosmosis in paper has been observed as a side effect during electro-chromatography [242], but paper has yet to be employed for electroosmotic pumping. Paper microchannels, unlike those made of silicone, wick fluids such as water and PC, thereby facilitating bubble-free device filling.

There are other properties of paper that make it attractive for the creation of soft actuators: it can be folded, bent, cut, and stacked to build 3D structures. It is also readily available, inexpensive, and reasonably mechanically robust. For microfluidics, papers with good wet strength (a measure of the ability to withstand rupture when the paper is wet) are filter paper and tissue paper.

6.3.3 Device Design

The device essentially comprises fluid-filled paper between a pair of electrodes covered by an elastic membrane (
Figure 61). Applying a voltage across the electrodes leads to EO pumping within the paper, in some cases along with other electrokinetic fluid motions, as discussed below. Transferring the fluid toward the membrane leads to its bulging outward. Elsewhere, not shown in the figure, the structure collapses to maintain constant volume. The membrane is thin and elastic to allow large displacements. Bulging membrane designs are used in valves and tactile displays. Pumping fluid between reservoirs within an elastomeric material, rather than under a membrane, would result in structural deformations.

Two configurations were investigated. In the "adjacent" layout (
Figure 61a), electrodes were situated side-by-side in a planar arrangement, with the paper on top of them. In the "stacked" layout (
Figure 61b), electrodes faced each other with the filter paper sandwiched between them. In both cases, the electrodes were placed as close together as feasible: from equations (2) and (3), both flow rate and pressure scale with the electric field, so decreasing the electrode separation lowers the required voltage. The planar configuration resulted in thinner devices, allowing them to be smaller and more bendable. Fabrication was also simpler, as discussed below, because it entailed fewer steps and no plasma bonding, and because either PDMS or Ecoflex could be used throughout the device. However, the smallest distance between electrodes was 0.5 mm, set by the ability of the cutting

machine. In the stacked configuration the electrode spacing was closer, since it was set by the paper thickness and did not depend on patterning.

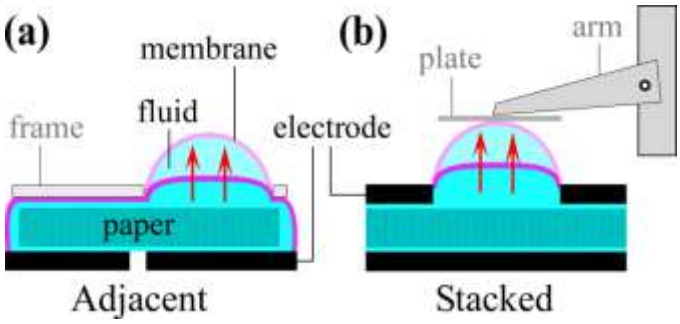

Figure 61. Device designs with a) adjacent and b) stacked electrodes. A paper microchannel layer is positioned between the electrodes. Fluid pumped through the paper inflates an elastomeric membrane. Force and deflection are measured using a transducer, the arm of which rests on a pressure-distributing plate placed on the membrane.

6.4 Fabrication

Because the goal was to create an electrically-controlled, fully flexible actuator, every part of the device needed to be compliant. Two elastomers were used in this work: PDMS for the structural components and the more flexible Ecoflex 00-50 for the actuating membrane. Thin film metal electrodes with serpentine shapes allow stretching [243], but they degrade under EO. Stretchable electrodes can also be made from composites containing conductive nanoparticles, such as carbon black (CB) [244,245] or exfoliated graphite (EG) [246], within an elastomeric host, but they have not previously

been used for EO. Elastomer/EG composites are more stretchable, but CB composites were chosen for this work because the CB mixed more uniformly into the elastomers and large strains were not required. The other materials used in the devices were paper (the microchannel layer), which is bendable but not stretchable, and liquid (the PC pump fluid). The fabrication sequences (Figure 62) for the two designs differed substantially, so they are described separately.

The fabrication method for the carbon-based electrodes required some development, as described in the Supporting Information. A volatile solvent, such as hexane, is typically used to lower the viscosity of the uncured elastomer/carbon mixture, but this negatively affects the cured film by lowering its conductivity, making it brittle, and producing small holes [247]. A solvent can also limit the substrate materials on which the electrodes can be applied. We investigated the effect of solvent on resistance and film quality and concluded that electrodes should be formed without hexane. In addition, PDMS and Ecoflex were compared as host polymers. Ecoflex outperformed PDMS, but we used PDMS for the electrodes because of one critical step in the fabrication process: oxygen plasma bonding of the layers to create thin devices. Plasma surface treatment was ineffective with Ecoflex.

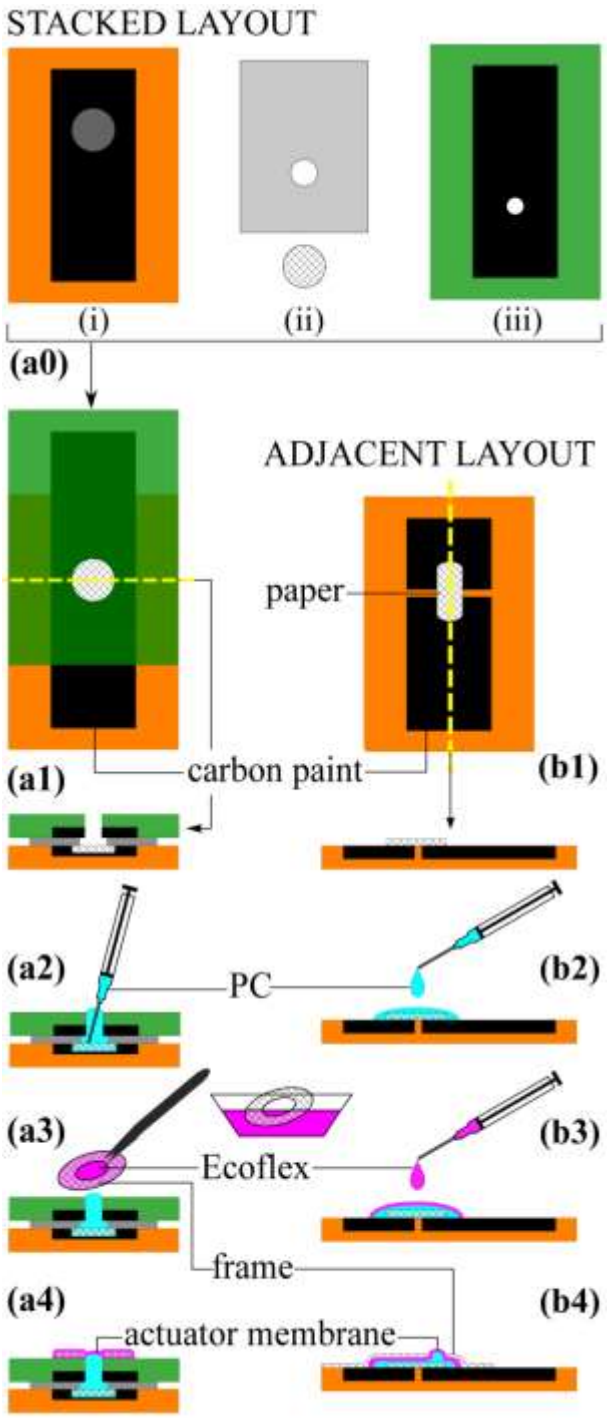

Figure 62. Fabrication process for actuators with stacked (a0-4) and adjacent (b1-4) electrodes. (a0) The stacked layout began with preparing (i) a bottom electrode layer (orange) with a reservoir, (ii) an insulating layer (gray) and a paper disk, and (iii) a top electrode layer (green). The electrode layers were patterned by doctor-blading C-PDMS over a stencil, curing, and embedding in PDMS. Holes were punched in the upper two layers to form the fluid port. (a1,b1) Assembly. (a1) The components of the stacked layout were plasma treated, aligned, and bonded. Overhead and cross-sectional views are shown; the section is indicated by the dashed line. (b1) In the adjacent layout the electrodes were patterned using a cutting machine and embedded in PDMS. The paper was placed over the electrodes. (a2,b2) Addition of pumping liquid. (a2) Liquid was added via the inlet hole. (b2) Liquid was dispensed onto the paper. (a3,b3) Encapsulation. (a3) A paper frame was dipped in uncured Ecoflex and laid over the inlet port. (b3) Ecoflex was dispensed directly on the PC droplet. (a4,b4) Completed devices. Frames defined the deflecting regions.

6.4.1 Adjacent Layout

In the adjacent layout, the silicone used for device fabrication could be either PDMS or Ecoflex. The base layer, on which the rest of the device was constructed, consisted of two electrodes embedded in a thicker layer of silicone (Figure 62b1). A large-area film of C-silicone (t = 0.5 mm) was formed on a plastic sheet using a stencil, the two electrodes were cut from that, and the rest of the film was peeled away. Silicone was cast over the electrodes (t = 1 mm) and cured, and this base layer was peeled off the substrate. The paper microchannel layer was cut into a rounded rectangle (1.5 cm × 1 cm) and placed across the electrodes. The pumping liquid, PC, was dispensed onto the paper using a syringe (0.1 mL, 30 gauge needle) until the paper was saturated; wicking action filled the microchannels (Figure 62b2). Excess PC formed a droplet around the paper and held its shape due to surface tension. The PC was encapsulated by dispensing liquid silicone (0.3 mL) around the base of the PC drop, at the liquid-substrate interface, until the silicone spread from the periphery of the droplet towards the top to form a thin film (Figure 62b3). The membrane was cured in an oven (65 °C, 1 hr). A paper frame with a circular opening (5 mm dia.) was cut and adhered to the film to define the actuating membrane shape. The frame was brush-coated with a thin film of silicone as an adhesive, positioned over the negative electrode, and cured (Figure 62b4).

The encapsulation method made use of the facts that PC does not mix with either PDMS or Ecoflex, and does not inhibit their curing. Uncured silicone was dispensed around the PC droplet using a syringe until it spread to cover the droplet surface; the fluid silicone

formed a film that was perfectly conformal with the surface of the PC. The silicone was cured to form a polymer membrane bonded to the substrate, resulting in a sealed liquid-filled cavity with no trapped air (air can cause electric sparking and device failure, as well as loss of force). An advantage of using Ecoflex for the membrane is that it cures faster (15 min) at room temperature than PDMS (> 24 hours), enabling quick encapsulation of PC without exposure to heat.

6.4.2 Stacked Layout

In the stacked layout all the layers were made from PDMS except the actuating membrane, which was made from Ecoflex. The stiffer PDMS limits deflection to the membrane area. Actuators were fabricated using a layer-by-layer lamination process, starting with creating two electrode layers and an insulating separator (Figure 62a1). C-PDMS electrodes (0.5 mm × 2.5 cm × 6.4 cm) were formed on glass using stencils. In the lower electrode (Figure 62a1i), a thinner circular stencil (0.4 mm × 1.33 cm) was placed in the center to form a reservoir. PDMS was spin coated over the slides (t = 1 mm) to embed the electrodes and allowed to rest at room temperature for at least one hour to allow air bubbles formed at the electrode-PDMS interface to escape. Peeling off the substrate exposed the conductive surfaces. A hole (5 mm dia.) was punched through the top electrode (Figure 62a1iii). An insulating PDMS layer (t = 0.5 mm) was formed by spin coating and manual cutting (3.8 cm × 6.4 cm), and a hole (8 mm dia.) was also

punched through its center (Figure 62a1ii). A piece of filter paper was cut (1.27 cm dia.) to fit inside the reservoir in the bottom electrode.

The four components were then assembled (Figure 62a2). The bottom electrode, insulating spacer, and paper circle were exposed to oxygen plasma. The paper was placed into the reservoir, and the insulating film brought into contact with the electrode, with the 8 mm hole centered over the reservoir, sandwiching the paper between them. The top electrode was then bonded to the insulating layer using the same process, with the punched holes aligned. The electrodes extended beyond the bonded area to allow power connections.

The device was then filled and sealed within 5 minutes of plasma exposure. PC (0.1 mL) was added through the hole in the top electrode layer (Figure 62a3) until some liquid protruded. The needle was held in contact with the surface of the paper. Filling the device after surface activation ensured wetting of the silicone surfaces, and so prevented trapping of air bubbles. A circular paper ring (i.d. 1.27 cm, o.d. 1.52 cm) was dipped into liquid Ecoflex (< 10 sec), resulting in a thin film suspended by surface tension, such as seen in the formation of soap films suspended on a ring support. The ring was aligned with the hole in the top electrode, and the Ecoflex instantly draped itself over the PC, conforming to the shape of the droplet and forming a membrane enclosing the liquid reservoir. The Ecoflex was allowed to cure at room temperature for 30 min. The final device dimensions were 5 x 50 x 100 mm^3, and its weight was 0.012 grams (average of three devices).

The membrane thickness could be tuned by varying the thickness of the paper ring, and also by extracting the ring slowly [248]. Curing the encapsulating film at room temperature allowed time for the liquid silicone to spread and form a thin membrane with a good bond between the membrane and the substrate. (For cross-sectional images of the membrane, see the Supplementary Information.) Ecoflex 00-50 is stiffer than Ecoflex 00-30 [230], but it was used because the 00-50 bonded to PDMS while the 00-30 peeled off readily, even after plasma treatment.

6.4.3 Observations

The cutting approach to patterning is better suited to a process sequence where the application of the electrode paste and the cutting process are automated and tightly controlled. To minimize the chances of damage to the substrate, doctor-blading through stencils was used instead, which is more forgiving in a lab setting.

PDMS and Ecoflex are both cured by platinum-catalyzed crosslinking [229,230]. However we observed differences in the bonding capabilities of these two polymers. Cured PDMS layers can be bonded to each other either by oxygen-plasma treatment or by using uncured PDMS as an adhesive. Cured Ecoflex layers can be bonded to each other or to cured PDMS only by adhering them with uncured Ecoflex or PDMS. Solidified Ecoflex could not be bonded to either solidified PDMS or Ecoflex by oxygen plasma

surface treatment. In order to make Ecoflex amenable to plasma-mediated bonding, we determined that uncured Ecoflex (1:1 mixture) should be adulterated with a small amount of PDMS (10:1 mixture), using at least 1:35 by weight of PDMS:Ecoflex. Blending the two silicones can also be used to adjust material stiffness of the layers.

In order to produce hydraulic actuators by additive manufacturing, we have developed a fabrication process that involves lamination and casting of successive layers. The approach has the potential to be adapted to a roll-to-roll process, which employs lamination. Alternatively, it may be possible to produce the devices by 3D printing, which would require printed elastomers that are stretchable. Ecoflex and PDMS are not currently printable because they are two-component thermosetting polymers: solidification occurs by cross-linking catalyzed by heat. These elastomers are typically patterned by casting them, in the liquid state, over molds. Printable elastomers are stiffer and more brittle [249], and their adhesion to Ecoflex liquid for encapsulation would need to be verified. For the electrodes, the printer would need to handle a viscous nanoparticle-containing paste.

Other reported encapsulation approaches include vapor-deposition of polymers such as parylene directly on a liquid [250], and casting of UV curable polymers on a liquid [251]. In general, the encapsulation technique will be determined by the nature of the underlying substrate as well as the particular liquid. The approach used in this work is suited for the encapsulation of nonvolatile liquids in silicone devices.

After forming the electrode layer, PDMS was cast over it. The high roughness of this surface sometimes caused air bubbles to be trapped when the PDMS was applied. Therefore, the samples were allowed to rest at room temperature to enable degassing before curing. Vacuum dessication was not applied because it led in some cases to PDMS creeping beneath the electrode layer.

It would be convenient to directly spin coat PDMS over the bottom electrode to create the insulating spacer, with the active electrode areas masked off. However, due to poor adhesion of tapes and other adhesives to silicone, the PDMS crept beneath the masks. The insulating layer therefore had to be fabricated as a free-standing film and later plasma bonded to the electrode.

Initial designs did not feature a reservoir to hold the filter paper; the paper was simply sandwiched between the layers. This created an air gap around the paper during bonding, and the trapped air could not be completely eliminated while filling the device, increasing the incidence of device failure. Due to the presence of a single port for filling the device, in order to minimize the chances of air entrapment, we introduced a reservoir with a diameter that was only slightly larger than the inlet port. To hold larger liquid volumes, for increased actuation stroke, a bigger reservoir must be incorporated. If the reservoir dimensions were increased in the plane of the device, the overall thickness of the device would be unaltered, keeping it easy to bend. However, the current design employed a single inlet port. Increasing the transverse reservoir area makes it more difficult to evacuate air trapped between the layers, near the edges of the reservoir away from the

inlet port. For bubble-free fluid filling, creating a deeper, rather than wider, reservoir will minimize trapped air. Thus the design would require optimization subject to dimensional constraints. If the design necessitated minimal device thickness, then two separate ports would be required, an inlet for filling and an outlet to allow air to escape. With a single inlet design, a syringe needle with a significantly smaller diameter than the reservoir is required, so that enough area is available for trapped air to escape. This work employed a 30 gauge needle (0.31 mm o.d.) to fill the reservoir (13.3 mm i.d.) through the port (12.7 mm i.d.). After plasma treatment, the device was filled slowly (0.1 mL/min) to allow air to escape as the reservoir was filled.

Filling the device with fluid immediately after plasma activation increases the surface energy of the silicone, which improves wetting; filling is then rapid simply by wicking, without the need for positive pressure, and the entrapped air is quickly displaced. The filling needle must be kept in contact with the paper while dispensing fluid to avoid splashing or spillage onto the surrounding silicone surface. Spillage outside the port onto the plasma-activated silicone prevents the formation of a good seal during liquid encapsulation. Although desiccation or negative pressure can be used to fill the device instead of surface activation, it increases the chances of liquid spillage due to bubbling as the air trapped in the paper and reservoir is removed.

Prior to determining polymer film casting as the most suitable method of encapsulation, we had attempted another approach to creating a sealed fluid reservoir: injection of the liquid using an ultra-fine needle, with the silicone self-sealing around the perforation

after filling. As the device became thinner, it became increasingly challenging to inject liquid without piercing through it. Also, in thin devices the silicone was unable to seal the perforation at the device operating pressure, and fluid leaked out at that site. (Another potential approach could be to fill the device with pumping liquid and freeze it in place, and then cast the membrane over the solid surface. However, PC freezes below -55°C, at which temperature the silicones will not cure.)

The dimensions of the device layers were chosen for ease of handling during fabrication and testing. In order to decrease the size and weight of the device, the areas of the electrodes, insulating layer, and frame could be reduced significantly without affecting performance.

6.5 Results: Actuator Performance

The key metrics used to evaluate actuator performance are displacement, force, and speed. Based on these values, work, power, and energy efficiency can be determined. Before characterizing the devices, however, the adjacent and stacked designs were compared qualitatively during actuation.

6.5.1 Electrode Configuration

The first objective was to determine whether the two layouts, adjacent and stacked, both worked as intended. EO flow would be toward the negative electrode if ζ was negative for the paper/PC combination.

6.5.2 Adjacent Layout

In the adjacent layout, 5 kV was applied, with the negative electrode under the membrane. Deflection was observed by eye (Figure 63a), and the membrane flattened again when the voltage was turned off (n = 3 devices). However, when the polarity was reversed the membrane did not further deflate, but instead bulged again. The flow was non-directional, unlike in EOF.

To investigate further, devices were fabricated with more closely spaced electrodes: the gap was reduced from 3 mm to 2, 1, and 0.5 mm (1 device each), and the experiment repeated. Deflection *decreased* with spacing, contrary to expectations for EO of increasing pressure with electric field.

To gain insight into the mechanism for the fluid flow, devices (n = 2) were fabricated without the paper microchannel layer (Figure 63b). The membrane deflected in the same way and to the same extent as for the previous devices, regardless of the sign of the voltage (± 5 kV), and again actuation occurred for both polarities.

Open devices were fabricated (n = 2) having the paper but not the encapsulating membrane (Figure 63c). Upon applying voltage, again irrespective of the direction, the PC moved to the gap between the electrodes and pushed the filter paper upward.

The device was finally pared down to just a droplet of PC over the electrodes (Figure 63d). The stationary droplet had a smooth, convex surface. The voltage was ramped from zero to 5 kV. Fluid started pooling between the electrodes at 50 V. Beyond 500 V the liquid bulge (seen by the light reflection) began moving in a circular motion between the electrodes. This behavior has previously been dubbed electrohydrodynamic circulating flow [252,253]. The fluid motion in this device was clearly not due to EO, but likely due to either the Sumoto effect [254] or the dielectric liquid bridge phenomenon [159,252,253].

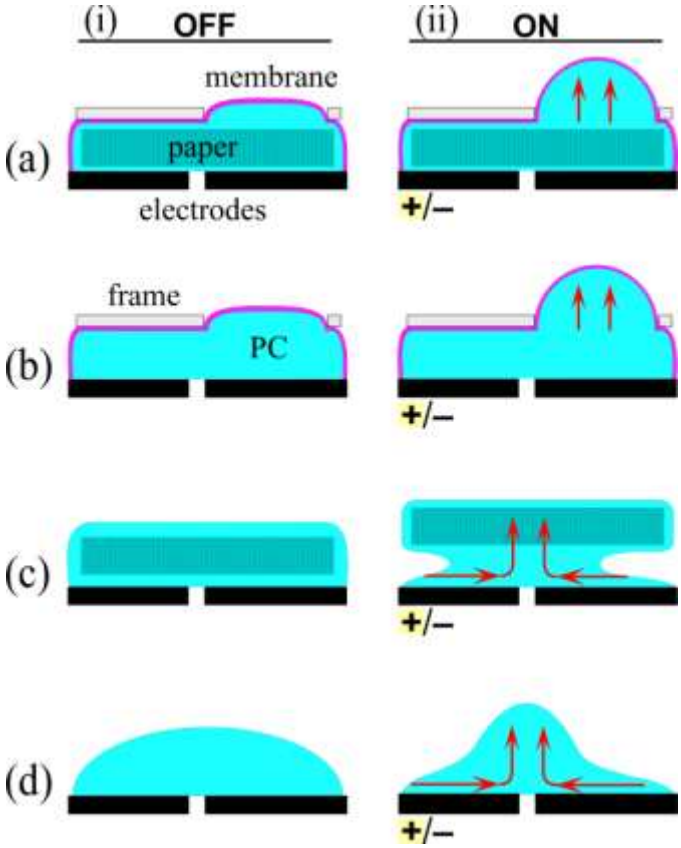

Figure 63. Schematic representation of fluid motion in the adjacent layout. (a)(i) The actuator comprised an actuating membrane encapsulating a pumping liquid and a paper microchannel layer above two planar electrodes. (ii) Application of voltage (5 kV) of either polarity caused membrane deflection. (b)(i) An actuator without the paper layer. (ii) Voltage of either polarity caused membrane deflection similar in magnitude to that in (a). (c)(i) An actuator without an encapsulating membrane, the liquid held by surface tension. (ii) Voltage of either polarity pulled the liquid between the electrodes, causing the paper to rise. (d) An actuator fabricated without paper and without an encapsulating membrane. (ii) Voltage of either polarity drew liquid toward the gap between the electrodes, forming a bulge with visible fluid circulation.

6.5.3 Stacked Layout

In order to force the field lines to pass through the microchannels, in the stacked layout the paper microchannel layer was sandwiched between the two electrodes (Figure 64ai). Fluid flow occurred from the positive to the negative electrode, consistent with a negative ζ potential, leading to membrane inflation (Figure 64aii). When the polarity of the field was reversed, the membrane moved downward (Figure 64aiii). Thus, flow in the stacked layout was directional, as expected for EO. Membrane deflection was observed beginning at 100 V, 50× lower than was required in the adjacent layout, even though the electrodes in both designs were spaced 3 mm apart. The lower operating voltage is therefore due to the face-to-face orientation of the electrodes.

A stacked layout without paper was then tested (Figure 64bi), in order to determine whether the flow phenomena was altered by the absence of microchannels. At 100 V the membrane inflated irrespective of the direction of the applied field (Figure 64bii,iii), although the deflection was smaller than when the microchannel layer was included. Flow in this device was thus attributed to the electrohydrodynamic effects previously seen in the adjacent layout.

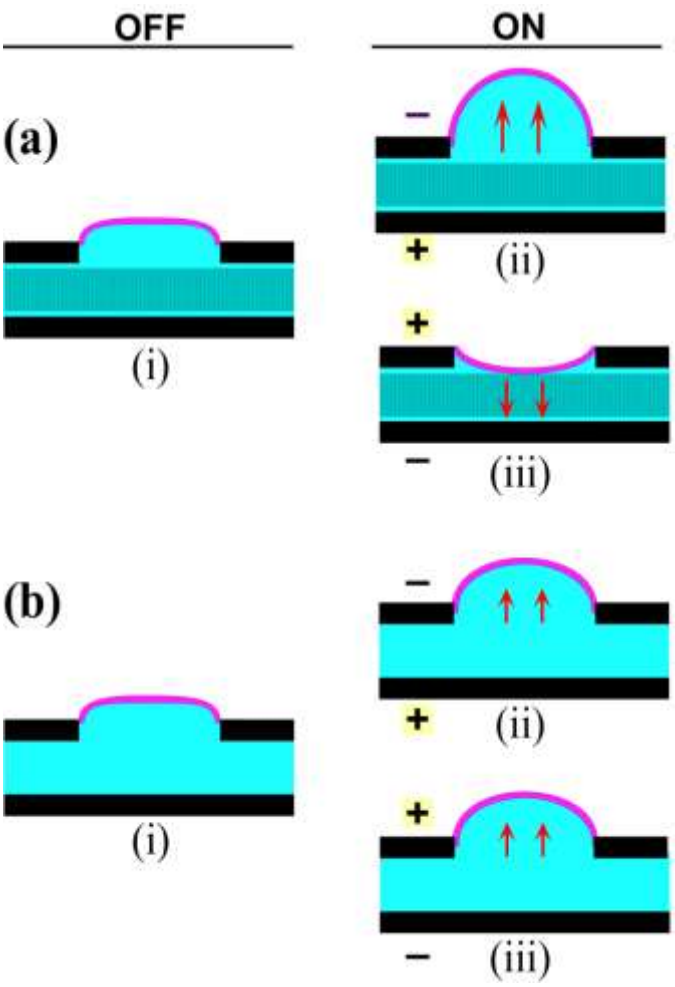

Figure 64. Schematic representation of fluidic actuation in the stacked layout. (a)(i) The actuator comprised an actuating membrane encapsulating the pumping fluid and a paper microchannel layer sandwiched between two electrodes. (ii) Application of negative voltage (100 V) to the top electrode caused membrane inflation, whereas (iii) reversing polarity caused membrane depression. (b)(i) An actuator without the paper layer. (ii) Negative voltage on the top electrode caused membrane inflation, but to a lesser extent than in (a), as did (iii) the reverse polarity.

Based on these observations we concluded that the stacked electrode design was better, from performance and controllability considerations, for miniature actuators. The following sections describe the performance characterization of the stacked electrode actuators only.

6.5.4 Actuator Displacement

The stroke of an actuator is its range of movement, which was taken as the membrane deflection. An inflating rubber membrane has the shape of a spherical cap [255] [256], and the maximum displacement under a given pressure depends on its stiffness and diameter. The pressure depends linearly on *E* for EOF (Equation (3)), but the relationship between pressure and deflection for a rubber membrane is nonlinear [255] [256].

Membrane displacement ($n = 3$ devices) was measured using a force-strain transducer in isotonic mode: a constant force of 1 ± 0.1 g was applied, and the displacement was measured over time. The positions of the force distribution plate and transducer arm were fixed as the voltages and, later, loads were varied. Voltages of 200, 400, and 600 V, with the negative potential on the top electrode, were applied, stepping on and off three times at each level. The voltage was switched after membrane deflection appeared to have stabilized. The raw data were corrected for linear drift (see the Supplementary Information).

The time trace for one cycle in one device is shown in Figure 65. The membrane inflated quickly by hundreds of μm, with similar deflections for each cycle. Some of the deflection curves showed spikes upon membrane inflation. These occurred randomly and were not specific to a sample or voltage range.

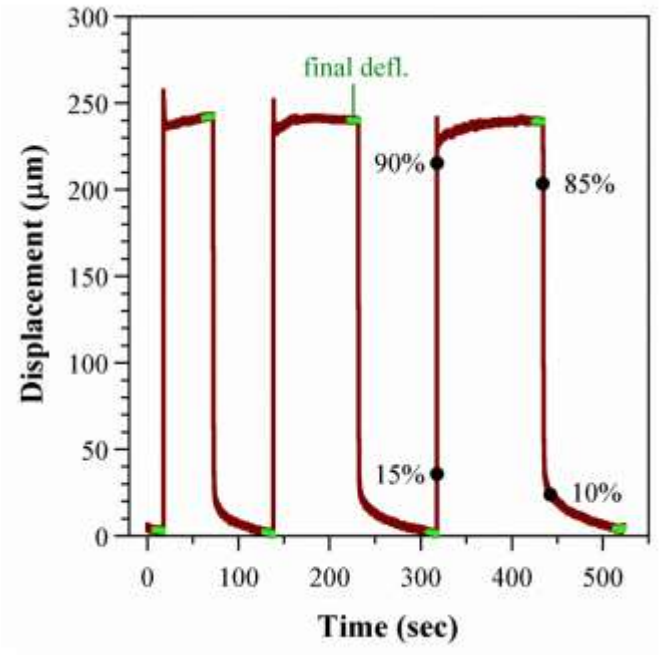

Figure 65. Membrane deflection over time in response to a cycle of three on/off pulses to 400 V (device 2). The points averaged to determine the deflection for each step are indicated (green), as are markers on one step illustrating the inflation values used to calculate τ_r and τ_f.

The average deflection during each step was obtained from the last 10 seconds (last 1000 points, sampling rate 0.01 sec) before the voltage was switched. The average of the three step averages is plotted as a function of voltage for three devices in Figure 66a. Deflection increased with voltage, as expected for EO. Run to run variation for a given device and voltage was ± 10 μm. Between devices, the variation in deflection was larger, up to 70 μm, due to the manual fabrication and the manual positioning of the force distribution plate and transducer. The variation did not depend on voltage.

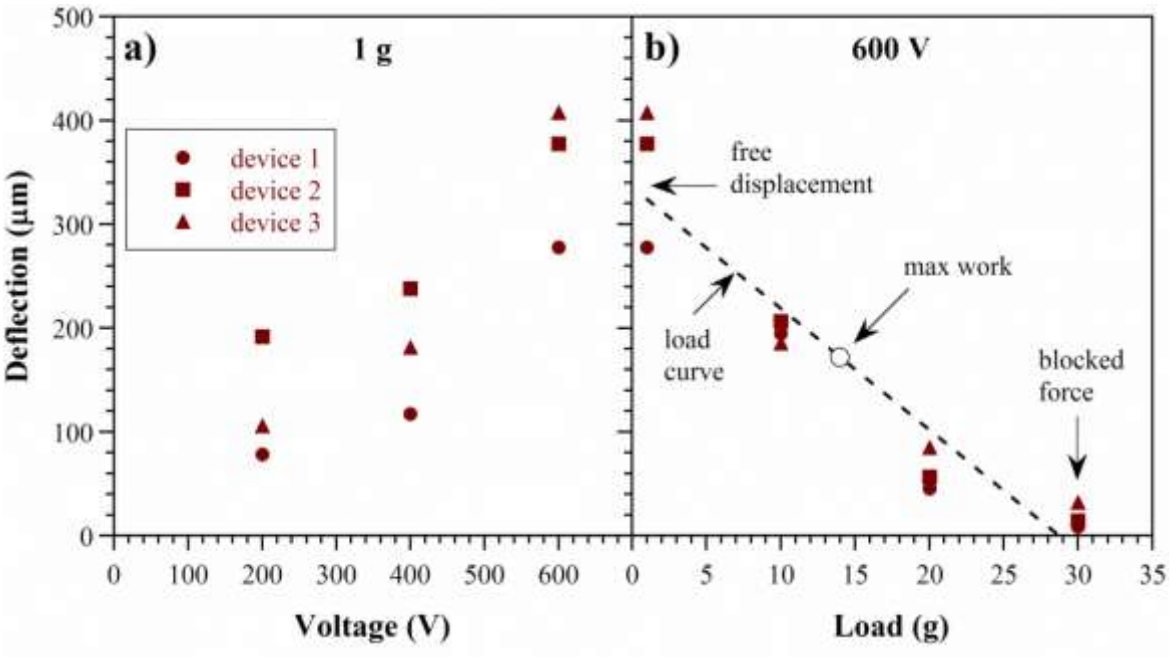

Figure 66. Membrane deflection in response to turning the voltage on and off. Error bars indicating the standard deviation of three runs at each voltage on the same device are smaller than the size of the data point marker. a) Membrane deflection versus voltage under a 1 g load. b) Load curve for the same devices at 600 V as the force on the membrane was increased. The dashed line is a linear curve fit to the average of the three devices.

The finding that deflection scales with voltage implies that the extent of actuation can be altered using the input electrical signal, which is significant for the development of versatile control systems for smart materials and soft robotics. In principle, stroke could be increased by raising the voltage up to the dielectric breakdown field of the pumping liquid (2.2 MV/cm for PC, equivalent to 0.66 MV in these devices [257]). However, voltages above 10 kV led to immediate device failure: we observed sparking and the

electrodes short-circuited, leading to noticeable Joule heating (the device became warm to the touch) as well as burn marks on the PDMS between the electrodes. In these devices, actuation was limited by the stiffness of the structure and volume of the fluid, as discussed below. For this reason and because of our interest in low-voltage operation, voltages above 600 V were not used during testing. Other methods to increase stroke might include switching to a pumping liquid with a higher dielectric limit, using microchannels with higher surface charge (zeta potential), or decreasing the membrane stiffness. Figure 67 compares the membrane deflections of the paper-based actuators to previous prototypes with microfabricated PDMS channels that had an electrode separation of 10 mm; the pumping liquid in both cases was PC and the membrane diameters 5 mm. The voltage required to achieve the same deflection in the new devices was more than an order of magnitude lower, attributed partly to the closer electrode spacing and partly to the use of Ecoflex for the membrane instead of PDMS.

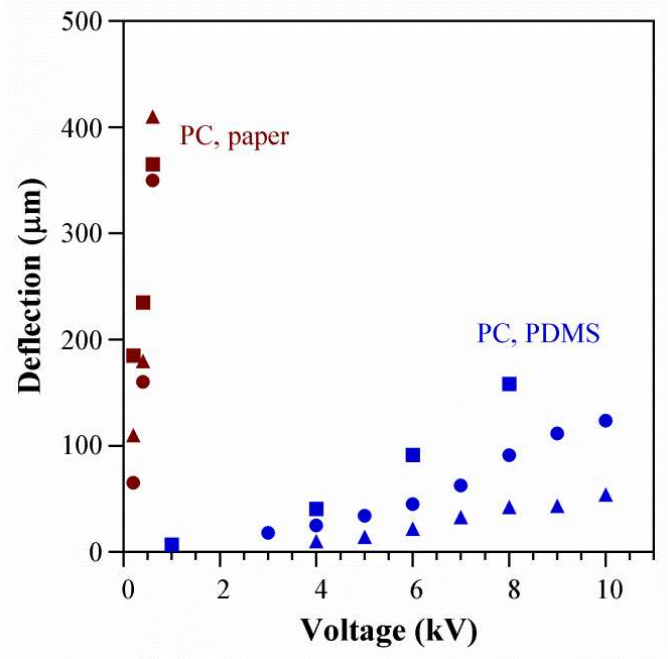

Figure 67. Deflection as a function of voltage in three paper-based stacked configurations (red) and in three PDMS microchannel devices (blue) [134], both filled with PC. The symbols for the stacked configuration have the same meaning as in Figure 66.

Performance of the devices progressively deteriorated over time, so they were tested immediately. Throughout the day on which the device was fabricated and filled with anhydrous PC, it consistently deflected to the same extent when turned on and off. The next day, the current through the device increased by three orders of magnitude (from 0.2 to 300 mA at 600 V), and the deflection diminished. Also, electrolytic gases (bubbles) and Joule heating were observed (device warm to the touch). Two days after fabrication, EOF no longer occurred. Silicone elastomers are water permeable [258], and the encapsulated PC was thus exposed to ambient moisture, which leads to degradation [134]. Device design changes to protect the PC are discussed below.

6.5.5 Actuator Force

An actuator must be able to do more than just move: it must generate enough force to perform useful work. The measurements in the previous section represented nearly free deflection, defined as deflection under zero load. This is an actuator's largest stroke (unless it requires pre-strain to function). To characterize force output, deflection is measured as increasingly larger loads are applied to create a "load curve". Deflection decreases until it goes to zero at the blocked force.

To the same three devices of section 6.5.4, increasing loads (1, 10, 20, and 30 g) were applied by the transducer arm, again in isotonic mode. At each value the voltage was stepped on and off three times to 600 V. The results are shown in Figure 66b.

Deflection was reduced almost to zero at 30 g. The load curve was nearly linear and consistent across devices. Deviation from linearity is likely due to a change in contact area between the force distribution plate and the membrane at different extents of bulging. At 30 g, there is no bulging and the plate makes contact with the entirety of the membrane. This load corresponds to a pressure of 15 kPa, based on the total membrane area (20 mm^2).

Figure 68 compares the forces from the stacked paper devices with those from microfabricated PDMS devices, which had 9 channels with a cross-sectional area of 150 × 40 μm^2 and a length of 1 cm and which had been tested with both water and PC

[106,134]. The stacked layout was able to generate a higher blocked force and did so at lower voltage. The free deflection was an order of magnitude larger than in PDMS channels filled with PC, presumably because the smaller channel diameters in the paper generated greater EO force (Equation (3)). This also suggests that the zeta potential in paper was substantial, even without taking steps to increase the surface charge of the cellulose pores. The large deflections in the water-filled channels [106] may have been partially due to the generation of some electrolytic gas.

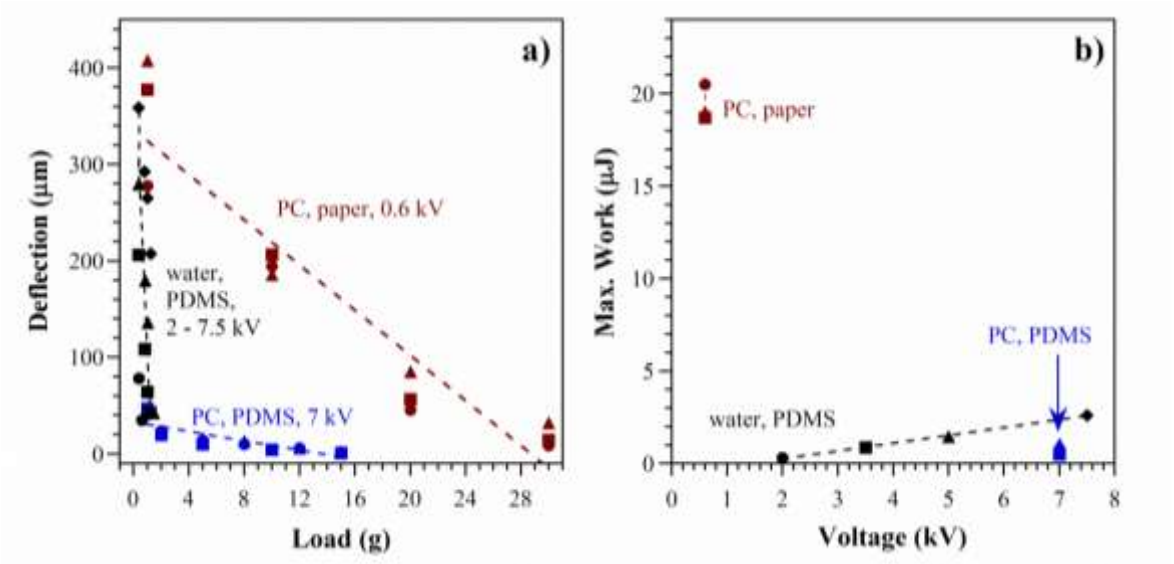

Figure 68. a) Deflection as a function of load for the stacked configuration of this paper (same data as in Figure 66b; symbols have the same meaning) and for previously presented PDMS microchannel devices, filled with either PC (blue) or water (black). b) Maximum work done by the paper-based actuator and the two PDMS devices.

The work done by an actuator is found by multiplying force by displacement. It is zero at the points of free load and blocked force and maximum at a point midway between the two. Using the deflection of 200 μm under a load of 10 g (Figure 68a), the work performed was 20 μJ. The paper-based actuators were capable of performing 10× more work at 10× lower voltage than PDMS devices with water (Figure 68b), increasing the scope for applications.

6.5.6 Actuator Speed

Speed is the third critical metric – not only must the actuator perform work, but it needs to do so in a reasonable time. The actuator speed during inflation is determined by the EO flow rate, while during deflation it is determined by the membrane stiffness, which provides the back-pressure.

The deflection versus time curves obtained during the above experiments were evaluated. The rise time τ_r was defined as the time it took to go from 15% to 90% of the average deflection, and the fall time τ_f from 85% back down to 10% (see Figure 65). The devices inflated quickly by EOF (τ_r = 0.1 sec) and deflated more slowly (τ_f = 1.5 sec) (Figure 69a). Increasing the voltage did not significantly alter the rise or fall times. Figure 69b illustrates that τ_r was unaffected by external loads. In contrast, τ_f decreased with increasing load. This was expected due to the increased force on the membrane, raising the back-pressure.

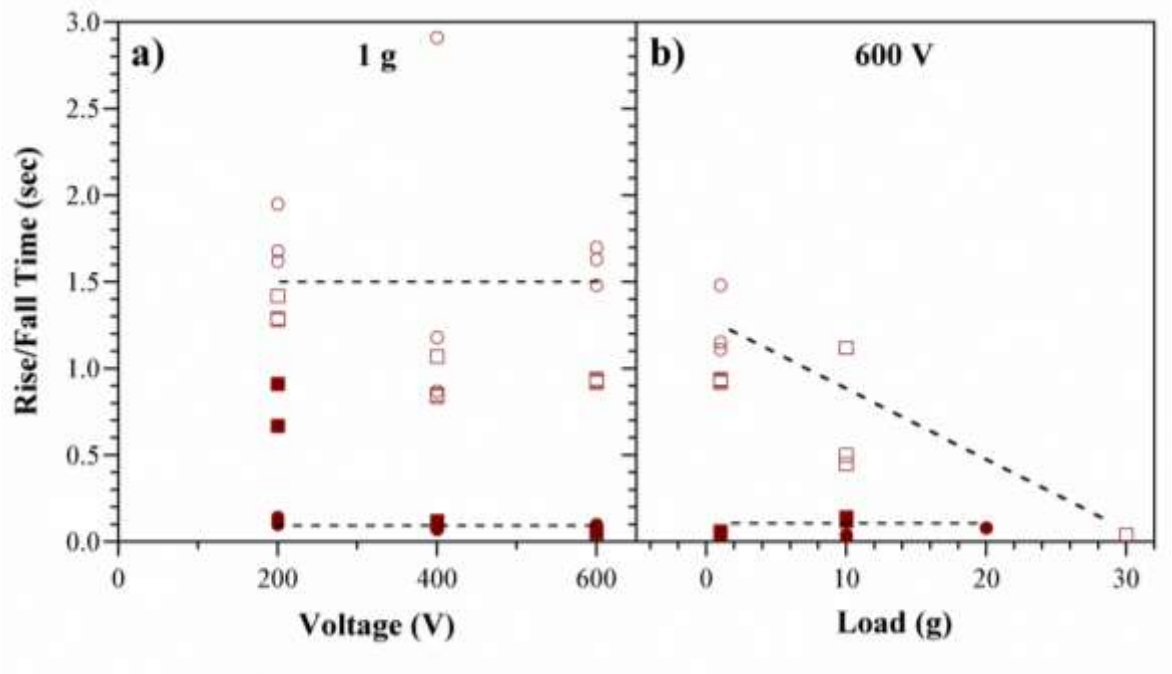

Figure 69. Rise (filled symbols) and fall (open symbols) times for two devices (1 and 2). Points represent individual on/off steps, three per device. a) Times as a function of voltage under minimal load. b) Times at a fixed voltage as a function of externally applied load.

In the PDMS microchannel device a break-in phenomenon was observed [134]: membrane inflation took longer during the first actuation cycle, but successive inflations were faster. This did not occur in the paper-based devices: the inflation time for the first cycle was similar to that in successive cycles.

Efficiency is defined as the work performed divided by the energy input. Under a load of 1 g, the current through the device at 600 V was 0.18 mA (refer to the SI for further

information). For a rise time of 0.1 sec, the energy input was 11 mJ. Using a work of 20 μJ from above yields an efficiency of 0.2%.

The rise and fall curves are compared with those in the PDMS microchannel devices in Figure 70, and the actuation times are summarized in Figure 71. The points in the latter represent the average (all voltages) τ_r (solid markers) and τ_f (open markers) for each device type. Inflation was substantially faster in the paper-based device, with τ_r an order of magnitude smaller. This is attributed to the larger cross-sectional area A_p available for electroosmotic pumping (Equation (2)). Assuming a 50% porosity in the paper, A_p = 0.6 cm^2 compared to $5*10^{-4}$ cm^2 for the previous microchannel devices. Deflation speeds, on the other hand, were similar. This was expected based on the physics of the restorative pressure-driven back-flow, since the membranes were of comparable stiffness (refer to the SI for further information).

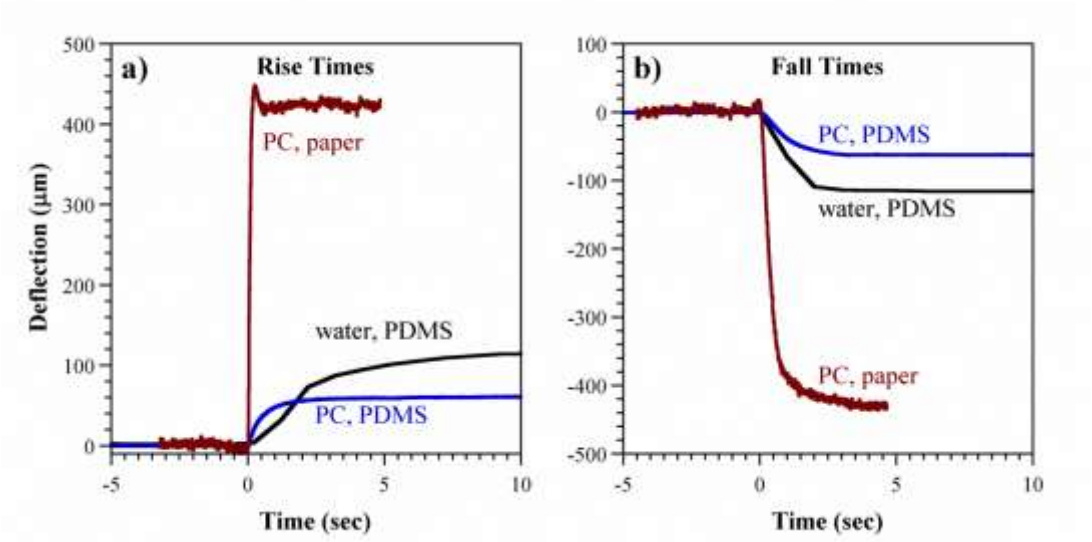

Figure 70. Comparison of deflection-time curves in the stacked configuration and in PDMS microchannel devices. a) Rise times and b) fall times with starting deflections set to zero to allow comparison. (Conditions: load = 1 g; paper/PC, 200 V; PDMS/PC, 7 kV; PDMS/water, 3.5 kV, but times are not voltage dependent).

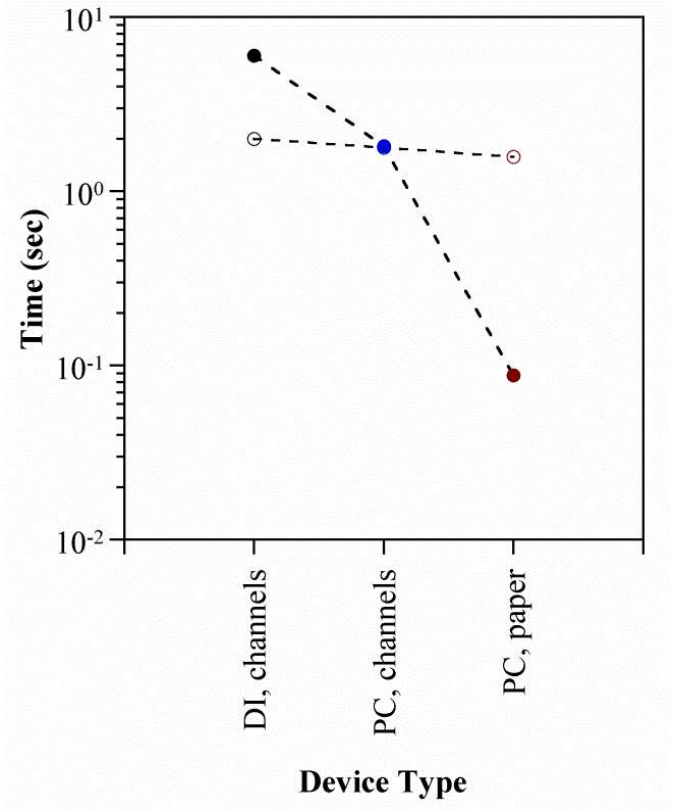

Figure 71. Summary of actuator response times in the paper-based stacked devices and previous microchannel devices using PC and DI water. Filled circles represent inflation and open circles deflation.

6.6 Discussion

In this work we have solved some of the principal challenges in developing microfluidic actuators. The external pump was eliminated by employing an electrically-driven pumping mechanism. The protruding fluidic tubes typically required for filling were abolished by employing a new fluid encapsulation process. The voltage was lowered by employing paper for the pumping surface, which also yielded a larger cross-sectional area and thus a greater flow rate. The force was raised by swapping PC for water as the fluid.

Additional steps can be taken to further enhance device performance in future work. Increasing actuator stroke is of immediate concern. The liquid is incompressible; therefore expansion in one part of the structure can only be achieved by collapse of another region. Currently expansion occurs at the more compliant Ecoflex membrane, while the stiffer PDMS and paper provide structural support and confine the actuation location. Whereas the previous PDMS prototype included a second, collapsible reservoir, this device did not. The membrane displacement could be raised by further lowering the stiffness of the reservoir's silicone base layer, already reduced in thickness under the paper, allowing it to deflect upward more easily, or by other features that allow structural crumpling.

Pumping force can theoretically (Equation 1 and 2) be increased by boosting the surface charge on the paper via chemical functionalization: highly charged groups can be added via polyelectrolyte deposition [259] or silane treatment [260]. Alternately, a different porous material with a higher surface charge and smaller pores can be employed instead. For example, we have observed EOF using sheets of spun polyethylene, cotton, polyurethane sponges, and glass microfiber filters in place of the paper. Fabrics may also be considered, which would improve the mechanical flexibility of the device.

Encapsulation prevents evaporative loss of the pumping fluid, protects the pumping fluid from external contamination (for PC, ambient moisture [134,154]), and keeps the pumping fluid from making contact with the external environment (e.g. microfluidic samples, biological tissue). Silicones swell in many liquids [258] and are permeable to

gases. The challenge is thus to devise a stretchable layer that is impermeable. One possibility would be to coat the device with an inorganic layer, such as a metal or oxide. To allow the non-stretchable bilayer to inflate, one could employ wrinkles [261]. The membrane would be inflated using a mechanical pre-load or by actuation, and coated in the expanded state. Subsequent collapse of the membrane would lead to wrinkling, maintaining continuity of the inorganic layer. With PC, the coating would need be deposited below 116 °C (PC flash point, [262]).

Autonomous devices that do not require an external high voltage power supply would be advantageous in some applications. To permit device operation with an on-board battery, as well as integrated circuit control, the voltage requirement must be reduced still further. One straightforward method is to decrease the distance between the electrodes. Ideally the channel layer between them would therefore be thin, in addition to having large surface area, high porosity, and high charge density.

Our fabrication process yielded a single, self-contained actuator unit. The process could be further developed to combine multiple actuators in series and parallel to form arrays, stacks, and complex multi-dimensional moving structures. Units could be joined in multiple orientations by plasma bonding, magnets, or adhesive. Electrical connections could be made with the conductive carbon composite, which can be easily applied and patterned. Composite structures employing materials with different stiffnesses would enable programming of the directionality of actuation.

The actuator developed in this work is thin and therefore rollable. This technology could therefore be useful for biomedical applications such as in an adjustable stent or artificial sphincter to control the flow of body fluids. A preliminary flow control test setup is described in the Supporting Information. Other applications of these actuators may be in miniature lenses, integrated pumps and valves for lab-on-a-chip microfluidics, soft robotic limbs and joints, and elastomeric surfaces that can change color or texture in response to an electrical stimulus.

6.7 Summary and Conclusions

Flexible devices were fabricated using layer-by-layer assembly of parts composed of silicone and paper. Electrodes were made of a conductive composite of carbon nanoparticles in silicone, and a porous paper pumping layer was sandwiched between them. After filling the device with pumping fluid, it was encapsulated with a film of liquid silicone that cured conformally over the fluid. The silicone skin then served as the actuating membrane.

Electroosmotic flow in the device utilized the pores in the paper as microchannels and the cellulose fibers as the charged walls. Another configuration with the electrodes adjacent to each other under the layer of paper, although having a simpler fabrication process, did

not result in EO, but in other electrokinetic motions. The device design must enforce only a single fluid path, through the paper, in order to achieve the desired pumping.

Actuator strokes of up to 400 μm and blocked forces of 30 g were achieved at only 600 V. Actuation was quick, taking less than 0.1 second. The performance was substantially improved over devices utilizing microchannels formed by soft lithography. Further improvements could be achieved in future work by modifications such as increasing the surface charge on the paper, adding a water barrier, and introducing collapsibility to the structure.

6.8 Acknowledgements

This work was partially funded by NSF under contract CNS 0931878, and we acknowledge the support of the Maryland NanoCenter and its FabLab. We thank Santa Fe Science and Technology, Inc. for the generous donation of their force/strain transducer software. We also particularly thank Matthew Bleakney for his contribution to the development and characterization of the carbon electrode recipe.

6.9 Author Contributions

DS and ES conceived and designed the experiments; DS performed the experiments; DS and ES analyzed the data; DS and ES wrote the paper.

6.10 Conflict of Interest Statement

The authors have filed invention disclosures on this work with their university. The authors have no other affiliations or involvement with organizations having a financial interest in the subject matter or materials discussed in this manuscript.

6.11 Supporting Information

6.11.1 Carbon Electrodes

Hexane lowers the viscosity of the uncured elastomer/carbon mixture, making it easier to process, but it lowers conductivity, leads to brittleness, and results in small holes [247]. The role of hexane was therefore investigated. The two elastomers also needed to be compared as hosts. For this work, Ecoflex 00-30 was used rather than 00-50 because it is softer.

PDMS-based films with 14 wt% carbon black were formed with varying amounts of hexane (Sigma-Aldrich) to determine the effect of the solvent on electrical resistance.

Five formulations were prepared with hexane at 0, 100, 150, 200, and 300% by weight, relative to the pre-polymer. Without hexane, the suspension was a thick paste that had to be applied by doctor blading; with hexane, the suspensions could be cast. These films were poured to a thickness 1 mm, although as they dried the samples with higher hexane fractions were thinner because the volatile hexane escaped. Four films of each concentration were formed on glass slides; 5 g of each mixture was deposited on the glass, and cured in a conventional oven for 2 hours at 65 ^{o}C, at which time they were dry to the touch.

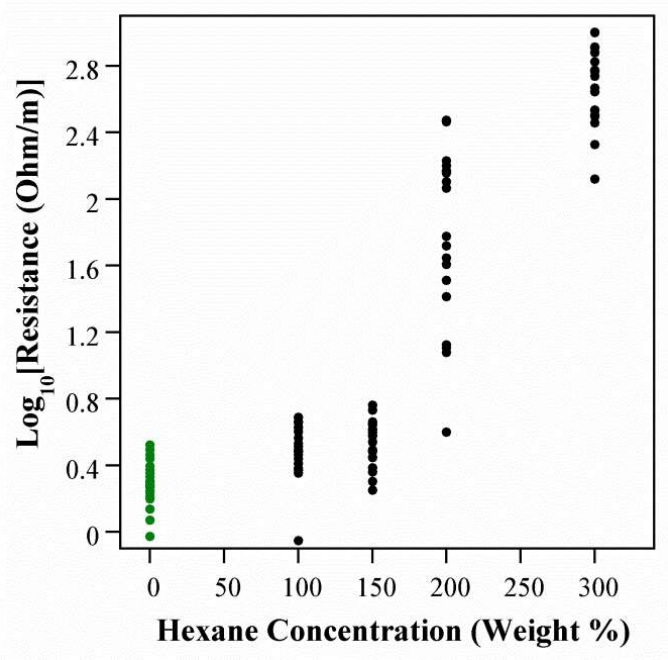

Figure SI 72. Resistance of cured PDMS with 14 wt% carbon black (log scale) as a function of the amount of hexane added to the prepolymer. Each point represents a single measurement (4 samples, 5 pts each).

Film resistance was measured using a multimeter (Fluke 179) at five locations on each sample, giving a total of 20 measurements at each hexane concentration. Electrical contact was made by manually applying the probe tips to the surface at a separation of 1

to 3 cm. The resistance was measured without removing the films from the substrates the day after they were cured (Figure SI 72).

The resistance increased with hexane concentration, despite the fact that the hexane was expected to have evaporated fully. When the measurements were repeated again later (≥ 24 hours) the resistance did not change noticeably. There was significant sample-to-sample variation, but those samples produced without hexane had an average resistance of 0.2 kΩ/cm, while those produced with 300% hexane had an average resistance of 50 kΩ/cm, a factor of 250 greater.

Visual observation of the films revealed that the homogeneity of the cured films decreased with hexane concentration. The carbon aggregated in some areas and cracks appeared. At several locations it was evident by inspection that the nanoparticles had settled at the bottom of the film, while the polymer formed an insulting layer on top. These issues were not observed in the films prepared without hexane.

Furthermore, hexane led to embrittlement. The samples were released from the glass; their edges were trimmed using a razor blade to just less than 5 cm x 7.5 cm, and the films were peeled off the glass slide slowly, taking care to minimize stretching of the film. The ends of the films were clamped (binder clips). One end was fixed and the other was stretched by hand over a ruler. The samples containing more than 200% hexane tore when the films were peeled from the glass. Samples with 100% and 150% tore at 20% strain. Therefore, the use of hexane for electrode preparation was minimized.

Films were produced without hexane, again at 14 wt%, with the two polymer hosts, PDMS and Ecoflex. The resistance was measured at various fixed strains, applied as described above, to determine the extent to which the electrodes could be stretched and how strain affected the conductivity. Measurements were made when the electrodes were still attached to the glass (0% strain), after peeling off the glass (assumed 1% for plotting purposes), and at 10 to 250% strains.

The Ecoflex outperformed the PDMS on every measure (Figure SI 73). The Ecoflex electrodes had lower resistance, the resistance varied less with strain, at a fixed strain the resistance among samples was more consistent, and they had a higher strain to failure. The carbon-PDMS films tore at strains above 200%, and carbon-Ecoflex films failed at 300% strain.

Despite these advantages, we used PDMS for the electrodes because of one critical step in the fabrication process: oxygen plasma bonding of the layers to create thin devices. Plasma surface treatment is an effective method of bonding PDMS to PDMS, without the application of additional layers of adhesive. It is not effective with Ecoflex.

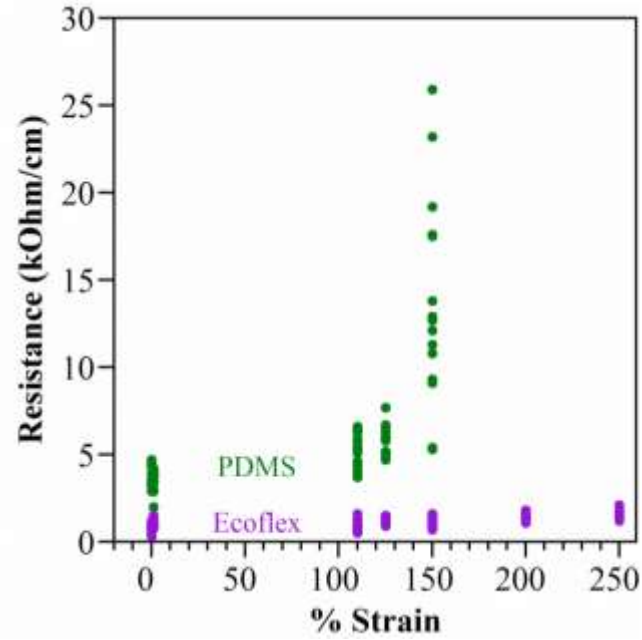

Figure SI 73. Resistance of carbon-PDMS and carbon-Ecoflex under strain. Each point represents a single measurement (4 samples, 5 pts each).

6.11.2 Fabrication

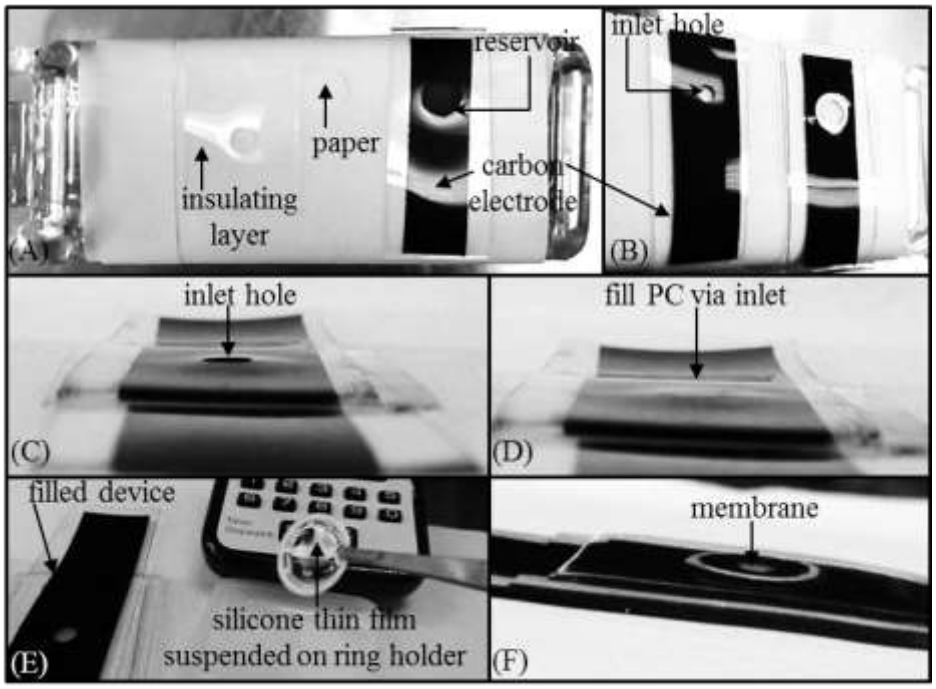

Figure SI 74. (A) The insulating layer, filter paper and positive electrode were exposed to plasma. The filter paper was placed in the reservoir. The insulating layer was then adhered to the electrode, sandwiching the paper between them. (B) The negative electrode was plasma bonded on top of the insulating layer. (C,D) The device was filled with PC through the inlet hole in the negative electrode. (E) A ring was dipped in liquid Ecoflex silicone to extract a thin film. The liquid film was placed over the inlet hole filled with PC and allowed to cure to form the final encapsulated device.

6.11.3 Deflection Data

The data shown in Figure 65 in the main paper were obtained by processing the raw deflection (Figure SI 75) from the force-strain transducer (Figure SI 76), for which upward motion corresponded to smaller values. First, drift was subtracted: a straight line across the entire cycle was calculated using the start and end points of the run (3 cycles). The curve was then flipped vertically, so that increasing displacement corresponded to inflation. Finally, the baseline offset at the start of the first cycle was subtracted to set to it to zero.

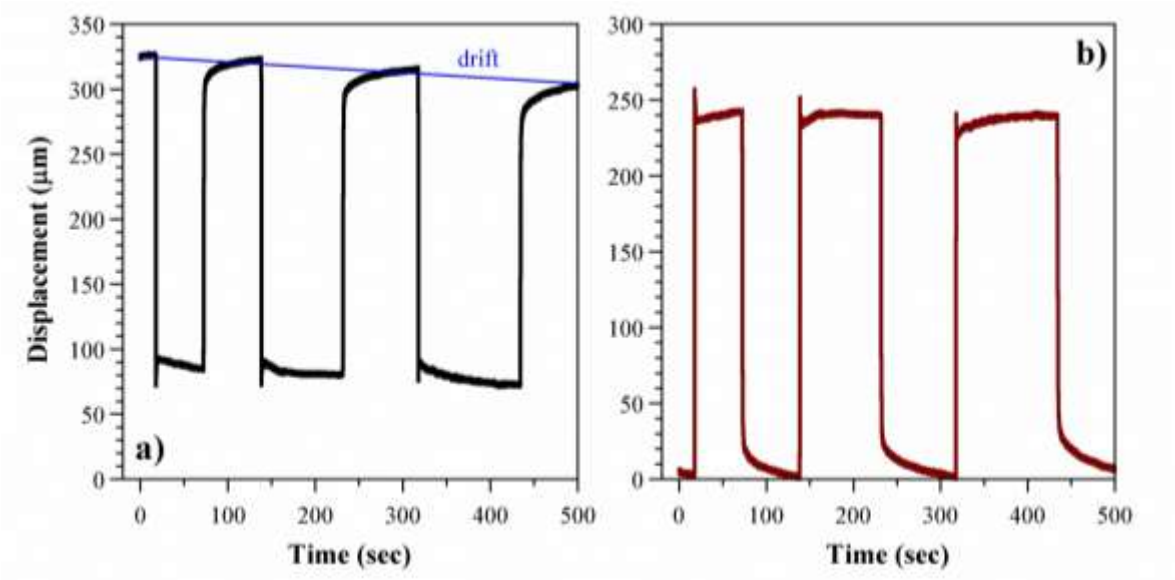

Figure SI 75. Data processing of deflection data collected over time using the force-strain transducer. The data presented in Figure 65 is shown again in a) and was obtained by processing the raw data shown in b) by removing the linear drift, inverting the rise and fall steps, and setting the baseline at the start of the experiment to zero.

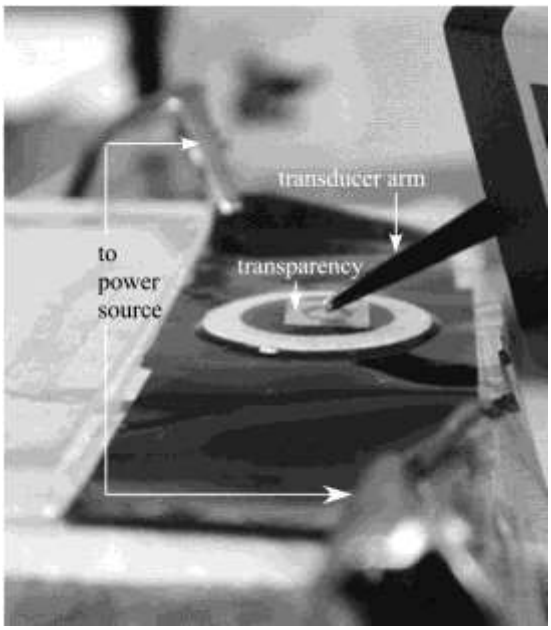

Figure SI 76. Experimental set up for measuring deflection or force.

6.11.4 Membrane Properties

Figure SI 77 shows a cross-section of a membrane, sectioned using a razor blade, from a stacked-layout actuator fabricated by film casting (Section 6.4.2). The membrane was thicker in the center (270 ± 36 μm, average of three samples) than at the periphery alongside the walls of the reservoir (168 ± 22 μm), although while casting the liquid Ecoflex film it initially appeared (by visual inspection) to be thinner at the center of the draped droplet. This membrane shape may develop as the film stabilizes after casting, during which a concave meniscus is formed, causing the Ecoflex to flow towards the center of the meniscus. The overall thickness is governed by the thickness of the ring that supports the film (190 μm).

In the Section 6.5.6 the flattening speeds of the various actuators were the same when the voltage was turned off. This is because their stiffnesses were similar. The reported elastic modulus of PDMS is 750 kPa [263], and that of Ecoflex is an order of magnitude smaller at 83 kPa [24]. In the previous microfluidic device [134] the PDMS membranes were 25 μm thick, and in the stacked paper-based device the Ecoflex membranes were an order of magnitude thicker, on average 220 μm. The stiffnesses, given by the product of thickness × modulus, were thus nearly equal at 18.8 and 18.3 N/m, respectively. To produce a thinner membrane, strategies may include decreasing the thickness of the ring and pre-bulging the droplet by applying an upward force at the base of the reservoir.

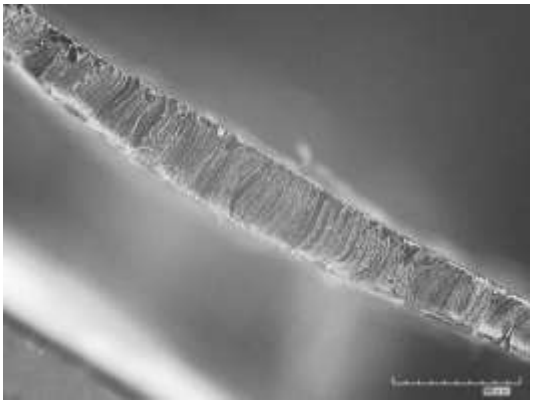

Figure SI 77. Micrograph of membrane cross section. The scale bar is 500 μm long.

6.11.5 Inverse Effect – Load Sensing

The current-voltage characteristics of the device were measured using a source-measure unit (Keithley 237). The instrument was programmed to source voltage and measure current simultaneously and continuously by a Matlab code with the Measurement and Automation Explorer module (National Instruments); a USB-to-GPIB adapter was used to connect the source-measure unit to the computer. Two devices were tested on two consecutive days. The current through the device was also measured with external loads applied on the membrane. Force was applied to the membrane by placing weights on top (Figure SI 78); a small piece of Kimwipe was placed between the membrane and weights to prevent stiction. The voltage sweep was repeated as the load was applied.

In order to determine the efficiency of the paper-based EOF actuator, the current-voltage characteristics were recorded ("0 g" curve). Two devices (1 and 2 in the main text) were tested. The voltage was increased in a linear sweep from 300 to 1100 V. The current changed proportionally as the voltage increased. The results from device 1 are shown in Figure SI 79.

When weight was added (15 – 45 g curves), the current decreased, with the *I*-*V* curves shifting downward with increasing load. However, when the load was removed ("0 g, unloaded") the current was not restored (within 5 min of unloading), but remained the same as it was under 45 g. The unloaded device was allowed to rest for 30 minutes to

allow the fluid pressure to equilibrate and the elastomers to relax. The position of the I-V curve after this ("0 g, unloaded, relaxed") was higher, approaching the starting position.

Figure SI 78. Experimental setup for studying the *I-V* characteristics of the paper-based stacked-layout electroosmotic actuator. The electrodes were connected to a source-measurement unit. The current was recorded as a function of applied voltage, and the influence of applied loads on current was studied.

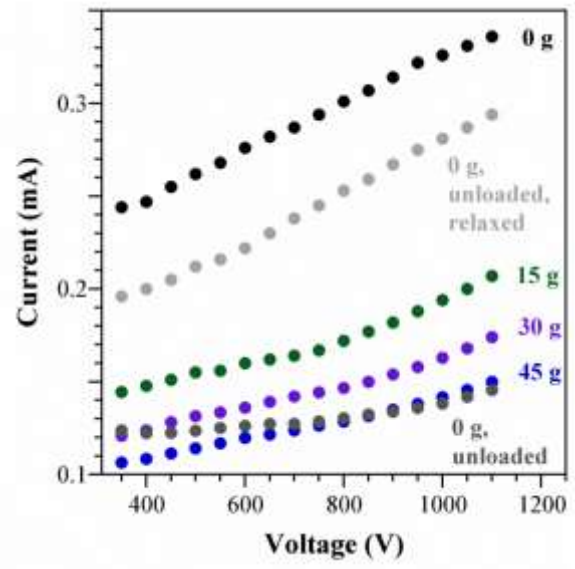

Figure SI 79. *I-V* curves recorded under applied loads of 0, 15, 30, 45, 0, and 0 grams (in that order) as the voltage was ramped linearly from 350 to 1100 V. The 45 gram weight was removed and a measurement was done at 0 g within 5 minutes (0 g, unloaded). After 30 minutes the 0 g measurement was repeated (0 g, unloaded, relaxed).

6.11.6 Flow Control

A single device was rolled and placed inside a rigid tube, with the electrodes extending outside the tube connected to the actuator power supply. Using a syringe pump a flow rate of 0.1 mL/s was applied to the tube (setup shown in Figure SI 80A). When voltage was applied to the actuator minimal alteration of flow was observed. This was likely because the magnitude of actuator stroke (400 μm was much smaller in comparison to the size of the tube (8.6 mm) (depicted in Figure SI 80B). Future work will therefore involve

optimization of the EO valve dimensions with respect to the flow conduit geometry, and combining multiple actuating units (cross section of smaller flow tube with four actuator units shown in Figure SI 80C, in order to achieve flow control.

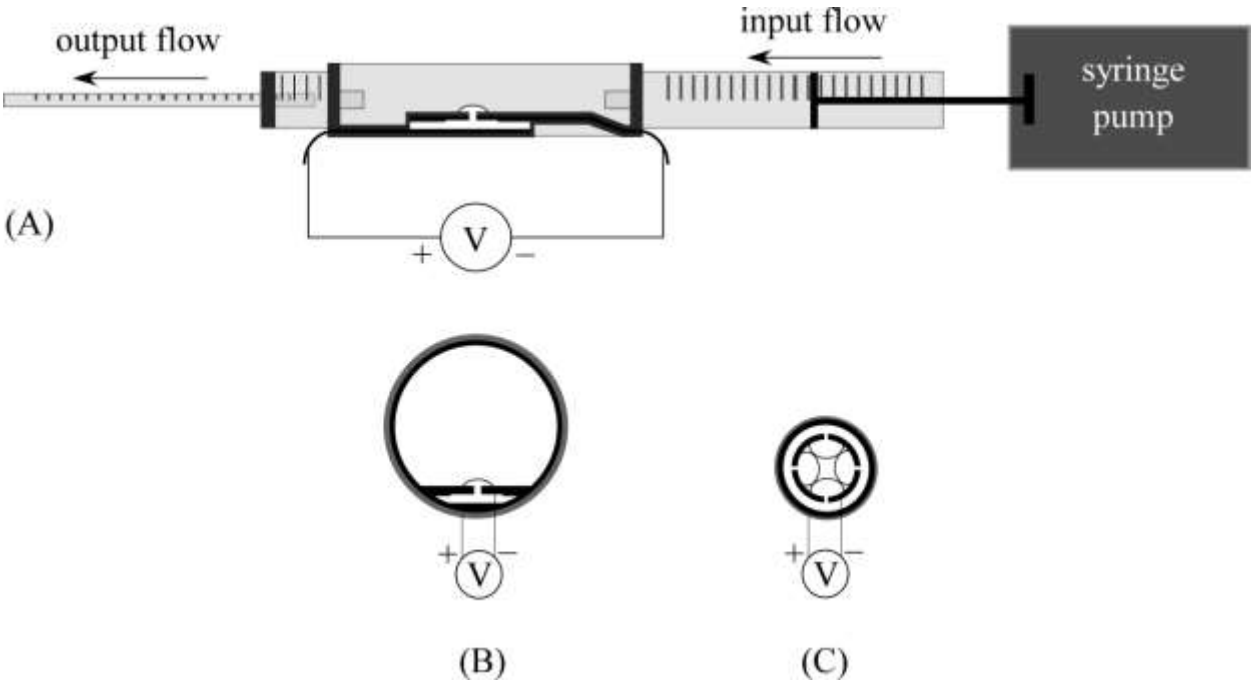

Figure SI 80. Schematic of flow control using EO actuation. (A) Transverse view of setup with a valve comprised of a single actuator, placed inside a flow tube. (B) Cross-section of the tube containing a single actuator. (C) Cross-section of proposed design: the valve size, and number of actuating membranes must be optimized relative to flow conduit size in order to modulate the effective cross-sectional area for flow.

6.11.7 Fabrication of the Adjacent Layout

The following figures were not submitted as a part of the journal publication.

Shown here are photographs of the steps involved in afbricating devices with the adjacent electrode layout. Either PDMS or Ecoflex can be employed as the silicone used as the base for the carbon paint and for the encapsulation steps. The device shown in these pictures was formed using Ecoflex. The electrodes were patterned using a benchtop cutter and then embedded in silicone (Figure 81). The paper microchannels were filled with PC by wicking (Figure 82). The PC was encapsulated by casting a layer of uncured silicone directly over it (Figure 83). A rectangular frame was adhered over the silicone film to define the actuating membrane (Figure 84). The final device is shown in Figure 85.

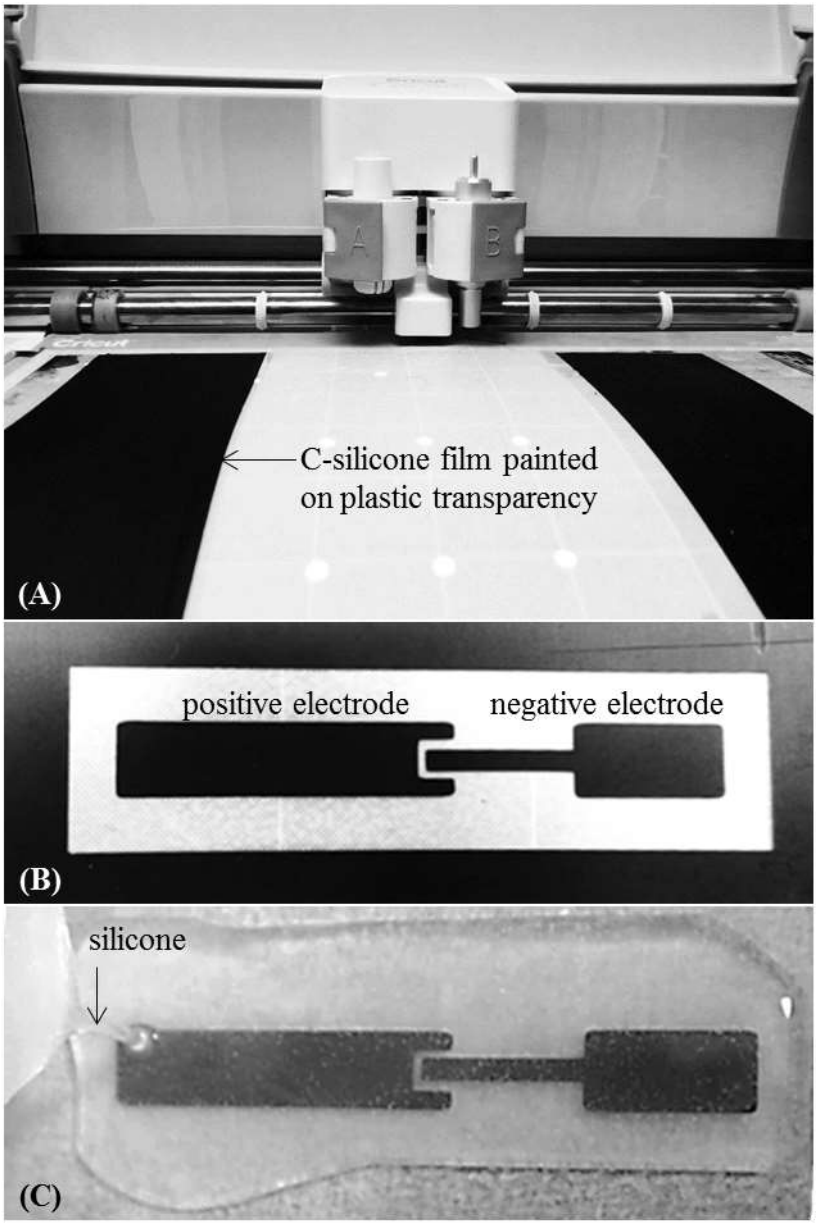

Figure 81. (A) The carbon paint was applied by squeegee on a plastic transparency. The film was patterned using the Cricut Explorer cutter. The cut pressure of the cutting blade was adjusted so as to not cut through backing transparency. (B) Patterned electrode film. (C) Silicone was poured over the patterned electrods to embed them at the base of the device.

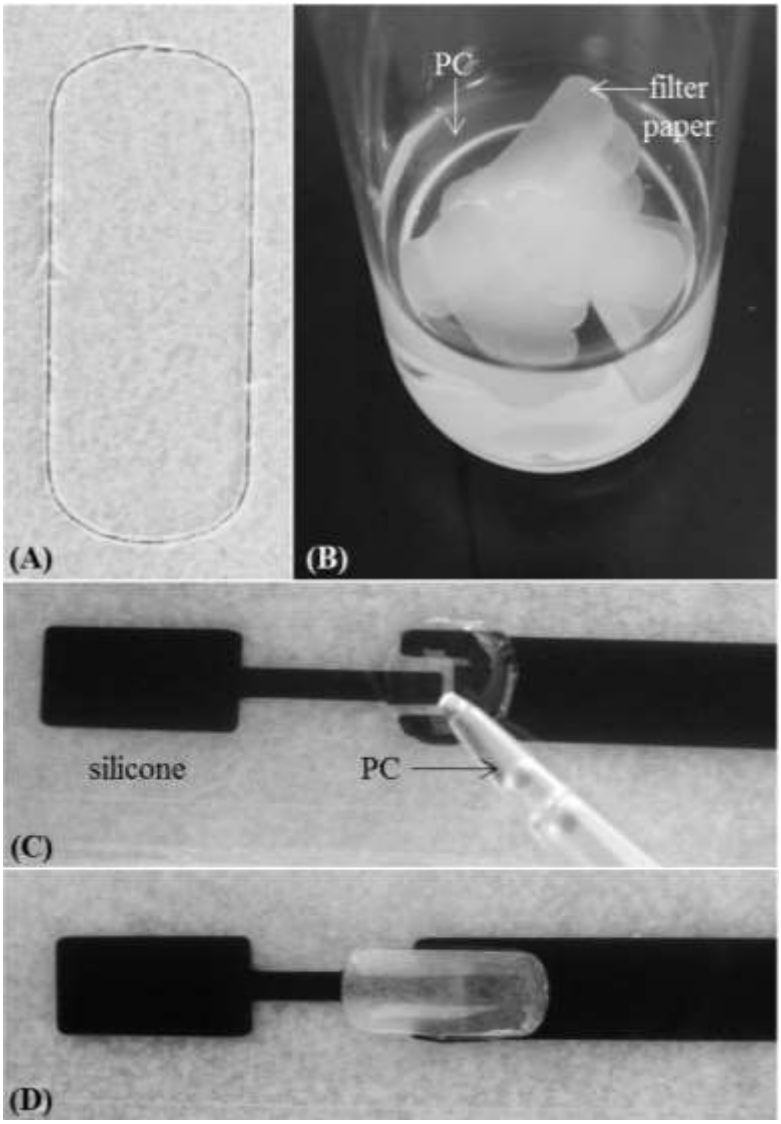

Figure 82. (A) Filter paper channel layer was shaped using the Cricut Explorer. (B) The filter paper was soaked in PC and dessicated to remove air bubbles. (C) A drop (50 μL) of PC was added between the electrodes. (D) The soaked paper was placed on the drop, across the electrodes, to form a wet connection (to avoid air trapping between paper channel and the hydrophobic silicone).

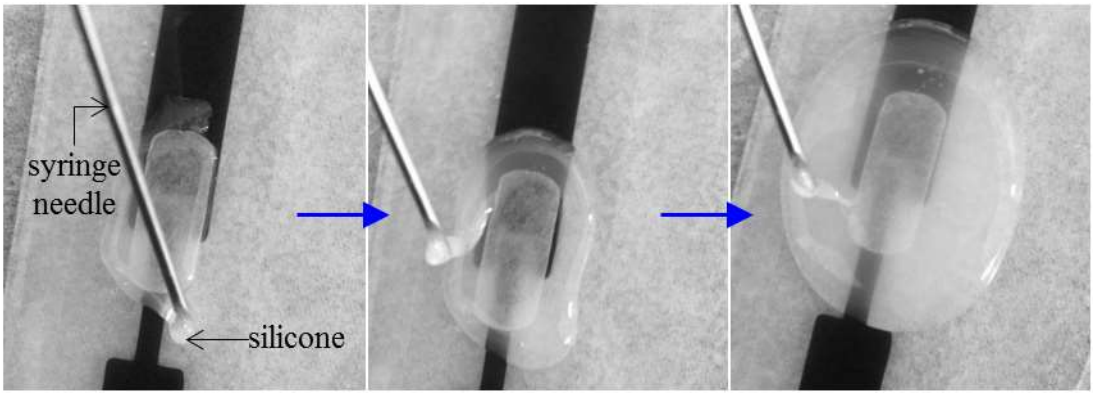

Figure 83. Liquid encapsulation in silicone. Silicone was applied using a syringe needle around the periphery of the PC-filled paper until it was fully covered. The silicone was dispensed slowly (taking about 1 min for each orbit around the paper) to allow the silicone to spread out over the liquid. After encapsulation the silicone was allowed to spread for an additional 10 min to create a thin skin over the liquid before placing it in the oven to cure.

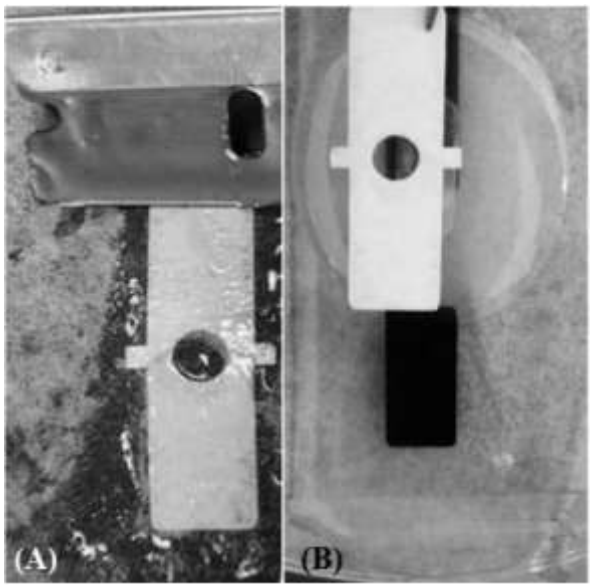

Figure 84. (A) A rectangular frame with a hole in the center was cut using the Cricut Explorer. A thin film of uncured silicone was applied to one side of the paper, scraping off the excess glue using a razor blade. The frame was glued over the silicone skin encapsulating liquid, to confine membrane deflection to the hole.

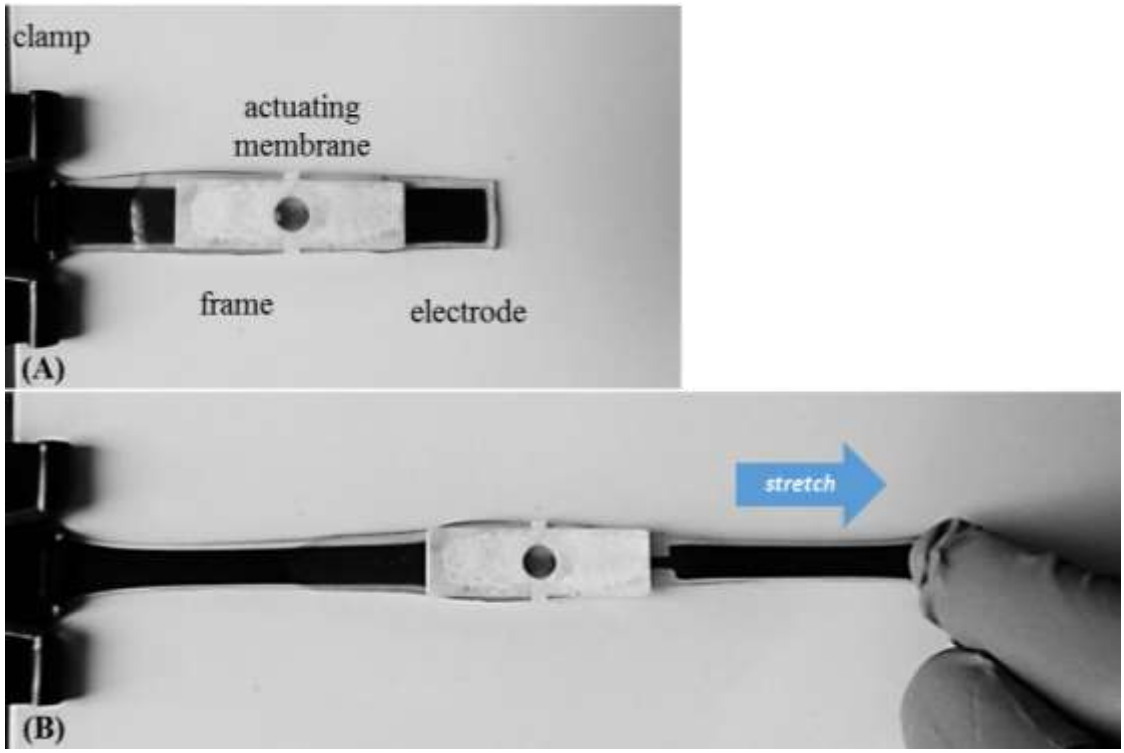

Figure 85. (A) The final device was thin (1-2 mm) and compact. (B) Fabricating the device with Ecoflex was useful to create a soft device that could be subject to large strains while maintaining conductivity of the electrodes.

7. **Conclusions**

7.1 Summary of Device Development

This work has resulted in a fully encapsulated soft actuator that exhibits stable performance at high electric fields. Bubble-free electroosmosis was achieved by replacing DI water with propylene carbonate as the pumping liquid. In this work, the operation time of the first prototype electro-nastic actuator was increased from only a few seconds to at least an hour without compromising actuator performance by making only one system modification: filling the device with PC instead of DI water.

Additionally, each component of the device was re-designed to create a fast, modular, high pressure EOF actuator that is amenable to integration with other actuator units or associated system components. The design modifications are summarized in Figure 86 and Figure 87.

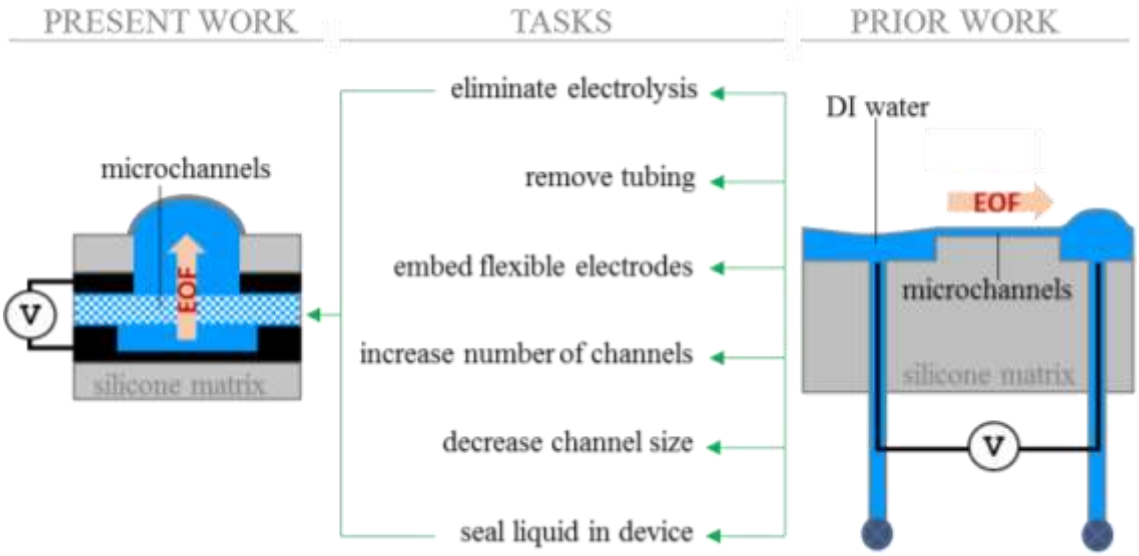

Figure 86. Summary of engineering challenges solved to improve the electro-nastic device. In the present work the pumping fluid was propylene carbonate; EOF was through the thickness of a sheet of filter paper; membrane deflection was parallel to the direction of EOF. In prior work with the original prototype the pumping fluid was DI water; EOF was along the length of the channels; membrane deflection was perpendicular to the direction of EOF.

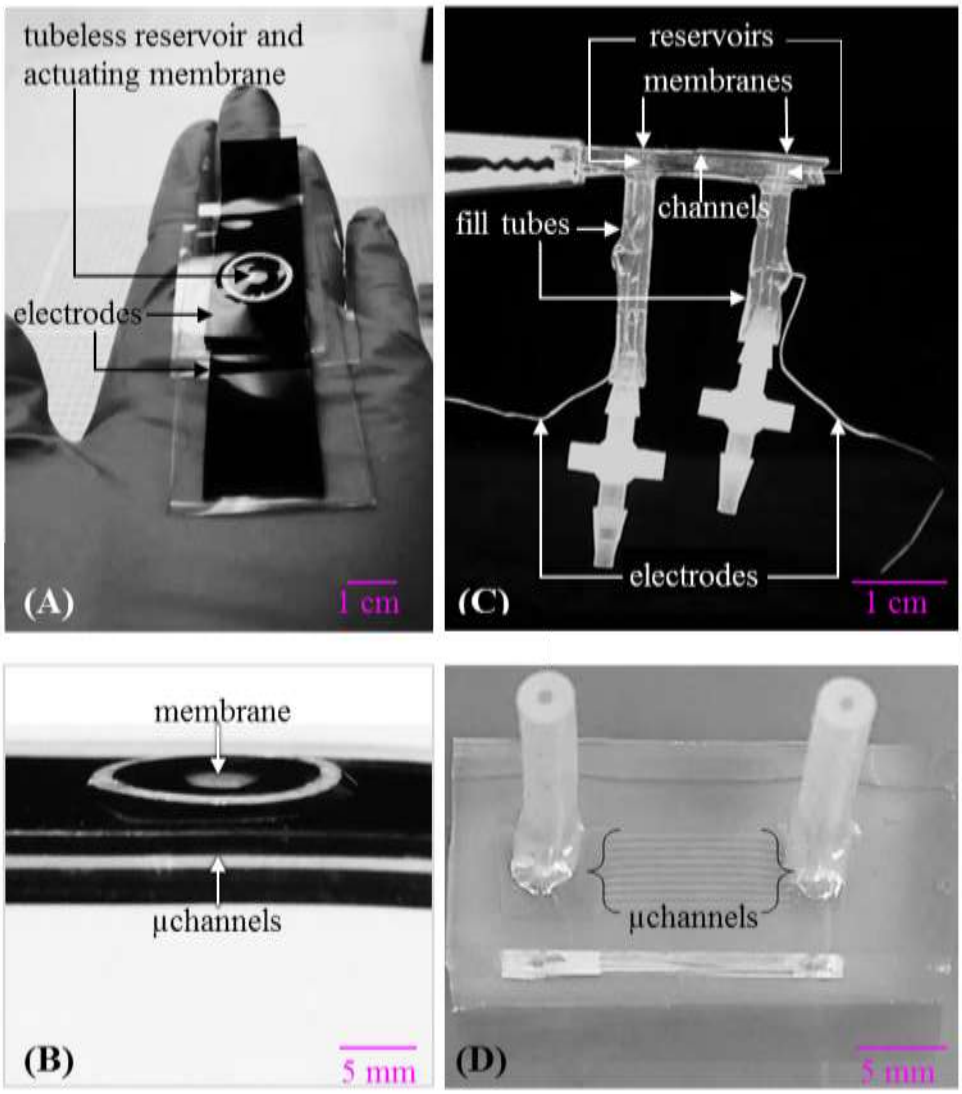

Figure 87. Comparison of the new paper-based device and the original PDMS-based electro-nastic device. (A) Overhead view of the paper-based EO actuator with elastomeric electrodes; fluid was filled and encapsulated without external tubing. (B) EOF was enabled by the thousands of micro/nano channels in filter paper. (C) Side view of original actuator prototype showing protruding tubing and electrode wires. (D) The original device consisted of two reservoirs connected by nine PDMS microfluidic channels.

In the new design the layout of the reservoirs and electrodes with respect to the channels was changed. The reservoirs were placed sideways on either end of the channels. EOF occurred horizontally along the length of the device, and the displaced fluid caused the membrane to bulge out perpendicularly to the EOF direction. In the current model, the reservoirs were positioned to face each other, with the channel layer sandwiched in between. This minimized back pressures/drag and maximized the fluidic surface area of the reservoir in contact with the pumping channel area. EOF occurred through the thickness of the porous pumping layer and caused membrane bulging in the same direction as EOF. The actuation schematics are shown in Figure 87B and Figure 87D. I also found that EO flow was remarkably improved with the opposite-facing electrode arrangement as compared to electrodes placed side by side, likely because the field lines were oriented to point directly into the channels and thereby exert more tangential force on the electric double layer at the channel walls (Figure 88). So, incorporating opposite electrodes may improve device operation in a variety of non-planar designs in microfluidics and MEMS applications.

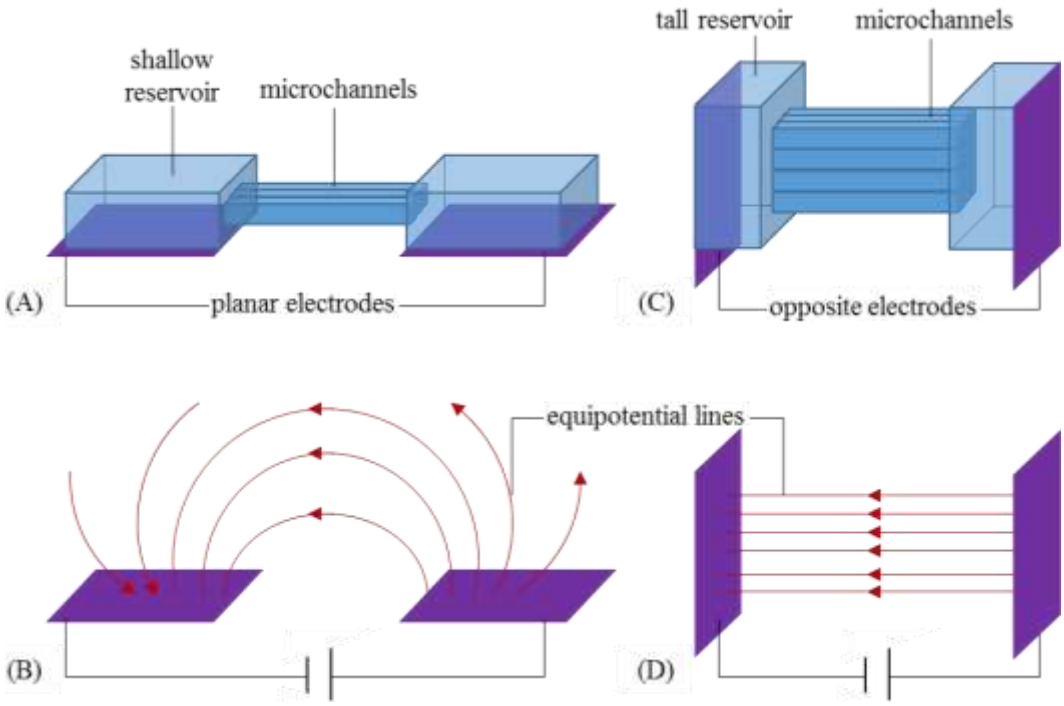

Figure 88. Electroosmosis is improved when electrodes are placed face-to-face, like in (C), instead of side-by-side like in (A). Electric field line illustrations in (B) planar electrodes where many of the electric field lines point away from the channels, and in (D) opposite facing electrodes they pass tangentially to the channel wall.

Porous materials were used instead of standard microfluidic channels. In the original electro-nastic prototype device (see Figure 87D), the channels were formed by replica molding off a planar SU-8 microfabricated mold. Meso-scale devices were created by replacing the microfabricated channels with flexible three-dimensional porous layers composed of silicone or paper to increase the channel density (refer Chapters 5 and 6). The porous channel layers were shaped using a benchtop cutter, so this eliminated the need for cleanroom microfabrication of the channels.

A tube-free filling technique was devised to load the pumping fluid into the microfluidic actuators. The tubing in the original prototype, and the plugs used to seal the tubes during actuation, added significant bulk to that device (see Figure 87C). In the literature, tube-free device filling has been performed by perforating the silicone with a fine syringe needle to inject fluid into the device [264]. This method was found to be unsuitable for EO actuator applications because the high pressures generated within the system caused the liquid to leak during actuation. In this work, liquid was dispensed directly into large (mm) reservoirs immediately after oxygen plasma treatment of the silicone and paper surfaces. The plasma-enhanced surface energy enabled facile wetting of the paper and the underlying silicone; the paper microchannels readily wicked liquid from the inlet reservoir through the microchannels to fill the device, without applying any external pressure applied at the inlet. There was no need to take steps to eliminate trapped air bubbles because the channels readily wicked the liquid due to surface tension, and the air was spontaneously displaced by the liquid.

The liquid was sealed within the paper-based device by film casting silicone on the filled reservoir, simultaneously forming the actuating membrane. The polymer seals the liquid and eliminates trapped air spontaneously, because the uncured polymer fluid is preferentially attracted to the liquid rather than air due to surface tension effects. This sealing technique relies on the immiscibility of the liquid to be encapsulated and the uncured polymer fluid; also the polymer fluid must have lower density than the liquid so that it forms a skin over the liquid as soon as it contacts it. This encapsulation technique

eliminated the plasma bonding step that was required to attach the actuating membrane in the original prototype.

The stiff protruding metal wire electrodes were replaced with embedded flexible carbon electrodes. The carbon electrodes were placed much closer, with a gap of only 3 mm between them (Figure 87B), by placing them on either side of the paper channel sheet. This resulted in reducing the operating voltage by an order of magnitude. Removing the protruding electrodes and tubing resulted in a compact flexible actuator which can be folded or rolled into various form factors. Figure 89 shows the actuator rolled into a cylinder, with the actuating membrane facing inwards, into a cylinder shape. Further details about using this set up for future flow control applications are described in Section 6.11.6.

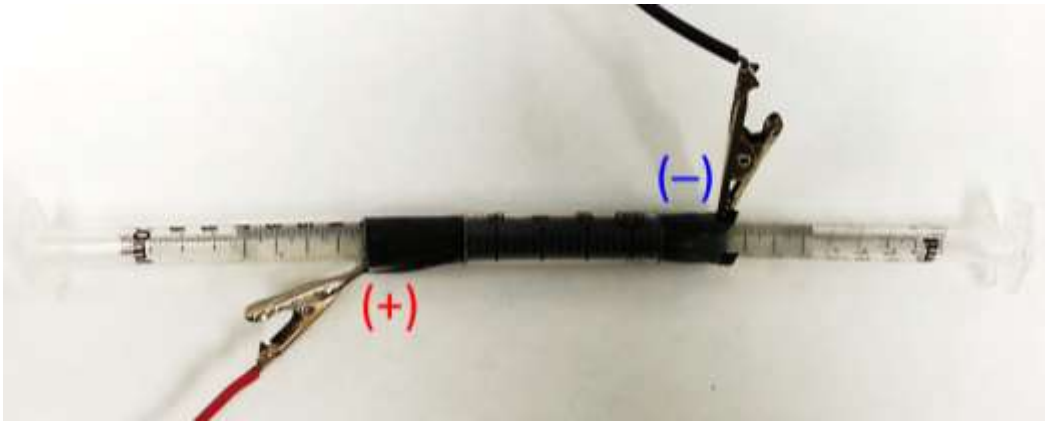

Figure 89. The paper-based actuator rolled up into a cylindrical tube.

7.2 Thoughts on Fabrication Processes

I explored a variety of machining techniques compatible with roll-to-roll processing towards creating a smart material with embedded electro-nastic units. The greatest challenge with designing soft actuators is to be able to fabricate thin elastomeric actuating membranes on the same mold as the high-aspect ratio reservoirs. The methods I considered for machining the elastomers were laser cutting and 3D printing.

Prior to employing porous materials, the most significant fabrication challenge was in integrating microchannels in meso-scale EO devices. George Kumi and Floyd Bates at Professor John Fourkas' lab helped me evaluate using multi-photon patterning to create high aspect ratio SU-8 2000 molds for the microchannels and reservoirs. (Multiphoton polymerization is a micro/nano-lithographic technique in which a laser beam is focused inside a sample to induce chemical transformations. In SU-8 the areas exposed to light become a crosslinked solid and the unexposed areas can be washed away.) Our tests concluded that although nanochannels (100 nm) could be formed, it was impractical (it will take several hours to penetrate mm-thick SU-8) for the high aspect ratio required for this device, and was limited to patterning only up to an optical depth of 500 μm of SU-8.

Researchers have employed microfabrication processes like direct-write laser [265], stereolithography [266], and the Lichtenberg effect [267] for creating three-dimensional microchannel devices. I consulted with Professor Victor Ugaz about creating channels by the Lichtenberg effect. He explained that in their lab they found that PDMS was not a

suitable material, and that this technique was better suited for rigid plastics. I was also able to discuss the prospects of using injection molding with Professor Satyendra. K. Gupta for creating high-aspect ratio devices with embedded microchannels. He explained that, to create a mold for PDMS casting with micron-sized features, a metal substrate would have to be patterned using micro-electric discharge machining (micro-EDM) [268]. The above processes require expensive equipment that were unavailable at UMD. So finally, the complex task of fabricating several microchannels in a mesoscale device was resolved by using inherently microporous flexible materials like paper which can be readily integrated into soft devices.

It was observed that the carbon-silicone paintable composites (carbon nanoparticle in a silicone base of PDMS or Ecoflex) was highly suited for forming electrodes for electroosmotic soft actuators because a) they were electrochemically stable, and b) they could be patterned using benchtop methods (refer Chapter 6 and Appendix A). It was concluded that microfabricated metal electrodes were less suited for this application due to the poor adhesion of the metal to the silicone substrate (see Appendix C).

Shown below in Figure 91 and Figure 92 are examples of device parts that were machined using the Cricut Explorer. It is evident that device is able to proficiently cut contours with curved as well as sharp millimeter-scale features. Figure 90 shows a pattern cut out in a film of stretchable conductive carbon that was later embedded in silicone. Figure 91 shows how multi-actuator arrays can be created by layer-by-layer fabrication on a single platform, using paper as the supporting material. Figure 92

depicts how actuator devices formed out of soft materials can be aligned and bonded by using design principles used in MEMS fabrication.

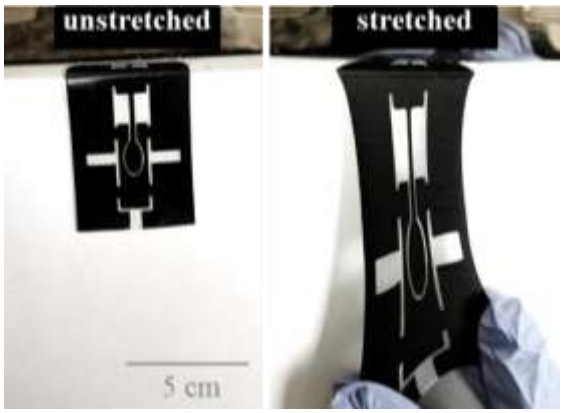

Figure 90. Stretchable C-Ecoflex pattern (black) made using the Cricut Explorer that was embedded in Ecoflex 0050 (transparent).

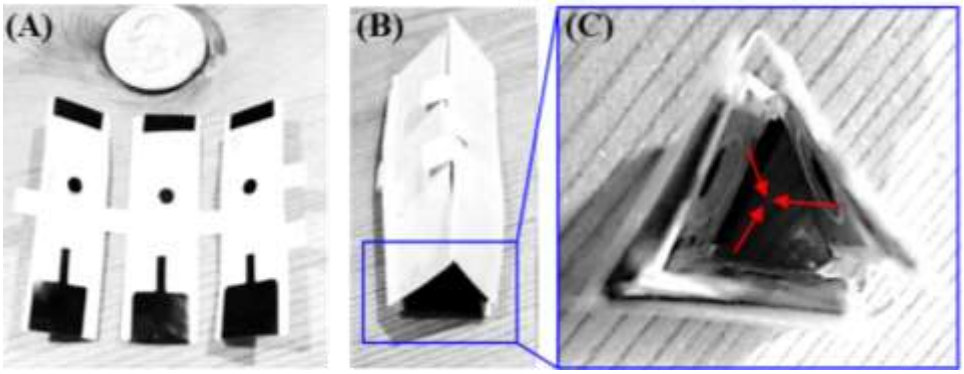

Figure 91. Photographs illustrating the design concept for a tri-actuator occlusion device composed of paper and silicone. (A) Three actuators were fabricated on a supporting paper frame. (B) The device was folded into a triangle and fastened by folding down the tabs at the edge of the frame. (C) Downhole view of the triangular device showing the three actuating membranes that are predicted to bulge towards the center of the triangle when actuated.

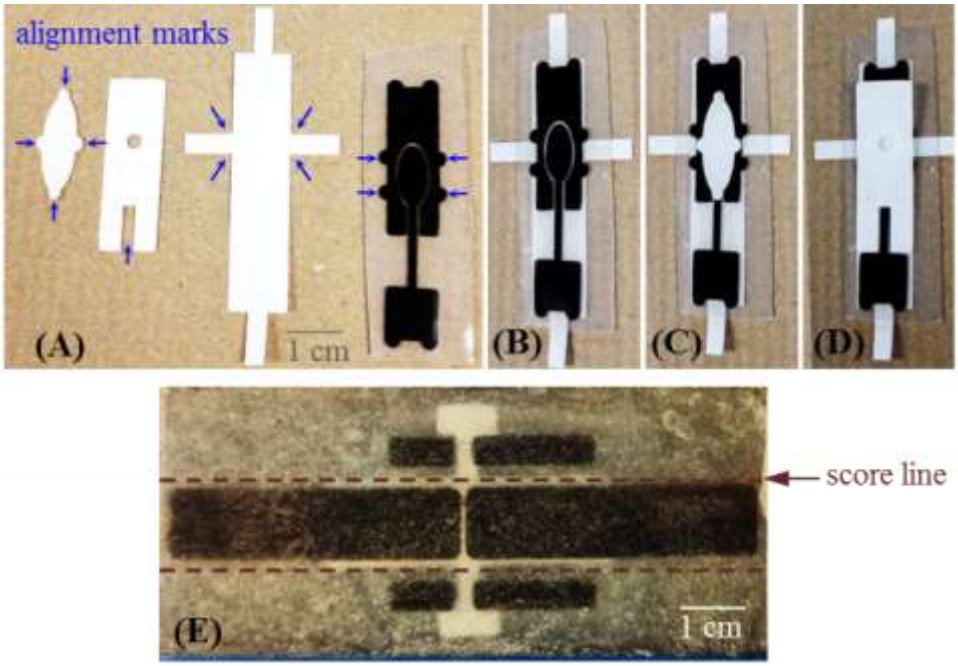

Figure 92. Photographs of device parts that were shaped using the Cricut Explorer machine. MEMS-type layer-by-layer fabrication was made possible by including alignment marks into the design of the parts. (A) The pumping channel layer, membrane frame, and back support were cut out of filter paper. The electrodes were formed by cutting out a film of cured C-Ecoflex paint and embedding it in Ecoflex. Alignment marks enabled the layer assembly, as shown in the sequence of images in (B), (C) and (D). (B) The electrode layer was positioned on the back support layer. (C) The pumping channel layer was placed across the electrodes. (D) The membrane frame was positioned so that the membrane opening was located in the center of the negative electrode. (E) An alternate example of alignment mark designs in which they were outside the device area, and could thus be cut away after device assembly. This photo was taken from behind the device, through the tissue backing. Uncured silicone was used as adhesive between each layer.

The quality of patterns achieved with the Cricut were impossible to produce using a vinyl cutter (Lynx 12, Sign Warehouse, Denison, TX), or using a CO_2 laser cutter (VLS360, Universal Laser Systems, Scottsdale, AZ). The vinyl cutter was suited to cutting vinyl sheets with adhesive and backing; it was not suitable for delicate samples like elastomer paint films or metal foils). Using laser ablation, I was able to successfully cut and engrave clean patterns in Delrin and paper samples, but not in silicones (both opaque and clear silicones failed). PDMS and Ecoflex experienced burning from the CO_2 laser, and the smallest feature size that could be achieved was 200 μm. Burnt PDMS residue was formed in the line of path which could be wiped off. The lines patterned by the laser had rough edges. The line had to be re-scored using a razor blade to peel off the PDMS. The laser cuts had penetrated into the glass slide, and the silicone near the trace lines had become brittle making it challenging to peel without breaking; an Exacto knife was required to aid the release of the unwanted sections. An example of C-Ecoflex patterned by laser ablation is shown in Figure 93.

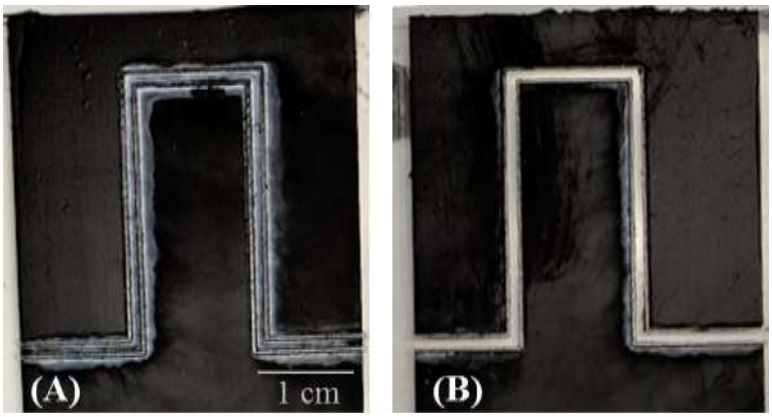

Figure 93. Traces cut in C-Ecoflex using a CO_2 laser ablation tool (VLS360, 90% speed, 13% power). (A) The trace lines were wide (100-200 μm) with rough edges. The white powdery deposit seen around the trace lines is burnt PDMS residue. (B) The burnt residue was wiped off, and the material between the traces was peeled with the aid to reveal the final pattern.

Apart from laser machining, which is a subtractive fabrication technique, I also fabricated device molds by depositing ABS plastic by 3D printing using the Objet Eden 350 machine. The ABS molds created did not have a smooth surface, because of the line-by-line deposition process. This caused the PDMS to become entrenched inside the grooves which caused damage to the PDMS during release. In addition, the PDMS remained uncured at several spots at the interface in contact with ABS, implying that ABS interferes with the PDMS crosslinking mechanism. This problem persisted even after treating the surface of the mold with mold release (Mann Ease Release 200). It may be possible to create suitable molds with the more recent 3D printers that are able to print a wide variety of materials at higher resolution.

7.3 Recommendations for Future Work

7.3.1 Design and Fabrication

7.3.1.1 Biomedical Valve

Electroosmotic membrane actuators can be used in many applications such as micro-positioning and tunable micro-optofluidic lenses. They may be integrated onto lab-on-chip devices to regulate flow [269] in the form of adjustable stents, sphincters, and catheters to dynamically regulate flows in the body. We envision that the paper-based actuator could have biomedical applications to create stents or artificial sphincter devices to control the flow of body fluids. The device could be rolled up and placed in a stent which is inserted inside a blood (or other body fluid) vessel (see Figure 94, Figure 89 and Section 6.11.6). When the actuator is turned on the membrane would inflate due to EOF so the vessel can be narrowed, and when turned off it would allow free flow through the vessel. The degree of blockage could be controlled by varying the applied electric field.

An implantable valve must be self-contained and composed of materials that are biocompatible. The present paper-based EO actuator is thin and flexible, so doctors could possibly insert it into a stent support for delivery into vessels in a collapsed state and later expanded within the vessel. The present device can be made smaller by trimming the electrodes and the excess silicone around the pumping area to be 1 cm long and 1 cm wide. The silicone membrane is strongly bonded around the membrane area, and therefore the silicone around the membrane can be trimmed away (to within one mm

from the edge of the inlet hole) without damaging the actuator. In its present design, the actuator can be operated using hundreds of DC volts. EOF has been reported at voltages as low as 10 V [108]. If the electrodes are brought closer, spaced less than a millimeter, then the device could be powered at tens of volts by an AC wall outlet with the help of an AC rectifier or using a 12 V DC battery. It is theoretically possible to reduce the voltage requirement by another order of magnitude to achieve EO actuation using a 1.5 V battery. To do this the electrodes must be brought even closer, reducing the gap to a few micrometers, sandwiching a thinner, a more porous material with smaller channels than filter paper in place of the filter paper layer. Additionally, low-voltage DC EOF can be enhanced by chemical modification of the channel material to increase the surface charge [270]. The force achieved at low voltages may be enhanced by incorporating multiple pumping regions (channels sandwiched between electrodes) [108].

The device must be designed so that the electroosmotic flow can generate enough force against the fluid flow in the vessel. It will be necessary to devise a mechanism to supply the electric power without causing harm to the patient. The actuator in its present form is composed of materials that are non-toxic: silicones are widely used for medical devices [271,272] because it is inert and resistant to fouling, propylene carbonate is approved for use in cosmetics and as a food additive [273,274], the carbon particles bound in silicone are likely to be biologically inert [271], and finally paper (composed of cellulose) is unanimously accepted to be a safe biomaterial. The fabrication processes developed in this work are potentially useful for building create devices out of other medically compatible soft materials like PTFE, HDPE, and PU [275].

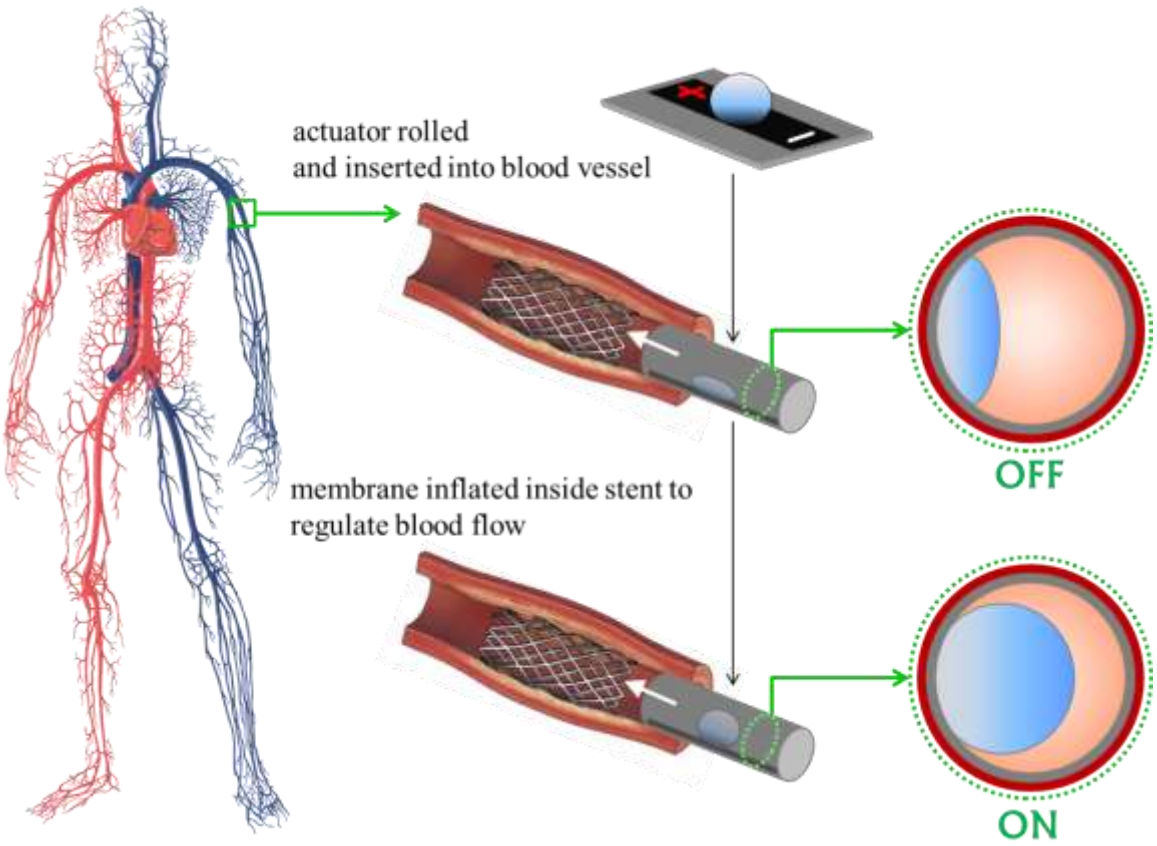

Figure 94. Implantable inflatable device for flow control of body fluids.

7.3.1.2 Multi-Actuator Networks

Roll-to-roll manufacturing processes are conventionally employed for large-scale production of microdevices [276,277]. It is expected that the layer-by-layer actuator fabrication processes developed during this research can be readily scaled up to commercially fabricate a number of actuators in series/parallel on a single platform. Many actuators could be fabricated by patterning, aligning, and bonding large sheets of electrode, channel, and elastomer materials to create sheets/slabs/cubes of actuators. The pumping fluid could be accurately deposited in the reservoirs by an automated pipetting

system (the company DYMAX produces a variety of programmable dispensing systems). The finished smart material could then be sized or shaped by cutting along the periphery of the actuator units. This also makes it easy to cut and remove any damaged actuator modules, if necessary. Alternatively, the actuator modules may be formed individually by a batch fabrication and later joined to form the smart material. The joints/fasteners must be compliant to allow continuous movement of the smart material. Elastomeric structures can be joined by plasma bonding or adhesives. Other electroactive materials may be employed to create tunable joints such as shape-memory fibers [278]. Reversible attachment may be achieved by incorporating magnetic particles into the silicone matrix to form magnetic elastomers [279]. Forming modular smart materials would require careful design of the electronic and fluidic connections to ensure that the actuator modules function independently as well synchronously.

This technology can be developed to create shape-changing "smart" materials consisting of arrays/stacks of multiple actuators in an elastomeric matrix, such that each actuator module can be individually controlled to deform in specified directions [280] (Figure 95).

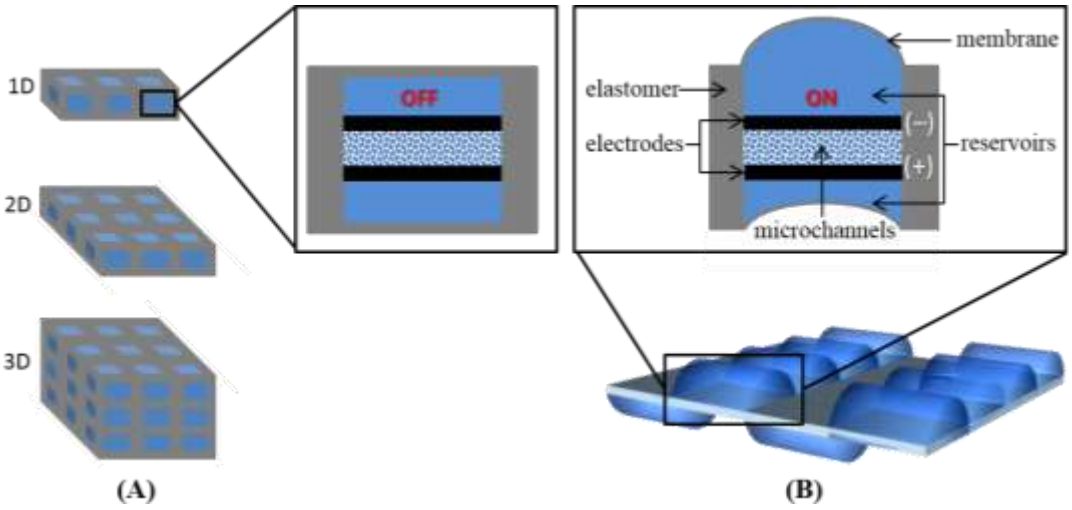

Figure 95. Actuator units comprising reservoirs, channels, and electrodes can be combined in various configurations to create "smart" structures. Each actuator unit would be addressable with an analog voltage, so the structures will be able to take on a variety of shapes.

The direction of actuation could be controlled by varying the magnitude and direction of the applied electric field to deform continuously from one shape into another shape. The regions of deformation by the EO force could be further defined by incorporating flexible but non-stretchable materials (such as paper, cloth, some polymers films such as parylene, metal foils, etc.) around the elastomeric structures. Different types of deformations such as bending, twisting, shortening, lengthening, and could be achieved by modifying the form factor of actuator cells. This would involve evaluating a) how to best place and shape channels, reservoirs, and electrodes to achieve desired shapes; b) how to actuate them to achieve desired shapes; and c) how to trade off stress, strain, speed against external loads.

7.3.1.3 Integrating Rigid Structures with Actuators

Shown below in Figure 96 and Figure 98 are illustrations of how electroosmotic actuators can be integrated with more rigid materials to achieve various reversible bending motions.

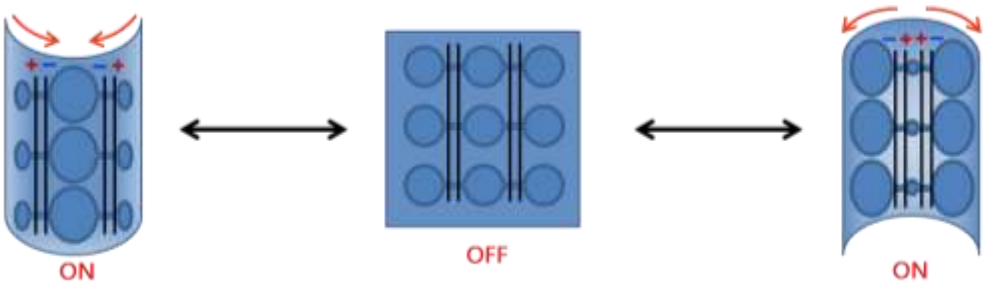

Figure 96. Design for a curling actuator. Actuators can be fixed to a thin flexible but inelastic substrate like paper or plastic transparency. The substrate can then be caused to roll up when a voltage is applied; the direction and extent of curling can be controlled by the direction of EO. When the EO is directed towards the middle of the sheet then fluid leaves the edge causes the sheet to curl inwards. Reversing the potential causes the fluid to apply pressure on the edges of the sheet causing it to bend outwards.

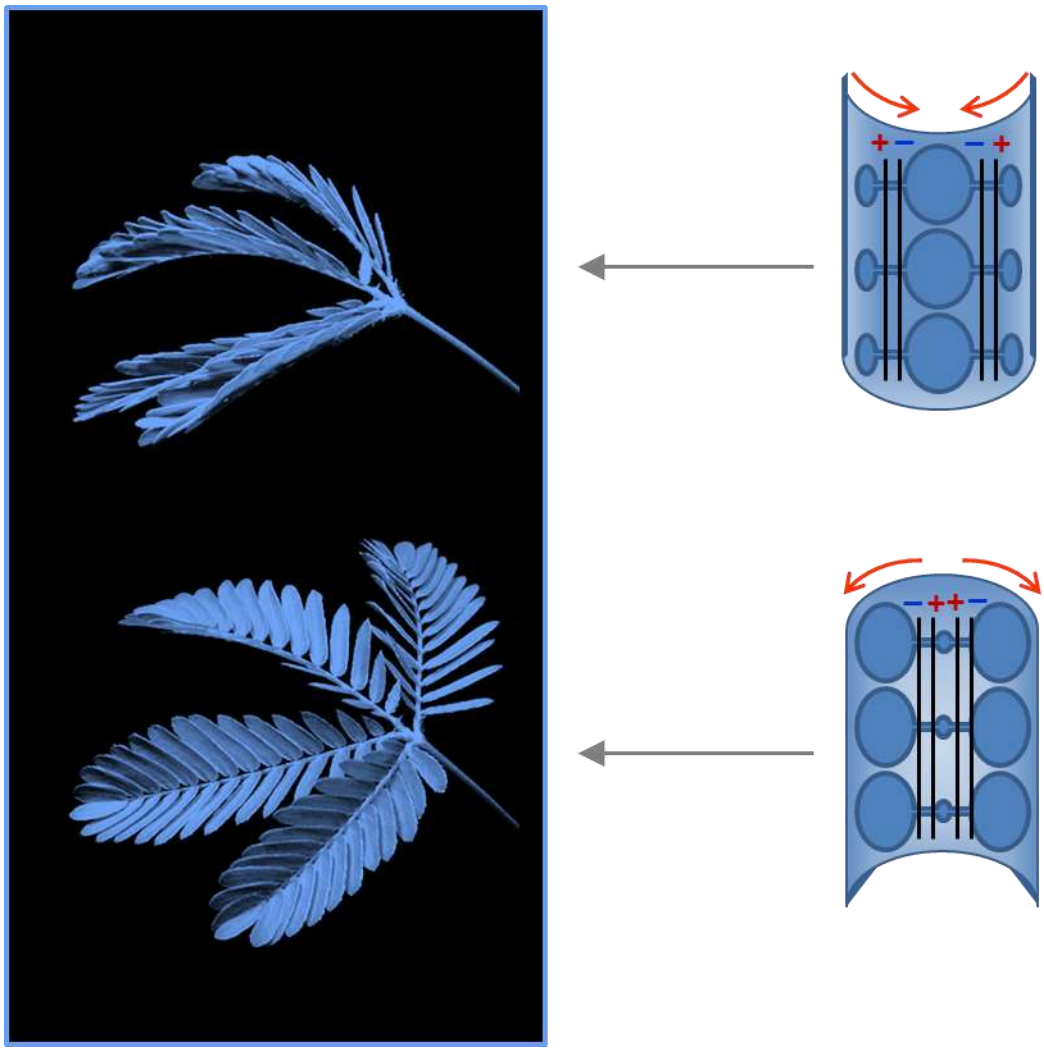

Figure 97. Mimicking plant movements with actuator cells driven by electroosmosis. Elastomeric leaf-shaped actuators, with embedded electrodes and fluid, can be made to open or close by modifying their turgidity using EOF to exhibit plant-like motion. This can enable plant-inspired solar-powered robotics.

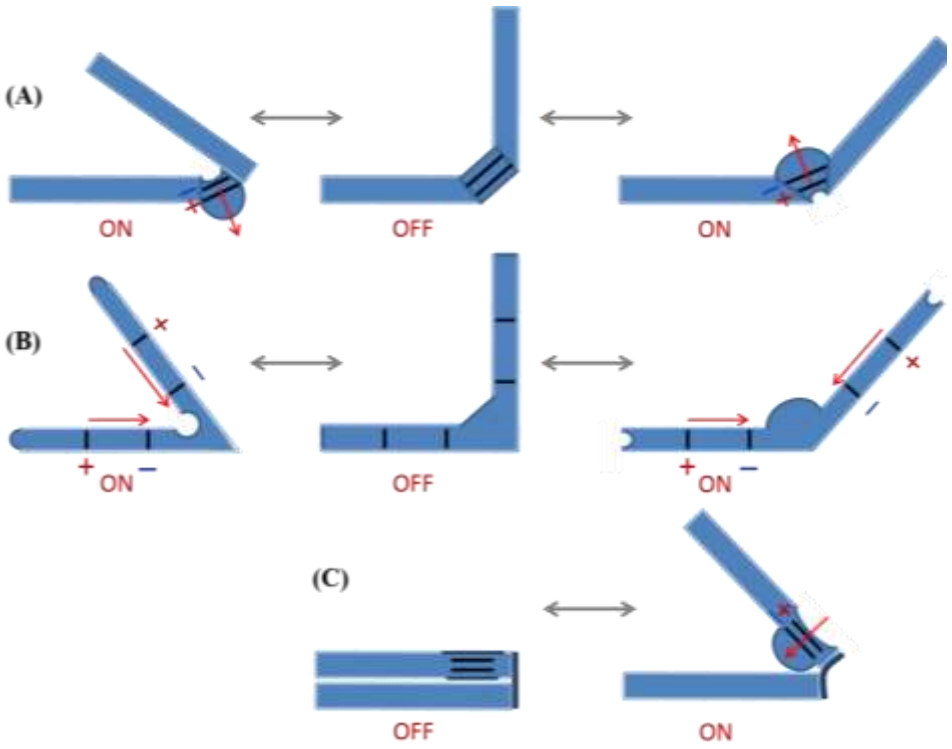

Figure 98. Designs for limb joints actuated by EOF. The angle of the joint can be varied by changing the magnitude and direction of the applied electric potential. (A) The actuator is located at the joint. It is fluidically and electrically isolated from the adjacent rigid limb segments. The electrodes and the pumping fluid are located within the actuator. (B) The actuating membrane is located at the joint. The pumping liquid is stored in rigid limb segments that are hollow. The electrodes are embedded inside the limbs to transport liquid towards the actuating joint. (C) Hollow rigid limb segments filled with pumping liquid are connected by a passive flexible hinge. The hinge can be bent by actuating the membrane located on one of the limbs. The electrodes are placed in line with the actuating membrane to transport fluid in the direction of actuation.

7.3.1.4 Actuators with Cylindrical Form Factor

For certain biomimetic applications it is desirable to use cylindrically-shaped actuators, such as those inspired by the design of animal structures like the hydrostatic skeleton of invertebrates or muscular hydrostats like tentacles, tongues, and trunks. Figure 99 and Figure 100 illustrate how to design electroosmotic actuators with a cylindrical form factor. These cylindrical designs can be further developed to form contractile actuators by integrating bellows and McKibben-type structures [281].

The device may pre-formed in a flat format (by applying the processes described in the thesis for making paper-based EO actuators), and later rolled to form the cylindrical shape. Alternatively, the channels and electrodes may be formed directly inside a cylindrical structure. The cylindrical tube can be made by coating a cylindrical structure with silicone (or any other polymer of choice), or else commercially available flexible tubing can be used. The carbon electrode paint can be painted on the outside of the tube, and then the tube can be turned inside out. Instead, the electrodes can also be pre-formed and inserted as ring electrodes (Figure 93A and Figure 93C), porous electrodes (Figure 93B), or slabs (Figure 93D). Similarly, to form the channels pre-formed porous materials can be inserted between the electrodes. The inserted electrodes and channel layer may be held in place by applying a thin layer of adhesive around their periphery before inserting them.

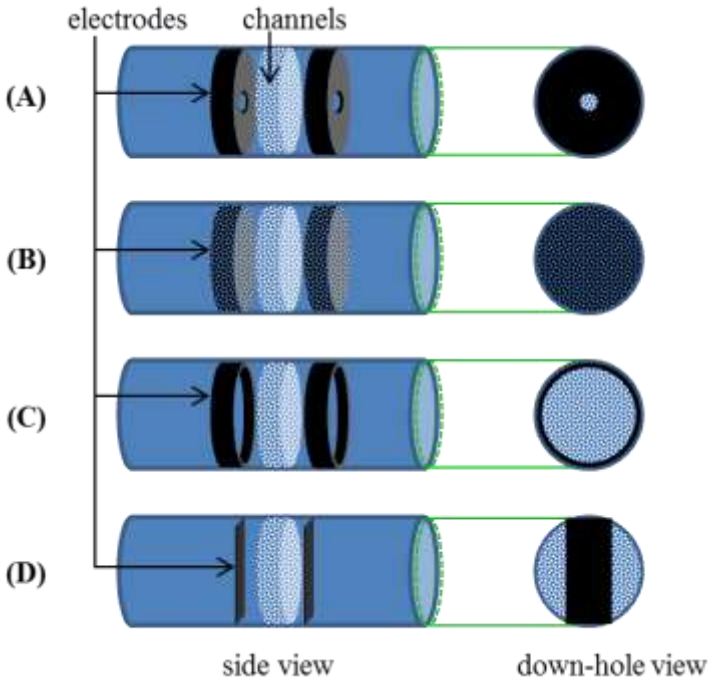

Figure 99. Design options for creating cylindrical actuators.

In the tubular configuration, it may also be able to evaluate different channel configurations to employ both EOF and the macroscale electrohydraulic flow effect that I observed in mm-scale tubes (refer Section 3.6.5 and Appendix F). If the microchannels are formed within a porous disk positioned between the electrodes, it is likely that EOF will be the dominant mechanism. In order to combine the forces from the mm-scale electrohydraulic flow effect with EOF, it might be valuable to incorporate ridges that run along the length of channel, or a porous foam onto the inner surface of the tube.

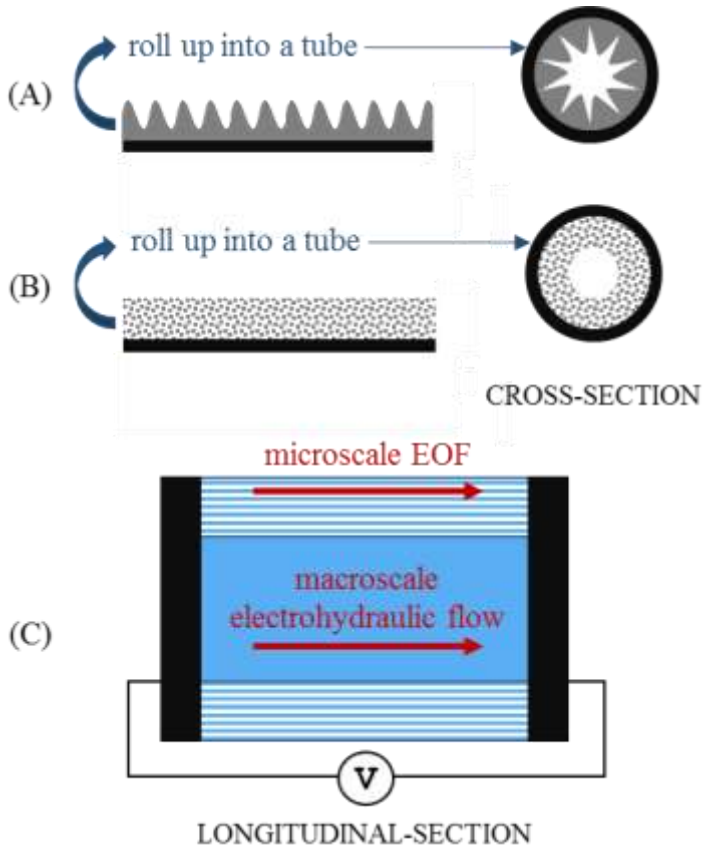

Figure 100. Design the tube for fast flow. (A) A sheet surmounted by a corrugated layer can be rolled up to form a tube with ridges that function as microchannels for EOF. (B) A sheet surmounted by a microporous channel layer can be rolled up in to a tube. (C) These designs would enable fluidic pumping along the length of the tube by both microscale EOF and macroscale electrohydraulic phenomena.

7.3.2 Materials and Methods

In addition to the methods described in this thesis, there are several other methods that could potentially be applied to fabricate multi-scale, high-aspect-ratio soft robots. The present work describes a fabrication process that involves casting silicone over patterned

molds, and the laminating the cured layers to form the EO actuators. In order to augment this work it would be valuable to employ rapid prototyping methods such as 3D printing, laser ablation, injection molding, stereolithography, and CNC machining. Presently, most machines show poor performance with machining popularly used silicones like PDMS. Newer 3D printers are now able to print elastomers of comparable compliance, although there is little information available about the chemical composition of these materials because they are proprietary. In the present design of the device the elastomer only serves a structural purpose and does not actively participate in EOF. However, to be suitable for forming EO actuators it is essential that the elastomer is able to demonstrate chemical resistance to PC. For laser-ablation patterning of the device layers I was able to contact the company Potomac Photonics in Baltimore, where they are able to create high resolution 3D micro-features in PDMS and other elastomers using Nd:YAG lasers instead of CO_2 lasers.

7.3.2.1 Channels

As discussed in the introduction, to obtain better actuation it is necessary to increase the EOF mobility ($\mu = \varepsilon\zeta/\eta$) and *E,* and to have a large cross-sectional pump area. In theory, increasing the zeta potential should increase actuator force. There is little information about the chemical nature of the electric double layer when pure PC comes in contact with a solid wall. In PC, the ionization of the surface is likely driven due the ability of PC to extract protons from neighbouring molecules, causing the channel wall to acquire a negative surface charge.

It is expected that the zeta potential of the double layer could be increased by attaching charged functional groups to the surface of the solid walls contacting the PC. Surface functionalization provides the capability to control the channel properties to direct the EO flow. For example, researchers have been able to achieve high electroosmotic pressures by cascaded pumping through channel sections with alternating positive and negative zeta potentials [108,238]. A design plan based on this approach is shown in Figure 101.

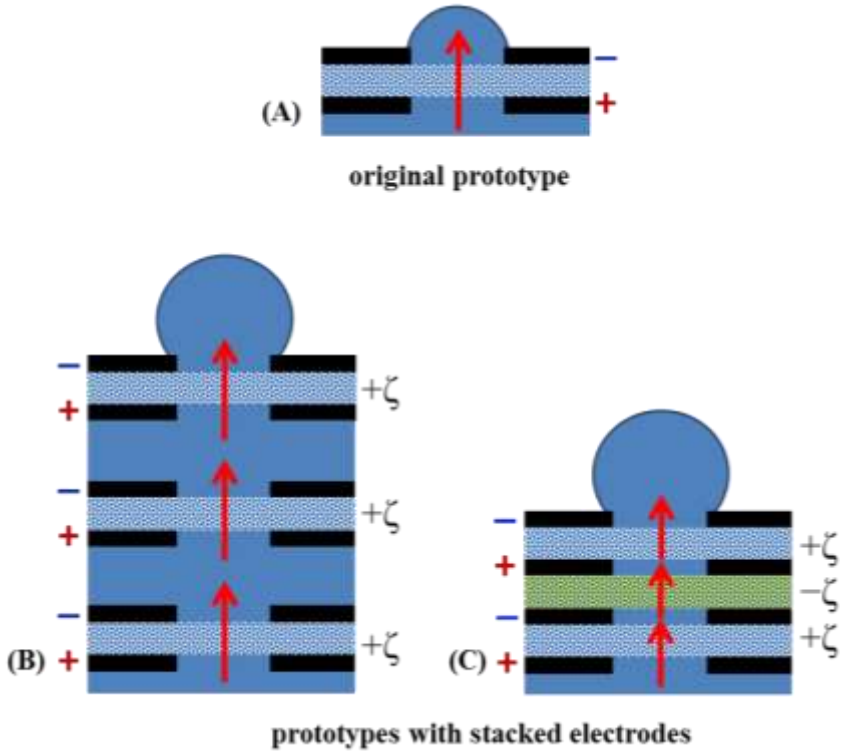

Figure 101. Design for devices with cascaded pumping regions. (A) The original prototype has a single layer of microchannels for EO pumping. The magnitude of actuation force can be increased by stacking pumping layers as shown in (B). In this design it would be required to provide each pumping layer a unique pair of electrodes. Successive electrodes can be employed if the materials with opposite zeta potential polarity are alternated as shown in (C).

The standard methods of surface functionalization of polymers are by silane treatment [282,283], polyelectrolyte layer-by-layer charge deposition [284], or by UV-crosslinking charged monomers [190,285]. I have been able to apply these methods for surface functionalization of PDMS channels (see Chapter 0), but it is expected that they also be able to increasing the surface charge of cellulose channels in paper. Additionally, there

are other methods by which the surface-charge of cellulose-based materials have been reportedly enhanced, including coating with polypyrrole [286] and by oxidation [287].

EOF can be further increased by incorporating a higher density of smaller micro/nano channels. The minimum size of EOF channels is determined by the size of the electric double layer. If the channel is too small it will cause the double layers of the top and buttom surface of the channel to overlap and distort the flow and the defining equations for EOF will no longer apply. There are several theoretical papers describing this [288,289] but there is no experimental data on the EO flow profiles in nanochannels. The thickness of the Debye layer is at the solid-liquid interface with PC is unknown, but based on the data available for pure, salt-free polar solvents, the minimum size for a channel would be 100 nm. One must also take into account the surface tension at the PC-channel interface, which can make it easy/difficult to fill the channels based on the affinity of the solid material for PC. For example it is much harder to fill PDMS microchannels (unless using organic liquids like alcohols, acetone, hexane, chloroform etc.) than it is to fill paper microchannels of the same size, because PDMS is highly hydrophobic. Unmodified PDMS channels often require application of vacuum to eliminate the trapped and fill the device. This can remedied by oxygen-plasma treatment before fillin. In contrast, paper-based channels readily wick a wide variety of liquids and the air is quickly displaced during the wicking process without the need for any vacuum application.

Presently, the device has only one sheet of filter paper as the EO channel layer. A logical next step would be to increase the number of layers of paper into the same area of the device. Stacking horizontal sheets on top of each other could make the device stiffer. Arranging vertical sheets of paper side-by-side would minimally compromise device flexibility. This may be easily done by folding/creping the paper, accordion-style, along the length of the device. Three-dimensional foams [290] and aerogels [291] have also been created from cellulose nano-fibrils by disintegrating paper. It would be important to choose a mechanical method of breaking down the paper into nano-fibrils, rather than a chemical manufacturing process, to avoid introducing ions into the paper (because the ions can become dissolved in the PC and cause electrolysis).

Cellulose acetate has been used for decades by biologists for electrophoretic applications and therefore could be valuable for creating flexible EO actuators. From a fabrication perspective, this may be a useful material to explore for EO actuators, provided it is chemically compatible (not degraded) with PC. Cellulose acetate has reportedly been used to create 3D printed structures, by dissolving it in acetone and extruding through a nozzle [292]. Thus, it may be possible to create 3D mesh structures for use as EO channels.

Microspun channels have found to be useful for microfluidics applications. [239]. Other materials that are chemically resistant to PC (such polyethylene, polyurethanes, polypropylene, rayon, glass wool etc. [293]), may be formed into 3D porous structures for EO channels. These materials are readily commercially available in various pre-

formed porous formats, and can be easily formed into woven, felted, spun (by electrospinning), fabrics and formed into 3D foams/sponges. Multiple pumping zones can be patterned in microchannel sheets by infusing the material with a photoresist, wax, or thermoplastic that can be patterned by application of light or heat. This will form non-porous boundaries for the channel zones, so that each zone can be discretely addressed.

To evaluate the applicability of the theoretical EOF equations (see eqns 1 and 2 intro), one needs to know the number of channels present in the porous materials. This would require measurement of the porosity of the channel matrices, perhaps by using a Gurley Densometer. It would be valuable to experimentally validate the findings of numerical studies that predict the electroosmotic flow profile in microcapillaries [294-297].

7.3.2.2 Electrical Connections

It has been observed that a face-to-face electrode layout is best suited for EOF. However, this would limit the flow past the electrodes, which would be in important in designs where multiple electrodes are needed for cascaded pumping. This can be resolved by using perforated electrodes. Perforated carbon electrodes can be formed by applying the carbon paint onto a mesh frame (Figure 102). Also, slits or holes can be cut into cured carbon electrode films using a punching or cutting tool.

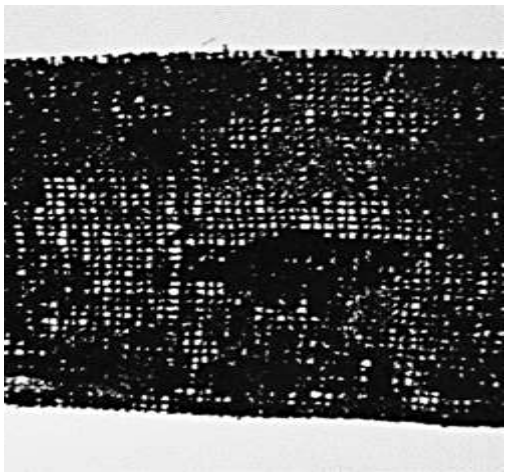

Figure 102. C-PDMS painted on cotton gauze to form a flexible mesh electrode.

Although fluidic tethers have been eliminated, the actuators are still tethered to the power supply. To realize an autonomous actuator a battery and a control chip must be mounted on the device, which connects to the elastomeric carbon electrodes. The advantage of using the carbon-silicone composite is that conductive traces covering the step height between the chip and the actuator electrodes can be patterned by painting or deposition with a dispensing nozzle. This process can be used to connect the mounted power chip and to the neighboring actuator modules, akin to wire bonding. I have found that conductive line traces can be patterned on PDMS substrates by dispensing the carbon paint with a syringe fitted with an 18 gauge needle. Therefore, it should be possible to apply well-defined traces using an automated nozzle-type tool. Additionally, the carbon electrodes may be interfaced with other types of flexible electrical connections including liquid metals (gallium-indium alloys) [298] and carbon-nanotube-based fibers [299,300] to create connections between neighbouring actuator units outside the pumping area. Also, new conductive paints can be formulated and tested for EOF by replacing the

carbon nanoparticles in the paint recipe with other materials such as platinum black powder.

Like most electrical phenomena, it should be possible to achieve both sensing and actuation modes in the electro-nastic devices by reversing the type of stimulus energy; i.e. instead of applying an electric field to cause mechanical force for actuation the system could be subjected to a mechanical force to achieve an electrical signal. It has been found that such a reverse phenomenon of electroosmosis does exist; a "streaming" current (or potential) can be produced in a system by applying a mechanical pressure gradient across the fluid-filled channels [301]. The resulting pressure-driven convective flow exerts a force on the electric double layer which results in electron flow (electric current) that is proportional to the pressure gradient. This phenomenon can be employed to achieve pressure sensing as well as actuation using the same soft device.

7.3.2.3 Pumping Liquid

More research is required to mitigate moisture-induced PC damage to increase actuator longevity. First, a moisture-barrier coating must be applied around the device because PDMS and Ecoflex silicones are permeable to gases [70-72,302]. Parylene [303], polyaniline [304], and metal/oxide coatings [305] have been used as moisture barriers. To allow stretchability of the actuating membrane and to prevent cracks in the moisture barrier, it may be required to pre-stretch the actuator membrane during the coating process. Second, a non-ionic moisture-scavenger material may be added to the PC that

can absorb the moisture before it damages the PC. However, I have not found this to be a practical long-term solution because it is mass-limited by the amount of absorbent available, which would require increasing the device dimensions in order to accommodate the absorbent particles.

The temperature of the actuator system must be measured during operation to investigate Joule heating effects on EOF. Although the currents through the system have been small (μA) parasitic Joule heating may still be occurring near the electrodes that could potentially affect PC chemistry over a long operation times. In addition, it is necessary to quantify possible electrothermal flow phenomena that can occur if there is a temperature-gradient induced by the electric field [306], which could enhance or inhibit EO flow.

Further studies of electroosmotic flow in salt-free organic solvents are needed. Based on the literature and this work it is clear that different flow phenomena dominate at different channel sizes, electrode geometry, pumping fluid chemistries, and applied electric fields. There is much scope for research to understand the structure of the electric double layer and the charge transport processes that result in mass transport in non-aqueous liquids, at large applied electric fields. PC is a polar aprotic liquid meaning it cannot release protons (H^+ ions) to a neighboring molecule but it can accept a proton, which may be released by dissolved impurities (such as water) or by molecules on the solid surface of the channel walls. It is worth testing measuring the pH of propylene carbonate; because it does not have ions it is expected to have a pH of 7. It is to be investigated if trace amounts of impurities in PC, such as water, play an influential role in enabling

electrokinetics. It has been reported that zwitterions can be added to increasing the dielectric constant, without raising the solution conductivity [307]. Experiments should be performed to see if EOF can be increased by adding zwitterions to PC.

There are many non-aqueous liquids cited in the literature as alternative pumping liquids for bubble-free electrokinetics (such as DMSO and acetonitrile) [308] which may have comparable EDL properties to PC for EOF. But the cyclical carbonate family of liquids appear to be better suited (than the cited liquids) for actuator applications due to their low volatility, non-toxicity, high dielectric constant, and stability when to subject to large electric fields. Another liquid in this family that should be evaluated for EO actuation is ethylene carbonate (EC) which has a higher dielectric constant than PC, and is favored in battery applications [154]. EC was not tested during this work because it is solid at room temperature. However, it has been found to liquefy when mixed with linear carbonates such as dimethyl carbonate (DMC) as well as with PC. EC melts at 37^{o}C so it may be possible to take advantage of parasitic Joule heating that may occurring when an electric field is applied may be able to liquefy the EC. This would confer a unique device attribute that has not been possible with PC so far, which is to reversibly solidify the pumping liquid. Warm EC could be dripped into a chilled reservoir/mold to form various solidified shapes of EC, which could then be encapsulated by film casting of the membrane over the solidified EC. Application of an electric field would then cause EC to melt by Joule heating to enable EO actuation of the custom-shaped membrane.

7.3.2.4 Membrane

The membrane in the latest prototype is formed by film casting the liquid elastomer over the pumping liquid and then curing it (see Chapter 6). This membrane is pinned around the edges to the inlet hole, and it forms a small dome when actuated. In order to increase the extent of deflection, it would be useful to increase the surface area of the actuating membrane. An approach for making a larger membrane (depicted in Figure 103) is to stretch the inlet hole over which the film is cast. This way a larger conformal film is formed over the liquid with no trapped air pockets. The membrane must be cured in this stretched state, so when it is released it causes the membrane to form wrinkles/corrugations that enable larger strains.

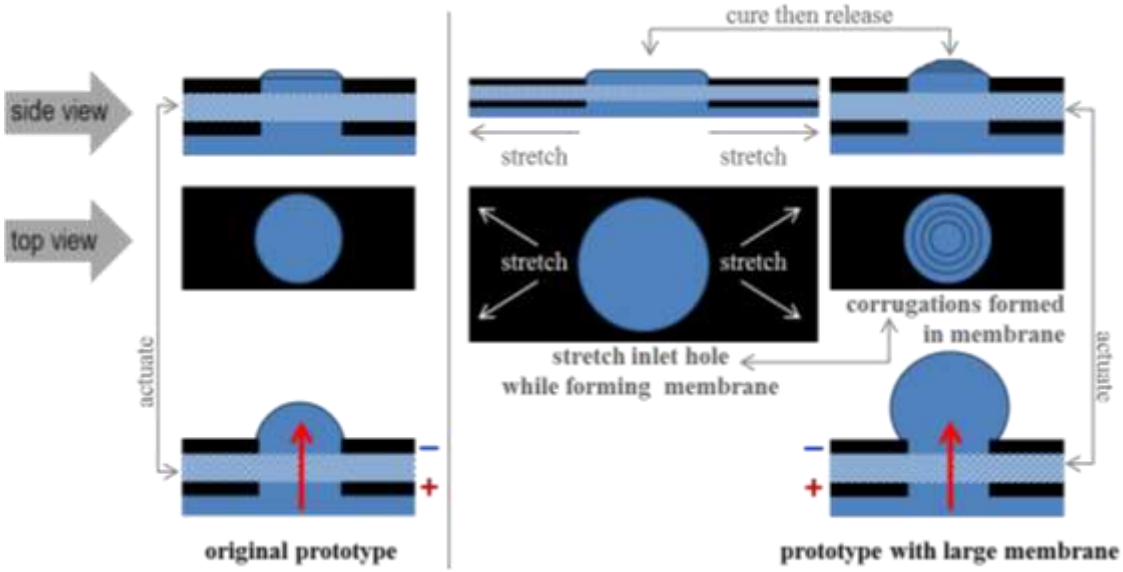

Figure 103. Illustration of fabrication process for making membranes that can undergo larger strains, by increasing membrane area.

Alternatively, the membrane can be formed in different unfurling shapes that show more dramatic change in shape like balloon, umbrella, accordion, or other origami-inspired shapes. The membranes can be formed by applying a thing coating on a mold. The formed membrane could be peel off the mold, or the mold could be made of a material that could be dissolved in order to avoid subjecting the membrane to peeling forces. The membrane could be affixed to the device by plasma bonding. Following plasma treatment, the device could be then filled from the supply side instead of expansion side. Then the supply side can be encapsulated by film-casting silicone, as previously described. Photocurable elastomers compatible with PC could enable hastening the encapsulation process, which presently uses thermally-cured silicones.

7.3.3 Modeling

Design inspiration can be sought from biological structures that are able to transmit hydraulic forces to dexterously perform load-bearing tasks by strategically combining stiff supporting structures with soft deformable structures. It would be beneficial to understand how plants and animals move [30,309], and apply mathematical models that can predict the dynamics of structures that are able to deform continuously.

Soft structures often undergo large continuous deformations, and theoretically have infinite degrees of freedom. This is difficult to model because the materials are highly compliant with nonlinear dynamics. Contact mechanics and adhesive forces strongly

affect the interaction of soft structures with their environment [310-312]. Modeling the electroosmotic actuator would be a multiphysics problem involving fluid mechanics, electro-fluidic interactions, solid mechanics to predict material deformation, and energy transmission analyses. Although the basic aspects of EO flow are understood models of EOF must take into account coupled electrochemical and electrohydraulic phenomena that can occur in EOF systems.

Optimization of the device dimensions would enable understanding the trade-offs to maximize actuator stress, stroke, and speed. The shape, size, and relative positions of reservoirs, electrodes, deflecting membrane can be adjusted to minimize backpressures but maximize EO, while minimizing external power requirements. Finally, simulations could determine how the actuator modules would behave when joined together in various 1D, 2D, and 3D formats.

8. **Intellectual Contributions and Products**

Several results from this research hold value for the microfluidics and soft robotics communities dealing with the topics of electrofluidics and additive/subtractive manufacturing with soft materials.

- It was demonstrated that electrolysis-free electrokinetics can be achieved using PC.
- Electroosmosis using PC was characterized, and it was concluded that PC can be substituted for water in existing EO devices for bubble-free operation.
- Soft porous materials were shown to be better suited for EO soft actuators, compared to conventional micromolded channels, because they are inherently composed of high density three-dimensional microchannel networks.
- A method was developed to fill and encapsulate the pumping liquid without tubing.
- It was established that elastomeric carbon-silicone composites can be used as electrochemically stable electrodes at thousands of volts.
- A new benchtop process was developed to fabricate fully sealed soft fluidic actuators, by the layer-by-layer assembly of paper, silicone and carbon composite materials.
- Electroosmotic pumping and the fabrication techniques developed in this work are amenable to forming sheets of actuator arrays.

The potential impacts of these results are summarized below.

1. Bubble-Free Electrokinetics

To create an actuator based on DC electroosmosis I had to eliminate electrolytic gas formation, because bubbles lead to short device lifetimes and inconsistent pumping. For this, I replaced water with PC as the pumping fluid and demonstrated bubble-free electroosmosis in a closed actuator. Thus far, DC EO systems typically use water and are open systems or have large headspaces to vent the electrolytic gases. For continuous operation of these devices, the fluid depleted by electrolysis must be constantly replenished from an external source. In contrast, PC does not generate gas up to at least 10 kV. It was demonstrated that Due to the electrochemical stability of PC it was possible to use non-inert electrodes, like galvanized steel, for EOF. With water, this is inconceivable because of its corrosive electrochemistry. It was established that the purity of the PC was crucial for maintaining pumping efficiency; the presence of salt or moisture in PC resulted in reduced electroosmosis and led to electrochemical degradation. These findings are useful for a wide range of electrokinetic technologies that require bubble-free operation.

2. Characterization of PC Electroosmosis

The electroosmotic flow of PC was characterized in PDMS and paper microchannels. It was determined that the flow rates for DI water and PC within PDMS microchannels were similar. The zeta potential of PC in PDMS was calculated to be twice that of water

in PDMS. Replacing water with PC in the PDMS microfluidic prototype device increased the actuator's load capacity by an order of magnitude, likely due to the elimination of the compliance introduced by gases from water electrolysis. It was inferred that PC-based EO pumps consume less power than water-based EO pumps, because at a given voltage, the current was three orders of magnitude smaller PC than in DI water. The paper actuator was able to lift twice the load that could be lifted by the PDMS microfluidic prototype actuator, and EO actuation was an order of magnitude faster.

3. Hydraulic Actuators Using Paper and Other Porous Materials

Increasing the number of microchannels while decreasing their individual size was necessary to create an actuator that can generate high pressures with fast actuation (see Equation 1 and Equation 2). Using porous materials in lieu of microfabricated channels is beneficial to create 3-dimensional microfluidic devices. It is challenging to achieve a flexible channel network by conventional microfabrication techniques, so instead I used flexible porous materials that are inherently composed of three-dimensional channel networks. In this work the structural, wicking, and porous properties of paper were employed to produce the first paper-based electrohydraulic soft actuator: I showed that paper was a well-suited material for electroosmotic pumping; the structural properties of paper (paper can bend but not stretch) were used to define the direction of actuator deformation.

I demonstrated that, apart from paper, woven or spun fabrics composed of cotton or polyethylene, and open-celled polyurethane foams, can also be used for electroosmotic pumping of DI water and PC. These materials have similar structural flexibility to paper, and I determined that it was possible to machine these materials using similar benchtop processes to create functional actuators. For further information refer Appendix D.

4. Liquid Filling and Encapsulation

A tube-free filling and encapsulation technique was developed which can be useful for creating closed micro/nano-fluidic systems. The inlet and outlet tubes used for filling microfluidic channels typically protrude out of the device. In actuator applications these tubes can prevent device integration and affect motion. Tubing was eliminated by filling the device using capillary forces (paper readily wicks liquids, PDMS wetting was enabled by oxygen plasma surface activation). Conventionally, thin polymer membranes are usually fabricated by spin coating the uncured polymer liquid on a flat substrate. The film is the cured and attached to the device by plasma bonding. Following this the device is filled with the liquid. This can lead to pockets of trapped air, in corners of the channels and the reservoirs, which are often difficult to eliminate. In this work, a novel liquid encapsulation method was devised, which involves directly casting a film of polymer over the liquid filled channels and reservoirs. In addition to sealing the liquid, the silicone skin formed over the liquid served as the actuating membrane, and was able to undergo large deformations (hundreds of μm) and endure the operating pressures of the

actuator (kPa). This is a new approach of forming in-situ membranes, which can be useful for a variety of polymeric actuator and microfluidic devices.

5. Elastomeric Carbon Electrodes for High-Voltage Electrofluidics

Robust flexible electrodes for high-voltage microfluidics were created with carbon-silicone conductive composite paints. C-PDMS and C-Ecoflex were found to be electrochemically stable in PC as well as DI water at high voltages, and they retained their conductivity under strain. These electrodes can be employed in a variety of devices that require flexible structures and involve high voltages in fluids. The conductive composite can be easily incorporated into soft, irregularly shaped devices because it can be applied like paint on a variety of surfaces, or formed into stretchable films that can be cut and shaped. C-PDMS can be incorporated into devices formed by standard PDMS soft lithography; it is possible to shape the paintable carbon electrodes in the same mold as the channels and reservoirs to create electrodes embedded in PDMS. C-PDMS electrodes can also be attached to PDMS devices by conventional oxygen plasma bonding. Standard cleanroom metal-deposition processes like sputtering, thermal, and e-beam evaporation are best suited for planar devices with less than 10:1 (height:width) aspect ratios. Paintable carbon-silicone electrodes are better suited for forming high-aspect ratio flexible electrodes (mm-scale) in three-dimensional soft devices. Additionally, it was observed that the carbon-paint electrodes were more stable than metal electrodes microfabricated on silicone (which peeled and cracked in the presence of liquid; see Appendix C).

6. Layer-by-Layer Fabrication Using Flexible Materials

The layer-by-layer device assembly process was formulated specifically to incorporate paper microfluidics into the elastomeric device. A key feature of this process is that there is no need to devise a bonding process to fix the microchannels to the silicone device, and the porous channel layer can be fixed simply by sandwiching it between the two electrode layers. This eliminates the challenges involved in plasma-bonding or adhesive-based bonding of materials with rough surfaces like meshes, fibrous materials, and foams to silicones. This enables the use of a variety of materials with various surface and chemical properties, as long as it is chemically resistant to PC. I used a benchtop machine to cut out or score intricate patterns by controlling only a single parameter which was the cutting pressure of the blade tip. Soft materials that I patterned include silicone and latex thin films as soft as skin, paper and cardboard, delicate tissue paper, fabrics, craft foams, vinyl sheets and adhesive tapes, and metal foils. The soft robotics community will find low-cost benchtop craft cutting machines to be a valuable addition to their subtractive manufacturing resources. In addition, the fabrication processes developed in this work make the large-scale production of electro-nastic actuators amenable to low-cost roll-to-roll manufacturing.

7. Electroosmosis: A New Actuation Paradigm For Soft Robotics

Electroosmotic pumping using propylene carbonate was shown to be useful for creating closed pumps that can operate on small fluid volumes. The materials and methods used in this work enable a variety of miniature, fully flexible electrofluidic robots, which has

thus far been unattainable due to the difficulties in fabrication, liquid encapsulation, and preventing electrochemical degradation. It is envisioned that the design and layer-by-layer fabrication process developed in this work can be useful to develop a roll-to-roll process for manufacturing of electroosmotic actuator units. The actuators could potentially be combined modularly in various configurations to form shape or texture changing sheets. This type of modular soft robotic design is uniquely enabled by electroosmosis: by using soft porous materials as microchannel matrices that can be cut and shaped, it is possible to make actuators in various form factors. Using porous matrices instead of conventional planar microfabricated channels enables scalability of EOF devices. The actuators can be also be affixed to substrates with wavy or irregular topographies. Furthermore, the actuators may be fabricated in a cylindrical form factor by inserting porous channel matrices within tubular structures for creating artificial muscles. Using EOF, fluid can be displaced over several centimeters without the need for special electrode geometries, which are required if employing electrowetting or electrohydrodynamic flow. This work demonstrates that electroosmosis can produce high force as well as large stroke in fully flexible devices. It is anticipated that this work on electroosmostic actuation will significantly contribute to the advancement of soft robotics.

Listed below are the products that resulted from this research.

Journal Publications

1. Sritharan, D., A. S. Chen, P. Aluthgama, B. Naved and E. Smela (2015). "Bubble-free electrokinetic flow with propylene carbonate." *Electrophoresis* 36(20): 2622-2629.
2. Sritharan, D. and E. Smela (2016). "Fabrication of a Miniature Paper-Based Electroosmotic Actuator." *Polymers* 8(11): 400.

Conferences

Posters Presented

1. Sritharan, D. and E. Smela (2011). "Electroosmotic Pumping for Shape-Changing Materials." *Gordon Research Conference on Microfluidics.* Waterville Valley, New Hampshire, USA.
2. Sritharan, D. and E. Smela (2015). "Paper-Based Microfluidic Actuator." *Workshop on Enabling Future Health Care: Role of Micro and Nano Technologies*. Napa, California, USA, Napa Institute and Transducer Research Foundation.

Talks Presented

1. Sritharan, D., M. Motsebo, J. Tumbic and E. Smela (2013). "Stable electroosmotically driven actuators." *SPIE EAPAD.* San Diego, California, USA, SPIE Proceedings. 8687. (Peer-reviewed publication)
2. Sritharan, D. and E. Smela (2013). "Electroosmotic Pumping for Shape-Changing Materials." *Annual Meeting for "Mechanics of Multifunctional Materials & Microsystems Program.* Arlington, Virginia, USA, US Air Force Office of Scientific Research.
3. Sritharan, D., M. Bleakney and E. Smela (2014). "Paper-Based Electroosmotic Device" *EuroEAP*. Linköping, Sweden, European Scientific Network for Artificial Muscles.
4. Sritharan, D. and E. Smela (2015). "Encapsulated Paper-Based Electroosmotic Microfluidic Device." *Workshop: Low-Budget, High-Payoff: Techniques/Resources for Innovative Micro/Nano R&D.* Laurel, Maryland, USA, Workshop: Low-Budget, High-Payoff: Techniques/Resources for Innovative Micro/Nano R&D.

Talks Contributed to

1. Smela, E. and D. Sritharan (2013). "Hydraulic 'Nastic' Actuators." *7th world Congress on Biomimetics, Artificial Muscles and Nano-Bio (BAMN).* Jeju, Korea, IOP Publishing.
2. Smela, E. and D. Sritharan (2015). "Hydraulic electroactive polymer actuators." *EuroEAP*. Tallinn, Estonia, European Scientific Network for Artificial Muscles.

3. Smela, E., D. Sritharan and P. Aluthgama (2017). “Challenges in realizing a self-contained hydraulically-driven contractile fiber actuator.” *Chemical Physics of Electroactive Materials: Faraday Discussion*, Cambridge, U.K., Royal Society of Chemistry.

Invention Disclosures

The following invention disclosures were filed with the Office of Technology Commercialization at the University of Maryland.

- Solvent-Free Conductive Carbon-Based Silicone Paint (PS-2014-178)
- Paper-Based Electroosmotic Device (PS-2014-088)
- Liquid Sealed between a Polymer and a Substrate (PS-2013-136)
- Bubble-Free Electroosmosis Using Propylene Carbonate (PS-2012-087)

9. Appendix A: Invention Disclosures

9.1 Bubble-Free Electroosmosis Using Propylene Carbonate (PS-2012-087)

9.1.1 Summary of the Invention

We have found that using propylene carbonate (PC) as the pumping liquid results in high electroosmostic flow (EOF) rates without the formation of gas bubbles.

9.1.2 Introduction

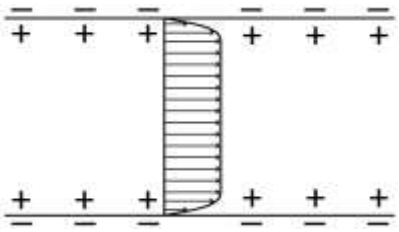

Figure 104. Cross-sectional view of a microchannel, illustrating the fixed charge on the walls, the compensating mobile double-layer charge in the fluid, and the fluid velocity profile.

When an electric field is applied across a liquid in a capillary or microchannel, bulk flow of the liquid is observed. (EO flow is seen in channels ranging in diameter from approximately 100 nm to 0.5 mm, depending on the materials.) This motion is referred to as *electroosmosis* and is caused by electrical forces acting on the ions in the electrical double layer at the channel wall/liquid interface. Electroosmosis has been studied

primarily in the context of capillary electrophoresis. EO is used for electrophoresis because the flow profile is flat, as shown in Figure 104, resulting in narrow bands of the separated species.

In electrophoresis, the elution time of the sample depends on the rate of EOF. The velocity of electroosmostic flow (EOF), v_{EOF}, is linearly proportional to the applied electric field, and it depends on (a) the materials used to construct the microchannel and (b) the liquid in contact with the channel wall:

$$(1) \quad v_{EOF} = \frac{\epsilon \zeta E}{\eta}$$

Higher velocity is achieved by using polar liquids with a high dielectric constant (ε) and low viscosity (η) and by using channels that have a high zeta potential (ζ). The zeta potential varies with the wall material and the pumping liquid.

Aqueous solutions have been the most commonly used pumping fluids. However, at the high voltages used for EOF, aqueous solutions undergo electrolysis and so create large amounts of gas. EOF systems are usually open to the atmosphere to allow these gases to escape, thus preventing their interference with flow in the system. Gas bubbles in the microchannel or capillary result in an electrical open circuit, stopping flow; they can also lead to device failure because they have a strong tendency to become permanently stuck.

We have developed “nastic” actuators [106] based on EOF pumping of water in a closed system. For those hydraulic devices, gas bubbles result in loss of pumping pressure because they are compressible.

9.1.3 Advantages of the Invention

A significant disadvantage of open systems is that the fluid is exposed to the atmosphere, allowing the liquid to flow out if the system is tilted, allowing fluid evaporation, and allowing the entry of contaminants. It has, however, been a challenge to fabricate closed electroosmotic systems because of gas generation. Using PC as the pumping fluid, closed systems have now been realized.

Closed systems would be advantageous as electroosmostic pumps that integrate with microfluidic chips. Closed system EO pumps would be portable and could thus be readily used with multiple devices and device types, or could be employed in hand-held systems. The components of the pump (the working liquid and the electrodes) would be isolated to prevent contamination. Closed EO pumps could enable the smooth, precise pumping of samples that use non-polar liquids that do not exhibit EO flow as well as the pumping of samples that could be damaged by high electric fields (for example, samples containing biological cells).

9.1.4 Prior Art

EOF using propylene carbonate has been studied in the context of capillary electrophoresis, and it was found that the flow rate decreased with salt concentration in PC [156]. High electric fields were used in that study, but the paper did not mention electrochemical effects because their test system was open to the atmosphere.

9.1.5 Reduction to Practice

Based on the literature, breakdown of PC occurs at 5 V [161]. We have discovered that significant breakdown only occurs if salt is added to the PC (Figure 105). No breakdown was observed up to several kilovolts in salt-free propylene carbonate (Figure 106). *This is an unexpected finding* because EOF has been studied primarily for chemical separations, in which the solvent always contains salt.

In plots of current versus voltage (Figure 106), there was only an Ohmic potential drop *and no reaction peaks*, showing that no electrochemical reactions occur. Consistent with this finding, no gas bubbles were observed at fields as high as 5 kV/cm for 15 min. Figure 107 shows photographs of the bubbles seen in water (A, B) versus the lack of bubbles in PC (C, D).

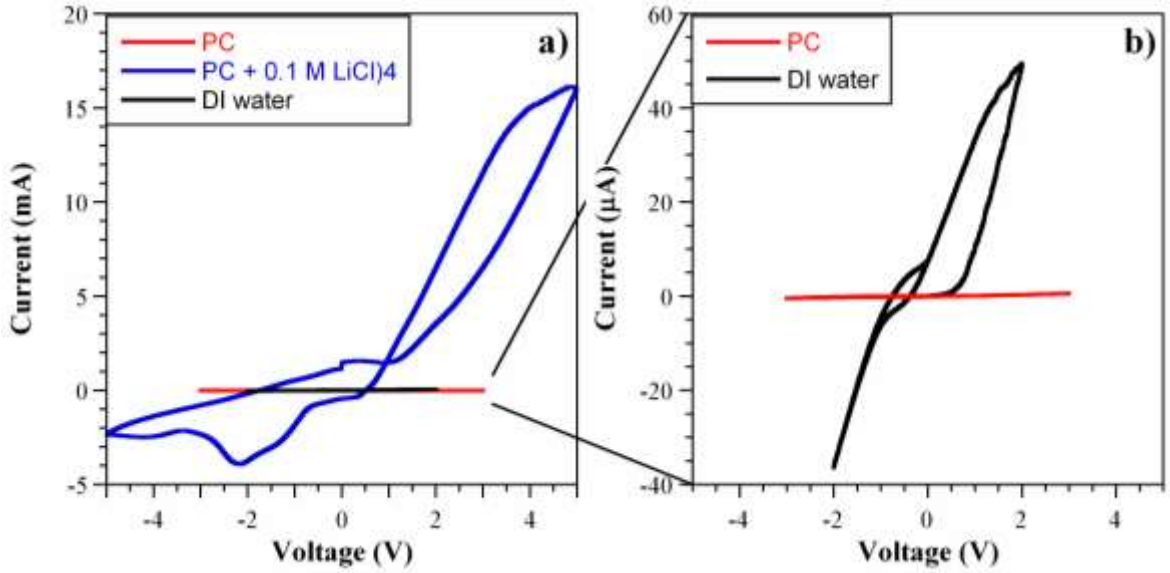

Figure 105. Current versus voltage (at low voltage) for water, propylene carbonate, and propylene carbonate with 0.1M $LiClO_4$. The current when a) salt is added is much higher than b) for solutions without salt.

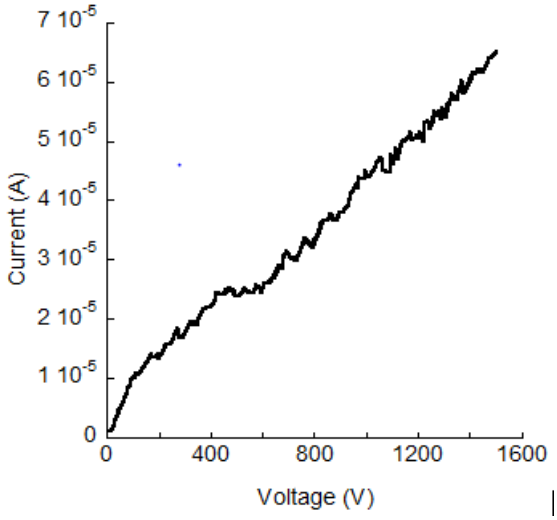

Figure 106. Current versus voltage (at high voltage) for propylene carbonate. (At 1500 V the electric field was 1500 V/cm).

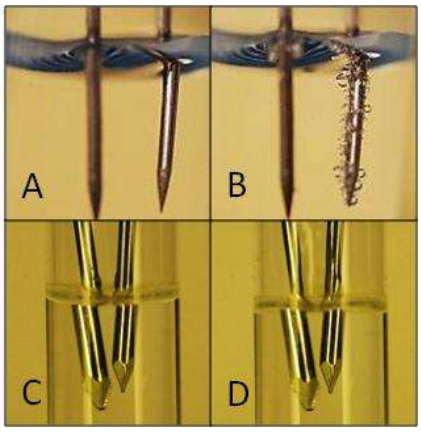

Figure 107. 150 V applied to DI water after A) 0 seconds and B) 5 seconds. 3200 V applied to propylene carbonate after C) 0 seconds and D) 15 minutes. In water, the brown color on the electrodes is due to a deposit. Such deposits are formed in aqueous solutions and in salt-containing PC, but not in PC alone, as is apparent in the lower figure.

EO pumping with PC in an open system is demonstrated in

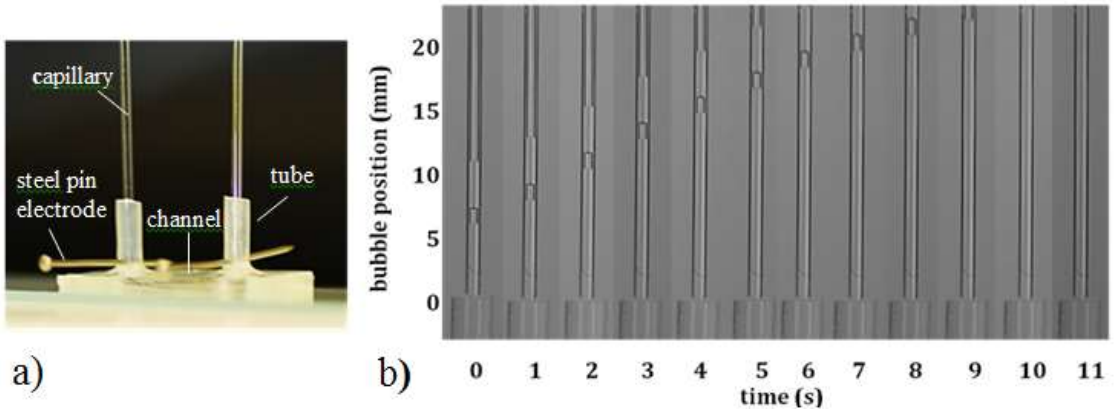

Figure 108. A voltage was applied across the channel, and the fluid displaced at a constant rate over time. EO pumping in a closed system is shown in

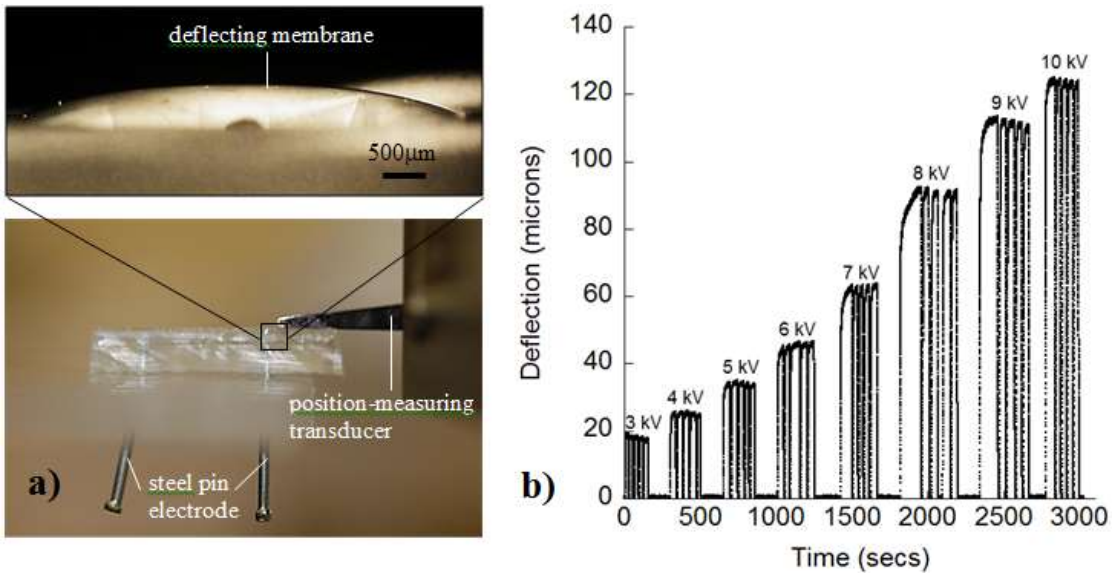

Figure 109. In this device, fluid reservoirs were surmounted by membranes that deflected as the fluid moved. The deflection increased with applied voltage and its amplitude was reproducible.

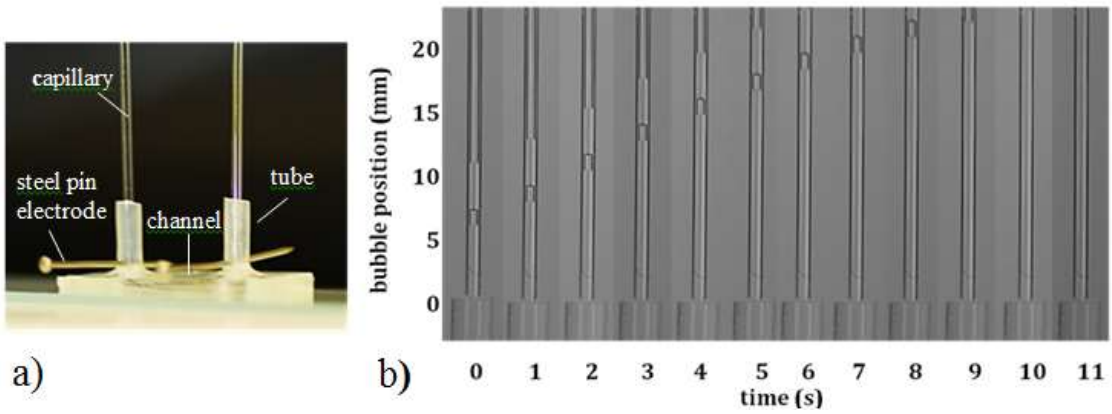

Figure 108. a) An open electroosmotic pump fabricated with the layout of Figure 110. The microchannel is not visible in this view, but is located where indicated. During pumping, fluid rises in one capillary and falls in the other. b) Displacement of the fluid in the capillary is visualized by the motion of the meniscus at the top of the fluid column and also by the air bubble, which was entrapped while filling fluid into the device.

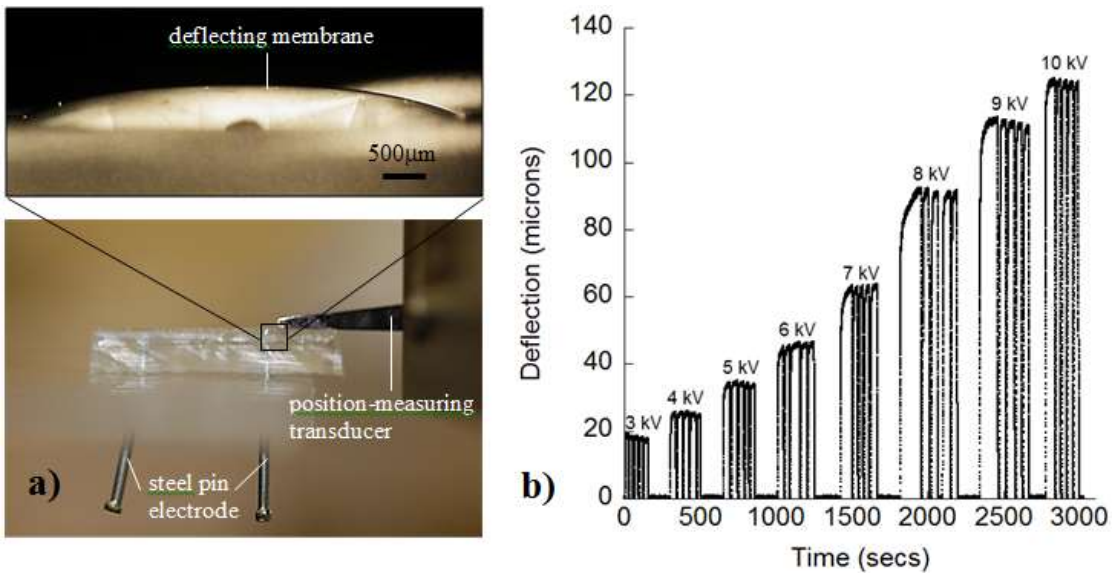

Figure 109. a) A sealed electroosmotic pump with membranes that deflect upon fluid pumping, as in Figure 111. The device comprises a microchannel, supply and expansion chambers, elastomeric membranes that seal the device and deflect as fluid is displaced due to EOF, and steel pins electrodes (inserted into the tubing). b) Deflection versus time as the indicated voltages were turned on and off.

If propylene carbonate is exposed to moisture for some time, it breaks down chemically [313]. These products result in a deposit on the electrodes of the EO device upon applying a voltage, and an increase in the reaction current (decrease in solution resistance) during chronoamperometric measurements. The propylene carbonate should therefore be kept dry before use.

9.1.6 Description of the Invention

The use of the invention is shown schematically in Figure 110. To use PC as a pumping fluid, it is filled into a structure having a small channel (such as a microchannel or capillary), and a high voltage is applied by electrodes connected to a power supply. The use of PC allows the application of high voltage, higher than is typically used in EOF pumping systems, which increases the flow rate and pressure.

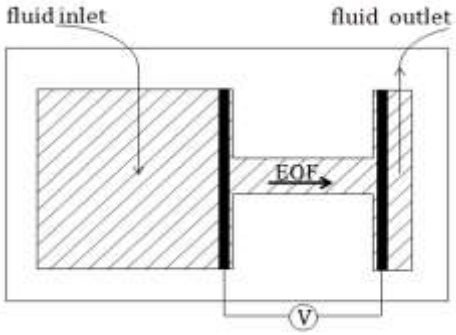

Figure 110. Schematic of electroosmotic pump with fluidic inlet and outlet.

Figure 111 shows the invention in the form of a sealed microfluidic system with two fluid reservoirs connected by a microchannel. Instead of a microchannel, a capillary can be used. To improve the pumping performance, the channel (microchannel or capillary) might be filled with a material (such as a porous polymer monolith or quartz beads) that increases the surface area or decreases the effective channel size. The channel is shown here as long, but it can be short; for example it may be formed be a membrane of porous material or a sieve. The fluid reservoirs might be connected by multiple channels, although only one is shown here. Electrodes are shown on either side of the channel, although they can also be within the channel.

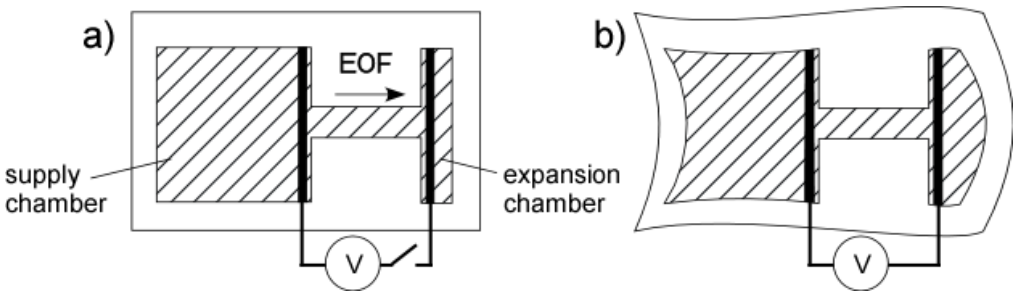

Figure 111. Schematic of a sealed electroosmotic pump. a) No voltage is applied. b) Voltage is applied and the fluid moves from left to right.

A sealed system includes members, for example membranes, that can displace to accommodate the change in volume of the reservoirs resulting from fluid flow. In Figure 111, the device is made from a material that can deform by stretching (an elastomeric material). Such a structure can be used for actuation [106]. The reservoirs are formed within an elastomer, whereby the walls are able to deflect. Additionally, the reservoirs and microchannels are sealed from the surrounding environment, whereby the propylene carbonate is confined within the device and species in the environment are prevented from entering the device. The fluid fills the cell entirely, so that there is no gas-filled headspace.

9.1.7 Possible Applications

There is a demand for microfluidic pumps that can provide smooth, precise flow with minimal fluctuation to replace syringe and peristaltic pumps. Pumps that are currently available in the market use aqueous liquids, which undergo electrolysis. Replacing the

fluid with propylene carbonate should significantly improve pump performance and longevity.

This bubble-free electroosmotic pumping mechanism is well suited for electroactive hydraulic soft robots inspired by muscular hydrostats – biological structures such as tentacles and the elephant trunk. Muscular hydrostats are liquid-filled cavities surrounded by musculature. Sealed elastomeric actuators can be created that bend and stretch using EOF.

9.2 Liquid Sealed between a Polymer and a Substrate (PS-2013-136)

9.2.1 Summary of the Invention

The invention concerns a liquid encapsulated within a polymer, especially an elastomer, without tubing or punctures, and a method for accomplishing this.

9.2.2 Introduction

Microfluidic devices are filled with liquid using ports and tubing, since they are typically open devices. However, for closed systems the tubing is cumbersome (protruding out from the device) and it needs to be closed, for example mechanically (using clamps, plugs) or with a sealant. These protrusions can interfere with the performance of the device, particularly in applications requiring flexible or compact devices.

Drugs and other compounds are sealed within vials using a rubber cap, which allows withdrawal of fluid using a syringe needle. Such an approach can be considered for adding liquid to closed polymeric/elastomeric microfluidic devices, but there are at least three significant issues. 1) This approach leaves punctures that leak under high pressure. Two punctures are needed: one for adding the fluid, and one for withdrawing the gas/air already in the device. Even at lower pressures, punctures magnify the risk of device failure. 2) Syringe filling becomes more difficult as the dimensions of the device decrease. The smallest syringe needles are 180 μm in diameter, comparable to or larger

than the smallest dimension of the liquid reservoirs. Even for larger reservoirs, needles easily pierce through thin polymer layers, which can result in accidental rupturing. 3) For thin-walled devices, and particularly with elastomers, it is difficult to maintain open cavities prior to filling: there is a risk of collapse and stiction.

We present a device in which fluid is encapsulated without tubes or punctures, and a method for creating such devices without tubing or syringe filling. The discussion focuses on devices with membranes, but thicker-walled devices can also be produced (in either a single step or by later adding a 2nd layer).

9.2.3 Prior Art

We found no prior work on encapsulating fluid in a polymer that was similar to this method. Thin films of silicone [314] with indentations have been formed by curing on water (the purpose was to create a film with indentations). Urethane [172] cast on water has been used to form a thin film. Methods of encapsulation for creating liquid capsules have been developed for the pharmaceutical industry, but these are not amenable to microfluidic devices. For example a gel and a fluid are coextruded from a spinneret and then pinched closed. For another example, microcapsules have been formed from emulsions.

9.2.4 Reduction to Practice

Overview: The liquid to be encapsulated is placed on a base (or "substrate") layer, where it holds its shape due to surface forces (discussed further below). Uncured liquid pre-polymer is dispensed over the liquid (Figure 112); it spreads over the surface of the liquid and flows down the sides onto the substrate. The prepolymer cures to form a polymer membrane bonded to the substrate, resulting in a sealed, liquid-filled cavity. The membrane is thinnest at the highest point of the droplet and thickest around the base due to surface tension and gravitational forces. The thickening at the base is beneficial to ensuring a good bond between the edges of the polymer membrane and the substrate. Encapsulation may be facilitated by freezing the liquid. One advantage of this technology is that the polymer is conformal with the surface of the liquid – there is no trapped air. The devices provide isolated containment of liquids for a wide array of applications.

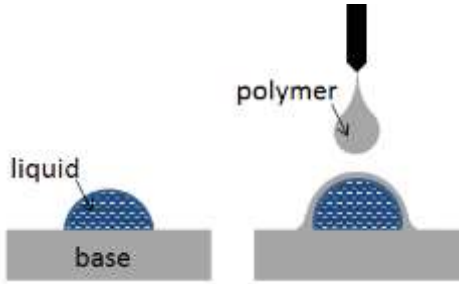

Figure 112. Adding the elastomer precursor over the liquid and base, forming a membrane.

Substrate: The polymer layer can be bonded to the substrate by either chemical or physical means. If the substrate is the same material as the membrane (for example, if both are polydimethylsiloxane (PDMS), an elastomer), they will bond covalently. Bonding can also be enhanced by surface treating the substrate. Many polymer pairs will form bonds, and if not then it may be possible to graft molecules onto the substrate surface to which the encapsulating polymer will bond. If the substrate and polymer are incompatible (i.e., no formation of covalent bonds), the substrate may be roughened to produce mechanical interlocking, or treated (chemically, with plasma, etc.) to increase secondary bonding.

Liquid: The polymer precursor should not completely dissolve in the liquid: the polymer should form a "skin" that is able to cure. If there is some degree of solubility or miscibility, then rapid curing, for example using UV light, can be employed. Alternatively, the fluid can be frozen.

If the fluid strongly wets the substrate, then surface treatment, or selective (patterned) surface treatment or other means of confining the fluid spatially may be required, some methods for which are discussed below.

9.2.5 Patterning the Fluid

In many applications, the fluid should have a predetermined shape (for example, two reservoirs joined by narrow microchannels), rather than the simple part of a sphere resulting from uniform surface tension. To produce diverse patterns, the surface energy of the substrate can be manipulated.

Functional groups can be selectively chemical grafted onto the surface to pattern the wetting of the liquid, or the surface can be selectively treated with self-assembled monolayers. Surface energy changes can also be produced by UV patterning or by masked plasma treatment. Electrowetting is another method to alter the surface tension of a liquid; electrowetting uses electric fields to control the liquid shape.

An alternative approach is to introduce another material, which is patterned. An absorbent layer (paper, thread, fabric) can hold the fluid in the desired configuration: a droplet placed on the absorbent material will wet it and spread to take its shape. Above the absorbent layer, the fluid in excess of the absorbed amount forms a meniscus. Such an approach can be enhanced by a hydrophobic substrate. Instead of an absorbent layer, a "ring" of material (such as SU8) can be used, serving as a "dam" to restrain the fluid within its boundaries.

9.2.6 Potential Applications

This method of filling can enable the creation of nastic devices, freestanding soft actuators, or fluidic displays. Soft robotics, electronic devices and biomedical devices benefit by not requiring tubing, allowing unobstructed motion and/or forming into tube shapes by rolling. The benefits of good encapsulation include protecting the fluid against contamination, and protecting the area outside the device from the fluid. For a nastic actuator filled with propylene carbonate (PC), the PC is degraded by water, and in a biomedical application the body may be damaged by the PC.

9.2.7 Possible Claims

8. A liquid contained between a polymer and a substrate, said polymer and substrate having no holes or ports.

9. An encapsulated fluid as in claim 8 wherein the fluid is partially encapsulated by a membrane.

10. An encapsulated fluid as in claim 8 in which no air or gas is enclosed with the fluid.

11. A structure as claimed in claim 8 in which an absorbent material is patterned on the substrate.

12. A structure as claimed in claim 8 in which a dam has been patterned on the substrate.

13. A method for encapsulating fluid within one or more polymers comprising the steps of

    providing a substrate,

    placing a fluid on said substrate,

    applying (casting) a prepolymer (uncured polymer) over the fluid,

    allowing the fluid to flow over the surface of the fluid and onto the substrate, and

    curing the cast polymer.

14. A method as claimed in claim 13 comprising the step of freezing the fluid prior to applying the prepolymer.

15. A method as claimed in claim 13 comprising the step of treating the substrate surface to enhance bonding between the substrate and the cast polymer.

16. A method as claimed in claim 13 comprising the step of selectively or globally treating the substrate surface to alter its fluid wetting properties.

17. A method as claimed in claim 13 comprising the step of introducing a patterned fluid absorbing material over the substrate.

18. A method as claimed in claim 13 comprising the step of introducing a patterned dam over the substrate to contain the fluid.

9.2.8 Update to PS-2013-136 (No. 62/085824)

9.2.8.1 Summary of the Invention

This is an update to the method described in PS-2013-136, our invention concerning a liquid encapsulated within a polymer.

9.2.8.2 Reduction to Practice

When the polymer used to encapsulate the liquid is viscous, and has a density similar or higher than that of the liquid, and then it may displace the liquid beneath it to form a thicker layer than expected. Instead of dispensing the polymer over the liquid, the liquid is dispensed at the base of the liquid, where it meets the substrate. The polymer forms a frame on the substrate and confines the liquid. Once the base layer of polymer has been dispensed and liquid has been confined, polymer is dispensed in a spiral manner working towards the top of the liquid drop until the liquid is eventually fully encapsulated. This enables makes a membrane that is thin at the highest point and thick at the base.

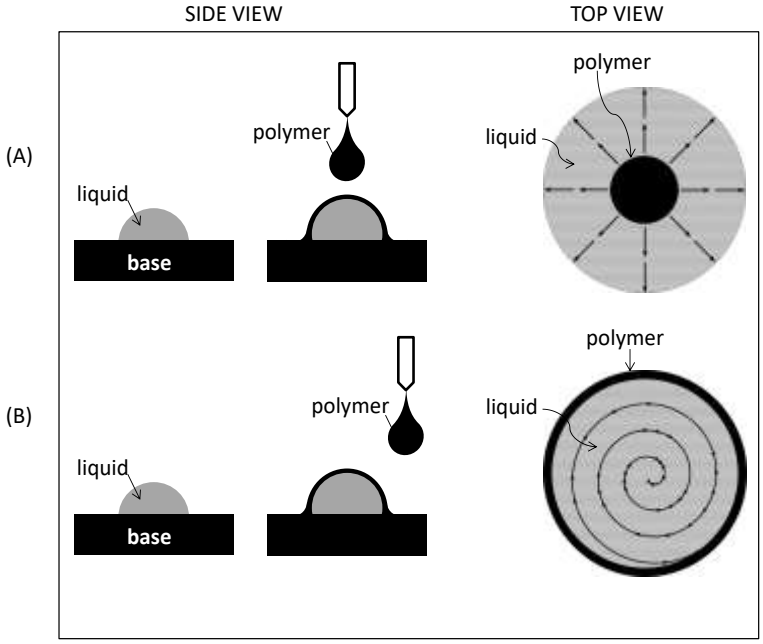

Figure 113. Top view of polymer dispensing pattern.

(A) Previously reported method of dispensing polymer: Polymer was dispensed at a fixed point over the liquid. Polymer was dispensed until it spread outward to form a film and completely encapsulate the liquid.

(B) Updated method of dispensing polymer: Polymer was dispensed starting at the base of the liquid (at the liquid-substrate interface). Polymer was dispensed moving from outside the liquid periphery towards the center of the drop to encapsulate the liquid.

Liquid Sealed between a Polymer and a Substrate

PS-2013-136

Executive Summary

Background:

Microfluidic devices are filled with liquid using ports and tubing, since they are typically open devices. However, for closed systems the tubing is cumbersome and it needs to be closed, for example mechanically (using clamps, plugs) or with a sealant. These protrusions can interfere with the performance of the device, particularly in applications requiring flexible or compact devices. Currently drugs and other compounds are sealed within vials using a rubber cap, which allows withdrawal of fluid using a syringe needle. Such an approach can be considered for adding liquid to closed polymeric/elastomeric microfluidic devices, but there are significant issues regarding leakage, scalability, as well as durability which can all lead to failure of the microfluidic device.

Innovation:

Researchers at the University of Maryland have developed a method to encapsulate fluid in a polymer for microfluidic applications. This method will aid in the production of microfluidic devices where fluid is encapsulated without tubes or punctures. This procedure places the liquid to be encapsulated on a substrate, and dispenses an uncured liquid pre-polymer over the liquid to form a polymer membrane bonded to the substrate base. The encapsulation technique is applicable when the polymer forms a secure bond

with the substrate material upon curing. This method can enable the creation of nastic devices, freestanding soft actuators, or fluidic displays. Soft robotics, electronic devices and biomedical devices benefit by not requiring tubing, allowing unobstructed motion and/or forming into tube shapes. These fluid-filled structures can be used in any number of biomedical devices including adjustable stents, stents with occasional motion, blood-flow regulating stents, artificial sphincters, and catheters. There are also applications in camouflage surfaces, micro-positioning, and tactile displays.

Advantages:

- Conformal coating
- No trapped air
- Isolated containment

Applications:

- Microfluidics
- Biomedical devices
- Nastic actuators
- Liquid based electronics
- Soft robotics

9.3 Solvent-Free Conductive Carbon-Based Silicone Paint (PS-2014-178)

9.3.1 Summary of the Invention

The invention concerns a conductive paint comprised of carbon black suspended in an elastomeric binder, without the use of thinning solvent. Methods of application of the paint to various surfaces, and post-application patterning are also described.

9.3.2 Introduction

In order to create fully flexible electronics, the electrodes used must be flexible. One approach is to use metal electrodes with serpentine or coiled shapes to allow bending and flexing. The other approach is use conductive elastomers which may either be a polymer that is inherently conductive, or it may be a composite of conductive micro/nano particles embedded in a flexible polymer. This invention is about such a composite that has good conductivity while undergoing large deformations.

The ideal conductive paint has a high density of conductive particles uniformly suspended within a low-modulus polymer matrix, and can be easily applied to a variety of substrates. In this work, we mixed conductive carbon black (amorphous graphite) powder into silicone elastomers. This paper describes the preparation of the conductive elastomer paint, and the techniques we used to apply the paint and pattern it on a variety of substrates.

9.3.3 Related Art

Our work on the carbon paint builds upon previous efforts to develop a conductive carbon-based PDMS silicone paint. Most work that has been reported contains one of three types of conductive carbon: carbon nanotubes, exfoliated graphite, or carbon black. Carbon black [244,245] and exfoliated graphite [246] are less expensive than carbon nanotubes and are therefore more suitable for large scale applications. Nanometer-sized carbon black particles are easily commercially available. Their small size enables the preparation of smooth textured paint that can be easily spread.

The elastomer used in all aforementioned reports is Sylgard 184 from Dow Corning [245,246,315]. Typically, solvent addition is seen as essential for making a uniform suspension of the conductive particles. The advantage of using the solvent is that it lowers the viscosity of the paint suspension, and thereby improves paintability and coverage of small surface features. The paint can be spin coated, dip coated, and cast. The disadvantages are that the final cured film has several artifacts, and the presence of the solvent limits the number of substrates to which the paint can be applied. The solvent of choice is usually nonpolar solvents such as hexane due to their high miscibility with PDMS; however, these solvents can damage a number of plastics, thereby limiting the scope of the paint.

It is also known that the solvent addition affects the mechanical integrity of the cured paint film [247]. For applications requiring high conductivity under strain, eliminating the solvent from the recipe results in a smooth film with higher homogeneity and conductivity.

To our knowledge only one other group has attempted to create carbon paint without the use of a solvent [245]. However their cured paint has a conductivity two orders of magnitude lower than ours. We suspect this is because our mixing technique ensures a more thorough distribution of the conductive particles within the PDMS.

9.3.4 Reduction to Practice

Paint recipe

In a glass vial, hexane was added to Sylgard 184 pre-polymer. Sample vials were prepared with hexane amounts of 0%, 100%, 150%, 200%, and 300% pre-polymer weight. To the polymer base, the carbon powder (40nm carbon black, Alfa Aesar 39724) was added as 14% of the combined hexane and pre-polymer. The mixture was stirred manually using wooden dowels. Then vial was capped and the paint was mixed in a vortex machine for 30 seconds at 2800 rpm. The paint was further mixed by sonication in a water bath at 40 kHz for 20 minutes. Sylgard 184 curing agent was added to the paint mixture; 1 part curing agent was added for 10 parts of pre-polymer. Again, the mixture

was stirred manually, vortexed for 30 seconds at 2800 rpm, and sonicated at 40 kHz for 1 minute.

The paints were cast on glass slides to a thickness of 1 mm. The paint with 0% hexane was thicker than the diluted formulations and needed to be spread out using a squeegee. After curing the paints in the oven at 65 ^{o}C for atleast 2 hours, the resistance was tested in five separate locations on each sample. Four samples were tested per formulation. The resulting data are shown in Figure 114.

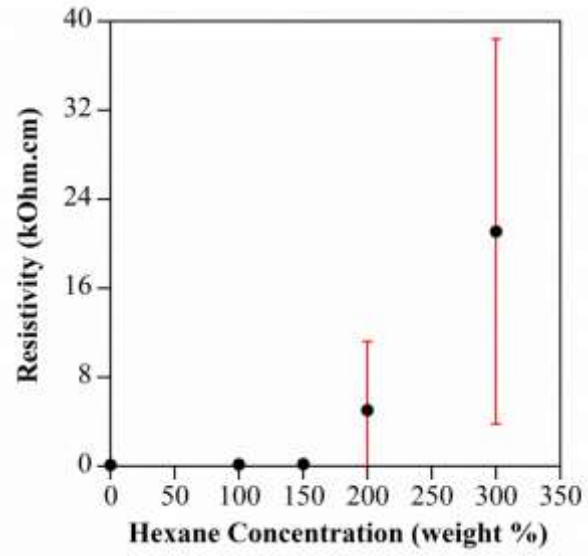

Figure 114. Change in resistivity of cured paint film with amount of hexane added to paint slurry. Hexane percentages are relative to Increasing

We found that conductivity sharply decreased when increasing amounts of added solvent (hexane). Samples that were free of organic solvent had an average resistance of 0.1 kΩ/cm. A sample made with the same technique using 300% solvent (based on PDMS

weight) had an average resistance of 22 kΩ/cm. We deduced that the solvent evaporation during the curing process is responsible for this. As more organic solvent was added to the mixture, it was observed that the homogeneity of the cured film decreased and that it became more brittle. In some areas, there was aggregation of carbon particles, while in others cracks appeared. At several spots, the conductive material settled at the bottom of the painted film, while the polymer formed an isolating layer on top. As seen in Figure 114, large variations were observed in samples prepared with paint containing high amounts of hexane. These issues were not observed in the paint prepared without the use of hexane.

Methods of Paint Application

The consistency of the conductive silicone paint without any hexane is thick: similar to that of toothpaste. The paste is smooth and easily spreadable. The method of application best suited to create flat films is squeegeeing or screen printing. Patterns may be created by application through a stencil. Due to its thick consistency it is also suited for sculpting thicker patterns and using piping/extrusion techniques.

After curing, the film can be easily cut using a razor blade. We have also been able to create well defined patterns using laser ablation using a CO_2 laser cutter. The speed and power required are dependent on the thickness of the painted film/structure. We were able to bond multiple layers by oxygen plasma treatment, when the elastomer used was Sylgard 184.

9.3.5 Potential Applications

The paint can withstand high voltages of at least 10 kV without visible deterioration. The paint is also stable when used to apply these high voltages in liquids. We have tested the electrodes in DI water and propylene carbonate, and no visible deterioration due to redox currents was observed up to at least 10 kV. The inertness and stability of the electrodes lends itself well to applications in biology, electrochemistry, and electrohydraulics.

We have also prepared paint that uses Ecoflex 0030 from Smooth On, Inc., instead of Sylgard 184. Parts A and B were mixed in equal proportion and added to carbon powder, followed by stirring, vortexing, and sonication as described earlier. The resistivity values were comparable to that obtained with Sylgard 184. The paint had a smoother consistency and spread more easily than the paint prepared using Sylgard 184. The advantage Ecoflex offers over Sylgard 184: it is 30 to 90 times more stretchable. The stretchability of the cured paint makes it applicable for soft robotics and smart fabrics/skin-like materials for wearable electronics.

9.4 Paper-Based Electroosmotic Device (PS-2014-088)

Electroosmosis (EO) is the motion of a liquid along a charged surface under an applied electric field. This effect becomes significant in micro-channels because of their high surface-to-volume ratios, and it can create substantial forces. Pumping velocity increases with cross-sectional area and pumping force is inversely related to channel size. In order to create larger devices that incorporate microscale features novel methods must be employed. There are several methods of incorporating microchannel networks [142], [146], [135], [127]. However these approaches and other cleanroom microfabrication processes are not readily applicable for the roll-to-roll fabrication of larger, high aspect ratio soft-robotics. We present a mesoscale electroosmotic pump fabricated from silicone and paper. Employing paper is a rapid and straightforward approach to create multi-scale devices that incorporate microchannel networks within macrostructures. Paper is highly porous and readily absorbs a variety of fluids through the microchannels between the cellulose fibers. Paper is easily available, inexpensive, and robust. It can be folded, bent, cut, and stacked. The flexibility of paper offers significant advantages to creating 3D structures for soft robot design.

The base layer consists of flexible electrodes embedded within a silicone substrate. The electrodes are composed of a carbon-silicone composite. A layer of paper covers the electrodes. Paper microchannels can be filled easily, simply by wicking, in contrast to silicone microfluidic channels. As a result, in our device we have been able to eliminate tubing that is typically required to fill microfluidic devices. To create a microfluidic

actuator it is imperative to create a completely closed system, to contain the pressure. Even if the tubing is clamped, the protruding tubes can affect the motion of the actuator and prevent integration with other devices. In this device, the liquid is directly dispensed on the paper placed over the electrode base layer. The hydrophobicity of the underlying silicone causes the excess unabsorbed liquid to form a droplet that takes the shape of the paper. Liquid silicone polymer is then cast over the liquid and cured, forming an encapsulated reservoir. The silicone skin formed over the drop serves as the actuating membrane. Thus, multiple goals were achieved in a single process: fabrication of the reservoir and membrane, and device encapsulation. We have found a method that can reliably pattern materials for our devices, without the need for significant funding, using a benchtop electronic cutting machine: Cricut Explore. This technique offers a highly affordable method to easily create intricate patterns within 5-10 seconds, with clean edges in a wide variety of materials, varying only one parameter, the cutting pressure of the blade. The silicone and paper layers were patterned, and then aligned and bonded to form the device. The novel processes that we have developed are amenable to roll-to-roll manufacturing.

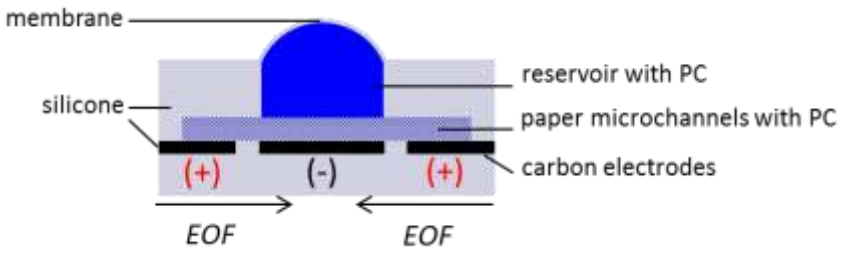

INSPIRATION

Movement in Plants by Osmosis

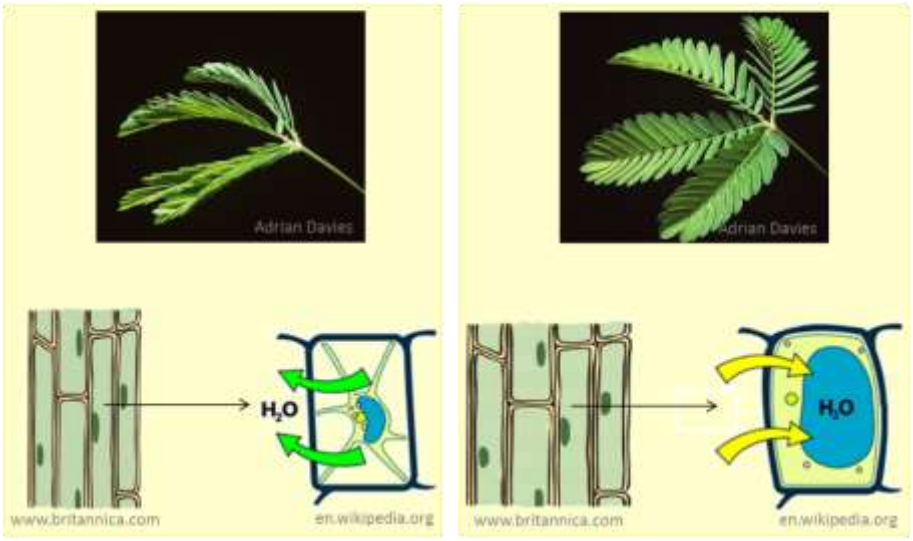

Electroosmotic Actuator: Concept

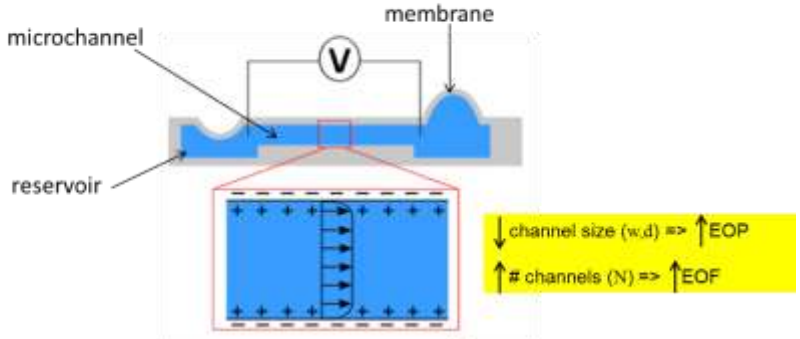

$$\text{Flow Rate (EOF)} = \text{Nwd}\frac{\varepsilon\zeta E}{\eta}$$

$$\text{Pressure (EOP)} = \frac{12\varepsilon\zeta EL}{d^2\left[1-0.63d/w\right]}$$

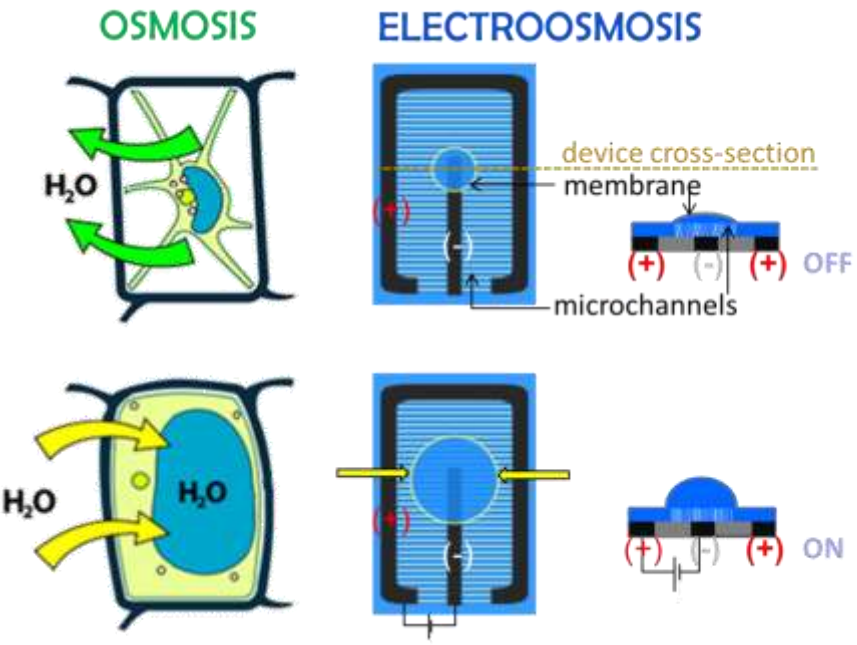

Traditional Microfluidic Fabrication

LIMITATIONS

- ✕ Requires cleanroom equipment for mold fabrication and bonding.
- ✕ Cannot make 3D networks easily.
- ✕ Multiple steps required.

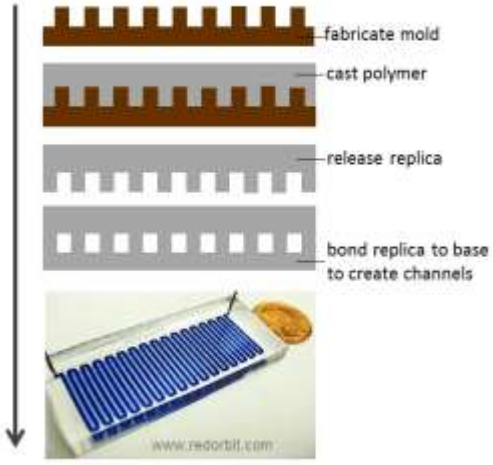

Soft Lithography

Electroosmotic Actuator: Benchtop Fabrication

Cricut Explore

Electronic printing and cutting machine

Layer-by-Layer Assembly

Fabrication Steps

1. Create vector drawing.
2. Cut out device layers.
3. Align and bond.

Materials

1. Silicone
2. Paper
3. Propylene Carbonate

Electroosmotic Actuator: Materials

Silicone → **flexible electrodes**

Ecoflex 0030 +  → 

15% (wt) carbon black

→ **liquid encapsulation**

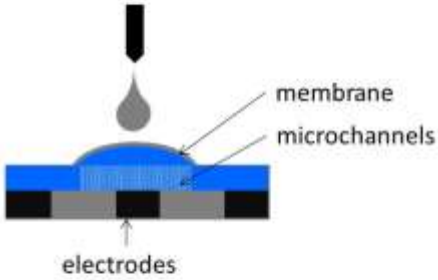

Paper → **microfluidic channel**

Whitesides group

Paper can be...

...cut,

...stacked,

...folded,

...and rolled.

Propylene Carbonate → **stable, polar pumping liquid**

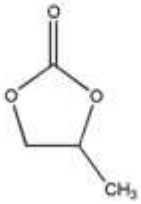

Electrolysis

DI water, 15 sec

PC, 900 sec

- Bubbles block channels and affect pressure
- Pumping fluid depletion
- Electrode corrosion
- Change in pH → change in zeta potential

Electroosmotic Actuator: Fabrication

Electrode Layer

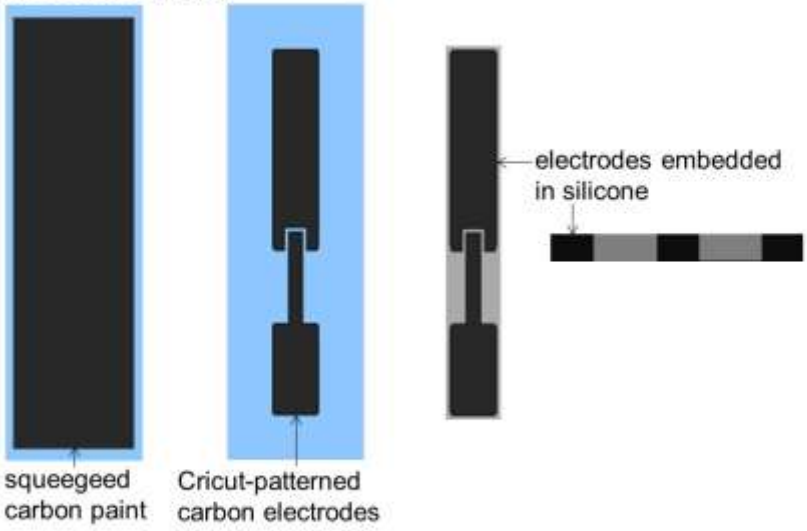

Microchannel Layer

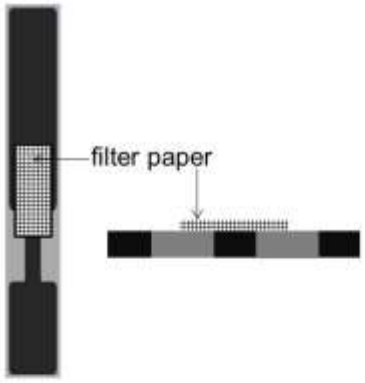

Filling Pumping Liquid

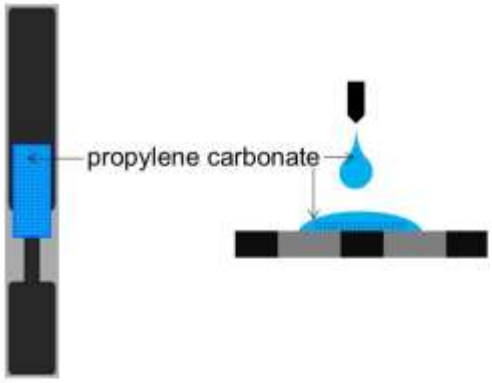

Liquid Encapsulation

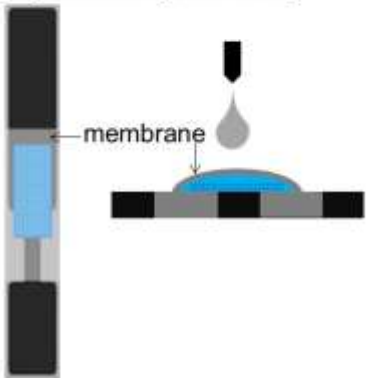

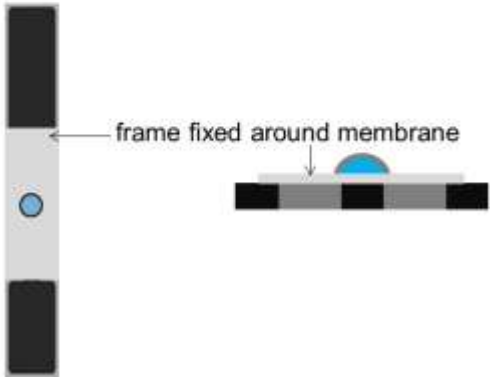

APPLICATIONS

Biomedical Valve

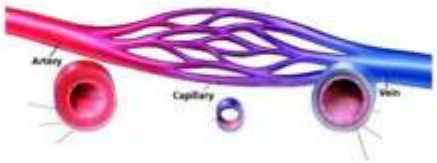

In collaboration with
Dr. Thorsten R. Fleiter
UNIVERSITY of MARYLAND MEDICAL CENTER

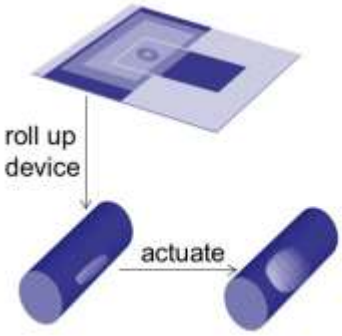

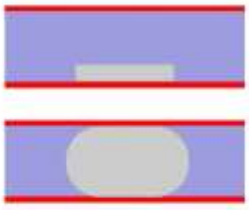

electrohydraulic arterial valves

address device electrically to
modulate blood flow during surgery

Smart Material

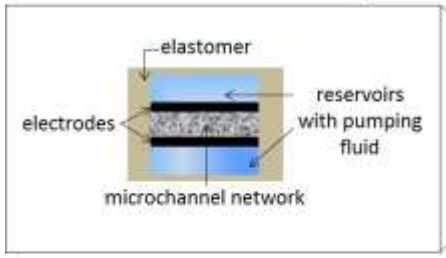

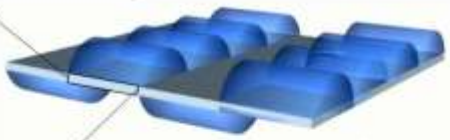

Actuate to change texture for
gripping etc.

Combined with rigid materials
to produce limb structures

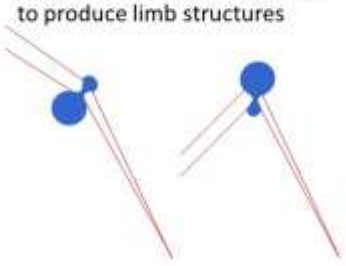

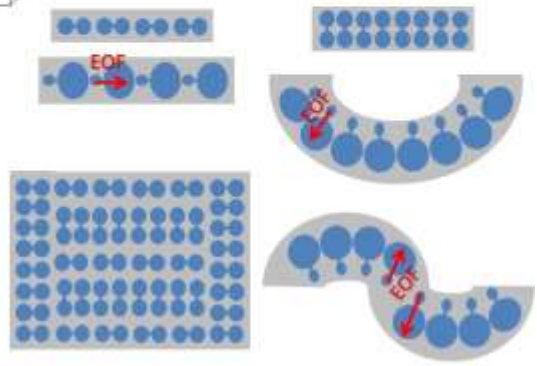

Cells combined with multiple orientations, layers
→ smart material.

10. Appendix B: Electrokinetic Flow in Large Tubes

10.1 Introduction

We have found directional electrokinetic fluid pumping can be achieved in large (mm) channels/tubes without the use of specially-shaped electrodes or micro/nano-scale channels. This type of electrokinetic fluid flow has not been previously reported in the literature. This phenomenon has the potential to open new application areas for meso- and macro- scale electrofluidics.

EOF has been known to scale inversely with channel diameter and has thus been employed for pumping applications using only in micro/nano-scale diameter channels (Equation 2). It was also previously known EO decreases with increasing ion concentration in of the pumping fluid. Prabhath Aluthgama and I conducted flow tests to monitor the effect of salt, channel material, channel diameter, electrode diameter, and applied voltage on flow.

10.2 Materials and Methods

The experimental set up was previously described in Section 3.6.5. PC and water were tested as pumping liquids. Syringe needles were used as cylindrical electrodes. The sharp ends of the needles were outside the fluidic system (which eliminated the formations of electrohydrodynamic jets). Needles of size 18 gauge, 22 gauge and 30

gauge were tested as electrodes. To test the effect of salt on flow solution of tetra-n-butylammonium tetrafluoroborate (TBTF) (Alfa Aesar) in PC in molar concentrations between 0 mM to 5mM were prepared by serial dilution from a 0.1M stock solution. The channel materials tested were glass, polyethylene, PDMS, PDMS-coated glass, and Ecoflex 0050. For each material type channel diameters of 3 mm, 5 mm, and 7 mm were tested. Electric fields were applied between 1.5 and 3.5 kV/cm. Flow was not observed below 1.5 kV/cm and in tube diameters greater than 10 mm.

10.3 Results

The data plotted in Figure 115 shows that the flow rate decreased dramatically with salt concentrations higher than 0.01 mM. At the higher salt concentrations the magnitude current increased, as expected, and Joule heating was observed (the electrodes were warm to touch at the end of the experiment). The direction of flow was consistently from the positive to the negative electrode at all concentrations. The decrease in flow with increasing salt concentration implies that this phenomenon requires a salt-free pumping liquid, similar to that needed for EOF.

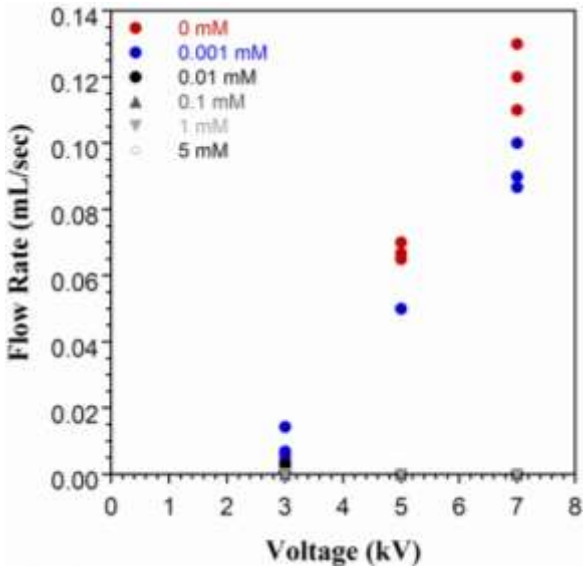

Figure 115. Effect of salt concentration on flow in a polyethylene tube of 3 mm diameter, using 22 gauge syringe needles as electrodes spaced by 2 cm.

Flow rate scaled with voltage (Figure 116). It was observed that the direction of fluid flow was reversed at high voltages and by increasing electrode size. This occurred regardless of the channel material. With 30 gauge needles, the direction of flow was from the positive to the negative electrode at 3, 5, and 7 kV. However, at 7 kV for larger electrode sizes (22, and 18 gauge) flow was opposite to the direction of the electric field, in all channel types. With 18 gauge electrodes at 5kV the flow was sometimes forward and sometimes reversed. The switch in direction was consistent when the experiments were replicated. The reversed flow using the 18 gauge needles was 50% faster than the forward flow using the 30 gauge needles at.

This flow reversal was not observed when the experiments were conducted using the original microfluidic prototype device (channels 40 μm deep and 150 μm wide; for

further device description see Section 1.3.4. The flow direction was independent of the electrode diameter or voltage, and always occurred in the direction of the electric field (+ to –). There was also no difference in flow rate between the two electrode sizes.

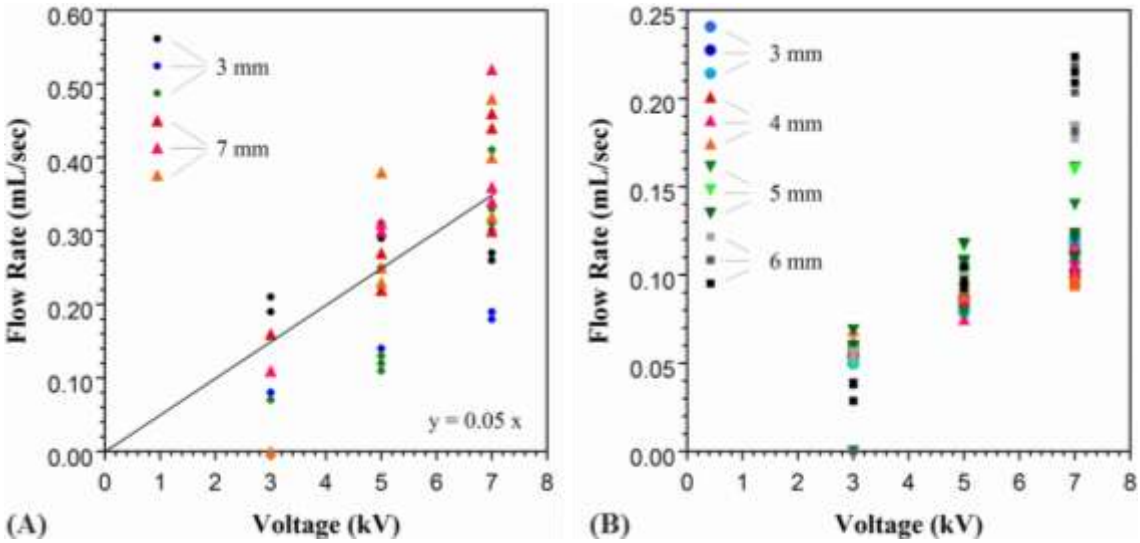

Figure 116. (A) PE, 30 gauge needles. Forward flow (+ to -). (B) glass, 30 gauge needles. Forward flow (+ to -).

When DI water was the pumping fluid no flow was observed at any of the test conditions and electrolysis ensued within seconds of applying the voltage implying that PC was the better-suited pumping fluid for this type of electrofluidic pumping.

The flow observed can be useful for forming large electro-fluidic devices composed of materials like polyethylene, PDMS, glass, or Ecoflex, for a wide variety of mesoscale applications. The flow rate depended on the tube material, and electrode size. (Fast PC EO flow was also observed in large diameter tubes (3-7 mm) formed of Ecoflex 0050 but flow was not quantified). These results are consistent with flow dominated by EO (wall

effects) as well as flow effects induced by electrode-liquid interface phenomena. This flow effect is thought to be different from electrohydrodynamic (EHD) flow [87-89], which is usually induced using an electrode with a sharp tip (such as a sharp needle), which injects electrons into the fluid. The electrons drag the fluid toward the other electrode. The shape of the second electrode is often in the shape of a ring. In these experiments the electrodes were cylindrical and symmetric, therefore the fast directional flows produced were surprising. It may be possible that electrothermal flow effects may be at play and causing this effect, and therefore in future investigations of this phenomenon it is recommended that the temperature of the electrodes are monitored.

11. Appendix C: Optimization Study to Minimize Voltage

This chapter is a reproduction of the report for the class ENME 610: Engineering Optimization. The report was prepared by Deepa Sritharan, Abraham Simpson Chen and Dinesh Mahadeo. All authors contributed equally to the project.

Abstract

This paper describes the design optimization of an electroactive polymer actuator that uses hydraulic pressure created by electroosmotic flow (EOF). The actuator was fabricated using a flexible silicone and has embedded micro-scale channels, reservoirs, and electrodes. Applying a high electric field causes one reservoir to expand as fluid is pumped into it, and the other reservoir to contract, resulting in deformation of the flexible actuator. Currently, thousands of volts are required to realize actuation. In order to realize real-world applications such as the voltage demand must be reduced while still achieve high actuation stress. In this project, we have deduced the optimal design of a rectangular electroosmotic channel using single-objective and multi-objective optimization techniques.

11.1 Introduction

Electroosmosis is a phenomenon that causes the motion of a liquid inside a channel under an applied electric field. A large family of microfluidic devices employ electroosmosis as a means to achieve stable, pulseless pumping of liquids in microfluidic devices [94]. Electroosmotic pumps are being developed as an alternative to mechanical pumps because no moving parts are involved, they are simpler to miniaturize for on-chip integration and they afford a high degree of flow control. Other applications include microvalves, micropositioners, soft robots, and active camouflage layers.

Electroosmosis is a surface phenomenon that occurs due to the electric double layer. An electric double layer is a structure that appears on the surface of an object when it is placed into a liquid. When a charged solid surface is placed in a polar liquid, counterions are attracted to the charged surface to maintain electrical neutrality. Thus there exists a double layer at the interface, one side of which is positive and the other side negative causing a potential drop. This potential difference at the interface of the solid and liquid is called the zeta potential.

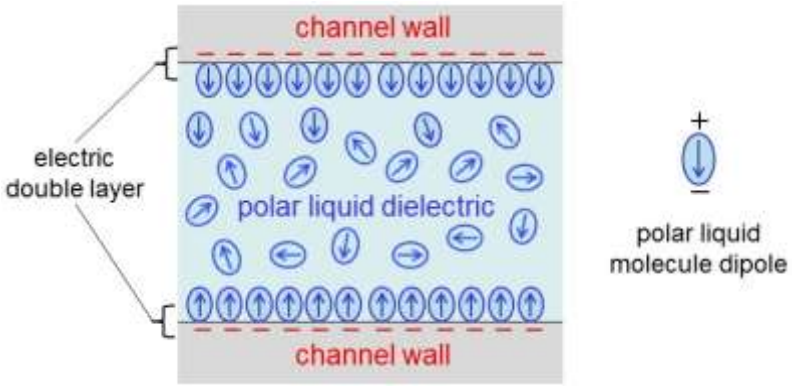

Figure 117: Electric double layer inside a fluid channel.

When a potential is applied across the conduit, the counterions in the liquid will be attracted to the electrode of opposite polarity and cause liquid motion towards the electrode. The liquid flowing at the walls will drag the bulk of the liquid in the channel. Flow originates at the walls and so, contrary to pressure driven flow, the no-slip condition does not apply and the resulting flow will have a nearly flat velocity profile.

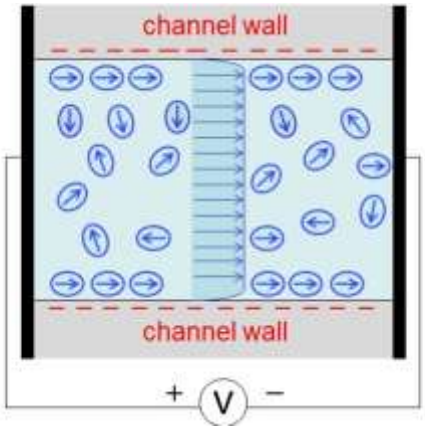

Figure 118. Electroosmosis inside the channel due to flow of mobile counterions in the liquid.

In a rectangular microchannel, the flow can be described by the following equations [106]:

19) $$\text{Velocity} = \frac{\varepsilon\zeta}{\eta}\text{E}$$

20) $$\text{Pressure} = \frac{12\varepsilon\zeta\text{L}}{\text{d}^2}\text{E}$$

Thus, in a channel of length *L*, a liquid with high permittivity (ε) and low viscosity (η), and a solid-liquid interface of high zeta potential (ζ) would result in fast electroosmotic flow. When the depth of the channel (*d*) is small, high pressures can be achieved using EOF. Both the velocity and pressure due to electroosmosis scale linearly with the magnitude of the applied electric field, E.

Since this phenomenon is most pronounced at the microscale, where the surface-volume ratio is higher, electroosmosis is being used to provide a convenient propulsion mechanism in miniature devices. However, in the current state of the art, high voltages are required for operation. This limits the portability of these devices. The approach that has been taken in order to reduce voltage requirements has been to use asymmetric AC electric fields. However, AC EOF has been found to be weaker than DC EOF and is more suited for flow manipulation, such as mixing, rather than pumping bulk volumes [109]. This technique also involves the complicated fabrication methodologies to create the

required asymmetric geometry of the electrodes. DC EOF requires simple fabrication techniques that lend themselves readily to large-scale device manufacture.

In this project, we have optimized the design of an electroosmostic channel that employs DC EOF and present the optimal number of electrodes and channel dimensions needed to generate maximum actuation stress using minimal input power.

11.2 Problem Definition and Formulation

11.2.1 Problem Definition

The design problem is set in the context of a micro-channel, which connects two chambers that contains the actuating fluid. The effects at the boundary of the chamber and channel and the dimensions of the chambers are ignored. The goals are to obtain minimum voltage demand while achieving maximum pressure exerted at the walls of the chamber. This will be reached by optimizing the channel's geometry, depth and width, and the numbers of electrode pairs and spacing within the channel.

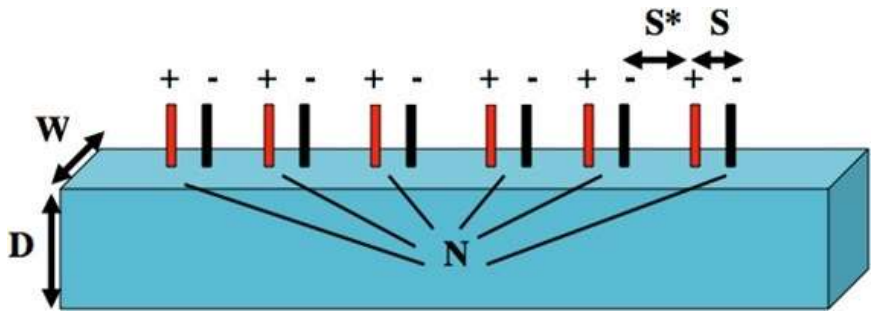

Figure 119: Schematic of a channel containing N pairs of electrodes. The design variables are channel width (w), channel depth (d), the spacing between electrodes within a pair (S) and the gap between the electrode pairs (S*).

11.2.2 Assumptions

- The flow effects contributed by the reservoir geometry is ignored.
- The channel is perfectly smooth and made of a homogenous material.
- The pumping liquid is homogenous and has constant resistivity.
- No electrochemisty occurs inside the channel. In reality, localized changes in ion concentrations and zeta potential occur due to electrochemical reactions. We have ignored these time-dependent material properties to simplify the analysis.
- Steady state, fully developed flow.
- Complete energy conversion, i.e. no losses to Joule heating effects.
- The electrodes are plates, i.e. non-planar.

11.2.3 Formulation

Design Variables:

D; W; S; S*

Design Parameters:

$\varepsilon = 64$ [155]; $\zeta = 100$ mV; $\rho = 10^5$ ohm/mm; E = 1000 V/mm; Lc = 10 mm

Constraints:

Number of electrode pairs must be greater or equal to 1.

$$2 - N \leq 0$$

$$2S - S^* - Lc \leq 0$$

We changed the constraints in terms of S and S^* since N was not a continuous variable.

Channel aspect ratio has a maximum due to limits of the fabrication methods that are used in these systems. It has to have a width to depth less than 10:1.

$$\frac{W}{D} - 10 \leq 0$$

The electrode spacing has a minimum based on fabrication limitations. These units are in mm.

$$0.01 - S \leq 0$$

The lower bounds are placed on the width and depth of channel because of fabrication limitations. The upper bounds are chosen because it is the limit at which the EOF phenomenon can be observed.

$$0.0001 - W \leq 0$$

$$W - 0.2 \leq 0$$

$$0.0001 - D \leq 0$$

$$D - 0.2 \leq 0$$

The power limit is placed because it is the maximum power that can be output by our available equipment.

$$T - 60 \leq 0$$

The lower bound for pressure was chosen as the minimum pressure the equipment can be measured. Units are in Pascals.

$$20 - P \leq 0$$

Objective Functions:

Power is T equal to the number of electrode pairs times voltage and current. Voltage is equal to the spacing between the negative and positive electrodes multiplied by the electric field. With the electric field set as a parameter, minimizing the power to results in minimizing the spacing between the electrodes and the number of electrodes, Current is also a function of the spacing because the resistance will change as spacing between electrodes vary.

$$T = \frac{\left(\frac{L_C + S^*}{S + S^*}\right) SDW * \vec{E}^2}{\rho}$$

The actuation stress ΔP_{MAX} was derived at steady state where the net flow is zero, i.e. the flow in the positive direction is equally opposed by back pressure and the EOF that occurs between pairs of electrodes.

$$\Delta P_{MAX} = \frac{12\varepsilon\zeta L_C}{D^2}\vec{E}\left(\frac{L_C + S^*}{S + S^*} - \frac{S}{S^*}\left(\frac{L_C + S^*}{S + S^*}\right) + \frac{S}{S^*}\right)$$

The left term $\frac{3\varepsilon\zeta L_C}{D^2}$ is from the pressure driven flow while the right term $\frac{L_C+S^*}{S+S^*} - \frac{S}{S^*}\left(\frac{L_C+S^*}{S+S^*}\right) + \frac{S}{S^*}$ describes the influence of the negative EOF flow on the overall pressure.

Final Problem Formulation:

Minimize:

$$T = \frac{\left(\frac{L_C + S^*}{S + S^*}\right) SDW * \vec{E}^2}{\rho}$$

Maximize:

$$\Delta P_{MAX} = \frac{12\varepsilon\zeta L_C}{D^2}\vec{E}\left(\frac{L_C + S^*}{S + S^*} - \frac{S}{S^*}\left(\frac{L_C + S^*}{S + S^*}\right) + \frac{S}{S^*}\right)$$

Subjected to:

$$g_1 = \frac{W}{D} - 10 \leq 0$$

$$g_2 = 0.01 - S \leq 0$$

$$g_3 = 0.0001 - W \leq 0$$

$$g_4 = W - 0.2 \leq 0$$

$$g_5 = \ 0.0001 - D \leq 0$$

$$g_6 = \ D - 0.2 \leq 0$$

$$g_7 = \ T - 60 \leq 0$$

$$g_8 = \ 20 - P \leq 0$$

$$g_9 = \ 2S - S^* - Lc \leq 0$$

11.3 Results and Discussion

The problem was initially formulated as a single-objective optimization problem with the other objective function treated as a constraint together with all other constraints in the problem. The single objective optimization problem was solved by two different single-objective optimization methods. The first approach was based on the Augmented Lagrangian Method (ALM) and evaluated using Matlab. The other method was using "fmincon" from the Matlab's optimization toolbox. The results from both techniques are compared side-by-side.

Next, the problem was formulated as a bi-objective optimization problem using two bi-objective methods, “fminimax” and “fgoalattain”, both canned approaches from Matlab’s optimization toolbox and compared the results using the Pareto plots.

11.3.1 Single-Objective Optimization

11.3.1.1 Augmented Lagrangian Method (ALM)

ALM was used to solve the constrained optimization problem. The algorithm for this method is summarized in the flow chart in Figure 120. In the flow chart, X is the set of design variables, λ is the Lagrange multiplier, r_p is the penalty factor, γ is the dilation factor.

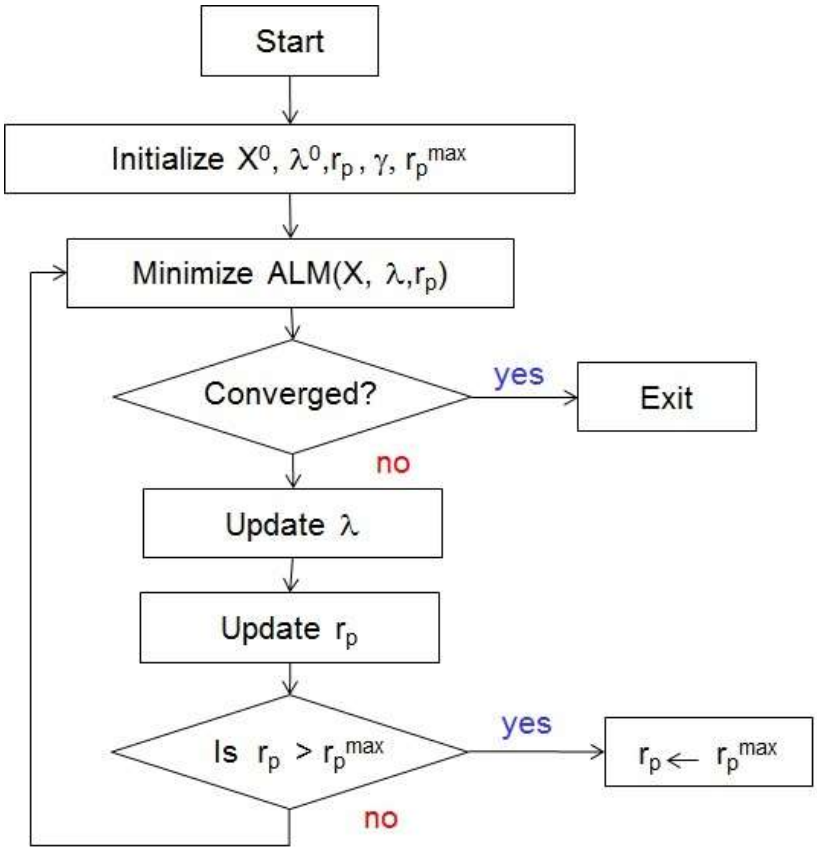

Figure 120: ALM Algorithm

For the single objective problem, there were two cases to solve, minimized power and maximized pressure. We chose ALM to solve these because using this method, a local minimum can be obtained starting from any point and the convergence of the method fast.

The initial point of d=0.1, w = 0.15, S=5, S*=1 was used for both single objective cases. The parameters for electric field, liquid properties, resistivity, and channel length were set using the values described in section 2.3. For each of the four design variables, upper and lower bounds were set based on physical limitations of the problem.

In both cases (minimizing power and maximizing pressure), three constants were used. The constraints for aspect ratio and channel length are used in both cases. The last constraint is the constraint on the function that is not the objective function. For minimized power, a minimum pressure is given, and for maximum pressure, a maximum power is given. The results obtained were close to the set tolerance. This resulted in incorrect outputs. Therefore the logarithm of the objective function was solved in order to avoid this numerical problem. The results based on the code in Section 11.8.1 can be seen in Table 7.

Table 7: Results using ALM single objective optimization

Case	Objective	D	W	S	S*	Function
1	Min(Power)	0.0001	0.0001	0.01	9.98	2.0665e-09
2	Max(Pressure)	0.0001	0.0010	0.0100	0.0241	1.1723e+08

11.3.1.2 Canned Approach from Matlab Optimization Tool Box

The fmincon function was used to solve the single objective forms of the problem. For the single objective problem, there were two cases to solve, minimized power and maximized pressure. The initial point of [0.1,0.15,5,1] was used for both single objective cases. The parameters for electric field, liquid properties, resistivity, and channel length

were set using the values described in section 2.3. For each of the four design variables, upper and lower bounds were set based on physical limitations of the problem.

In both cases (minimizing power and maximizing pressure), three constants were used. The constraints for aspect ratio and channel length are used in both cases. The last constraint is the constraint on the function that is not the objective function. For minimized power, a minimum pressure is given, and for maximum pressure, a maximum power is given. The initial formulations based on the assumed initial can be seen in Table 82.

Table 8: Initial results using single objective function fmincon

Case	Objective	D	W	S	S*	Function
1	Min(Power)	0.0062	0.0001	0.0899	3.5938	2.0665e-06
2	Max(Pressure)	0.0001	0.0010	0.0100	0.0241	1.1723e+08

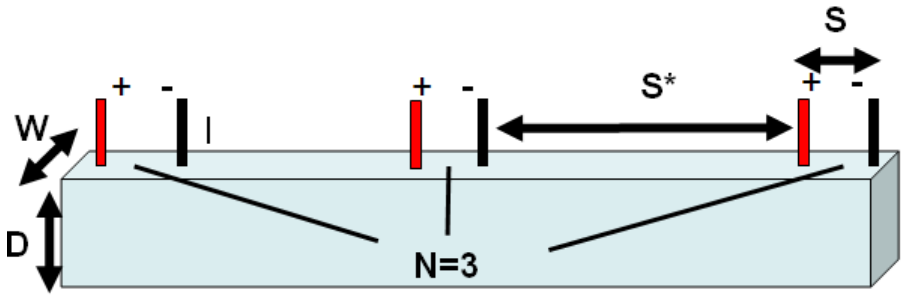

Figure 121: Initial Results using Single Objective Function – Case 1: Min(Power)

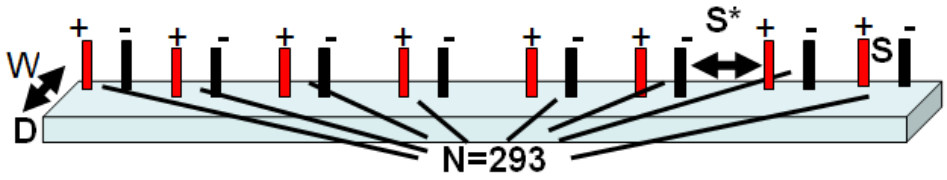

Figure 122: Initial Results using Single Objective Function - Case 2: Max(Pressure)

Looking at the two results from the single objective cases, we can see that the generated geometries are significantly different. For the first case, where power is minimized, there are few electrodes with large spacing between them. This makes sense, as power consumption scales with the number of electrodes. For the second case, pressure is optimized with many electrodes and a very small channel.

The algorithm gave slightly different values for the optima, compared to the ALM. As the solver reached a local minimum, the initial values were changed closer to the solutions given by ALM in order to see where the canned approach would find a local optimum near the optimum point identified by ALM. For the case of power, and initial condition of x0=[.005,.0001,.01,9] was used, while for the case of pressure and initial condition of x0=[.0001,.0001,.01,0241] was used. Results for these modified starting points can be seen in Table 9.

Table 9: Revised results using single objective function fmincon

Case	Objective	D	W	S	S*	Function
1	Min(Power)	0.0050	0.0001	0.0100	9.0000	1.0544e-07

2	Max(Pressure)	0.0001	0.0001	0.0100	0.0241	1.1723e+08

In both of these cases, it can be seen that changing the initial condition led to a new optimum that had a lower value than the initial configuration. It can be seen that while the local extrema identified using the initial values did not represent the optimal values for the problem for the power function, it did for the pressure function.

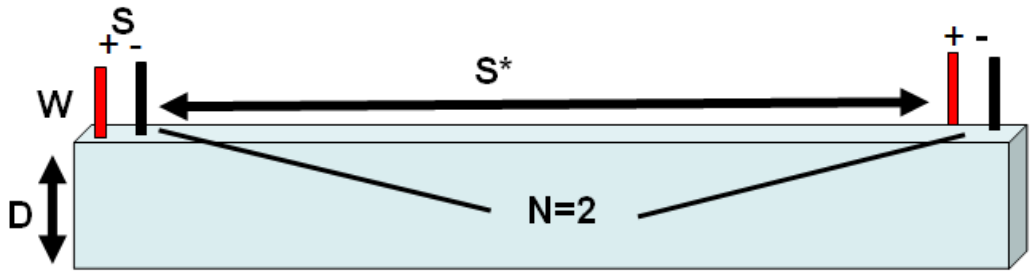

Figure 123. Revised results using ALM points as initial - Case 1: Min(Power)

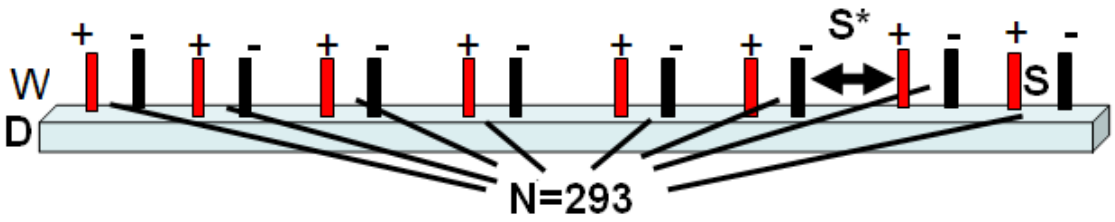

Figure 124. Revised results using ALM points as initial - Case 2 Max (Pressure)

The results displayed in figures 7 and 8 indicate the optimal solutions for the two objective functions. For Case 1, minimizing power, there are very few electrode pairs as the power consumed increases with the number of electrodes. For case 2, there are many more electrodes, and the channel is very narrow. This is consistent with the idea that a smaller channel makes it easier to generate a higher pressure.

11.3.2 Bi-Objective Optimization

The Matlab programs fminimax and fgoalattain were used to solve the bi-objective problem. The programs were used to solve for local optimums at many different initial starting points, with nested for loops that varied the design variables: depth, spacing between electrode pairs, and spacing of adjacent electrode pairs. For the fminimax program, good and bad values were used to scale the functions to the same magnitude and the design variables corresponding to each optimum point were printed in order to obtain the optimum geometries. When graphing all the optimums the Pareto curves were obtained (Figure 125, Figure 6).

In both cases, four constraints and two pairs of lower and upper bounds were used. The constraints were aspect ratio of depth to width, channel length, and constraints on the two objective functions. The lower and upper bounds were based on physical limitation of the problem.

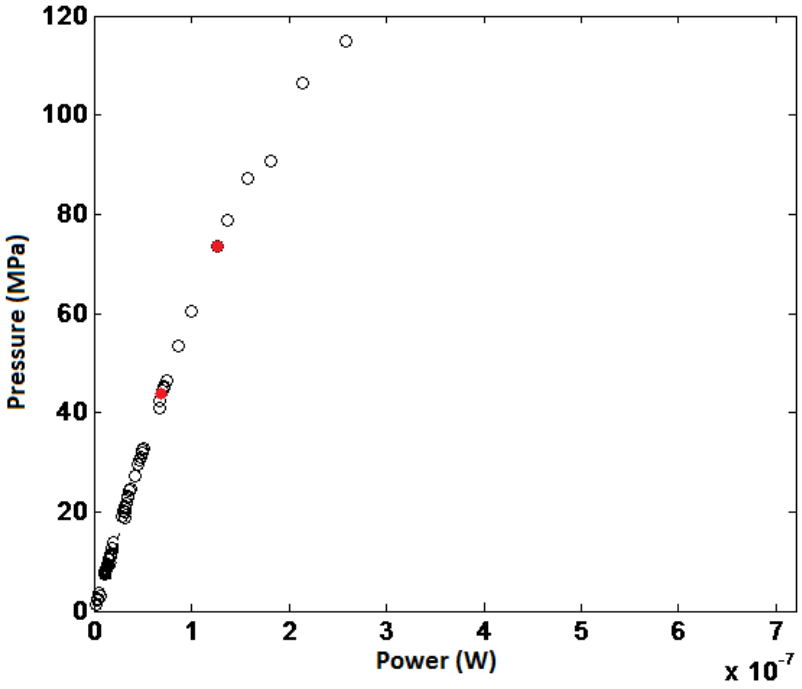

Figure 126. Pareto curve from fminimax

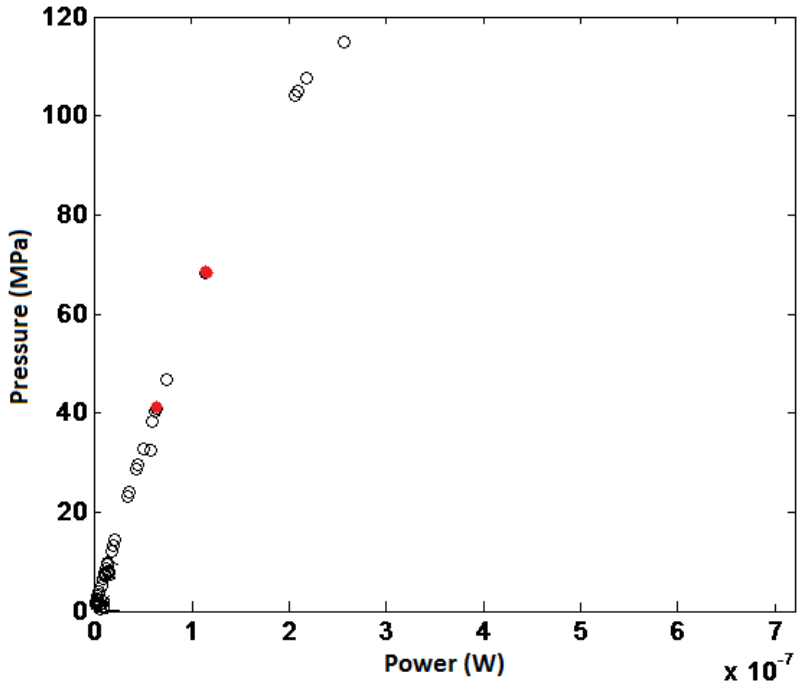

Figure 127. Pareto curve from fgoalattain

Looking at the Pareto curves, we can see that both curves are almost identically. This shows the tradeoff between minimizing power while maximizing pressure. As power is minimized, pressure also decreases, exhibiting a parabolic relationship. It is also observed that the Pareto points exhibit the power and pressure values that are in between the maximum pressure and minimum power found in the single objective formulations.

The solutions corresponding to the red points marked on the Pareto curves are shown below in Table 10.

Table 10. Solutions to selected Pareto points in Figure 126 and Figure 127.

		D	**W**	**S**	**S***	**N**	**Power**	**Pressure**
Units		**mm**	**mm**	**mm**	**mm**		**Watts*10^{-7}**	**MPa**
fminimax	Case 1	0.0001	0.0001	0.01	0.1309	72	0.72	45.21
	Case 2	0.0001	0.0001	0.01	0.0699	126	1.26	73.54
fgoalattain	Case 3	0.0001	0.0001	0.01	0.1302	72	0.72	45.41
	Case 4	0.0001	0.0001	0.01	0.0773	115	1.15	68.43

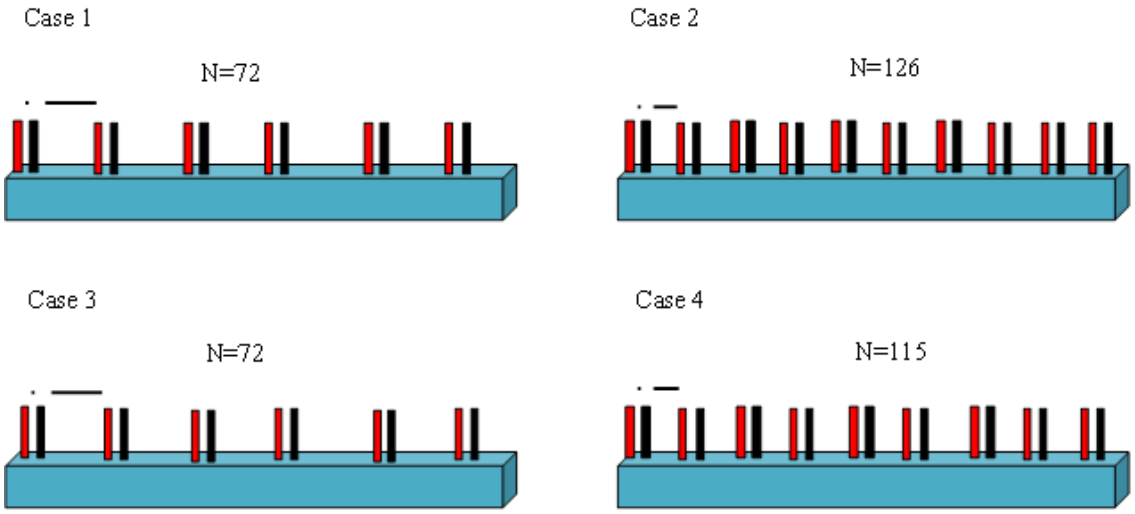

Figure 128. Physical representation of selected optimal solutions. The dashed lines (— —) above the electrodes represent S and S* respectively.

The Pareto curve is essentially saying that the optimal design would be a channel that is as small as what current fabrication methods can achieve, which in this case is 100 nm both in width and depth, and minimum electrode spacing to minimize necessary voltage, which contributes to minimizing power. Then, by varying S* the power consumption and achievable pressure can be increased or decreased to design purposes and still be on the Pareto frontier.

Physically, though, the answers are not accurate. It is possible to have hundreds of electrodes built within a span of 10mm using MEMs technology, however the assumptions we made to simplify the equation for the current in the power function assume that the electrodes are plates parallel to the cross-section of the channel that allow liquid to flow through them; the power necessary to obtain pressure in the MPa would be

significantly higher if the model was more realistic, with planar electrodes. Other factors are non-homegeous surfaces and liquid properties, which can negatively affect the electroosmoic flow and increase the amount of power necessary to obtain high pressure. Also, the amount of power wasted due to heat loss would increase as the number of electrode pairs increase, thus greatly increasing the power necessary to achieve high pressure.

11.4 Parametric Study

For each of the canned one-objective formulations, a parametric study was carried out using the electric field (E) and the length of the channel (Lc). This allowed a better understanding of the relationship between the objective functions and these parameters for which assumptions were made.

11.4.1 Parametric Study: One Objective-Power – Effect of E

Changing the value of E in the one-objective formulation for minimizing power yielded the following results. As seen in the graph below, increasing E led to an increase in the power consumed by the system, even though the variables stay the same. For scenario 1, the solver indicated that no feasible solution was found, indicating that limiting the electric field too much made the system unable to generate the minimum pressure identified in the constraints. Scenario 5 highlighted a shift in the design, where the electric field was so strong that the pressure requirements could be met using reduced channel geometry.

Table 11. Parametric Study on E (Lc=10;MuxGamma=5.76;100<E<1000000) [f=Power]

Scenario	E	x1 (D)	x2 (W)	x3 (S)	x4 (S*)	Power
1	10	0.0050	0.0001	0.0100	9.0000	1.0544e-11
2	100	0.0050	0.0001	0.0100	9.0000	1.0544e-09
3	500	0.0050	0.0001	0.0100	9.0000	2.6360e-08
4 (base)	1000	0.0050	0.0001	0.0100	9.0000	1.0544e-07
5	10000	0.0001	0.0001	0.0100	9.0000	2.1088e-07

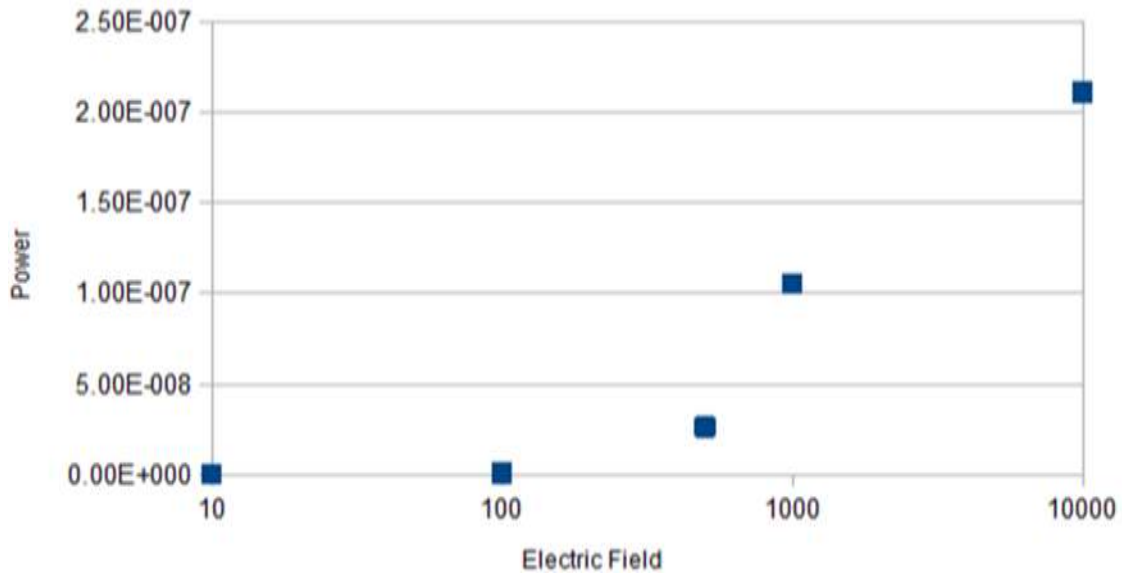

Figure 129. Parametric study: effect of electric field on power.

11.4.2 Parametric Study: One Objective-Power – Effect of Lc

Changing the value of Lc in the one-objective formulation for minimizing power yielded the following results. As seen in the graph below, increasing Lc led to an increase in the power consumed by the system, even though most of the design variables stayed the same. It was observed that the spacing between adjacent electrode pairs was reduced for scenarios where the channel length was smaller than the base case. It is interesting that for these cases there was not much of a shift in power once the channel length got smaller than 7.5 millimeters. For cases where the length of the channel was larger than the base case, it was observed that there was a significant increase in power, which makes sense as longer channels require additional electrode pairs, due to the upper limit on spacing between the electrodes.

Table 12. Parametric Study on Lc (E=1000;MuxGamma=5.76;5<Lc<25) [f=Power]

Scenario	Lc	x1 (D)	x2 (W)	x3 (S)	x4 (S*)	Power
1	2.5	0.0050	0.0001	0.0100	2.4800	9.9745e-08
2	5	0.0050	0.0001	0.0100	4.9800	9.9689e-08
3	7.5	0.0050	0.0001	0.0100	7.4800	9.9634e-08
4(base)	10	0.0050	0.0001	0.0100	9.0000	1.0544e-07
5	15	0.0050	0.0001	0.0100	9.0000	1.3319e-07

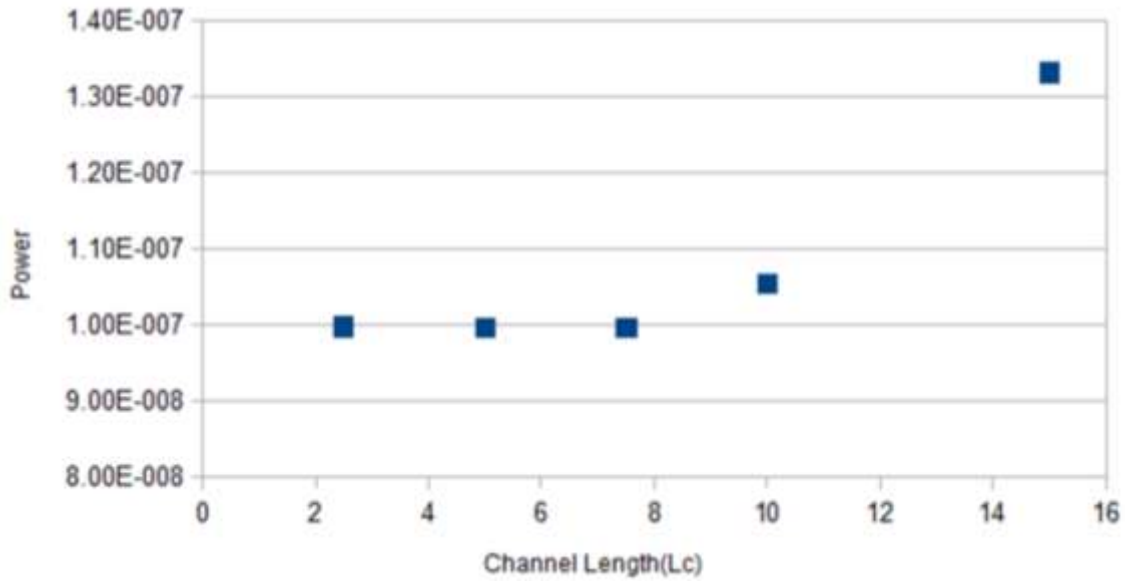

Figure 16. Parametric study: effect of channel length on pressure.

11.4.3 Parametric Study: One Objective-Pressure – Effect of E

Changing the value of E in the one-objective formulation for maximizing pressure yielded the following results. As seen in the graph below, increasing E led to an increase in the pressure generated by the system, even though the variables stay the same. For scenarios 1 through 4, the reduced E meant that there was an enormous drop in the pressure generated. Conversely, in can be seen that increased E led to much higher generated pressure.

Table 13. Parametric Study on E (Lc=10;MuxGamma=5.76;1<E<1000000)

[f=Pressure]

Scenario	E	x1 (D)	x2 (W)	x3 (S)	x4 (S*)	Pressure
1	10	0.0001	0.0001	0.0100	0.0241	1.1723e+06
2	25	0.0001	0.0001	0.0100	0.0241	2.9308e+06
3	50	0.0001	0.0001	0.0100	0.0241	5.8615e+06
4	100	0.0001	0.0001	0.0100	0.0241	1.1723e+07
5 (base)	1000	0.0001	0.0001	0.0100	0.0241	1.1723e+08
6	5000	0.0001	0.0001	0.0100	0.0241	5.8615e+08
7	10000	0.0001	0.0001	0.0100	0.0241	1.1723e+09

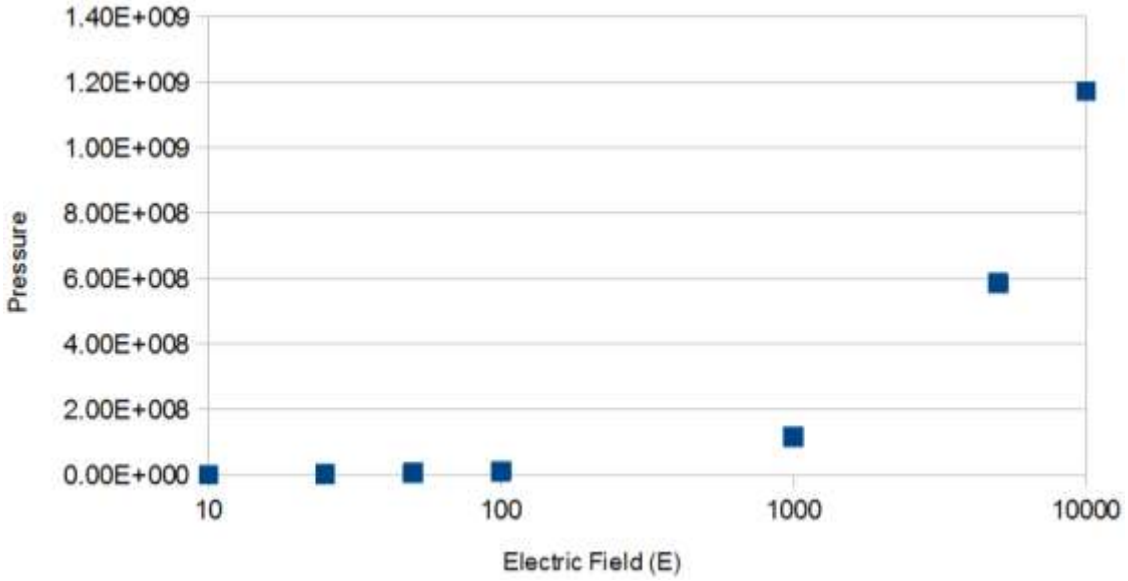

Figure 130. Parametric study: effect of electric field on pressure.

11.4.4 Parametric Study: One Objective-Pressure – Effect of Lc

Changing the value of Lc in the one-objective formulation for maximizing pressure yielded the following results. As seen in the graph below, increasing Lc led to an increase in the pressure. This relationship looks exponential. For lower channel lengths, there was less pressure than in the optimized case.

Table 14. Parametric Study on Lc (E=1000;MuxGamma=5.76;5<Lc<25)

[f=Pressure]

Scenario	Lc	x1 (D)	x2 (W)	x3 (S)	x4 (S*)	Pressure
1	5	0.0001	0.0001	0.0100	0.0241	2.9448e+07
2(base)	10	0.0001	0.0001	0.0100	0.0241	1.1723e+08
3	15	0.0001	0.0001	0.0100	0.0241	2.6335e+08
4	20	0.0001	0.0001	0.0100	0.0241	4.6780e+08
5	25	0.0001	0.0001	0.0100	0.0241	7.3058e+08

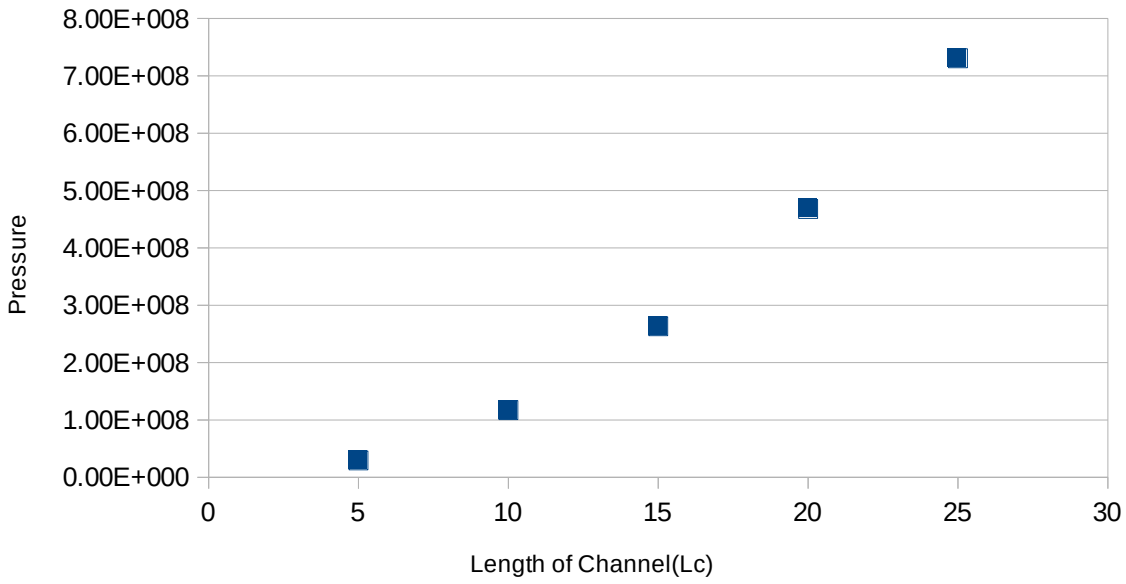

Figure 131: Parametric study: effect of channel length on pressure

11.5 Conclusions

This project successfully demonstrated the application of optimization techniques to solve a practical problem in the field of micro fluidics. Several canned and coded approaches were used to examine the tradeoffs in the design of a microfluidic channel that uses electroosmotic flow. The direct conflict between the goal of maximizing the pressure generated by electrodes used to create flow in the channel and the goal of minimizing power consumption of the system was examined through comparisons using single and multiple objective formulations.

The single objective case demonstrated the nature of the conflicting goals. Both the canned fmincon and the coded ALM methods identified that there were differences in design based on the chosen objective function. For minimized power, both methods identified that small spacing and a minimum number of electrodes led to a system that could provide a minimum pressure. Similarly, for maximized pressure, both methods led to a design where over a hundred optimally spaced electrodes were used in the design of the channel. The difference in the geometries of these designs identified that there was some tradeoff between these two objectives.

The bi-objective formulation of the problem showed how the tradeoff between these two objectives led to the creation of a Pareto Frontier. Both fminimax and fgoalattain methods led to the creation of a Pareto Frontier as the improvement of one goal was complemented with the worsening of the other. Points sampled along the frontier had geometries that were between the two extreme designs that were seen in the single objective formulation. Several parametric studies demonstrated that these differences were due to the conflicting objectives and not the selection of parameter values. Changing the electric field and the length of the channel impacted the optimal solution of one of the objectives by improving it, but diminished the optimal solution for the other objective.

This project highlighted the conflicting objectives that exist in the design of a microfluidic channel that uses electroosmotic flow. The goals of maximizing channel pressure and minimizing power consumption are contradictory, and optimization can be

used to generate different designs that tradeoff the two goals. Certain assumptions, such as electrode geometry and material properties were idealized in a way that results in the calculation of theoretical values that are much more desirable than their experimental counterparts. However, this project successfully demonstrated that tradeoffs exist in the design of microfluidic systems, and that designers must be careful in matching their designs with desired performance.

11.6 Nomenclature

Variables		
Symbol	**Term**	**Definition**
D	Depth of Channel	The depth of the channel. This is a design variable.
N	Number of Electrodes	The number of electrodes along the channel. This is a design variable.
S	Spacing of Electrodes	The spacing between electrodes in the same pair. This is a design variable.
W	Width of Channel	The width of the channel. This is a design variable.

Parameters		
Symbol	**Term**	**Definition**

P	Power	The power consumed generating the electric field in the channel. This is an objective function that we are trying to minimize.
Pr	Pressure	The pressure generated inside the chamber. This is an objective function that we are trying to maximize.
E	Electric Field	The electric field between each electrode pair. This is fixed to simplify the problem.
Lc	Length of Channel	The total length of the channel, from reservoir to reservoir. This parameter is assumed to be fixed to simplify the problem.
S*	Spacing between Electrode Pairs	The spacing between adjacent pairs of electrodes. This is a derived parameter based on Lc, N, and S.
ε	Permittivity	The electrical resistance found when creating an electric field in a fluid. This is a material property of the fluid and is constant.
ζ	Zeta Potential	The electric potential between the slipping plane and boundary in a system with bulk fluid flow. This is a material property of the fluid and the wall material and is constant.
η	Viscosity	The physical resistance of a fluid that is being deformed. This is a material property of the fluid

		and is constant.

11.7 Appendix I Sample Results

The following line in the command prompt yields the plot shown in Figure 132.

```
xspace = linspace(0,1000,2^8);
for i=1:length(xspace),[~,fval_ALM(i)] =
Deepa_optimization_project_1_maxP(xspace(i)); end
figure; plot(xspace,fval_ALM,'o')
```

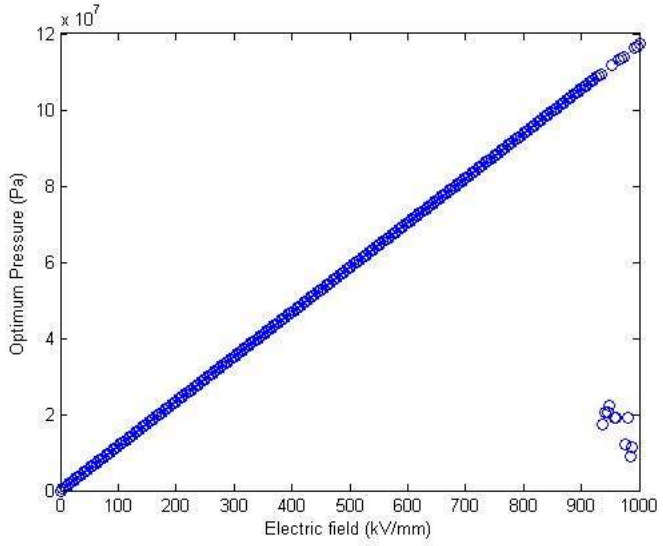

Figure 132. ALM results for pressure with varying electric field.

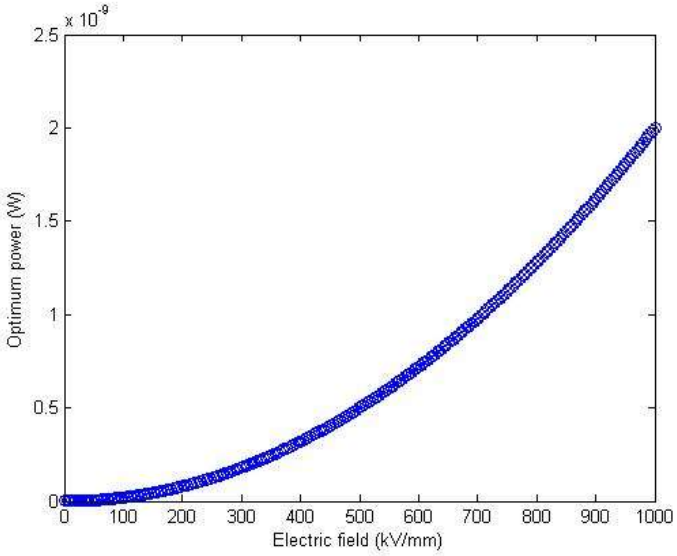

Figure 133. ALM results for power with varying electric field.

11.7.1 Single-objective Optimization Canned Approach for Power

Local minimum possible. Constraints satisfied.

fmincon stopped because the predicted change in the objective function is less than the default value of the function tolerance and constraints are satisfied to within the default value of the constraint tolerance.

<stopping criteria details>

Active inequalities (to within options.TolCon = 1e-06):

lower upper ineqlin ineqnonlin

2

x = 0.0065 0.0001 0.0464 3.7408

f = 1.0940e-06

11.7.2 Single-objective Optimization Canned Approach for Pressure

Local minimum possible. Constraints satisfied.

fmincon stopped because the size of the current search direction is less than twice the default value of the step size tolerance and constraints are satisfied to within the default value of the constraint tolerance.

<stopping criteria details>

Active inequalities (to within options.TolCon = 1e-06):

lower upper ineqlin ineqnonlin

1

3

x = 0.0001 0.0010 0.0100 0.0241

f = -1.1723e+08

11.7.3 Bi-objective Optimization Fminimax: Raw Pareto Graph

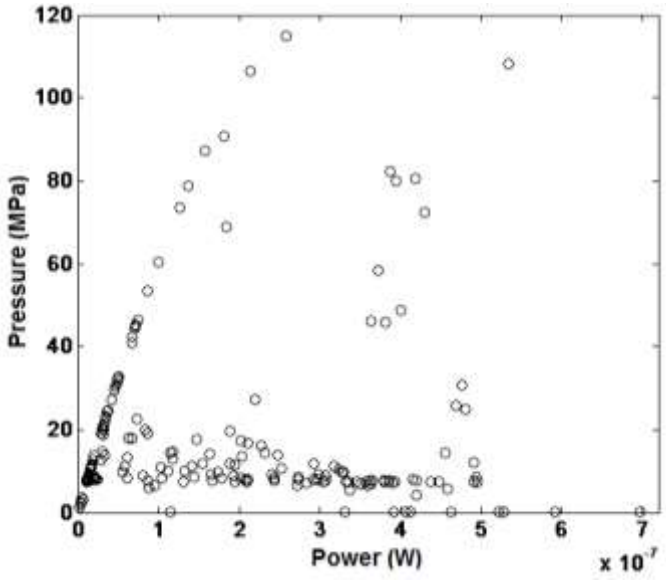

Figure 134. Bi-objective Optimization Fminimax: Raw Pareto Graph

11.7.4 Bi-objective Optimization Fgoalattain: Raw Pareto Graph

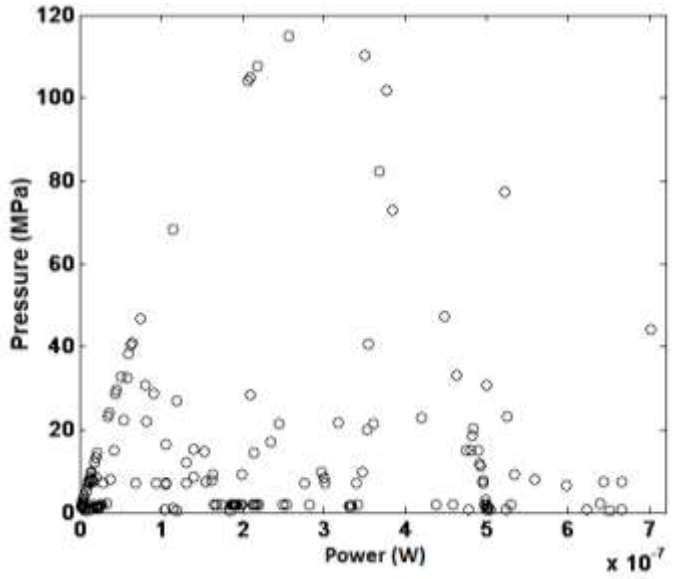

Figure 135. Bi-objective Optimization Fgoalattain: Raw Pareto Graph

11.8 Appendix II Computerized Codes

11.8.1 Single-Objective Approach: Augmented Lagrangian Method

```
function [sols,fval] =
Deepa_optimization_project_1_minJ(varargin)


lambda = zeros(3,1);
rp = 1;
gamma = 1.5; % rp dilation factor
rp_max = 1/eps; % penalty factor
Tol_cons = 1e-8;  % constraint violation tolerance
```

```
options = optimset('fmincon');


options.TolX = 1e-10;
options.TolFunc = 1e-10;
options.MaxIter = 100;
options.MaxFunEvals = 2000;
options.Display = 'off';
options.Algorithm = 'active-set';
epsilon = 566.656E-9;  % Farad/mm
zeta = 0.1; % volts
L = 10;
if nargin < 1
E = 1000;  % electric field kV/mm
else
E = varargin{1};
end
rho = 1E5;
% S = x(1); S* = x(2); D = x(3); w = x(4);


x0=[0.01,9,.005,0.0001];


warning('off');
sols=x0;
iter = 0;
```

```
LB=[0.01,0.01,0.0001,0.0001];
UB=[10,9.99,0.2,0.2];

while iter<=500  % Keep running the loop
    [sols,fval] = fmincon(@(x)
ALM_obj_func(x,lambda(1),lambda(2),lambda(3),rp,E),sols,[],[],[],
[],LB,UB,[],options);
    if
norm(ineq_cons_func(sols,lambda(1),lambda(2),lambda(3),rp,E),Inf)
<= Tol_cons
        break;
    end
    % Update lambda and, possibly, rp
    lambda = lambda +
2*rp*ineq_cons_func(sols,lambda(1),lambda(2),lambda(3),rp,E);
    rp = min(gamma*rp,rp_max);
    iter = iter+1;
end
fval = exp(fval);

function out = obj_func(x,varargin)
epsilon = 566.656E-9;  % Farad/mm
E = varargin{1};  % electric field
zeta = 0.1; % volts
```

```
L = 10;  % distance in mm
rho = 1E5; % resistivity

out = ((L+x(2))/(x(1)+x(2)))*E^2*x(1)*x(4)*x(3)/rho;
out = log(out);

function out = ineq_cons_func(x,varargin)
% S = x(1); S* = x(2); D = x(3); w = x(4);
epsilon = 566.656E-9;  % Farad/mm
E = varargin{5};  % electric field
zeta = 0.1; % volts
L = 10;  % distance in mm
rho = 1E5; % resistivity

out(1)=max((x(2)+2*x(1))-L,-varargin{1}/2/varargin{4});
out(2)=max(x(4)-10*x(3),-varargin{2}/2/varargin{4});
out(3)=max(20-
((12*epsilon*zeta*L*E)/x(3)^2)*(((L+x(2))/(x(1)+x(2)))-
(x(1)/x(2))*(((L+x(2))/(x(1)+x(2)))-1)),-
varargin{3}/2/varargin{4});
out = out(:);


function out = ALM_obj_func(x,varargin)
% S = x(1); S* = x(2); D = x(3); w = x(4);
```

```
out = obj_func(x,varargin{5})+...

dot(cell2mat(varargin(1:3)),ineq_cons_func(x,varargin{1},varargin
{2},varargin{3},varargin{4},varargin{5}))+...

varargin{4}*sum(ineq_cons_func(x,varargin{1},varargin{2},varargin
{3},varargin{4},varargin{5}).^2);
```

11.8.2 Single-Objective Canned Approach: Power

```
function SemProj_OneObj_Power
%x = [D,W,S,S*]= [x1,x2,x3,x4]
%Sets initial, upper, and lower bounds for variables
x0=[.01,.15,5,1];
xl=[.0001,.0001,.01,.01];
xu=[.2,.2,10,9.98];


%Parameters
E=1000; Lc=10;EpsilonxZeta= 5.66656e-8;rho = 1e5;
options=optimset('Algorithm','active-set');

[x,f]=fmincon(@LinF,x0,[],[],[],[],[253],[xu],@LinCon,options,E,Lc,Epsi
lonxZeta,rho)

%Objective function for Power
```

```
function f = LinF(x,E,Lc,EpsilonxZeta,rho)
f= ((Lc+x(4))/(x(3)+x(4)))*E^2*x(3)*x(2)*x(1)/rho ;


%Constraints
function [C,Ceq]=LinCon(x,E,Lc,EpsilonxZeta,rho)
C(1) = x(2)-10*x(1)
C(2) = (20-((12*EpsilonxZeta*Lc*E)/x(1)^2)*(((Lc+x(4))/(x(3)+x(4)))-
(x(3)/x(4))*(((Lc+x(4))/(x(3)+x(4)))-1)))
C(3) = (x(4)+2*x(3))-Lc
Ceq=[];
```

11.8.3 Single-Objective Approach: Augmented Lagrangian Method

```
function [sols,fval] =
Deepa_optimization_project_1_maxP(varargin)
% This function optimizes a function with inequality-equality
constaints using the augmented Lagrangian method

lambda = zeros(3,1);
rp = 1;
gamma = 1.5; % dilation factor
rp_max = 1/eps; % penalty factor
Tol_cons = 1e-8;  % Constraint violation tolerance

options = optimset('fmincon');

options.TolX = 1e-10;
options.TolFun = 1e-10;
options.MaxIter = 100;
options.MaxFunEvals = 2000;
options.Display = 'off';
epsilon = 566.656E-9;  % permittivity in Farad/mm
zeta = 0.1; % zeta potential in volts
L = 10;  % channel length in mm
if nargin < 1
    E=1000; % electric field V/mm
```

```
else
    E = varargin{1};
end
rho = 1E5;

% S = x(1); S* = x(2); D = x(3); w = x(4);

x0=[5,1,0.01,0.15];

%sols = fminunc(@(x) -obj_func(x),x0,options);
warning('off');
sols=x0;
iter = 0;

LB=[0.01,0.01,0.0001,0.0001]; % lower bound
UB=[10,9.99,0.2,0.2]; % upper bound

while iter<=500
    [sols,fval] = fmincon(@(x)
ALM_obj_func(x,lambda(1),lambda(2),lambda(3),rp,E),sols,[],[],[],
[],LB,UB,[],options);
    fval = -fval;
```

```
    if
norm(ineq_cons_func(sols,lambda(1),lambda(2),lambda(3),rp,E),Inf)
<= Tol_cons
        break;
    end
% Update lambda and, possibly, rp
        lambda = lambda +
2*rp*ineq_cons_func(sols,lambda(1),lambda(2),lambda(3),rp,E);

    rp = min(gamma*rp,rp_max);
    iter = iter+1;
end

function out = obj_func(x,varargin)
% S = x(1); S* = x(2); D = x(3); w = x(4);
epsilon = 566.656E-9;  % Farad/mm
if nargin<1
E = 1E3;  % electric field
else
E = varargin{1};
end
zeta = 0.1;
L = 10;
rho = 1E5; % resistivity of propylene carbonate in ohm/mm
```

```
out = -((12*epsilon*zeta*L*E)/x(3)^2)*(((L+x(2))/(x(1)+x(2)))*(1-
x(1)/x(2))+x(1)/x(2));

function out = ineq_cons_func(x,varargin)
% S = x(1); S* = x(2); D = x(3); w = x(4);
epsilon = 566.656E-9;  % Farad/mm
if nargin<1
E = 1E3;  % electric field
else
E = varargin{5};
end
zeta = 0.1; % volts
L = 10;  % distance in mm
rho = 1E5; % resistivity

out(1)=max((x(2)+2*x(1))-L,-varargin{1}/2/varargin{4});
out(2)=max(x(4)-10*x(3),-varargin{2}/2/varargin{4});
out(3)=max(((L+x(2))/(x(1)+x(2)))*E^2*x(1)*x(4)*x(3)/rho-60,-
varargin{3}/2/varargin{4});
out = out(:);



function out = ALM_obj_func(x,varargin)
% S = x(1); S* = x(2); D = x(3); w = x(4);
out = obj_func(x,varargin{5})+...
```

```
dot(cell2mat(varargin(1:3)),ineq_cons_func(x,varargin{1},varargin
{2},varargin{3},varargin{4},varargin{5}))+...

varargin{4}*sum(ineq_cons_func(x,varargin{1},varargin{2},varargin
{3},varargin{4},varargin{5}).^2);
```

11.8.4 Single-Objective Canned Approach: Pressure

```
function SemProj_OneObj_Pressure
%x = [D,W,S,S*]= [x1,x2,x3,x4]
%Sets initial, upper, and lower bounds for variables
x0=[.1,.15,5,1];
xl=[.0001,.0001,.01,.01];
xu=[.2,.2,10,9.98];


%Parameters
E=1000; Lc=10;EpsilonxZeta= 5.66656e-8;rho = 1e5;
options=optimset('Algorithm','active-set');

[x,f]=fmincon(@LinF,x0,[],[],[],[],[253],[xu],@LinCon,options,E,Lc,Epsi
lonxZeta,rho)

%Objective function for Power
function f = LinF(x,E,Lc,EpsilonxZeta,rho)
```

```
f= ((12*EpsilonxZeta*Lc*E)/x(1)^2)*(((Lc+x(4))/(x(3)+x(4)))-
(x(3)/x(4))*(((Lc+x(4))/(x(3)+x(4)))-1));


%Constraints
function [C,Ceq]=LinCon(x,E,Lc,EpsilonxZeta,rho)
C(1) = x(2)-10*x(1)
C(2) = (-60+((Lc+x(4))/(x(3)+x(4)))*E^2*x(3)*x(2)*x(1)/rho)
C(3) = (x(4)+2*x(3))-Lc
Ceq=[];
```

11.8.5 Bi-Objective Canned Approach: fminimax

```
function SemProj_BiObj fminimax
%% Defining variables and parameters
%x=[D,W,S,S*]=[x1,x2,x3,x4]
lb=[0.0001, 0.0001,0.01,0.01]; %lower bounds
ub=[0.2, 0.2, 10, 9.99]; %upper bounds


%parameters%
E=1000; Lc=10; epsilonxzeta=5.6666e-008; rho=1e5;


%linear constraints and coefficients
A=[0 0 -1 0;0 0 2 1];
b=[-0.01, Lc]';


%good values obtained by Assuming desirable N=50, V=10 Volts, I=1e-6
good=[5e-4, -7e6];
ypoint=[0,0,0,0];


%% For loop to vary initial starting point
%counters
c1=0;c2=0;c3=0;
W=0.1; %set width to be a constant since it doesnt affect the initial
point
        that much if varied


for k=1:10
```

```
    x1(k)=0.0001+0.001*k;
    c1=c1+1;
    bad=[1.2e-3+k*9e-4, -1.4e3-k*2e5]; %bad values were chosen based on
                                       undesirable solutions
    for j=1:5
        x3(j)=0.01+0.05*j;
        c2=c2+1;
        for i=1:5
            x4(i)=0.01+0.01*i;
            c3=c3+1;
            x0(c3,1)=x1(k);
            x0(c3,2)=W;
            x0(c3,3)=x3(j);
            x0(c3,4)=x4(i);
            [x,fxopt]=fminimax(@EOFObj,x0(c3,:),A,b,[],[],lb,ub,...
                @NonLinCon,[],E,Lc,rho,epsilonxzeta,good,bad);
                    for m=1:2
                        %rescaling objective function solutions back to
                        original magnitude
                        ff(m)=fxopt(m)*(bad(m)-good(m))+good(m);
                    end


            f1(c3)=ff(1);
            f2(c3)=ff(2);
            ypoint(c3,:)=x;
        end
    end
end
```

```
ypoint %prints all the x values for each optimal solution...
       %so I can get the solutions to selected Pareto points
[f2sort,indxf2]=sort(f2);
f1sort=f1(indxf2);
plot(f1sort,-f2sort/1e6,'ko')
xlabel('Power (W)')
ylabel('Pressure (MPa)')

%% Nonlinear constraints on Power, Pressure, and aspect ratio
function [C,Ceq]=NonLinCon(x,E,Lc,rho,epsilonxzeta,good,bad)

C(1) = -60+((Lc+x(4))/(x(3)+x(4)))*E^2*x(1)*x(2)*x(3)/rho;
C(2) = (20-(12*epsilonxzeta*Lc*E/(x(1)^2))*((Lc+x(4))/(x(3)+x(4))-...
    x(3)/x(4)*(Lc+x(4))/(x(3)+x(4))+x(3)/x(4)))*10^-10;

C(3) =-10+x(2)/x(1);
Ceq=[];

%% Objective Function: With good and bad values scaling objective
functions before it goes into the fminimax program
function f=EOFObj(x,E,Lc,rho,epsilonxzeta,good,bad)

f1=((Lc+x(4))/(x(3)+x(4)))*E^2*x(1)*x(2)*x(3)/rho;
f2=-1*(12*epsilonxzeta*Lc*E/(x(1)^2))*...
    ((Lc+x(4))/(x(3)+x(4))-x(3)/x(4)*(Lc+x(4))/(x(3)+x(4))+x(3)/x(4));

f(1)=(f1-good(1))/(bad(1)-good(1));
```

```
f(2)=(f2-good(2))/(bad(2)-good(2));
```

11.8.6 Bi-Objective Canned Approach: fgoalattain

```
function SemProj_BiObjgoalattainment
%% Defining variables and parameters
%x=[D,W,S,S*]=[x1,x2,x3,x4]
lb=[0.0001, 0.0001,0.01,0.01]; %lower bounds
ub=[0.2, 0.2, 10, 9.99]; %upper bounds


%parameters
E=1000; Lc=10; epsilonxgamma=5.6666e-008; rho=1e5;
A=[0 0 -1 0;0 0 2 1];
b=[-0.01, Lc]';


%Assuming desirable N=50, V=10 Volts, I=1e-6 then Power=5e-4
goal=[5e-4, -7e6];
weight=[1,1];


%% For loop to vary initial starting point
%counters
c1=0,c2=0,c3=0;
D=0.1;
for k=1:10
    x1(k)=0.0001+0.0001*k;
    c1=c1+1;
    for j=1:10
        x3(j)=0.01+0.03*j;
```

```
        c2=c2+1;
        for i=1:5
            x4(i)=0.01+0.01*i;
            c3=c3+1;
            x0(c3,1)=x1(k);
            x0(c3,2)=D;
            x0(c3,3)=x3(j);
            x0(c3,4)=x4(i);
            [x,fval]=fgoalattain(@BiObj,x0(c3,:),goal,weight,...

A,b,[],[],lb,ub,@NonLinConst,[],E,Lc,rho,epsilonxgamma);
                for m=1:2
                    ff(m)=fval(m);
                end

            f1(c3)=ff(1);
            f2(c3)=ff(2);
            ypoint(c3,:)=x; %to record the x values for all the optimal
                            solutions
        end
    end
end
ypoint %prints all the x values for each optimal solution...
       %so I can get the solutions to selected Pareto points

[f2sort,indxf2]=sort(f2);
f1sort=f1(indxf2);
```

```
plot(f1sort,-f2sort/1e6,'ko')
xlabel('Power (W)')
ylabel('Pressure (MPa)')

%%Nonlinear constraints on Power, Pressure, and aspect ratio
function [C,Ceq]=NonLinConst(x,E,Lc,rho,epsilonxgamma)

C(1) = -60+((Lc+x(4))/(x(3)+x(4)))*E^2*x(1)*x(2)*x(3)/rho;
C(2) = 20-(12*epsilonxgamma*Lc*E/(x(1)^2))*((Lc+x(4))/(x(3)+x(4))-...
    x(3)/x(4)*(Lc+x(4))/(x(3)+x(4))+x(3)/x(4));
C(3) =-10+x(2)/x(1);
Ceq=[];

%% Objective Function
function f=BiObj(x,E,Lc,rho,epsilonxgamma)

f(1)=((Lc+x(4))/(x(3)+x(4)))*E^2*x(1)*x(2)*x(3)/rho;
f(2)=-1*(12*epsilonxgamma*Lc*E/(x(1)^2))*...
    ((Lc+x(4))/(x(3)+x(4))-x(3)/x(4)*(Lc+x(4))/(x(3)+x(4))+x(3)/x(4));
```

11.9 Appendix III Derivations

11.9.1 Power Equation

For the purpose of optimizing power with numerical methods, the variables must be continous, so we converted we converted number of electrode pairs $N = \frac{L_C+S^*}{S+S^*}$.

$I = \frac{V}{R};\ V \sim voltage, R \sim resistance$

$V = \vec{E}S;\ \ E \sim electric\ field$

$R = \frac{\rho S}{A}; \rho \sim electrical\ resistivity, A \sim cross\ sectional\ area\ between\ electrodes$

Insert into power function

$$T = NVI$$

$$T = \frac{L_c + S^*}{S + S^*} V^2 * \frac{DW}{\rho S}$$

$$T = \frac{\left(\frac{L_C + S^*}{S + S^*}\right) SDW * \vec{E}^2}{\rho}$$

11.9.2 Pressure Equation

$Q_{\pm EOF} = v_{\pm EOF} WD$ Flowrate due to positive and negative EOF

$v_{EOF} = \mu_{EO} E;\ v_{-EOF} = \mu_{EO} E^*$ Velocity due to positive and negative EOF

$\mu_{EO} = \frac{\varepsilon \zeta}{\eta}$ electro osmotic mobility

$E^* = \frac{ES}{S^*}; N = \frac{L_C + S^*}{S + S^*}$ Electric field and spacing of adjacent electrode pairs

$Q_{PDF} = \frac{2W}{3\eta}\left(-\frac{\partial p}{\partial x}\right) D^3$ Pressure driven flow

Insert equations into the total flow rate equation:

$$Q_{TOT} = N Q_{EOF} - (N-1) Q_{-EOF} + Q_{PDF}$$

$$Q_{TOT} = \mu_{EO} DW\left(\vec{E} N - \overrightarrow{E^*} N + \overrightarrow{E^*}\right) - \frac{2W}{3\eta}\left(\frac{\Delta P}{L_C}\right) D^3 = 0$$

$$\mu_{EO} DW\left(\vec{E} N - \overrightarrow{E^*} N + \overrightarrow{E^*}\right) = \frac{2W}{3\eta}\left(\frac{\Delta P}{L_C}\right) D^3$$

$$\frac{3\eta L_c}{2WD^3} \mu_{EO} DW\left(\vec{E} N - \overrightarrow{E^*} N + \overrightarrow{E^*}\right) = \Delta P$$

$$\frac{3\eta L_c}{2D^2} \frac{\varepsilon \zeta}{\eta}\left(\vec{E} N - \overrightarrow{E^*} N + \overrightarrow{E^*}\right) = \Delta P$$

$$\Delta P_{MAX} = \frac{12\varepsilon\zeta L_C}{D^2}\vec{E}\left(N - \frac{S}{S^*}N + \frac{S}{S^*}\right)$$

$$\Delta P_{MAX} = \frac{12\varepsilon\zeta L_C}{D^2}\vec{E}\left(\frac{L_C + S^*}{S + S^*} - \frac{S}{S^*}\left(\frac{L_C + S^*}{S + S^*}\right) + \frac{S}{S^*}\right)$$

11.10 Appendix IV Presentation Slides

Slide 1

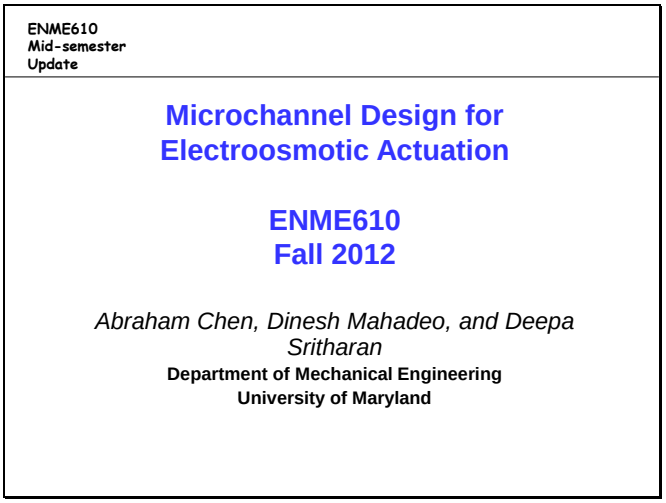

Slide 2

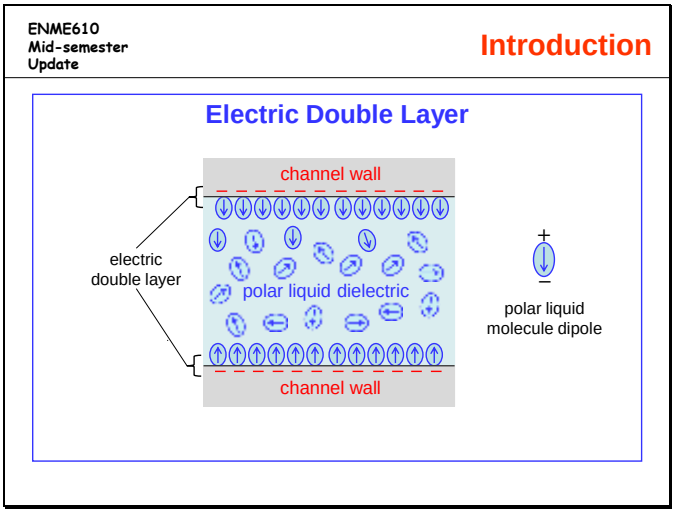

A **double layer** (**DL**, also called an **electrical double layer**, **EDL**) is a structure that appears on the surface of an object when it is placed into a liquid. When a charged solid surface is placed in a polar liquid, counterions are attracted to the charged surface to maintain electrical neutrality. Thus there exists a double layer at the interface, one side of which is positive and the other side negative causing a potential drop. This potential difference at the interface of the solid and liquid is called the zeta potential.

Slide 3

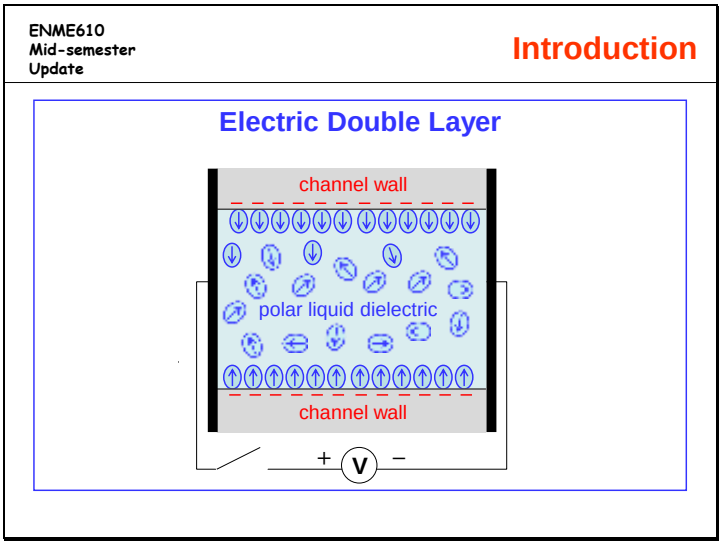

If a channel is filled with liquid and a potential is applied across the conduit….

Slide 4

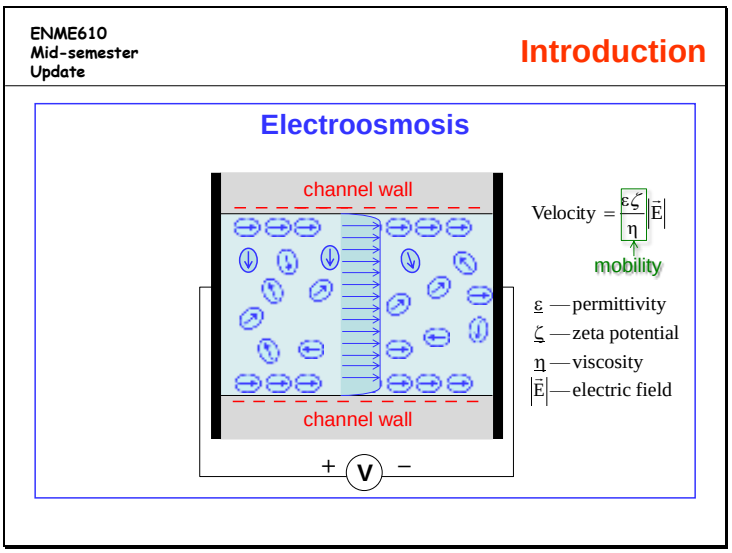

…..the counterions in the liquid will be attracted to the electrode of opposite polarity and cause liquid motion towards the electrode. The liquid flowing at the walls will drag the bulk of the liquid in the channel. Flow originates at the walls and so contrary to pressure driven flow, the no-slip condition does not apply and the resulting flow will have a uniform flow profile.

Slide 5

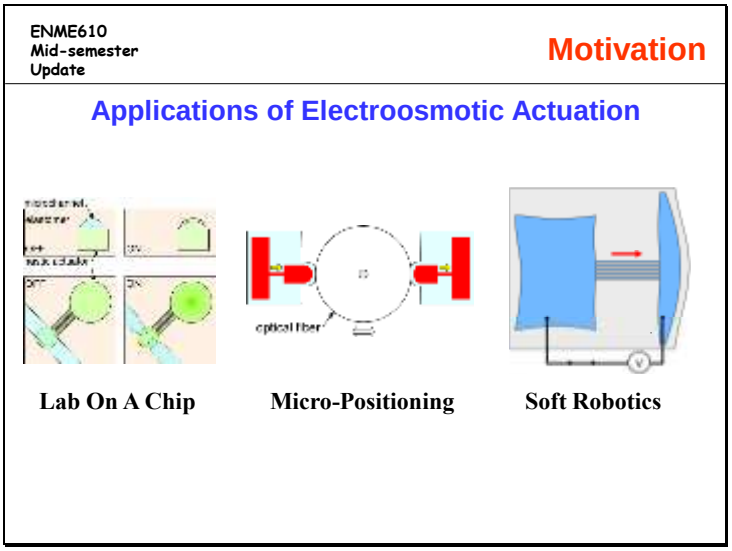

There are several potential applications of this electrohydraulic flow. Since this phenomenon is most pronounced at the microscale, where the surface-volume ratio is higher, EOF can be applied to create microfluidic pumps and valves, micropositioners and microactuators for soft robotics.

Slide 6

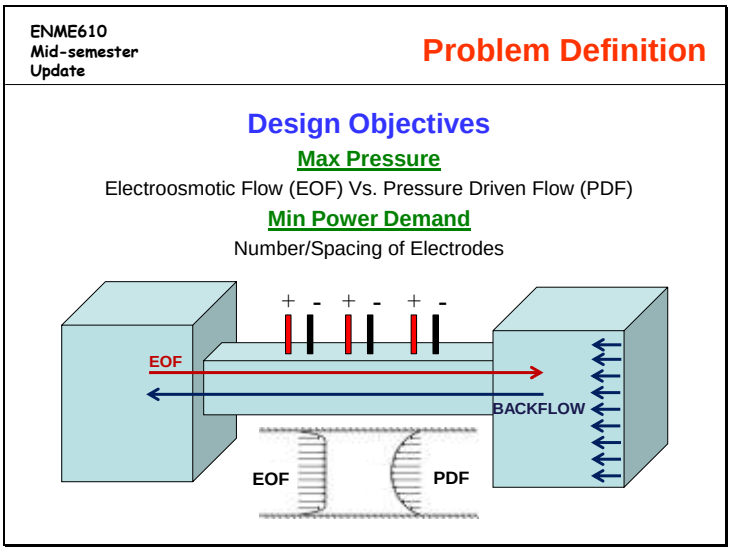

Our semester project is about designing a microfluidic channel that uses osmotic flow to actuate a soft robot. The image at the bottom, illustrates what the system would look like, two chambers linked by a channel, where electrodes are used to create flow inside the channel. This entire system can be made inside of a polymer, in this case PDMS. The

result, is that the force caused by the EOF will cause a deflection in the side of the membrane.

Our first goal is to maximize pressure inside the channel. The EOF will be counteracted by pressure driven flow as the EOF hits the walls of the chamber. The first problem we will have will be choosing a channel geometry that gives us the largest amount of generated pressure. This is important as having a high pressure will mean more force on the side of the chamber and therefore more deflection and actuation.

Our second goal is minimizing voltage demand. Instead of having a single pair of electrodes, we can place several electrode pairs along the length of the channel. However, selecting different numbers of electrodes and spacing will result in different amounts of EOF generated.

Slide 7

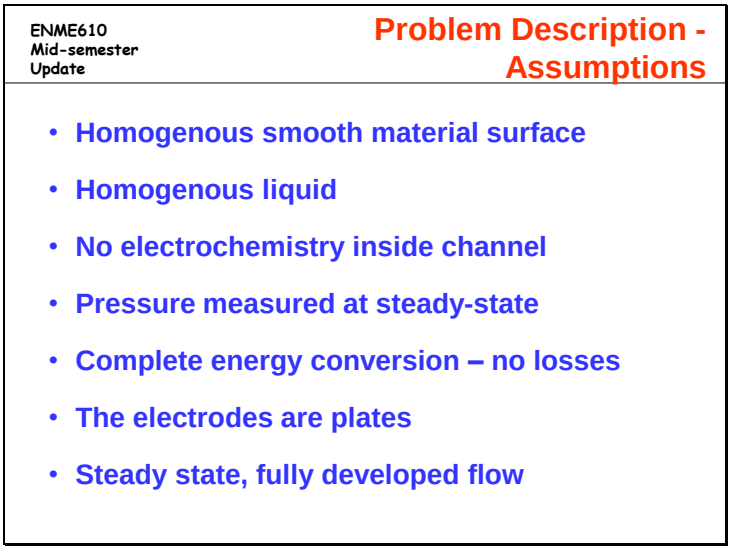

We had to make several assumptions for our project in order to simplify the problem. First, we had to assume that the channel is made of a homogenous smooth material with no imperfections. The equations for EOF that we are using are based on this assumption. Second, we had to assume a homogenous liquid, as dealing with local material properties would severely complicate our analysis. We also had to assume that no electrochemisty is happening inside the channel. Time-dependent material properties would make solving this problem even more difficult. Another assumption that made sense to us was to consider pressure at steady state, i.e. maximum deflection has to be achieved. This allows us to more easily calculate backflow and set up our equations. We also chose to assume that there was complete energy conversion, i.e. the voltage provided to the system is only used to cause EOF, and important detail for our Voltage goal.

Slide 8

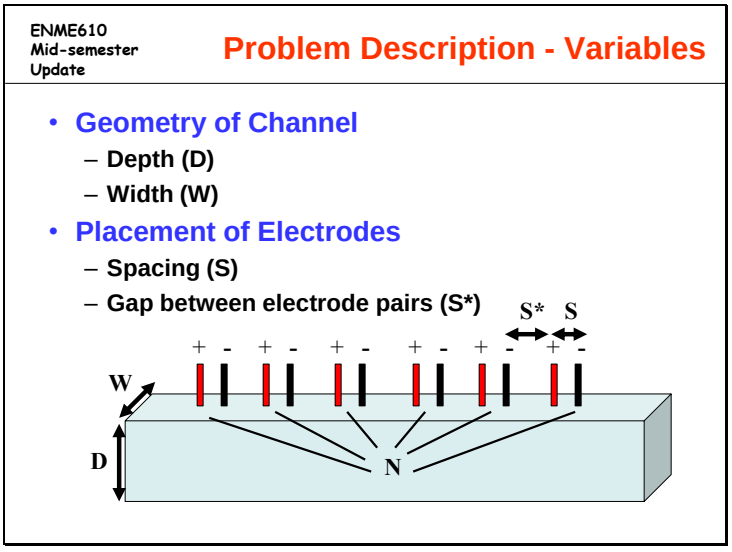

There were four design variables that need to be optimized for this system. The depth and width of the channel must be determined. The spacing between the each pair of electrodes and the number of electrode pairs were our other two variables.

Slide 9

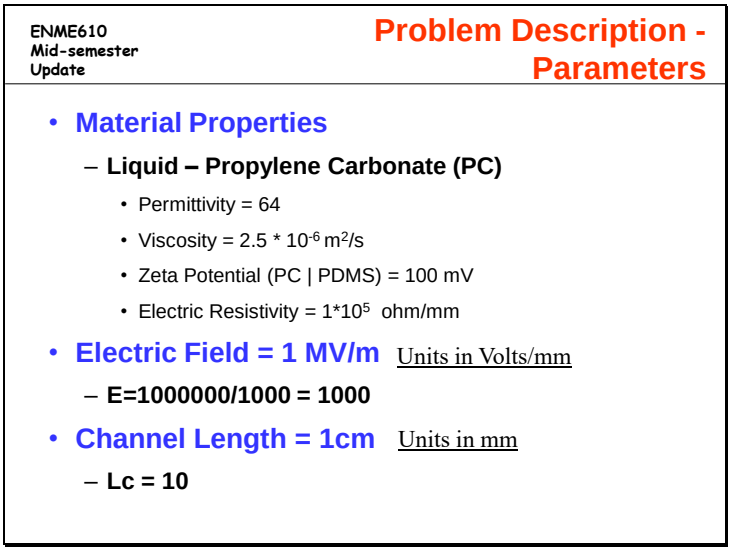

Our problem had several parameters, some that were physically defined for us, and some that we selected to make the problem solvable. The material properties of the liquid are important for calculating EOF, and are fixed. We decided to limit the electric field within our problem in order to simplify the problem. We fixed our channel length, as it would allow us to use the number of electrodes and spacing of electrodes as the only two length-based properties.

Slide 10

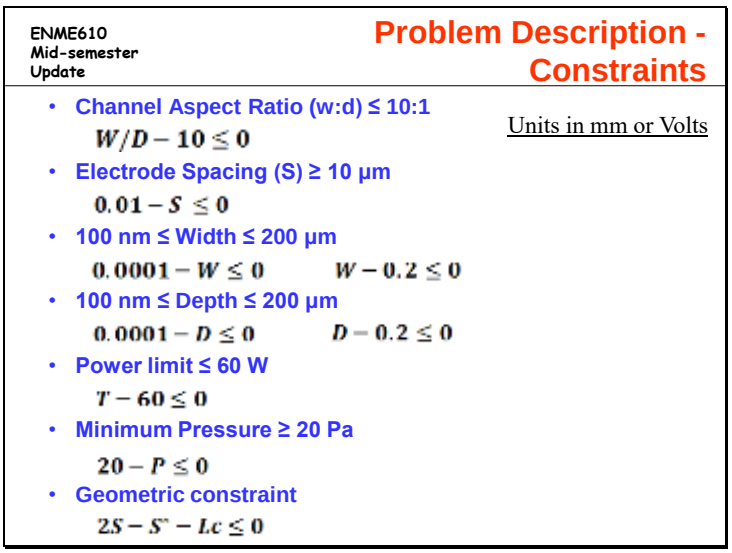

We had several constraints when we set up this problem. The channel aspect ratio has a maximum due to limits of the fabrication methods that are used in these systems. A minimum was placed on the electrode spacing based on fabrication limitations. Limits were placed on the width and depth because of fabrication limitations and the range within which the phenomenon is observed. We also set a hard voltage limit based on the equipment used in this type of laboratory application. We chose a minimum for pressure, as we wanted to ensure that each cycle passed the pressure requirement to have actuation in our system.

Slide 11

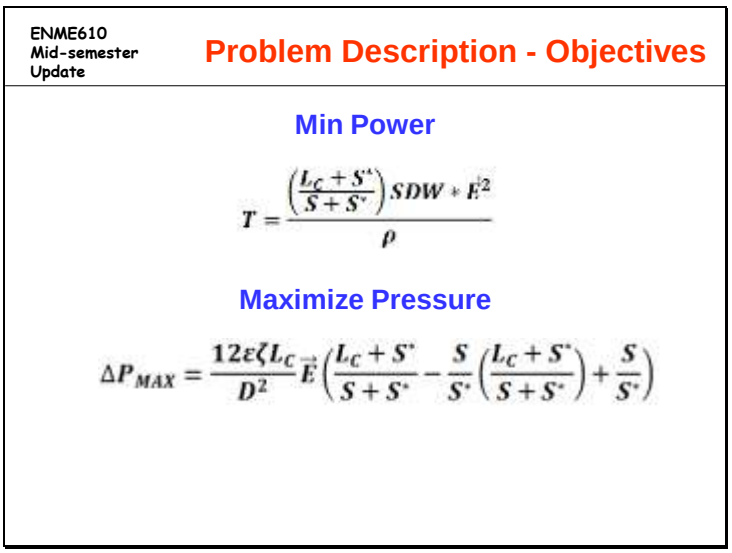

Objective Functions

-1st goal is to minimize voltage while maintaining a set electric field. This is so that the amount of energy used to obtain the maximum pressure is minimized. The equation is straight forward, the voltage is equal to the spacing between the negative and positive electrodes multiplied by the electric field.

-2nd goal is to maximum the pressure, and thereby achieving maximum actuation. Most important to note that the pressure is inversely proportional to the squared of the depth and it is linearly proportional to the electric field. The equation is derived from the interaction of the EOF flow, the opposing EOF flow, and the pressure driven flow. So the left term is from the pressure driven flow while the right term describes the influence of the negative EOF flow between the pairs of electrodes, on the overall max pressure.

Slide 12

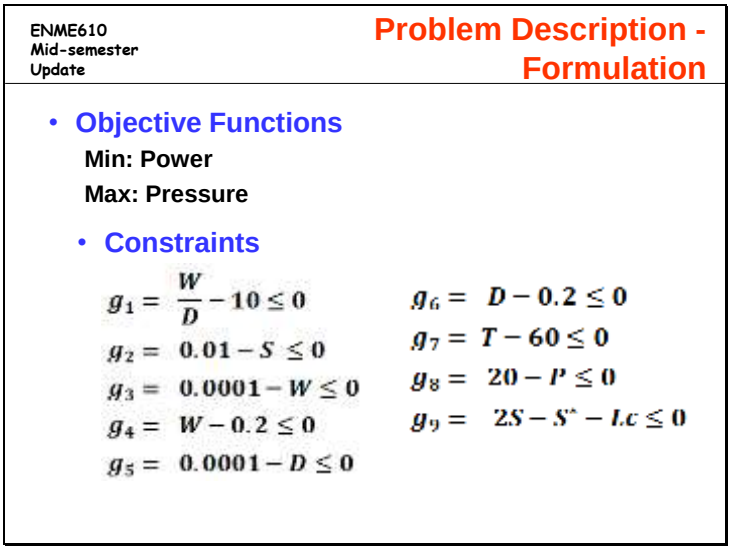

Here is the entire problem written out. We have two objective functions, one that minimizes the voltage and the other, which maximizes the pressure. And we have seven inequality constraints, based on geometry and spacing constraints.

Slide 13

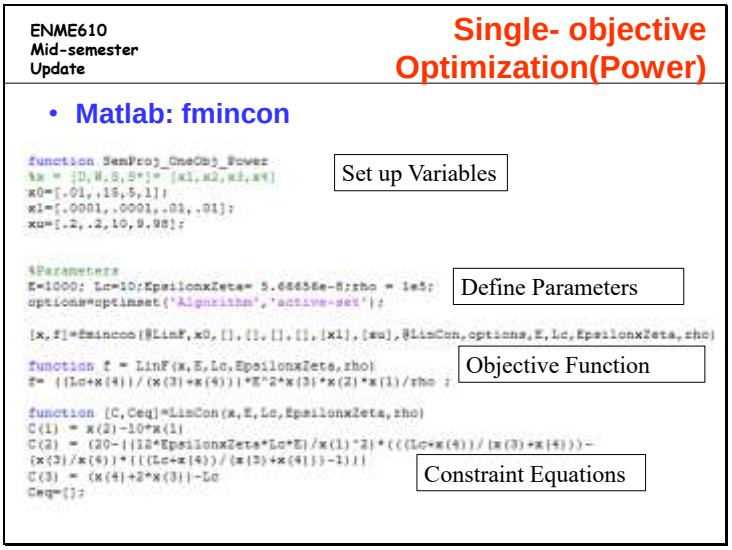

This is the code for the single objective solution using Matlab's fmincon function. In this version of the code, the objective function is Power. We can see that we sup up initial and bounds for our variables, defined all of our parameters and objective function, and set up the constraint equations. The three constraints we used were the aspect ratio constraint, the pressure constraint, and the geometry constraint.

Slide 14

ENME610
Mid-semester
Update

Single- objective Optimization(Power)

- **Matlab Output(Initial)**
  - **x = 0.0062 0.0001 0.0899 3.5938**
  - **f = 2.0665e-06**
- **Matlab Output (ALM seeded)**
  - **x = 0.0050 0.0001 0.0100 9.0000**
  - **f = 1.0544e-07**

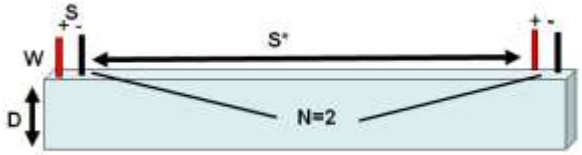

This is the output for the single objective problem with power as the objective. There are very few electrode pairs as the power consumed increases with the number of electrodes.

Slide 15

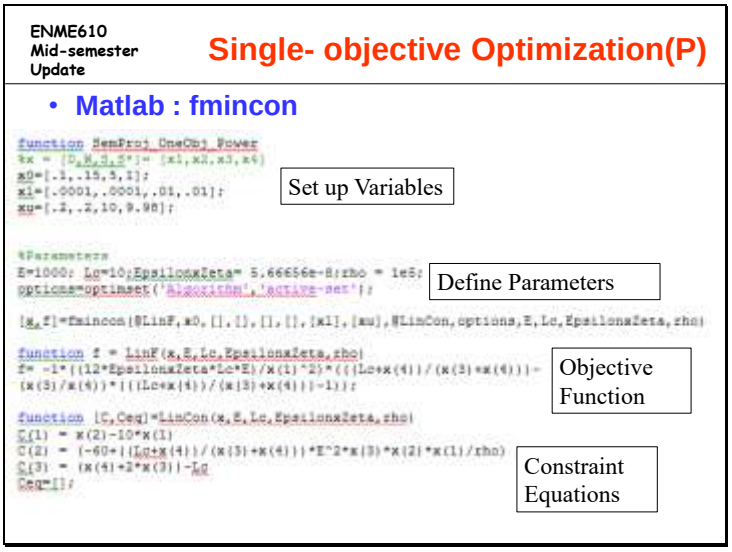

This is the code for the single objective solution using Matlab's fmincon function. In this version of the code, the objective function is Pressure. We can see that we sup up initial and bounds for our variables, defined all of our parameters and objective function, and set up the constraint equations. The three constraints we used were the aspect ratio constraint, the power constraint, and the geometry constraint.

Slide 16

ENME610
Mid-semester
Update

Single- objective Optimization(P)

- **Matlab Output**
  - **x = 0.0001 0.0010 0.0100 0.0241**
  - **f = 1.1723e+08**
- **Matlab Output**
  - **x = 0.0001 0.0001 0.0100 0.0241**
  - **f = 1.1723e+08**

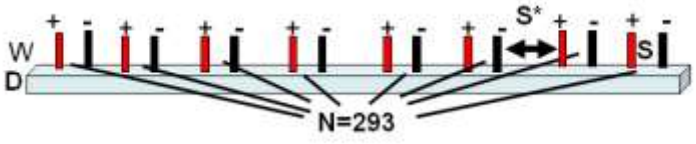

This is the output for the single objective problem with pressure as the objective. There are many more electrodes, and the channel is very narrow in this solution.

Slide 17

ENME610
Mid-semester
Update

Augmented Lagrangian Method (ALM)

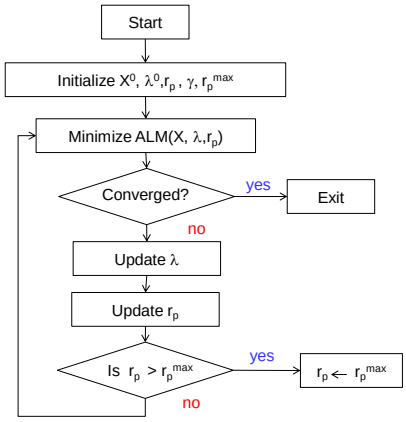

Slide 18

ENME610
Mid-semester
Update

ALM-Power

Based on output, to minimize power requirements, we need 2 electrodes placed on either end of the channel.

Min Power = 2 x 10^{-9} Watts

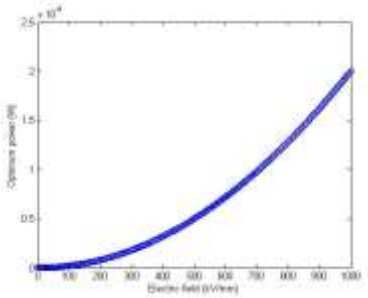

The output pressure increases for upto 293 electrode pairs after which it drops again. This is because the influence of the opposing EOF flow increases.

Slide 19

ENME610
Mid-semester
Update

ALM-Pressure

Based on output, to maximize electroosmotic pressure, we need 293 electrodes spaced on 24 microns apart.

Max Pressure = 117 MPa

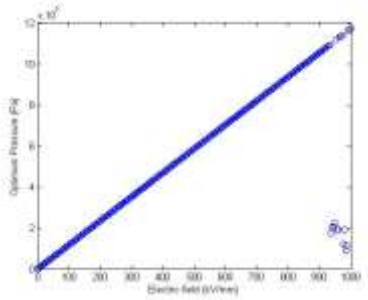

The output pressure increases for upto 293 electrode pairs after which it drops again. This is because the influence of the opposing EOF flow increases.

Slide 20

ENME610
Mid-semester
Update

ALM-fmincon comparison

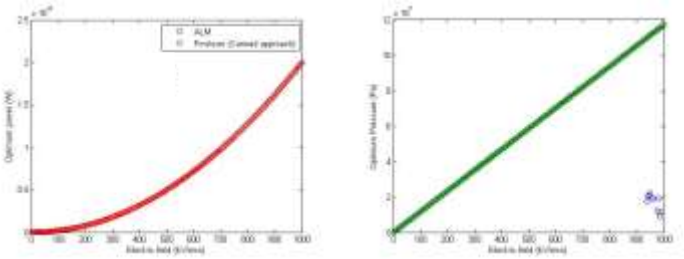

Slide 21

ENME610
Mid-semester
Update

Parametric Study (E)

- **Power**

Parametric Study on E (Lc=10;MuxGamma=5.76;100<E<1000000)						
Scenario	E	x1 (D)	x2 (W)	x3 (S)	x4 (S*)	Power
1	10	0.0050	0.0001	0.0100	9.0000	1.0544e-11
2	100	0.0050	0.0001	0.0100	9.0000	1.0544e-09
3	500	0.0050	0.0001	0.0100	9.0000	2.6360e-08
4 (base)	1000	0.0050	0.0001	0.0100	9.0000	1.0544e-07
5	10000	0.0001	0.0001	0.0100	9.0000	2.1088e-07

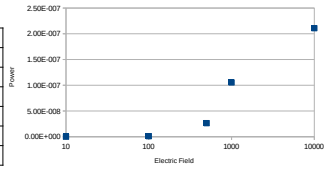

- **Pressure**

Parametric Study on E (Lc=10;MuxGamma=5.76;1<E<1000000)						
Scenario	E	x1 (D)	x2 (W)	x3 (S)	x4 (S*)	Pressure
1	10	0.0001	0.0001	0.0100	0.0241	1.1723e+06
2	25	0.0001	0.0001	0.0100	0.0241	2.9308e+06
3	50	0.0001	0.0001	0.0100	0.0241	5.8615e+06
4	100	0.0001	0.0001	0.0100	0.0241	1.1723e+07
5 (base)	1000	0.0001	0.0001	0.0100	0.0241	1.1723e+08
6	5000	0.0001	0.0001	0.0100	0.0241	5.8615e+08
7	10000	0.0001	0.0001	0.0100	0.0241	1.1723e+09

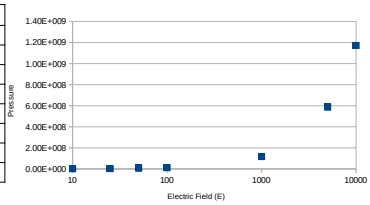

A parametric study was done for E. As E increases, it can be seen that Power increases as does pressure.

Slide 22

ENME610
Mid-semester
Update

Parametric Study (Lc)

- **Power**

Parametric Study on Lc (E=1000;MuxGamma=5.76;5<Lc<25)

Scenario	Lc	x1 (D)	x2 (W)	x3 (S)	x4 (S*)	Power
1	2.5	0.0050	0.0001	0.0100	2.4800	9.9745e-08
2	5	0.0050	0.0001	0.0100	4.9800	9.9689e-08
3	7.5	0.0050	0.0001	0.0100	7.4800	9.9634e-08
4(base)	10	0.0050	0.0001	0.0100	9.0000	1.0544e-07
5	15	0.0050	0.0001	0.0100	9.0000	1.3319e-07

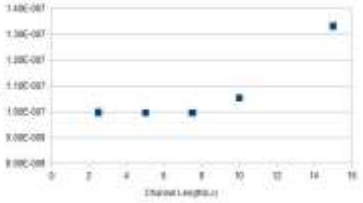

- **Pressure**

Parametric Study on Lc (E=1000;MuxGamma=5.76;5<Lc<25)

Scenario	Lc	x1 (D)	x2 (W)	x3 (S)	x4 (S*)	Pressure
1	5	0.0001	0.0001	0.0100	0.0241	2.9448e+07
2(base)	10	0.0001	0.0001	0.0100	0.0241	1.1723e+08
3	15	0.0001	0.0001	0.0100	0.0241	2.6335e+08
4	20	0.0001	0.0001	0.0100	0.0241	4.6780e+08
5	25	0.0001	0.0001	0.0100	0.0241	7.3058e+08

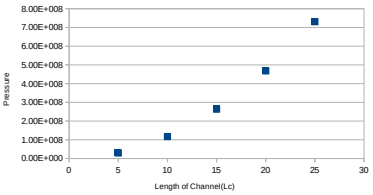

A parametric study was done for Lc. As Lc increases, it can be seen that Power increases as does pressure.

Slide 23

ENME610
Mid-semester
Update

Multi-objective Optimization

- **Results: Pareto Curves**

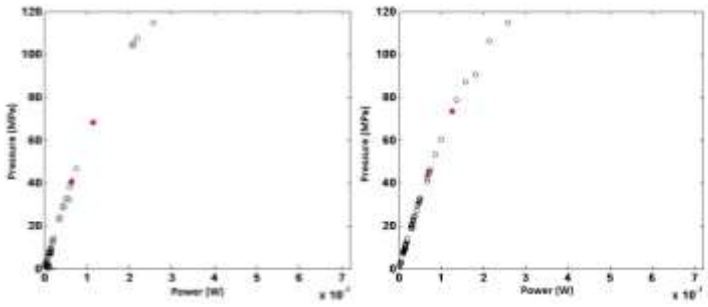

fminimax fgoalattain

This is the Pareto curve that was found by using fminimax and fgoalattain. A nested for loop was used to vary the initial starting points for D, S, and S*. Points that were found

inside the Pareto curve was erased to make the graph look more clean. The curve shows the tradeoff between power and pressure. As the amount of power used increases, the pressure increases. This is due to the increase in the number of electrodes necessary to output power. The red dots are the selected points on the curve that will be discussed in the next slide.

Slide 24

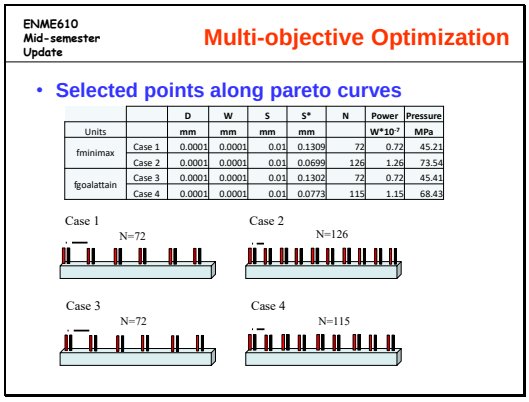

		D	W	S	S*	N	Power	Pressure
Units		mm	mm	mm	mm		$W*10^{-7}$	MPa
fminimax	Case 1	0.0001	0.0001	0.01	0.1309	72	0.72	45.21
	Case 2	0.0001	0.0001	0.01	0.0699	126	1.26	73.54
fgoalattain	Case 3	0.0001	0.0001	0.01	0.1302	72	0.72	45.41
	Case 4	0.0001	0.0001	0.01	0.0773	115	1.15	68.43

These are selected points that we obtained from the Pareto curves and these are the physical representation of the solutions. You can see that in order to increase pressure the number of electrode pairs must be increased since D,W, and S are already at their lower limits. Thus, the only variable that can influence power and pressure is S*.

Slide 25

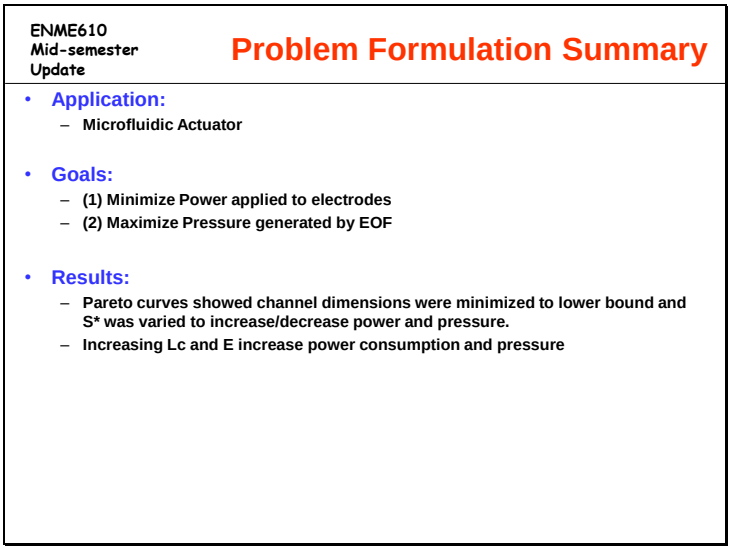

-Our overall purpose is to minimize the power and maximize the pressure for our microfluidic actuator. By doing this, we will be able to obtain the lowest energy use for the largest actuation.

-We have four variables which include the geometric parameters (depth and width of the channel) and the electrode placement parameters (spacing of the electrodes and the space between adjacent pairs of electrodes).

-The parameters includes the material properties of the liquid which would be the mobility, the applied electric field, and the channel length.

The Pareto curves for both bi-objective functions show are exhibit the same trend and are similar in values. The solutions all minimize the physical dimension of the channel to its lower bound while varying S* to increase/decrease power and pressure. The parametric study showed that with increasing Lc or E, the power consumption and pressure will increase.

Slide 26

ENME610
Mid-semester
Update

References

1. Kirby, B.J. (2010). Micro- and Nanoscale Fluid Mechanics: Transport in Microfluidic Devices: Chapter 6: Electroosmosis. Cambridge University Press.
2. CRC Handbook (1992)
3. Piyasena et al (2009). Electroosmotically driven microfluidic actuators, Sensors and Actuators B: Chemical.

12. Appendix D: Flexible Metallic Structures

12.1 Microfabrication of metal electrodes on PDMS

12.1.1 Introduction

The third objective was to reduce the operating voltage to minimize power consumption, and electrochemical degradation of the pumping liquid. In addition, for the soft actuator to deform the electrodes must be able to stretch while maintaining good electrical conductivity, so the wire electrodes used in the first prototype must be replaced with flexible electrodes.

I have tried two approaches to fabricate elastomeric electrodes: patterning thin film metal electrodes directly on PDMS films, and mixing carbon nanoparticles into an elastomeric host to create a conductive paint (see Sections 6.2.3 and 9.3).

12.1.2 Materials and Methods

I photopatterned SU-8 on PDMS and used it as a shadow mask during metal deposition (as described by Patel et al. 2009). I was able to achieve crack-free smooth metal patterns with sharp edges using the following procedure. The PDMS film was prepared by spin coating 10:1 PDMS mixture on a silicon dioxide wafer (500 rpm for 60 sec) and curing at 100 ^{o}C for 10 min on a hot plate. Then SU-8 2025 was spin-coated (350 rpm for 10 sec, and 2000 rpm for 50 sec) over the cured PDMS film spin-coat. The SU-8 was

soft-baked at 65 ^{o}C for 45 min and cool down to 50 ^{o}C (baking at temperatures higher than 65 ^{o}C caused the SU-8 to pull away from the PDMS). The SU-8 was exposed to UV light (365 nm) through a mylar photomask (mask aligner, intensity for 10 sec). After exposure the SU-8 was hard baked at 95 ^{o}C for 6 min and then cooled down to 50 ^{o}C. The sample was then immersed in SU-8 developer and sonicated for 1 min. Post development the sample was baked in an oven at 120 ^{o}C for 20 min and cooled down to 50 ^{o}C. No cracks were observed on SU-8 were inspected and found to be free of cracks or other defects. The sample was then oxygen plasma treated (conditions) to improve the metal adhesion to PDMS. The sample was then loaded (soon after baking and plasma treatment) into the e-beam (or thermal) deposition chamber and pumped down overnight, and metal was deposited the next day (conditions). The SU-8 was peeled off easily from the PDMS using tweezers, leaving behind sharp metal traces on the PDMS surface. Instead of loading immediately after the final baking step, some samples were allowed to rest overnight, at atmospheric conditions. The next day they were plasma treated and loaded into the deposition chamber which was pumped down overnight. The metal was deposited as described previously.

12.1.3 Results

I found that patterning the films using conventional wet etching and lift-off methods resulted in wrinkles and cracks in the metal layers due to swelling of the PDMS, and that a dry process is required for patterning metal on silicones (Figure 136). The metal films

on these samples were cracked, possibly to outgassing during deposition (of the ambient moisture and gases absorbed by the PDMS while resting overnight; baking at high temperatures drives out these gases) which caused the PDMS to deform and crack the metal films.

Although the process created defect-free metal traces, the films cracked when the PDMS was peeled off the wafer, implying that further design optimization was required for creating electrodes that could withstand actuation forces. In order to increase the stretchability of the metal films (so that they retain their conductivity under stress) they can be formed on elastomeric substrates that are held stretched during deposition so that the metal forms corrugations upon polymer relaxation, and they can be patterned as zig-zag traces [243,316]. Apart from the risk of delamination from the silicone during high strain and long-term cyclical loading, they were also found to experience pitting and delamination due to the electrochemistry that occurred in the EO devices when using water as the pumping liquid. The fidelity of the thin film electrodes was not tested with PC EO. We found that the elastomeric electrodes formed by mixing carbon powder into silicone were well suited for EO actuator fabrication (see section xx).

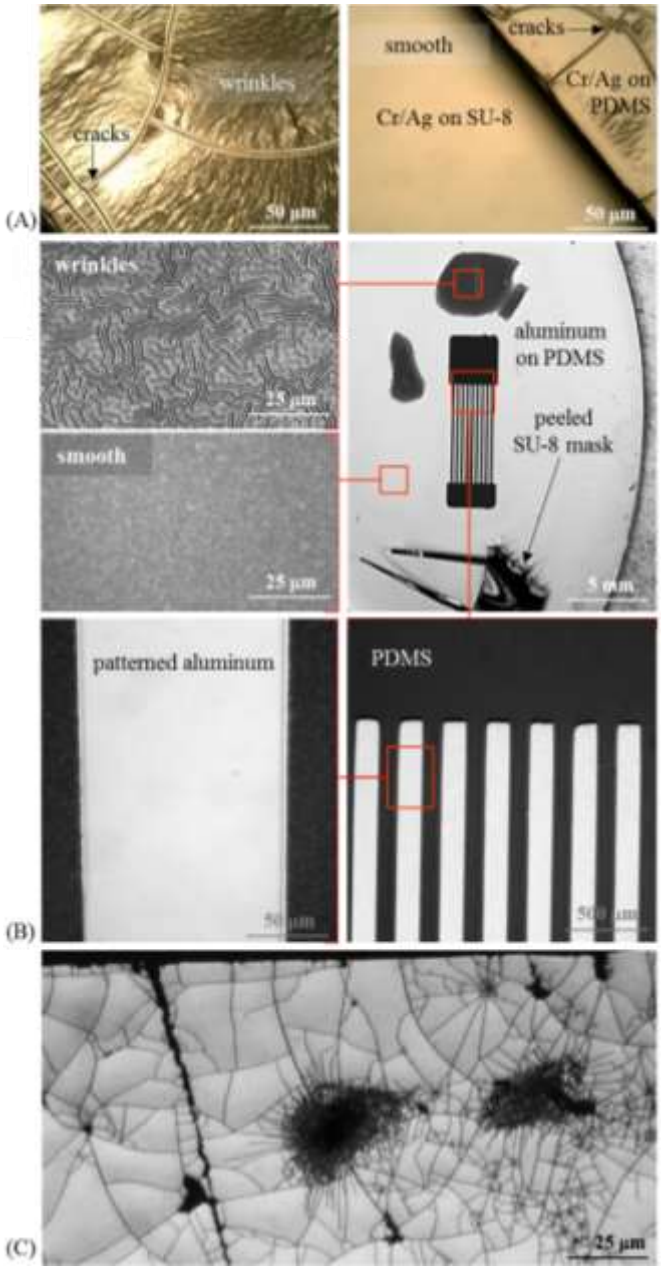

Figure 136. (A) Smooth metal films achieved in samples degassed by baking. (B) Cracks were observed on PDMS but not SU-8 after metal deposition. This is possibly due to outgassing from the PDMS during deposition. (C) Cracks formed in metal patterned on PDMS by lift-off process.

12.2 Metal mesh electrodes

To reduce the operating voltage for EOF it is necessary to reduce the electrode spacing. This can be accomplished without microfabrication by sandwiching the filter paper sheet between plate electrodes, effectively reducing the electrode spacing to that of the thickness of the paper sheet. To obtain past the electrodes it would be necessary for the electrodes to have perforations. Therefore, I tested three types of mesh-type metal electrodes. A single device was tested three times for each of the experiments and the results were repeatable.

The first was a commercially available stainless steel woven mesh with a pore size of 25 μm. The mesh was flexible and fabric-like and easily cut, indicating that it could be useful for soft robot fabrication. Two squares were cut out with scissors with narrow strip for making the power connections. A sheet of Whatman 1 filter paper was placed between the two mesh electrodes. The paper was cut slightly larger than the electrodes to ensure that they were electrically isolated. A couple drops of superglue were applied at the edges of the sandwich to hold it together. The mesh was tested for EOF using the set up shown in Figure 137. Fast EOF of more than 1 mL/s was observed at 200 V in this test.

A more robust test set up (Figure 138) was later created by 3D printing (ABS plastic printed using the Objet Eden 350 machine) that could be used for testing the applicability of various types of mesh electrodes and channel layers formed of porous sheet materials.

A flow rate of 0.15 mL/s was seen at 1 kV with this set up. The lower flow rate was attributed to the wider gap (3 mm) between the electrodes in the 3D printed device. In the prior setup up the electrodes were conformal with the paper sheet and spaced by only a couple hundred microns.

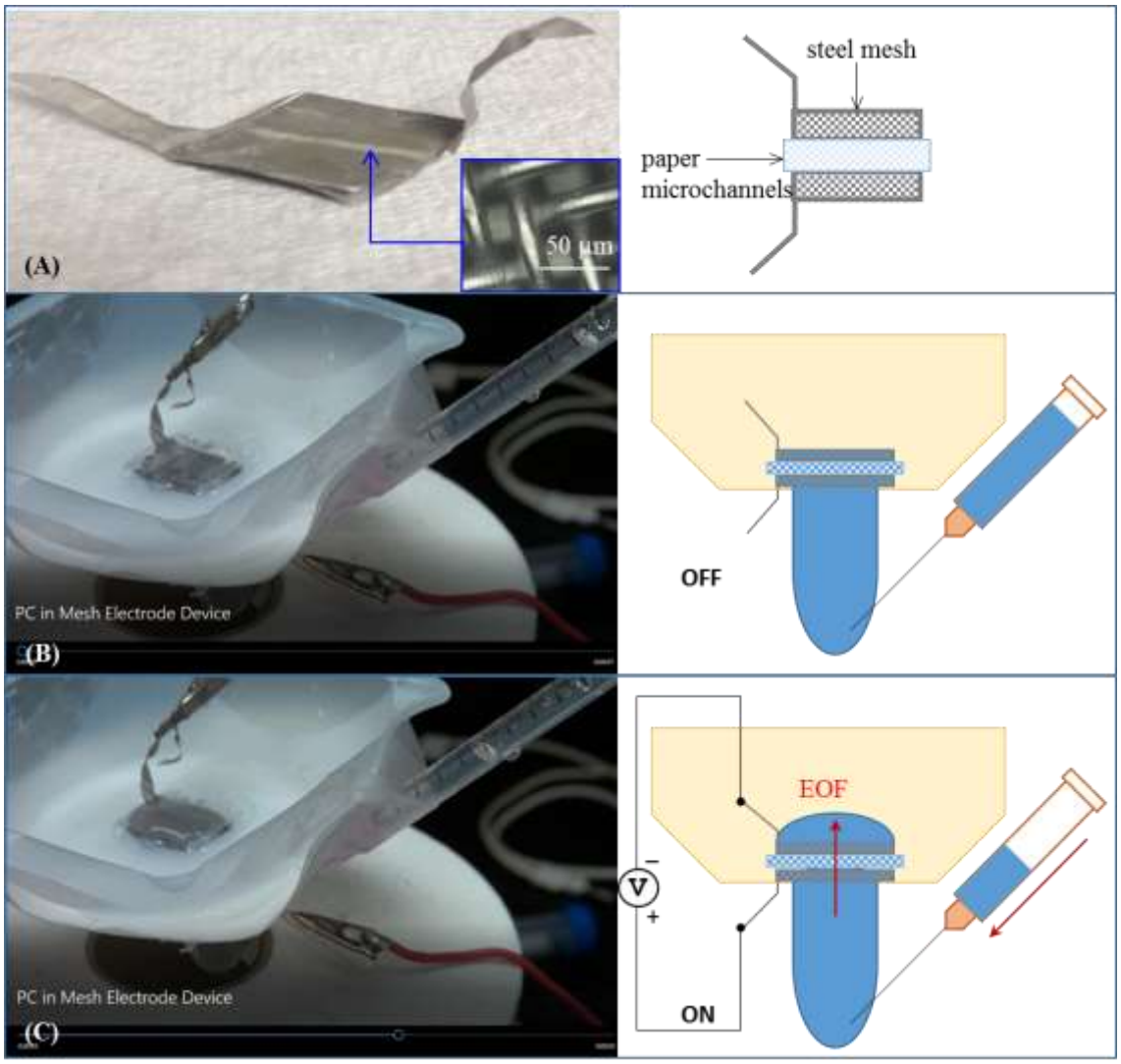

Figure 137. (A) Stainless steel mesh electrodes were placed on either side of a sheet of filter paper microchannels to form a sandwich. (B) The sandwich was fixed in an opening cut in the base of a plastic dish. A plastic pipette bulb was attached beneath the opening as a liquid reservoir. A syringe with needle (30 gauge) was inserted into the bulb to provide liquid to the reservoir; the plunger was removed. PC was added to the syringe to fill the reservoir until the paper microchannels and mesh electrodes were fully wet. (C) When voltage was applied the liquid was rapidly drawn out of the syringe and pushed upwards past the negative electrode to fill the plastic dish.

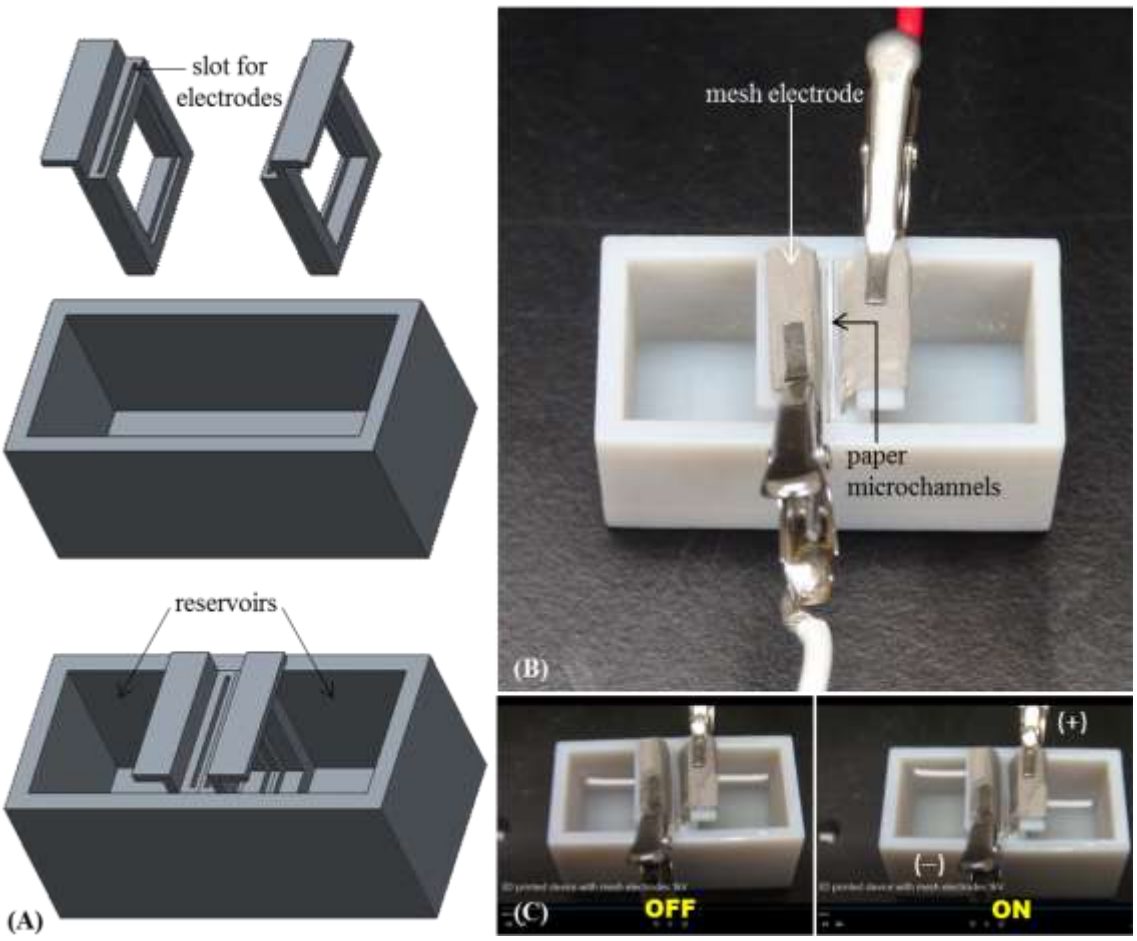

Figure 138. (A) 3D printed device for testing mesh-type electrodes and channels for EOF. The device consisted of slotted holders for the electrode and channel layers. (B) Steel mesh electrodes were inserted into the built-in slots, and a sheet of filter paper was sandwiched between them. (C) Both reservoirs were filled with equal amounts of PC. When voltage was applied PC flowed out of the reservoir on positive potential side through the electrodes and paper towards the reservoir on the negative potential side.

The second type of mesh electrodes were formed out of Whatman 1 filter paper by coating it with platinum (50nm) by e-beam deposition with a titanium adhesion layer

(20nm). Multiple surface layers of cellulose were coated conformally with platinum (as shown in Figure 139B) to form a conductive layer; the side that was unexposed to the e-beam was unmodified and remained uncoated as shown in Figure 139A.

The paper-based mesh electrodes were tested for EO pumping using the 3D printed device as shown in Figure 139C. The device was filled with PC and 1 kV was applied across Whatman 1 filter paper microchannels. EOF was observed to occur with fluid leaving the positive electrode reservoir and filling the negative electrode side. However, within tens of seconds of applying voltage the metal coating started flaking off the paper into the PC, causing the current to increase from μA to A. In conclusion, these paper-based electrodes were not suitable for EOF because of the poor adhesion of the deposited metal to the paper.

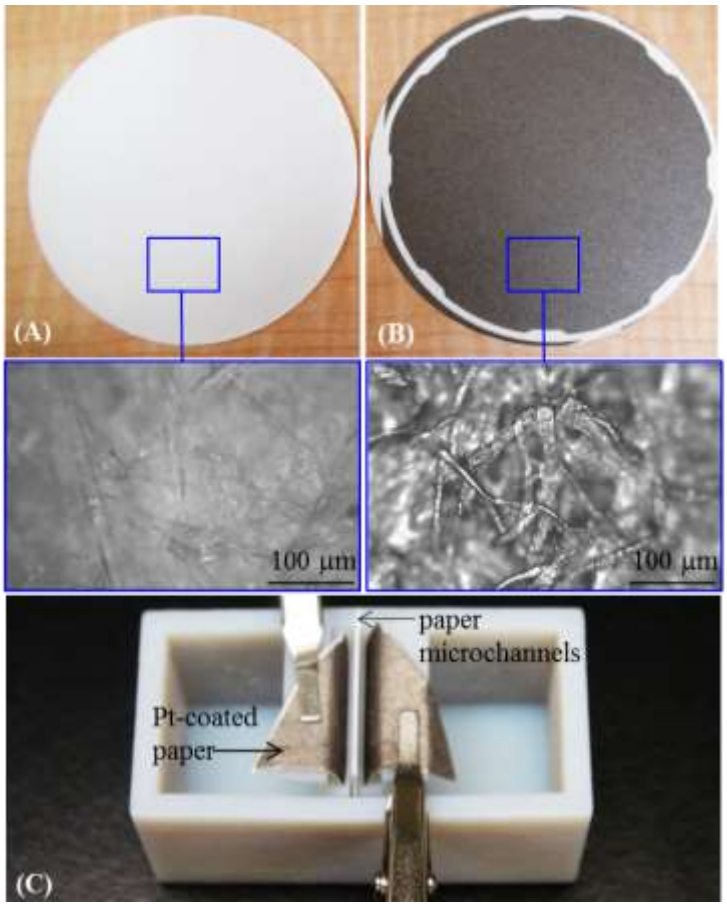

Figure 139. (A) Whatman 1 cellulose filter paper. Microscope photograph showing fibrous cellulose network. (B) Whatman 1 cellulose filter paper coated with Ti/Pt using e-beam deposition. Microscope photograph showing coated cellulose fibers. (C) Testing paper-based platinum mesh electrodes for EO pumping using the 3D printed test device.

The third type of mesh electrode that was tested was an electroplated nickel mesh created by Im Deok Jung at Pusan National University, Korea under the guidance of Professor Jong Soo Ko. This mesh consisted of circular 10 μm perforations spaced by 10 μm. The electroplating process is described in the paper by Lee et al [317]. The test samples were

taken from the middle portion of the film where the best features were observed, as opposed to the edges that had smaller perforations. The smaller hole sizes in edge area was attributed to the higher electric field concentration during electroplating.

These meshes were tested using the 3D printed device using filter paper channels. Fast EOF on the order of 0.2 mL/s was observed. However, these films were significantly more fragile than the commercial steel meshes.

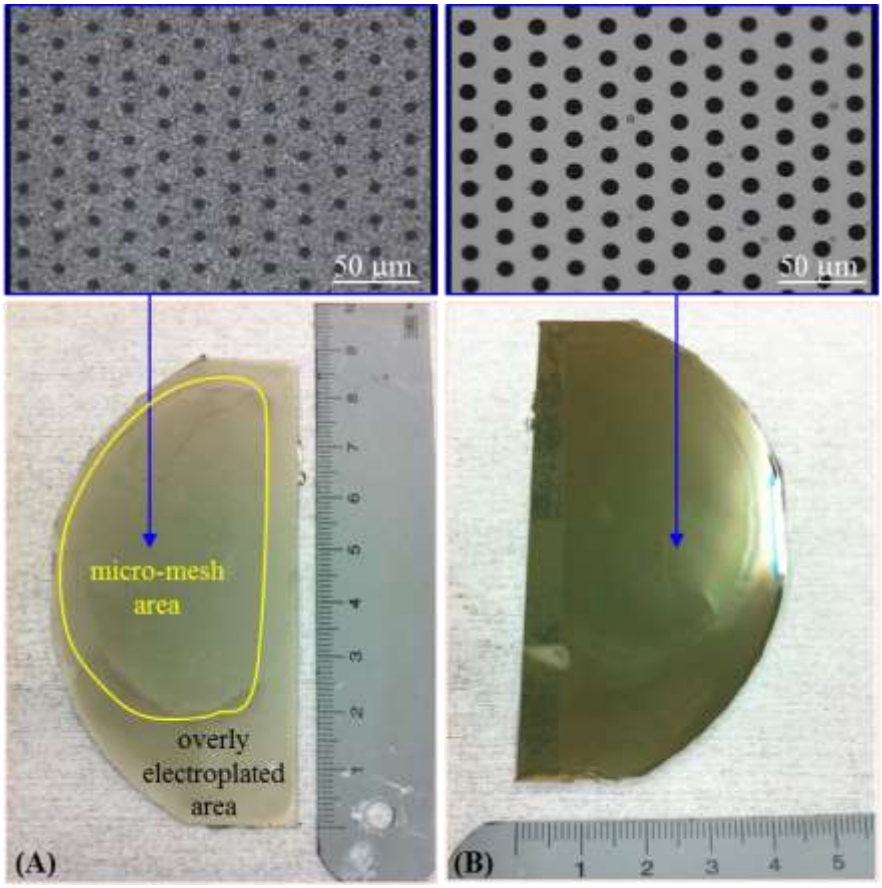

Figure 140. Electroplated nickel meshes microfabricated by Im Deok Jung at Pusan National University. (A) The electroplated film was rougher on the side exposed to the electroplating solution and this side had perforations slightly smaller than 10 µm. (B) The side of the film facing the supportive substrate was smooth and had well-formed 10 µm perforations.

I concluded that the commercial steel micromesh was the most promising perforated electrode material of the three materials tested due to its flexibility, strength, and fast EOF.

13. Appendix E: Porous Materials for EO

Apart from paper the following porous materials were tested for EOF using PC and DI water as pumping liquids. They were tested using the 3D printed device described previously in Figure 138 with steel mesh electrodes. They were also tested using the set up described in Section 3.6.5 by inserting the porous test materials inside the polyethylene tube between the electrodes. Voltages ranging from 100 V to 1 kV were applied. The porous materials that tested positively for EO pumping were used to form actuators: actuators with design as described in Section 6.4.2 were formed by substituting the porous test materials for the paper microchannel layer.

A cellulose aerogel sample was provided by Hong Li who worked with Professor Liangbing Hu. The aerogel was prepared as described by Hamedi et al [318]. The aerogel was a lightweight, opaque, rigid, brittle, powdery cake when dry. It became a soft elastic translucent material when wet. The material was able to absorb PC. A thin slice of about 1 mm was cut off the wet aerogel for testing in the 3D printed set up. When voltage was applied high currents and subsequent electrolysis were observed and no EOF occurred. The aerogel was inserted inside a polyethylene tube and 500 V was applied. This caused high currents (amperes) to occur and the tube melted due to Joule heating. Similar results were obtained when using DI water as the pumping fluid. It was concluded that the high currents were being caused due to ionic impurities in the aerogel.

Next, I tested Whatman glass microfiber filter paper. The glass filter paper was softer than cellulose filter paper, and was expected to be ideal for EOF-based soft actuators because of the surface properties of glass. However, when tested using the 3D printed set up and in the polyethylene tube no EOF was observed, with DI water or PC, and large currents (amperes) and bubble formation were observed indicating that there were ionic contaminants present in the glass filters that impeded EOF.

Commercial porous membranes were tested: anion exchange membrane AMI-7001S (Membranes International Inc., Ringwood, NJ), 1.2 μm and 5 μm Whatman Nucleopore Track-Etch Membranes, or nitrocellulose membranes (Thermo Fisher Scientific) used in protein blotting, but no EOF was observed up to 10 kV using eith PC or DI water.

I also observed fast EOF with oxide-coated metal mesh for use as channels: the metal nickel mesh described in Figure 140 was coated with parylene (1 μm, PDS 2010 SCS Labcoter 2) and SiO_2 (1 μm, PECVD Oxford Plasmalab System 100). EOF was observed with PC as well as DI water. These meshes were not further pursued for actuator fabrication due their fragility. However, the test proves that oxide-coated metal meshes can be useful for EO pumping, although more robust form factors such as woven meshes would be required.

EO pumping of PC and DI water was successfully achieved using the following materials: bath tissue paper (likely cellulose with polymer binders), Kimtech Science KimWipes (likely cellulose), disposable coffee filter paper (likely cellulose or

polypropylene), cleanroom wipe (likely polypropylene/rayon/polyester/cellulose), polar fleece (polyethylene terephthalate), polyurethane open-cell sponges. I was able to pattern these materials using the Cricut Explorer cutter into various shapes, and was able to substitute them for the paper microchannel layer. Actuator devices were created using these materials and membrane actuation was confirmed, using PC as pumping liquid, but not quantified.

14. Appendix F: Microwave Oxygen Plasma Bonding

14.1 Introduction

Plasma-activated bonding is the most preferred method of joining PDMS pieces because this is a clean and dry process that does not require an intermediate adhesive layer. The seal formed is strong and irreversible; PDMS rupture occurs before bond failure. A commercial plasma stripper is typically used for this procedure. We tested an inexpensive alternative approach that utilizes a kitchen microwave oven and a standard glass desiccator. I learnt this method from Dr. Jason Kralj at the National Institute of Standards and Technology at Gaithersburg, and optimized the bonding conditions for our laboratory. There are also other groups who have reported success with the microwave plasma bonding method [319].

Plasma can be generated at room temperature when gas maintained at a low pressure is exposed to high frequency (GHz) microwave radiation. When a PDMS sample is exposed to oxygen plasma, oxygen ions bombard its surface removing low molecular weight surface impurities, while oxidizing the uppermost atomic layer of the PDMS. Oxidation of the functional groups in PDMS ($-CH_3$) makes them polar ($-CH_2OH$, $-COOH$, or $-OH$), which causes the PDMS hydrophobic surface to become hydrophilic. This transformation makes the PDMS highly adhesive to surfaces with complementary functional groups, enabling PDMS/PDMS or PDMS/glass bonding. Figure 141 depicts the reactions involved in this process.

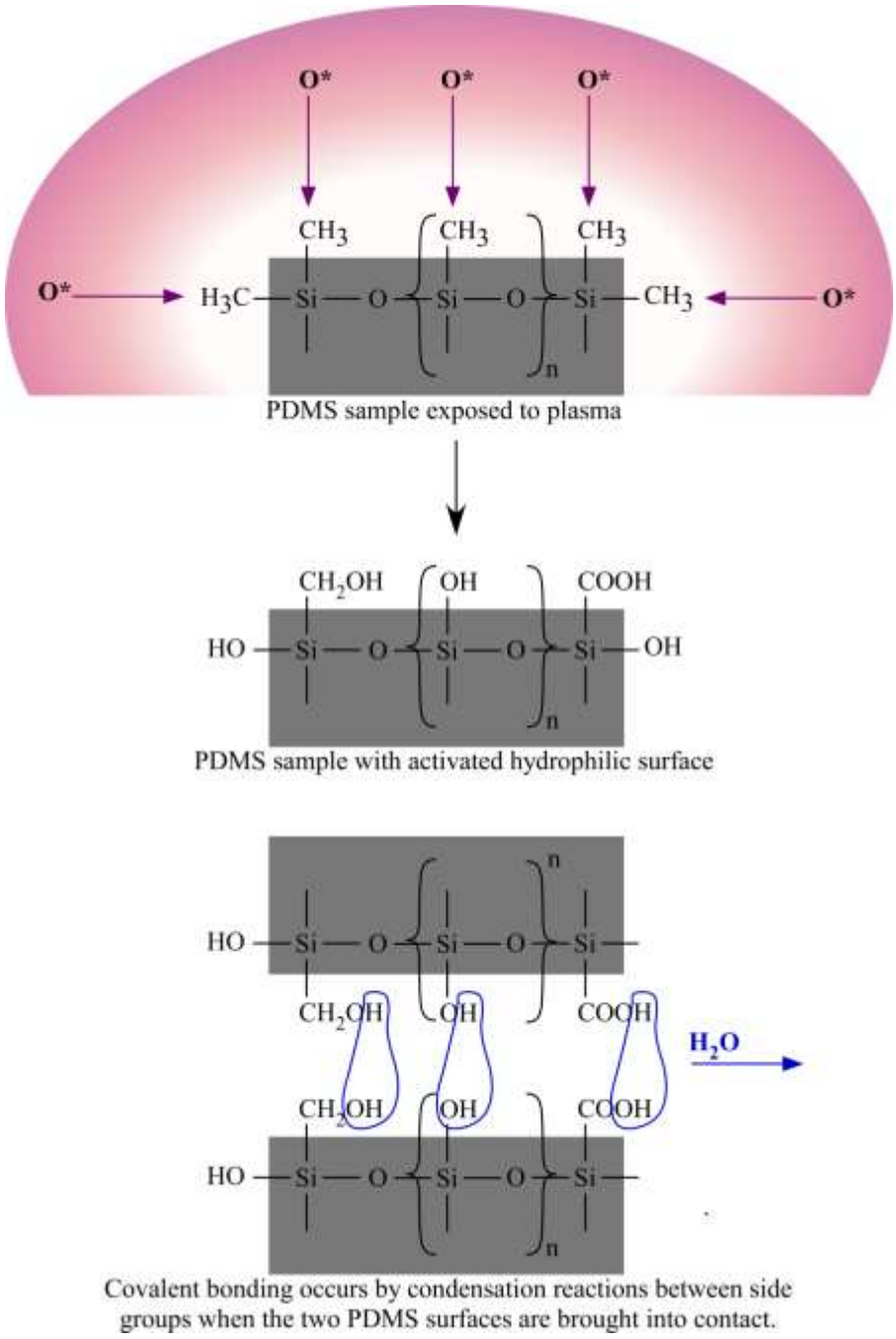

Figure 141. Schematic of PDMS-PDMS bonding by surface activation using oxygen plasma.

14.2 Materials and Methods

Plasma was generated with a 1250W countertop microwave oven (Panasonic, NNSD967S) that emits radiation at a frequency of 2.45 GHz. The vacuum pump used was xx. A Wheaton Dry-Seal desiccator (250 mm inner diameter) equipped with a perforated aluminum plate was used. A borosilicate glass beaker (about 3 inches high) was used as the stage for holding the samples during exposure. PDMS samples were prepared using the Sylgard184 silicon elastomer kit from Dow Corning.

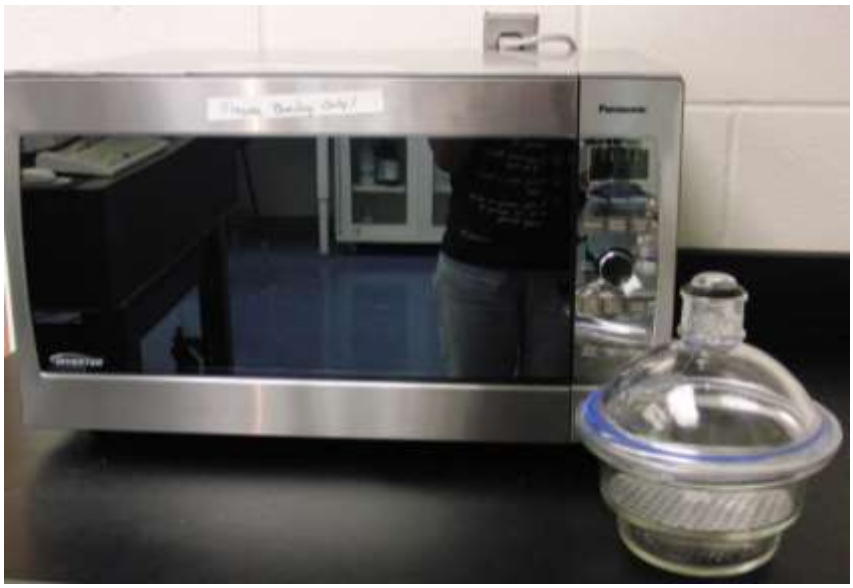

Figure 142. Photograph of the microwave and desiccator used for plasma bonding.

Samples were prepared by mixing 10 grams of polymer base with 1 gram of curing agent. The liquid mixture was poured into a plastic Petri dish and degassed in a vacuum desiccator. The PDMS was then cured at 65 ^{o}C for 1-2 hours. The solidified elastomer

was then cut into 1 inch pieces using a razor blade. The PDMS samples were handled with clean gloves to avoid surface contamination.

The desiccator was set up for plasma treatment as shown in Figure 143. The beaker was inverted and placed in the center of the perforated aluminum plate. The samples to be bonded were placed on the base of the beaker, with the target surfaces facing up. The desiccator was then closed and connected to the vacuum pump.

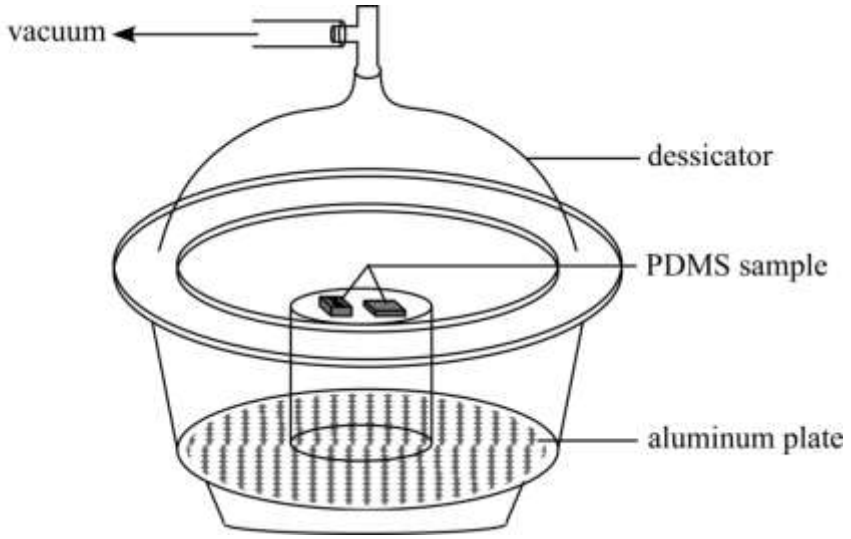

Figure 143. Illustration of desiccator set up.

The system was evacuated for 2-5 min and then sealed off. Then, desiccator containing air at low pressure was placed into the microwave oven on the turntable. The power was tested between 30% and 100% of the maximum power, and microwave exposure time was varied 10-30 seconds.

14.3 Results

The efficacy of the plasma treatment on hydrophobicity was gauged by observing the wetting of the PDMS surface by water. Water was dispensed (200 μL) on the exposed PDMS surface. The water immediately formed a film covering the surface of the PDMS if the treatment was successful, indicating hydroxylation. The water formed beads on the surface if the treatment was not successful. For each bonding test, an extra piece of PDMS was placed to test wettability. It was observed that uniform wettability was indicative of bonding success; strong PDMS-PDMS and PDMS-glass adhesion was achieved, and the PDMS or glass was damaged before the bond could be broken.

It was observed that the plasma color was more intense in the upper portion of the jar. Using the beaker to elevate the samples towards the top portion of the jar enabled exposure to the denser plasma layer. Samples that were placed close to the plate had little to no change in surface properties, and experienced a higher chance of burning. It was observed that whenever PDMS burning occurred the surface actually became highly hydrophobic, possibly due to the formation of a soot layer [320].

The optimum evacuation time was observed to be 3-4 minutes. No plasma was observed when evacuation was done for less than 2 minutes. The plasma color generated was visually monitored at different microwave power settings. It was observed that plasma ignited with 3-7 seconds of turning on the microwave. The optimum setting was found to be at 60% power of the maximum power, and 15 seconds of microwave operation time.

Under these conditions, the plasma was a mixture of purple and white colors. At 30% to 50% operating power, the plasma was a faint pink color of lower intensity. Above 70% power, yellow and orange hues appeared and the PDMS edges burned within 5-10 seconds. Increasing plasma exposure time beyond 30 seconds caused burning at all power conditions. PDMS-glass bonding was found to have a higher rate of success and was more tolerant of variations in plasma treatments than PDMS-PDMS bonding.

The previous literature [319] mentions that an additional oxygen purge prior to plasma must be performed for effective surface treatment. To test this hypothesis the above tests were repeated with the following modification. Before placing the desiccator in the microwave, the vacuum chamber was pumped down for 30 minutes, followed by purging oxygen through the desiccator for 5 minutes, followed by vacuum again for 3-5 min. We did not observe any visible benefits of adding this step to the process and concluded that ambient air which (was at approximately 40% humidity at the time of the experiments) produced satisfactory results.

Some precautions must be taken while carrying out these experiments. While plasma treatment results in a bond of high strength, it demands high standards in surface geometry. The surface must be free of impurities and particulates, with negligible roughness. Typically if the PDMS surface is reflective and smooth by visual inspection then bonding by this method can be expected to be successful. Direct contact with the target surfaces to be bonded must be avoided as much as possible. The samples can be cleaned and stored by adhering Scotch tape to the target surface. It was also noted that

newly formed PDMS bonded better than older samples. The silicone O-ring in the Dry-Seal desiccator holds vacuum without the need for vacuum grease which may react undesirably with the plasma. The aluminum desiccator plate provided usually has a rough texture. The surface may be sanded to further increase the roughness. This increases the likelihood of quick plasma ignition with minimal heating effects. The microwave must be free of flammable contaminants, and ideally reserved for only plasma bonding jobs. The jar must be placed close to RF emitter in microwave in order strike the plasma. Long exposure times (> 30 seconds) may cause the desiccator to become hot, particularly around the top portion. Additionally, the desiccator must be checked for cracks or chips before use to prevent implosion. It is also recommended that safety eyeglasses be worn when viewing the plasma. After exposure, the vacuum must be released in a fume hood; a sharp chlorine-like odor was detected during our experiments indicating the presence of ozone. Thus, precautions must be taking to limit exposure to the toxic gas, likely formed by the recombination of oxygen ions produced by the plasma.

15. Appendix G: Bioinspiration for Design

Plants and animals exhibit a variety of movements using soft deformable structures. Studying the form and functionality of these highly evolved biological structures can provide valuable inspiration for engineering new devices composed of compliant materials. Organisms exhibit movements when triggered by internal or external stimuli. Specialized receptor cells sense stimuli (such as sound, light, heat, or touch) and activate biochemical pathways that instruct effector cells to generate physiological responses to the stimuli. Single cells achieve motility by means of specialized structures (examples shown in Figure 144) such as microfilaments such as cilia [321] and flagella [322], and pseudopodia [323,324]. In multicellular organisms motion is achieved by specific arrangements of cells that are modularly organized into tissue materials, which form the organs that effect motion (examples shown in Figure 145 and Figure 146).

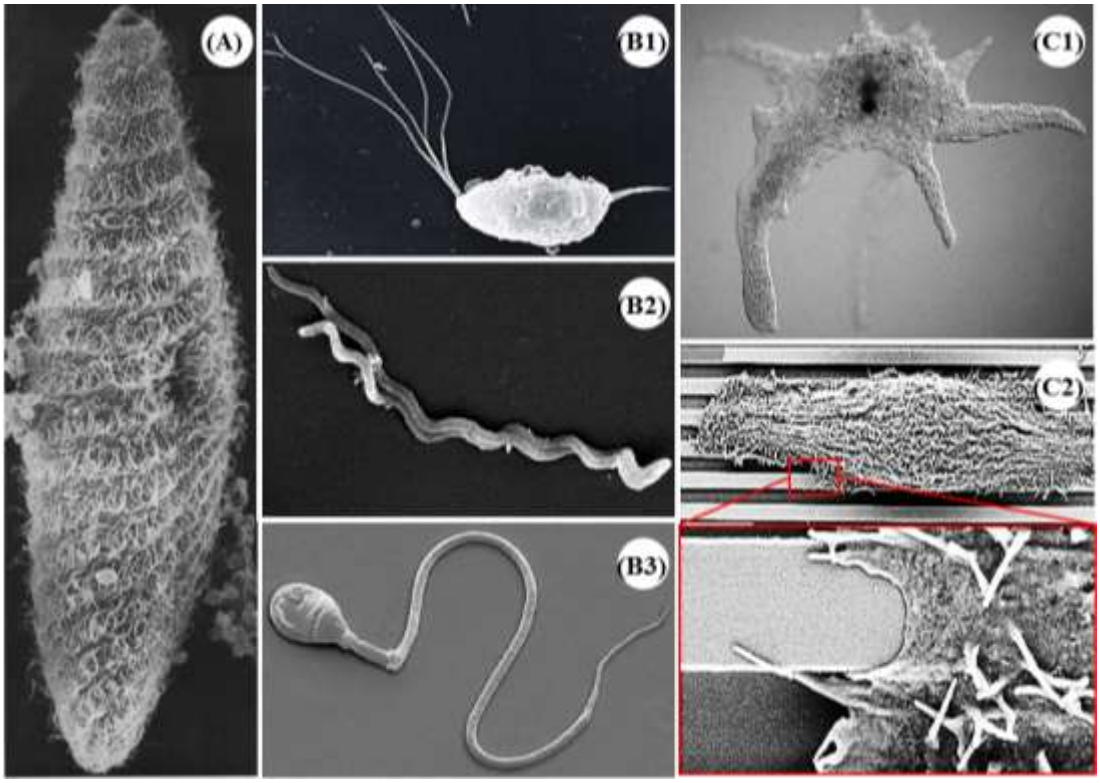

Figure 144. Single-cell motion. (A) Protozoan paramecium locomotes by moving the cilia covering its body in whiplash motions [325]. Flagella are actuated in helical motions to propel protists like trichomonads (B1) [326], spirochetes (B2) [327], as well as spermatozoa in animals (B3) (photo credit: Steve Gschmeissner). Pseudopodia are temporary cytoplasmic limb projections used by amoebae (C1) (photo credit: Tsukii Yuuji) and animal epithelial cells (C2) [328] for crawling and phagocytic actions.

15.1 Soft Animal Structures

In animals muscles enable complex gaits, load-bearing, and dexterity. Animal muscle is a soft material that can be electrically actuated to achieve extension, bending and twisting

motions. When a stimulus is sensed neurons send electrical commands to trigger contractile proteins, which use chemical energy (in the form of adenosine triphosphate, ATP) and generate muscle motion. The activated muscle contracts and generates stress, thereby exerting force on the environment, achieving remarkable performance metrics [4,207,329]. There are several types of musculature; and they can be oriented radially, longitudinally, transversely, obliquely and/or helically to achieve a range of motions. These complex arrangements of musculature can vary between species, conferring each with unique capabilities.

Two types of hydrostatic muscular structures have been identified to be of interest for inspiring the development soft robots: hydrostatic skeletons and muscular hydrostats [4]. These load-bearing structures function based on the principle that water is incompressible at physiological pressures. They store elastic energy, and when stimulated they transmit forces to perform complex actions without any rigid support. The musculature itself provides skeletal support, in addition to generating the force for movement.

Hydrostatic skeletons are found in soft-bodied invertebrates, such as caterpillars, sea anemones, and jelly fish; in contrast vertebrates and arthropods have rigid, jointed skeletons. Hydrostatic skeletons are liquid-filled cavities surrounded by a wall made of muscle and connective tissue. Under pressure the liquid resists volume change; therefore a decrease in one dimension of the cavity would cause other dimensions to increase. Thus, cylindrical contractions result in lengthening, and longitudinal contractions shorten the animal's body [4,329].

In contrast to hydrostatic skeletons, muscular hydrostats do not contain distinct fluid-filled cavities, and are composed almost exclusively of muscle. Muscle tissue itself is composed predominantly of water and is therefore soft but incompressible; to maintain constant volume under applied pressure the shape of the muscle changes. Examples of muscular hydrostats are cephalopod tentacles, animal tongues, the elephant trunk, and the feet of mollusks and echinoderms [4,207].

Figure 145. Moving structures in animals. (A) Octopus uses its tentacles to unscrew the lid off a jar containing prey (photo credit: Jorgen Jessen). (B) Chameleon extends its tongue to grab prey (photo credit: Paul Souders); the tip of their tongue produces a highly viscous mucous which causes the prey to stick by viscous adhesion. (C) Elephant grasping a twig with its trunk (photo credit: Scotch Macaskill) ; the elephant trunk, in addition to being used for olfaction, is used to transport water and soil, to uproot trees, as well as delicately handle small objects using the finger-like lobes at the distal end of the trunk. The (D) inchworm (photo credit: Edward Nurcombe) and the (E) jellyfish (photo credit: Diana Robinson) have hydrostatic skeletons surrounded by musculature which enables them to perform a variety of actions.

15.2 Soft Plant Structures

Plants may not have neuro-muscular systems allowing them to locomote or behave like animals. Despite their sessile nature, they are able to exhibit a remarkable variety of movements for seed dispersal, seeking nutrition, modulating water retention, and self-defense. In his book, "The Power of Movement in Plants", Charles Darwin describes the rich repertoire of plant motion, achieved without nerves, muscles or bones. Plant organs exhibit movements that can occur over several timescales: a flower blooms and closes within a few hours, a tendril can curl around a stick in minutes, and a Venus flytrap snaps in fractions of a second.

Plant movements can be permanent or reversible. Plants have evolved several mechanisms to actuate organs; fundamentally this is achieved by plant cells changing their shape by pumping water in and out of their cells by osmotic processes. Osmotic pressure is generated by solvent flux across a semi-permeable membrane (i.e. cell wall), from a region of higher solvent chemical potential (i.e. lower solute concentration) to a region of lower solvent chemical potential (i.e. higher solute concentration) [330]. When multiple plant cells are aligned they can cause macroscopic changes in shape of the plant [331-333].

Deformation under osmotic potential is isotropic; directional actuation is achieved by preceding biochemical cues and anisotropy in plant structures [334]. The direction of deformation of the plant organ is geometrically constrainted by cell shape, size, and

composition. The cell wall is composed of cellulose fibrils embedded in a matrix of hemicellulose, lignin and pectin; the cellulose fibrils are oriented to ensure that the cell deforms in a specific direction when pressurized [335]. The shaping of the plant cells is dictated by growth hormones which respond to environmental stimuli such as light, gravity, touch, temperature, and humidity [336].

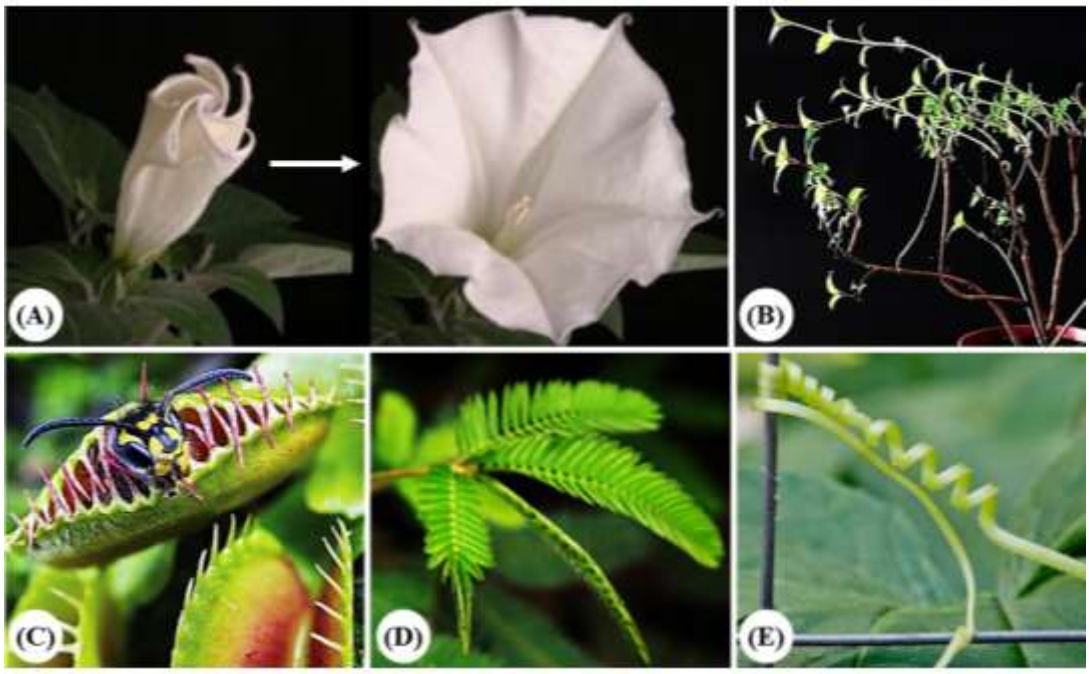

Figure 146. Moving structures in plants. (A) The moonflower is closed in the day and blooms at night due to photonasty (photo credit: Ted Kinsman). (B) A plant placed in shady location bends and grows towards the source of light due to phototropism (photo credit: Andrew Lambert). (C) Venus fly trap (photo credit: Chris Mattison) closes to trap prey and the (D) leaves of mimosa plant (photo credit: Pedro Lourenco Venda) close in self-defense when touched due to thigmonasty. (E) A cucumber tendril locates and wraps itself around a trellis by thigmotropism. (photo credit: Bill Vriesema)

Plant motion is broadly classified into two categories: tropic movements and nastic movements [336]. **Tropic movements** are made by the plant to change the shape of its organs in response to an external stimulus. These movements are irreversible. The direction of the stimulus controls the pattern of growth; when a stimulus is received auxin

hormones are produced to cause plant growth, towards or away from the stimulus, to maximize plant health. Phototropism is the movement of plants to mediate cell exposure to sunlight for food production via photosynthesis. If a plant is rooted in a shady location then, light-sensitive plant pigments signal the auxins to elongate cells on the farthest side from the light, and direct the growth of plant limbs towards the light source. Gravitropism causes plant shoots to move away from gravity, and plant roots towards gravity. Gravity is detected in cells in the root and shoot tips via dense structures called statoliths; the statoliths settle at the bottom of the cell and the position of the statoliths determines the direction in which the auxins are released. Similarly, plants also contain touch receptors which enable tendrils seek a support structure and wrap themselves around it upon making contact, by thigmotropism. **Nastic movements** are reversible plant movements that occur in response to environmental stimuli but unlike tropic movements, the direction of the response is independent of the direction of the stimulus. For example, rapid motion response to touch stimulus (thigmonasty) is seen in the Venus flytrap and Mimosa plants. The leaves of the carnivorous Venus flytrap plant are modified into a trapping device to catch prey. The surface of the trap is covered with sensory hairs; when an insect makes contact the leaf is triggered to snap shut, within hundreds of milliseconds, to trap the prey. This mechanism is complex and not fully understood; the plant is able to conserve energy resources by a highly accurate detection mechanism: the leaves trap only living prey and ignore non-prey triggers such as rain drops, and the traps shut only when at least two touch stimuli have been received by the hair(s) within tens of seconds. When a hair bends, it applies pressure on the cells around its base. The increased pressure gets converted to an action potential, which is analogous

to electrical nerve impulse in animals [337]. This signals some of the plant cells in the flytrap to release ions, which is followed by osmotic efflux of water leading to the cell to contract, causing the trap structure to close. The rapid closing (milliseconds) of the Mimosa leaves in response to touch is also explained by a similar action-potential driven mechanism.

In addition to tropic and nastic mechanisms, which involve active signal processes, movements are also enabled by passive osmotic mechanisms; drying or moistening of dead tissue structures causes differential contractions or expansions of cells causing a change in curvature; this mechanism enables seedpods to open and disperse seeds into their environment [338]. The hygroscopic actuation of pine cones is one such phenomenon that has inspired actuator design [339]. Passive transport does not demand any energy because molecules are transported along their concentration gradient. In contrast active signaling processes involve the transport of molecules against their concentration gradient are require the plant to expend energy; passive transport events follow active transport events in order to restore the chemical equilibrium.

16. **Bibliography**

1. A. Albu-Schaffer, O. Eiberger, M. Grebenstein, S. Haddadin, C. Ott, T. Wimbock, S. Wolf, and G. Hirzinger, "Soft robotics," IEEE Robot. Autom. Mag., 15 (3), 20-30 (2008).

2. M. I. Tiwana, S. J. Redmond, and N. H. Lovell, "A review of tactile sensing technologies with applications in biomedical engineering," Sens. Act. A, 179**,** 17-31 (2012).

3. C. Mavroidis, C. Pfeiffer, K. J. DeLaurentis, and M. J. Mosley, "Prosthetic, orthotic, and other rehabilitative robotic assistive devices actuated by smart materials" (Google Patents, 2002).

4. D. Trivedi, C. D. Rahn, W. M. Kier, and I. D. Walker, "Soft robotics: Biological inspiration, state of the art, and future research," Appl. Bionics. Biomech., 5 (3)**,** 99 - 117 (2008).

5. M. J. Madou, Fundamentals of microfabrication: the science of miniaturization, (CRC press, 2002).

6. C. L. Tien, Microscale energy transfer, (CRC Press, 1997).

7. V. Kaajakari, "Practical MEMS: Design of microsystems, accelerometers, gyroscopes, RF MEMS, optical MEMS, and microfluidic systems," Las Vegas, NV: Small Gear Publishing (2009).

8. C. Liu, "Recent developments in polymer MEMS," Adv. Mater., 19 (22)**,** 3783-3790 (2007).

9. R. Seo-Zindy and R. Heeks, "Researching the Emergence of 3D Printing, Makerspaces, Hackerspaces and FabLabs in the Global South: A Scoping Review and Research Agenda on Digital Innovation and Fabrication Networks," The Electronic Journal of Information Systems in Developing Countries, 80 (2017).

10. D. I. Walsh, D. S. Kong, S. K. Murthy, and P. A. Carr, "Enabling Microfluidics: from Clean Rooms to Makerspaces," Trends in Biotechnology (2017).

11. M. Vaezi, H. Seitz, and S. Yang, "A review on 3D micro-additive manufacturing technologies," Int. J. Adv. Manuf. Tech., 67 (5-8)**,** 1721-1754 (2013).

12. T. J. Hinton, A. Hudson, K. Pusch, A. Lee, and A. W. Feinberg, "3D printing PDMS elastomer in a hydrophilic support bath via freeform reversible embedding," ACS biomaterials science & engineering, 2 (10)**,** 1781-1786 (2016).

13. H.-B. Liu and H.-Q. Gong, "Templateless prototyping of polydimethylsiloxane microfluidic structures using a pulsed CO2 laser," J. Micromech. Microeng., 19 (3)**,** 037002 (2009).

14. H. Lipson, "Challenges and opportunities for design, simulation, and fabrication of soft robots," Soft Robotics, 1 (1)**,** 21-27 (2014).

15. K.-J. Cho, J.-S. Koh, S. Kim, W.-S. Chu, Y. Hong, and S.-H. Ahn, "Review of manufacturing processes for soft biomimetic robots," IJPEM, 10 (3)**,** 171-181 (2009).

16. R. L. Truby and J. A. Lewis, "Printing soft matter in three dimensions," Nature, 540 (7633)**,** 371-378 (2016).

17. X. Wang, S. Chen, M. Kong, Z. Wang, K. D. Costa, R. A. Li, and D. Sun, "Enhanced cell sorting and manipulation with combined optical tweezer and microfluidic chip technologies," Lab Chip, 11 (21)**,** 3656-3662 (2011).

18. C. Yi, C.-W. Li, S. Ji, and M. Yang, "Microfluidics technology for manipulation and analysis of biological cells," Anal. Chim. Acta, 560 (1)**,** 1-23 (2006).

19. A. Ghanbari, H. Abdi, B. Horan, S. Nahavandi, X. Chen, and W. Wang, "Haptic guidance for microrobotic intracellular injection," IEEE/RAS-EMBS BioRob, (IEEE), p. 162-167 (2010).

20. W. J. Li and N. Xi, "Novel micro gripping, probing, and sensing devices for single-cell surgery," IEEE IEMBS, (IEEE), vol. 1, p. 2591-2594 (2004).

21. R. A. Beasley, "Medical robots: current systems and research directions," Journal of Robotics, 2012 (2012).

22. C. Bergeles and G.-Z. Yang, "From passive tool holders to microsurgeons: safer, smaller, smarter surgical robots," IEEE Trans. Biomed. Eng., 61 (5)**,** 1565-1576 (2014).

23. M. Cianchetti, T. Ranzani, G. Gerboni, T. Nanayakkara, K. Althoefer, P. Dasgupta, and A. Menciassi, "Soft robotics technologies to address shortcomings in today's minimally invasive surgery: the STIFF-FLOP approach," Soft Robotics, 1 (2)**,** 122-131 (2014).

24. T. Ranzani, G. Gerboni, M. Cianchetti, and A. Menciassi, "A bioinspired soft manipulator for minimally invasive surgery," Bioinspir. Biomim., 10 (3)**,** 035008 (2015).

25. H. E. Martin and E. B. Ellis, "Biopsy by needle puncture and aspiration," Ann. Surg., 92 (2)**,** 169 (1930).

26. M. J. Tierney, T. G. Cooper, C. A. Julian, S. J. Blumenkranz, G. S. Guthart, and R. G. Younge, "Surgical robotic tools, data architecture, and use" (Google Patents, 2001).

27. M. Cianchetti and A. Menciassi, "Soft Robots in Surgery," in Soft Robotics, p. 75-85 (Springer, 2017).

28. C. J. Payne, I. Wamala, C. Abah, T. Thalhofer, M. Saeed, D. Bautista-Salinas, M. A. Horvath, N. V. Vasilyev, E. T. Roche, and F. A. Pigula, "An Implantable Extracardiac Soft Robotic Device for the Failing Heart: Mechanical Coupling and Synchronization," Soft Robotics (2017).

29. D. Rus and M. T. Tolley, "Design, fabrication and control of soft robots," Nature, 521 (7553)**,** 467-475 (2015).

30. B. A. Trimmer, "Animal Models for Non-pneumatic Soft Robots," in Soft Robotics, p. 47-55 (Springer, 2017).

31. J. Hughes, U. Culha, F. Giardina, F. Guenther, A. Rosendo, and F. Iida, "Soft Manipulators and Grippers: A Review," Front. Robot. AI., 3**,** 69 (2016).

32. B. Trimmer, "Soft robots," Current Biology, 23 (15)**,** R639-R641 (2013).

33. Y.-L. Park, B.-r. Chen, N. O. Pérez-Arancibia, D. Young, L. Stirling, R. J. Wood, E. C. Goldfield, and R. Nagpal, "Design and control of a bio-inspired soft wearable robotic device for ankle–foot rehabilitation," Bioinspir. Biomim., 9 (1)**,** 016007 (2014).

34. I. M. Koo, K. Jung, J. C. Koo, J.-D. Nam, Y. K. Lee, and H. R. Choi, "Development of soft-actuator-based wearable tactile display," IEEE Trans. Robot., 24 (3)**,** 549-558 (2008).

35. S. Kim, C. Laschi, and B. Trimmer, "Soft robotics: a bioinspired evolution in robotics," Trends in biotechnology, 31 (5)**,** 287-294 (2013).

36. K. Asaka and H. Okuzaki, Soft Actuators: Materials, Modeling, Applications, and Future Perspectives, (Springer, 2014).

37. K. J. Kim and S. Tadokoro, Electroactive polymers for robotic applications, (2007).

38. Y. Bar-Cohen, "Electroactive polymers as artificial muscles-reality and challenges," AIAA SDM, Seattle WA, (Gossamer Spacecraft Forum) (2001).

39. F. Carpi and E. Smela, Biomedical applications of electroactive polymer actuators, (John Wiley & Sons, 2009).

40. S. B. Lang and S. Muensit, "Review of some lesser-known applications of piezoelectric and pyroelectric polymers," Appl. Phys. A, 85 (2)**,** 125-134 (2006).

41. K. S. Ramadan, D. Sameoto, and S. Evoy, "A review of piezoelectric polymers as functional materials for electromechanical transducers," Smart Mater. Struct. , 23 (3)**,** 033001 (2014).

42. R. Kornbluh, R. Pelrine, J. Eckerle, and J. Joseph, "Electrostrictive polymer artificial muscle actuators," IEEE ICRA, (IEEE), vol. 3, p. 2147-2154 (1998).

43. A. J. Lovinger, "Ferroelectric polymers," Science, 220 (4602)**,** 1115-1121 (1983).

44. H. S. Nalwa, Ferroelectric polymers: chemistry: physics, and applications, (CRC Press, 1995).

45. F. Carpi, D. De Rossi, R. Kornbluh, R. E. Pelrine, and P. Sommer-Larsen, Dielectric elastomers as electromechanical transducers: Fundamentals, materials, devices, models and applications of an emerging electroactive polymer technology, (Elsevier).

46. M. Lyons, Electroactive Polymer Electrochemistry: Part 1: Fundamentals, (Springer Science & Business Media).

47. M. Lyons, Electroactive Polymer Electrochemistry: Part 2: Methods and Applications, (Springer Science & Business Media).

48. Y. Osada, H. Okuzaki, and H. Hori, "A polymer gel with electrically driven motility," Nature, 355 (6357)**,** 242 (1992).

49. T. Tanaka, I. Nishio, S.-T. Sun, and S. Ueno-Nishio, "Collapse of gels in an electric field," Science, 218 (4571)**,** 467-469 (1982).

50. M. Shahinpoor, Y. Bar-Cohen, J. O. Simpson, and J. Smith, "Ionic polymer-metal composites (IPMCs) as biomimetic sensors, actuators and artificial muscles-a review," Smart Mater. Struct. , 7 (6)**,** R15 (1998).

51. E. W. H. Jager, E. Smela, and O. InganÃ¤s, "Microfabricating conjugated polymer actuators," Science, 290 (5496)**,** 1540-1545 (2000).

52. E. Smela, "Conjugated polymer actuators," MRS bulletin, 33 (03)**,** 197-204 (2008).

53. E. Smela, "Conjugated polymer actuators for biomedical applications," Adv. Mater., 15 (6)**,** 481-494 (2003).

54. R. B. Bird, W. E. Stewart, and E. N. Lightfoot, Transport phenomena, 2nd ed. (John Wiley & Sons, 2007).

55. M. De Volder and D. Reynaerts, "Pneumatic and hydraulic microactuators: a review," J. Micromech. Microeng., 20 (4)**,** 1-19 (2010).

56. E. Brown, N. Rodenberg, J. Amend, A. Mozeika, E. Steltz, M. R. Zakin, H. Lipson, and H. M. Jaeger, "Universal robotic gripper based on the jamming of granular material," Proc. Natl. Acad. Sci. U.S.A., 107 (44)**,** 18809-18814.

57. H. M. Jaeger, "Celebrating soft matter's 10th anniversary: Toward jamming by design," Soft Matter, 11 (1)**,** 12-27 (2015).

58. R. F. Shepherd, F. Ilievski, W. Choi, S. A. Morin, A. A. Stokes, A. D. Mazzeo, X. Chen, M. Wang, and G. M. Whitesides, "Multigait soft robot," Proc. Natl. Acad. Sci. U.S.A., 108 (51)**,** 20400-20403 (2011).

59. F. Ilievski, A. D. Mazzeo, R. F. Shepherd, X. Chen, and G. M. Whitesides, "Soft robotics for chemists," Angew. Chem. Int. Ed. , 50 (8)**,** 1890-1895 (2011).

60. M. Wehner, M. T. Tolley, Y. Mengüç, Y.-L. Park, A. Mozeika, Y. Ding, C. Onal, R. F. Shepherd, G. M. Whitesides, and R. J. Wood, "Pneumatic energy sources for autonomous and wearable soft robotics," Soft Robotics, 1 (4)**,** 263-274 (2014).

61. A. Menciassi and P. Dario, "Bio-inspired solutions for locomotion in the gastrointestinal tract: background and perspectives," Philosophical Transactions of the Royal Society of London A: Mathematical, Physical and Engineering Sciences, 361 (1811)**,** 2287-2298 (2003).

62. L. Liwei, A. P. Pisano, and A. P. Lee, "Microbubble powered actuator," TRANSDUCERS, (IEEE), p. 1041-1044 (24-27 June 1991, 1991).

63. J. Ji, J. Chaney, M. Kaviany, P. L. Bergstrom, and K. D. Wise, "Microactuation based on thermally-driven phase-change," TRANSDUCERS, (IEEE), p. 1037-1040 (1991).

64. D. M. van den Broek and M. Elwenspoek, "Explosive micro-bubble actuator," Sens. Act. A, 145**,** 387-393 (2008).

65. C. D. Onal, X. Chen, G. M. Whitesides, and D. Rus, "Soft mobile robots with on-board chemical pressure generation," ISRR, Flagstaff, Arizona, p. 1-16 (2011).

66. M. Wehner, R. L. Truby, D. J. Fitzgerald, B. Mosadegh, G. M. Whitesides, J. A. Lewis, and R. J. Wood, "An integrated design and fabrication strategy for entirely soft, autonomous robots," Nature, 536 (7617)**,** 451-455 (2016).

67. L. Hsu, J. Ramunas, J. Gonzalez, J. Santiago, and D. G. Strickland, "Toward an Electrolytic Micropump Actuator Design with Controlled Cyclic Bubble Growth and Recombination," ECS Trans., 35 (30), 3-11 (2011).

68. D. A. Ateya, A. A. Shah, and S. Z. Hua, "An electrolytically actuated micropump," Rev. Sci. Instrum., 75 (4), 915-920 (2004).

69. R. Sheybani, H. Gensler, and E. Meng, "Rapid and repeated bolus drug delivery enabled by high efficiency electrochemical bellows actuators," TRANSDUCERS, (IEEE), p. 490-493 (

70. T. C. Merkel, V. I. Bondar, K. Nagai, B. D. Freeman, and I. Pinnau, "Gas sorption, diffusion, and permeation in poly (dimethylsiloxane)," Journal of Polymer Science Part B: Polymer Physics, 38 (3), 415-434 (2000).

71. L. K. Massey, Permeability properties of plastics and elastomers: a guide to packaging and barrier materials, (William Andrew, 2003).

72. W. L. Robb, "Thin Silicone Membranes-Their Permeation Properties and Some Applications," Ann. N. Y. Acad. Sci., 146 (1), 119-137 (1968).

73. E. T. Carlen and C. H. Mastrangelo, "Surface micromachined paraffin-actuated microvalve," J. Microelectromech. Syst., 11 (5), 408-420 (2002).

74. J. S. Lee and S. Lucyszyn, "Design and pressure analysis for bulk-micromachined electrothermal hydraulic microactuators using a PCM," Sens. Act. A, 133 (2), 294-300 (2007).

75. M. Lehto, "Paraffin actuators in microfluidic systems" (Acta Universitatis Upsaliensis, 2007).

76. A. Castellanos, Electrohydrodynamics, (Springer, New York, 1998).

77. H.-C. Chang and L. Y. Yeo, Electrokinetically driven microfluidics and nanofluidics, (Cambridge University Press Cambridge, UK:).

78. S. Wall, "The history of electrokinetic phenomena," Curr. Opin. Colloid Interface Sci., 15 (3), 119-124.

79. A. Ramos, Electrokinetics and Electrohydrodynamics in Microsystems, (SpringerWienNewYork, New York, 2011).

80. M. Z. Bazant and T. M. Squire, "Induced-Charge Electrokinetic Phenomena: Theory and Microfluidic Applications," Phys. Rev. Lett., 92 (6), 066101:066101-066104 (2004).

81. N. E. Jewell-Larsen, E. Tran, I. A. Krichtafovitch, and A. V. Mamishev, "Design and optimization of electrostatic fluid accelerators," IEEE Trans. Dielectr. Electr. Insul., 13 (1), 191-203 (2006).

82. E. D. Fylladitakis, M. P. Theodoridis, and A. X. Moronis, "Review on the history, research, and applications of electrohydrodynamics," IEEE Trans. Plasma Sci., 42 (2), 358-375.

83. S. F. Bart, L. S. Tavrow, M. Mehregany, and J. H. Lang, "Microfabricated electrohydrodynamic pumps," Sens. Act. A, 21 (1-3), 193-197 (1990).

84. A. Richter, A. Plettner, K. Hofmann, and H. Sandmaier, "A micromachined electrohydrodynamic (EHD) pump," Sens. Act. A, 29 (2), 159-168 (1991).

85. A. Ongkodjojo Ong, "Electrohydrodynamic Microfabricated Ionic Wind Pumps for Electronics Cooling Applications," Case Western Reserve University (2013).

86. M. Z. Bazant, "Electrokinetics meets electrohydrodynamics," Journal of Fluid Mechanics, 782, 1-4 (2015).

87. M. R. Pearson and J. Seyed-Yagoobi, "Experimental study of EHD conduction pumping at the meso-and micro-scale," Journal of Electrostatics, 69 (6), 479-485 (2011).

88. J. Darabi, M. Rada, M. Ohadi, and J. Lawler, "Design, fabrication, and testing of an electrohydrodynamic ion-drag micropump," J. Microelectromech. Syst., 11 (6), 684-690 (2002).

89. K. Mori, H. Yamamoto, K. Takemura, S. Yokota, and K. Edamura, "Dominant factors inducing electro-conjugate fluid flow," Sens. Act. A, 167 84-90 (2011).

90. J. Kedzierski, K. Meng, T. Thorsen, R. Cabrera, and S. Berry, "Microhydraulic Electrowetting Actuators," J. Micromech. Microeng., 25 (2), 394-400 (2016).

91. S. Manakasettharn, "Electrowetting-Controlled and Electrically-Tunable Bio-Inspired Micro/Nanostructures and Optofluidic Devices," The University of Wisconsin-Madison (2013).

92. N. B. Crane, A. A. Volinsky, P. Mishra, A. Rajgadkar, and M. Khodayari, "Bidirectional electrowetting actuation with voltage polarity dependence," Appl. Phys. Lett., 96 (10), 104103 (2010).

93. B. J. Kirby, "Electroosmosis," in Micro- and Nanoscale Fluid Mechanics: Transport in Microfluidic Devices, edited by B. J. Kirby (Cambridge University Press, 2010).

94. X. Wang, C. Cheng, S. Wang, and S. Liu, "Electroosmotic pumps and their applications in microfluidic systems," Microfluid. Nanofluid., 6 (2), 145-145 (2009).

95. H. Yike, L. Xiaohong, L. Shu, and Y. Tianying, "Development of mean-field electrical double layer theory," Chin. Phys. B 25 (1), 016801:016801-016807 (2016).

96. M. A. Brown, A. Goel, and Z. Abbas, "Effect of electrolyte concentration on the stern layer thickness at a charged interface," Angew. Chem. Int. Ed., 55 (11), 3790-3794 (2016).

97. G. Ocvirk, M. Munroe, T. Tang, R. Oleschuk, K. Westra, and D. J. Harrison, "Electrokinetic control of fluid flow in native poly (dimethylsiloxane) capillary electrophoresis devices," Electrophoresis, 21 (1), 107-115 (2000).

98. W. Schrott, Z. Slouka, P. Červenka, J. Ston, M. Nebyla, M. Přibyl, and D. Šnita, "Study on surface properties of PDMS microfluidic chips treated with albumin," Biomicrofluidics, 3 (4), 044101 (2009).

99. Y. Sood, R. Tyagi, S. Tyagi, P. Pande, and R. Tondon, "Surface charge of different paper making raw materials and its influence on paper properties," JSIR, 69 (4), 300-304 (2010).

100. M. M. Davis, Acid-base behavior in aprotic organic solvents, (US National Bureau of Standards, Washington DC, 1968).

101. K. Bohinc, V. Kralj-Iglič, and A. Iglič, "Thickness of electrical double layer. Effect of ion size," Electrochim. Acta, 46 (19), 3033-3040 (2001).

102. Q.-H. Wan, "Effect of electrical double-layer overlap on the electroosmotic flow in packed-capillary columns," Anal. Chem., 69 (3), 361-363 (1997).

103. D. G. Haywood, Z. D. Harms, and S. C. Jacobson, "Electroosmotic flow in nanofluidic channels," Anal. Chem., 86 (22), 11174-11180 (2014).

104. W. Qu and D. Li, "A model for overlapped EDL fields," J. Colloid Interface Sci., 224 (2), 397-407 (2000).

105. L. Onsager, "Electric moments of molecules in liquids," Journal of the American Chemical Society, 58 (8), 1486-1493 (1936).

106. M. E. Piyasena, R. Newby, T. J. Miller, B. Shapiro, and E. Smela, "Electroosmotically driven microfluidic actuators," Sens. Act. B, 141 (1)**,** 263-269 (2009).

107. P. G. Erlandsson and N. D. Robinson, "Electrolysis-reducing electrodes for electrokinetic devices," Electrophoresis, 32 (6-7)**,** 784–790 (2011).

108. Y. Takamura, H. Onoda, H. Inokuchi, S. Adachi, A. Oki, and Y. Horiike, "Low-voltage electroosmosis pump for stand-alone microfluidics devices," Electrophoresis, 24 (1-2)**,** 185-192 (2003).

109. M. Z. Bazant, "AC electro-osmotic flow," in Encyclopedia of Microfluidics and Nanofluidics, Vol. 1, edited by D. Li, p. 8-14 (Springer, 2008).

110. M. Z. Bazant and T. M. Squires, "Induced-charge electrokinetic phenomena," Curr. Opin. Colloid Interface Sci., 15 (3)**,** 203-213 (2010).

111. H. M. A. Ramos, N. G. Green, A. Castellanos, "AC Electric-Field-Induced Fluid Flow in Microelectrodes," J. Colloid Interface Sci., 217**,** 420–422 (1999).

112. A. Ramos, H. Morgan, N. G. Green, A. Gonzalez, and A. Castellanos, "Pumping of liquids with traveling-wave electroosmosis," J. Appl. Phys., 97 (8)**,** 084906 (2005).

113. A. Ramos, H. Morgan, N. G. Green, and A. Castellanos, "AC electrokinetics: A review of forces in microelectrode structures," J. Phys. D: Appl. Phys., 31 (18)**,** 2338-2353 (1998).

114. T. S. Mansuripur, A. Pascall, and T. Squires, "Asymmetric flows over symmetric surfaces: capacitive coupling in induced-charge electro-osmosis," New Journal of Physics, 11 (7)**,** 075030 (2009).

115. R. J. Messinger and T. M. Squires, "Suppression of Electro-Osmotic Flow by Surface Roughness," Phys. Rev. Lett., 105 (14)**,** 144503: 144501-144504 (2010).

116. A. J. Pascall, "Investigations of Induced Charge Electrokinetic Phenomena," UNIVERSITY OF CALIFORNIA Santa Barbara (2010).

117. A. Ajdari, "Pumping liquids using asymmetric electrode arrays," Phys. Rev. E, 61 (1)**,** R45-R48 (2000).

118. L. H. Olesen, H. Bruus, and A. Ajdari, "AC electrokinetic micropumps: the effect of geometrical confinement, Faradaic current injection, and nonlinear surface capacitance.," Phys. Rev. E, 73 (5)**,** 056313 (2006).

119. J. Wu, "AC electro-osmotic micropump by asymmetric electrode polarization," J. Appl. Phys., 103 (2), 024907 (2008).

120. P. Selvaganapathy, Y. L. Ki, P. Renaud, and C. H. Mastrangelo, "Bubble-free electrokinetic pumping," J. Micromech. Microeng., 11 (5), 448-453 (2002).

121. S. Mutlu, C. Yu, P. Selvaganapathy, F. Svec, C. H. Mastrangelo, and J. M. Frechet, "Micromachined porous polymer for bubble free electro-osmotic pump," IEEE MEMS, (IEEE), p. 19-23 (2002).

122. R. B. Schasfoort, S. Schlautmann, J. Hendrikse, and A. Van Den Berg, "Field-effect flow control for microfabricated fluidic networks," Science, 286 (5441), 942-945 (1999).

123. N. J. Sniadecki, C. S. Lee, P. Sivanesan, and D. L. DeVoe, "Induced pressure pumping in polymer microchannels via field-effect flow control," Anal. Chem., 76 (7), 1942-1947 (2004).

124. W. I. Wu, P. R. Selvaganapathy, and C. Y. Ching, "Transport of particles and microorganisms in microfluidic channels using rectified ac electro-osmotic flow," Biomicrofluidics, 5 (1), 914-916 (2011).

125. D. Breite, M. Went, A. Prager, and A. Schulze, "Tailoring membrane surface charges: A novel study on electrostatic interactions during membrane fouling," Polymers, 7 (10), 2017-2030 (2015).

126. T. A. Edison, "Means and method for preventing depletion of electrolyte.," U. S. A. patent (1912).

127. S. Yao, D. E. Hertzog, S. Zeng, J. C. J. Mikkelsen, and J. G. Santiago, "Porous glass electroosmotic pumps: design and experiments," J. Colloid Interface Sci., 268 (1), 143-153 (2003).

128. C.-W. Lin, S. Yao, J. D. Posner, A. M. Myers, and J. G. Santiago, "Toward orientation-independent design for gas recombination in closed-loop electroosmotic pumps," Sens. Act. B
128 (1), 334-339 (2007).

129. M. Devanathan and Z. Stachurski, "The adsorption and diffusion of electrolytic hydrogen in palladium," Proc. R. Soc. A, (The Royal Society), vol. 270, p. 90-102 (1962).

130. S. P. Sitaram, J. O. Stoffer, and T. J. O'Keefe, "Application of conducting polymers in corrosion protection," Journal of Coatings Technology, 69 (866)**,** 65-69 (1997).

131. R. A. Bull, F. R. F. Fan, and A. J. Bard, "Polymer Films on Electrodes VII. Electrochemical Behavior at Polypyrrole-Coated Platinum and Tantalum Electrodes," Journal of the Electrochemical Society, 129 (5)**,** 1009-1015 (1982).

132. M. Moini, P. Cao, and A. J. Bard, "Hydroquinone as a buffer additive for suppression of bubbles formed by electrochemical oxidation of the CE buffer at the outlet electrode in capillary electrophoresis/electrospray ionization-mass spectrometry," Anal. Chem., 71 (8)**,** 1658-1661 (1999).

133. J. Galvao, B. Davis, M. Tilley, E. Normando, M. R. Duchen, and M. F. Cordeiro, "Unexpected low-dose toxicity of the universal solvent DMSO," FASEB 28 (3)**,** 1317-1330 (2014).

134. D. Sritharan, A. S. Chen, P. Aluthgama, B. Naved, and E. Smela, "Bubble-free electrokinetic flow with propylene carbonate," Electrophoresis, 36 (20)**,** 2622-2629 (2015).

135. S. Zeng, C. Chen, J. C. J. Mikkelsen, and J. G. Santiago, "Fabrication and characterization of electroosmotic micro pumps," Sens. Act. B, 79 (2-3)**,** 107-114 (2001).

136. S. E. Kim, R. S. List, J. G. Maveety, A. M. Myers, Q. T. Vu, R. Prasher, R. Mahajan, and G. Vandentop, "Using external radiators with electroosmotic pumps for cooling " USA patent US6992381 B2 (2005).

137. J. Santiago, J. Posner, F. B. Prinz, T. Fabian, J. Eaton, S.-W. Cha, C. Buie, D. Kim, H. Tsuru, J. Sasahara, T. Kubota, and Y. Saito, "Fuel cell with electroosmotic pump," USA patent US7799453 B2 (2004).

138. J. P. Kutter, K. B. Mogensen, H. Klank, and O. Geschke, "Microfluidics-Components," in Microsystem Engineering of Lab-on-a-chip Devices edited by H. Klank, O. Geschke, and P. Telleman, p. 39-77 (Wiley-VCH, Weinheim, 2004).

139. H. Bruus, "Theoretical Microfluidics," in, p. 51 (Oxford University Press, New York, 2008).

140. S. Pennathur and J. G. Santiago, "Electrokinetic transport in nanochannels: 1. Theory," Anal. Chem., 77 (21)**,** 6772-6781 (2005).

141. B. J. Kirby and E. F. Hasselbrink, "Zeta potential of microfluidic substrates: 1. Theory, experimental techniques, and effects on separations," Electrophoresis, 25 (2)**,** 187-202 (2004).

142. L. Chen, J. Ma, F. Tan, and Y. Guan, "Generating high-pressure sub-microliter flow rate in packed microchannel by electroosmotic force: potential application in microfluidic systems.," Sens. Act. B, 88 (3)**,** 260–265 (2003).

143. R.-L. Chen, C.-H. Chen, B.-C. Chen, and C.-L. Chen, "Electroosmotically actuated hydrogel for nastic actuation," in Plants and Mechanical Motion: A Synthetic Approach to Nastic Materials and Structures, edited by N. M. Wereley and J. M. Sater, p. 87-97 (DEStech Publications, Inc., Lancaster, Pennsylvania, 2012).

144. A. Luque, J. M. Soto, F. Perdigones, C. Aracil, and J. M. Quero, "Electroosmotic impulsion device for integration in PCB-MEMS," IEEE CDE, Seville, (IEEE), p. 119-122 (2013).

145. T. E. McKnight, C. T. Culbertson, S. C. Jacobson, and M. J. Ramsey, "Electroosmotically induced hydraulic pumping with integrated electrodes on microfluidic devices," Anal. Chem., 73**,** 4045-4049 (2001).

146. J. A. Tripp, F. Svec, J. M. J. Fréchet, S. Zeng, J. C. Mikkelsen, and J. G. Santiago, "High-pressure electroosmotic pumps based on porous polymer monoliths," Sens. Act. B, 99 (1)**,** 66-73 (2004).

147. S. G. Bratsch, "Standard Electrode Potentials and Temperature Coefficients in Water at 298.15 K," J. Phys. Chem. Ref. Data, 18 (1)**,** 1–21 (1989).

148. R. V. Chebiam and V. M. Dubin, "Electroosmotic pump apparatus that generates low amount of hydrogen gas," USA patent US 7149085 (2006).

149. M. A. Schroeder, K. S. Salloum, M. Perbost, M. Lebl, and J. D. Posner, "Radial flow electroosmotic pump," Sens. Act. A, 169 (1)**,** 250–255 (2011).

150. T. M. Woudenberg, Z. T. Bryning, and R. B. Kowallis, "Bubble-free and pressure-generating electrodes for electrophoretic and electroosmotic devices," USA patent US7357852 (2008).

151. J. G. Santiago and S. Zeng, "Control of electrolysis gases in electroosmotic pump systems," USA patent US7134486 (2006).

152. S. Debesset, C. J. Hayden, C. Dalton, J. C. T. Eijkel, and A. Manz, "An AC electroosmotic micropump for circular chromatographic applications," Lab Chip, 4 (4)**,** 396-400 (2004).

153. C.-C. Huang, M. Z. Bazant, and T. Thorsen, "Ultrafast high-pressure AC electro-osmotic pumps for portable biomedical microfluidics," Lab Chip, 10 (1)**,** 80-85 (2010).

154. K. Xu, "Nonaqueous liquid electrolytes for lithium-based rechargeable batteries," Chem. Rev., 104**,** 4303-4417 (2004).

155. Huntsman Corporation, "Comparative Solvents Data: Jeffsol Alkylene Carbonates" (2001), p. 3,14.

156. A. Seiman, M. Vaher, and M. Kaljurand, "Monitoring of the electroosmotic flow of ionic liquid solutions in non-aqueous media using thermal marks," J. Chromatogr. A, 1189 (1-2)**,** 266-273 (2008).

157. B. J. Kirby, "The diffuse structure of the electrical double layer," in Micro- and Nanoscale Fluid Mechanics: Transport in Microfluidic Devices, edited by B. J. Kirby, p. 199-218 (Cambridge University Press, 2010).

158. C.-H. Chen and J. G. Santiago, "A Planar Electroosmotic Micropump," J. Micromech. Microeng., 11 (6)**,** 672-683 (2002).

159. E. C. Fuchs, J. Woisetschlaeger, K. Gatterer, E. Maier, R. Pecnik, G. Holler, and H. Eisenkoelbl, "The floating water bridge," J. Phys. D: Appl. Phys., 40**,** 6112–6114 (2007).

160. K. J. Aoki, C. Li, T. Nishiumi, and J. Chen, "Electrolysis of pure water in a thin layer cell," J. Electroanal. Chem., 695**,** 24-29 (2013).

161. S. A. Campbell, C. Bowes, and R. S. McMillan, "The electrochemical behaviour of tetrahydrofuran and propylene carbonate without added electrolyte," J. Electroanal. Chem. Interfac. , 284 (1)**,** 195-204 (1990).

162. B. J. Kirby and E. F. Hasselbrink, "Zeta potential of microfluidic substrates: 2. Data for polymers," Electrophoresis, 25 (2)**,** 203–213 (2004).

163. X. Ren, M. Bachman, C. Sims, G. P. Li, and N. Allbritton, "Electroosmotic properties of microfluidic channels composed of poly(dimethylsiloxane)," J. Chromatogr. B, 762 (2)**,** 117-125 (2001).

164. G. Ocvirk, M. Munroe, T. Tang, R. Oleschuk, K. Westra, and D. J. Harrison, "Electrokinetic control of fluid flow in native poly(dimethylsiloxane) capillary electrophoresis devices," Electrophoresis, 21 (1)**,** 107-115 (2000).

165. A. J. Bubendorfer, B. Ingham, J. V. Kennedy, and W. M. Arnold, "Origin of Electrokinetic Variability in Microfluidic Devices Cast on SU-8 Epoxy," Proc. ESA Annual Meeting on Electrostatics, Notre Dame, Indiana, (Electrostatics Society of America), p. 1-6 (2014).

166. H. Hillborg and U. W. Gedde, "Hydrophobicity recovery of polydimethylsiloxane after exposure to corona discharges," Polymer, 39 (10)**,** 1991-1998 (1998).

167. J. N. Israelachvili, Intermolecular and Surface Forces third ed. (Academic Press, San Diego, 2011).

168. D. Sritharan, M. Motsebo, J. Tumbic, and E. Smela, "Stable electroosmotically driven actuators" in SPIE EAPAD; Vol. 8687 (SPIE Proceedings, San Diego, California, USA, 2013).

169. Casa Software Ltd., "Basic Quantification of XPS Spectra" (2008), p. 1-7.

170. L. Chen, J. Ma, and Y. Guan, "Study of an electroosmotic pump for liquid delivery and its application in capillary column liquid chromatography," J. Chromatogr. A, 1028 (2)**,** 219-226 (2004).

171. A. B. D. Brown, C. G. Smith, and A. R. Rennie, "Pumping of water with AC electric fields applied to asymmetric pairs of microelectrodes," Phys. Rev. E, 63 (1)**,** 016305-016305 (2000).

172. H. Bae and M. Yu, "Miniature Fabry-Perot pressure sensor created by using UV-molding process with an optical fiber based mold," Optics Express, 20 (13)**,** 14573-14583 (2012).

173. J. M. Crowley, G. S. Wright, and J. C. Chato, "Selecting a working fluid to increase the efficiency and flow rate of an EHD pump," IEEE Trans. Ind. Appl, 26 (1)**,** 42-49 (1990).

174. A. J. Bard and L. R. Faulkner, Electrochemical Methods: Fundamentals and Applications 2nd ed. (Wiley, 2000).

175. H. H. Ku, "Notes on the use of propagation of error formulas," J. Res. Nat. Bur. Stand., 70 (4)**,** 263-273 (1966).

176. I. S. Sokolnikoff, Mathematical theory of elasticity, (McGraw-Hill, 1956).

177. G. A. Holzapfel, Nonlinear Solid Mechanics: A Continuum Approach for Engineering, (Wiley, 2000).

178. R. H. Pritchard, P. Lava, D. Debruyne, and E. M. Terentjev, "Precise determination of the Poisson ratio in soft materials with 2D digital image correlation," Soft Matter, 9 (26)**,** 6037-6045.

179. M. Liu, J. Sun, Y. Sun, C. Bock, and Q. Chen, "Thickness-dependent mechanical properties of polydimethylsiloxane membranes," J. Micromech. Microeng., 19 (3)**,** 035028 (2009).

180. A. L. Smith, "The Coblentz Society Desk Book of Infrared Spectra ", 2nd ed., edited by C. D. Carver (The Coblentz Society), p. 1-24.

181. National Institute of Advanced Industrial Science and Technology, "Spectral Database for Organic Compounds".

182. J. Ufheil, A. Wursig, O. D. Schneider, and P. Novak, "Acetone as oxidative decomposition product in propylene carbonate containing battery electrolyte," Electrochem. Commun., 7 (12)**,** 1380-1384 (2005).

183. D. L. Pavia, G. M. Lampman, G. S. Kriz, and J. A. Vyvyan, "Infrared Spectroscopy," in Introduction to Spectroscopy: A Guide for Students of Organic Chemistry p. 30-86 (W. B. Saunders Co., Philadelphia, 1979).

184. Horiba Jobin Yvon, "Raman Data and Analysis" (2013), p. 1-2.

185. J. B. Lambert, H. F. Shurvell, and R. G. Cooks, "Introduction to Organic Spectroscopy," in, 1st ed., p. 174-177 (Macmillan, 1987).

186. J. Jorni and C. W. Tobias, "Electrodeposition of the alkali metals from propylene carbonate," J. Appl. Electrochem., 5**,** 279-290 (1975).

187. K. Faure, M. Albert, V. Dugas, G. Crétier, R. Ferrigno, P. Morin, and J. L. Rocca, "Development of an acrylate monolith in a cyclo-olefin copolymer microfluidic device for chip electrochromatography separation.," Electrophoresis, 29 (24)**,** 4948-4955 (2008).

188. C. Yu, M. C. Xu, F. Svec, and J. M. J. Frechet, "Preparation of monolithic polymers with controlled porous properties for microfluidic chip applications using photoinitiated free-radical polymerization," J. Polym. Sci. A Polym. Chem., 40 (6)**,** 755-769 (2002).

189. C. Yu, F. Svec, and J. M. J. Frechet, "Towards stationary phases for chromatography on a microchip: Molded porous polymer monoliths prepared in capillaries by photoinitiated in situ polymerization as separation media for electrochromatography," Electrophoresis, 21 (1)**,** 120-127 (2000).

190. J. Krenkova, A. Gargano, N. A. Lacher, J. M. Schneiderheinze, and F. Svec, "High binding capacity surface grafted monolithic columns for cation exchange chromatography of proteins and peptides," J. Chromatogr. A, 1216 (40)**,** 6824-6830 (2009).

191. D. Lee, F. Svec, and J. M. J. Frechet, "Photopolymerized monolithic capillary columns for rapid micro high-performance liquid chromatographic separation of proteins," J. Chromatogr. A, 1051 (1-2)**,** 53-60 (2004).

192. M. J. Yoo, D. S. Hage, and P. Wang, Monolithic Chromatography and its Modern Applications, (ILM Publications, St. Albans, 2010).

193. C. Yu, M. H. Davey, F. Svec, and J. M. J. Frechet, "Monolithic porous polymer for on-chip solid-phase extraction and preconcentration prepared by photoinitiated in situ polymerization within a microfluidic device," Anal. Chem., 73 (21)**,** 5088-5096 (2001).

194. J. D. Ramsey and G. E. Collins, "Integrated microfluidic device for solid-phase extraction coupled to micellar electrokinetic chromatography separation," Anal. Chem., 77 (20)**,** 6664-6670 (2005).

195. J. K. Liu, C. F. Chen, C. W. Tsao, C. C. Chang, C. C. Chu, and D. L. Devoe, "Polymer Microchips Integrating Solid-Phase Extraction and High-Performance Liquid Chromatography Using Reversed-Phase Polymethacrylate Monoliths," Anal. Chem., 81 (7)**,** 2545-2554 (2009).

196. J. M. Burke and E. Smela, "A novel surface modification technique for forming porous polymer monoliths in poly(dimethylsiloxane)," Biomicrofluidics, 6 (1)**,** 016506-016506-016510.

197. J. Liu, C.-F. Chen, C.-W. Chang, and D. L. DeVoe, "Flow-through immunosensors using antibody-immobilized polymer monoliths," Biosensors and Bioelectronics, 26 (1)**,** 182-188.

198. P. Wang, Z. L. Chen, and H. C. Chang, "A new electro-osmotic pump based on silica monoliths," Sens. Act. B, 113 (1)**,** 500-509 (2006).

199. M. F. Bedair and R. D. Oleschuk, "Fabrication of porous polymer monoliths in polymeric microfluidic chips as an electrospray emitter for direct coupling to mass spectrometry.," Anal. Chem., 78 (4)**,** 1130-1138 (2006).

200. E. C. Peters, M. Petro, F. Svec, and J. M. Frechet, "Molded rigid polymer monoliths as separation media for capillary electrochromatography. 1. Fine control of porous properties and surface chemistry," Anal. Chem., 70 (11)**,** 2288-2295 (1998).

201. K. M. Chen, X. Jiang, L. C. Kimerling, and P. T. Hammond, "Selective self-organization of colloids on patterned polyelectrolyte templates," Langmuir, 16 (20), 7825-7834 (2000).

202. A. Brask, D. Snakenborg, J. P. Kutter, and H. Bruus, "AC electroosmotic pump with bubble-free palladium electrodes and rectifying polymer membrane valves," Lab Chip, 6 (2), 280-288 (2006).

203. P. H. Paul and D. J. Rakestraw, "Electrokinetic high pressure hydraulic system " patent US6019882 (2000).

204. J. Krumme, "Valve for controlling flow of a fluid," US patent US4327772 A (2007).

205. B. J. Kirby, T. J. Shepodd, and E. F. J. Hasselbrink, "Voltage-addressable on/off microvalves for high-pressure microchip separations," J. Chromatogr. A, 979, 147–154 (2002).

206. M. E. Piyasena, B. Shapiro, and E. Smela, "A new EAP based on electroosmotic flow: nastic actuators" in SPIE EAPAD; Vol. 7287 (SPIE, 2009).

207. W. M. Kier and K. K. Smith, "Tongues, tentacles and trunks: the biomechanics of movement in muscular-hydrostats," Zool. J. Linnean. Soc., 83, 307–324 (1985).

208. W. C. Dickison, Integrative Plant Anatomy, (Academic Press, 2000).

209. J. Rossmeisl, A. Logadottir, and J. K. Nørskov, "Electrolysis of water on (oxidized) metal surfaces," Chem. Phy., 319 (1-3), 178–184 (2005).

210. W. N. Haynes, CRC Handbook of Chemistry and Physics, Vol. 92 (CRC Press, 2011).

211. N. A. Mishchuk, T. Heldal, T. Volden, J. Auerswald, and H. Knapp, "Micropump based on electroosmosis of the second kind," Electrophoresis, 30, 3499–3506 (2009).

212. Y. C. Kim, S.-H. Kim, D. Kim, S.-J. Park, and J.-K. Park, "Plasma extraction in a capillary-driven microfluidic device using surfactant-added poly (dimethylsiloxane)," Sens. Act. B
145 (2), 861-868 (2010).

213. W. Yang, Y. G. Nam, B.-K. Lee, K. Han, T. H. Kwon, and D. S. Kim, "Fabrication of a Hydrophilic Poly (dimethylsiloxane) Microporous Structure and

Its Application to Portable Microfluidic Pump," Japanese Journal of Applied Physics, 49 (6S)**,** 06GM01 (2010).

214. S. Waheed, J. M. Cabot, N. P. Macdonald, T. Lewis, R. M. Guijt, B. Paull, and M. C. Breadmore, "3D printed microfluidic devices: enablers and barriers," Lab Chip, 16 (11)**,** 1993-2013.

215. D. Sritharan and E. Smela, "Fabrication of a Miniature Paper-Based Electroosmotic Actuator," Polymers, 8 (11)**,** 400 (2016).

216. M. Kohl, "Microactuators," in Shape Memory Microactuators, p. 5-24 (Springer, 2004).

217. F. Daerden and D. Lefeber, "Pneumatic artificial muscles: actuators for robotics and automation," EJMEE, 47 (1)**,** 11-21 (2002).

218. C.-P. Chou and B. Hannaford, "Measurement and modeling of McKibben pneumatic artificial muscles," IEEE Trans. Robot. Autom. , 12 (1)**,** 90-102 (1996).

219. M. B. Pritts and C. D. Rahn, "Design of an artificial muscle continuum robot," IEEE ICRA, New Orleans, USA, (IEEE), vol. 5, p. 4742-4746 (2004).

220. A. D. Marchese, R. K. Katzschmann, and D. Rus, "A recipe for soft fluidic elastomer robots," Soft Robotics, 2 (1)**,** 7-25.

221. K. Suzumori, S. Endo, T. Kanda, N. Kato, and H. Suzuki, "A Bending Pneumatic Rubber Actuator Realizing Soft-bodied Manta Swimming Robot," IEEE ICRA, p. 4975-4980 (2007).

222. R. V. Martinez, J. L. Branch, C. R. Fish, L. Jin, R. F. Shepherd, R. M. D. Nunes, Z. Suo, and G. M. Whitesides, "Robotic Tentacles with Three-Dimensional Mobility Based on Flexible Elastomers," Adv. Mater., 25 (2)**,** 205-212 (2013).

223. R. F. Shepherd, A. A. Stokes, R. M. D. Nunes, and G. M. Whitesides, "Soft Machines That are Resistant to Puncture and That Self Seal," Adv. Mater., 25 (46)**,** 6709-6713 (2013).

224. S. A. Morin, R. F. Shepherd, S. W. Kwok, A. A. Stokes, A. Nemiroski, and G. M. Whitesides, "Camouflage and Display for Soft Machines," Science, 337 (6096)**,** 828-832.

225. B. Mosadegh, P. Polygerinos, C. Keplinger, S. Wennstedt, R. F. Shepherd, U. Gupta, J. Shim, K. Bertoldi, C. J. Walsh, and G. M. Whitesides, "Pneumatic

Networks for Soft Robotics that Actuate Rapidly," Adv. Funct. Mater., 24 (15), 2163-2170 (2014).

226. M. De Volder, "Capillary Based Sealing," in Surface Tension in Microsystems: Engineering Below the Capillary Length, edited by P. Lambert, p. 211-226 (Springer, Berlin, Heidelberg, 2013).

227. D. A. de Koninck, F. M. Lopez, D. Briand, and N. F. d. Rooij, "Foil-level fabrication of inkjet-printed pyroMEMS balloon actuators," IEEE MEMS, p. 64-67 (2012).

228. P. L. Bergstrom, J. Jin, L. Yu-Ning, M. Kaviany, and K. D. Wise, "Thermally driven phase-change microactuation," J. Microelectromech. Syst., 4 (1), 10-17 (1995).

229. D. Corning, "Sylgard 184 Silicone Elastomer: Product Information," 1-4 (2014).

230. Smooth-On, "Ecoflex Series: Product Overview," (2014).

231. P. T. Martone, M. Boller, I. Burgert, J. Dumais, J. Edwards, K. Mach, N. Rowe, M. Rueggeberg, R. Seidel, and T. Speck, "Mechanics without muscle: biomechanical inspiration from the plant world," ICB, 50 (5), 888-907.

232. J.-w. Kim, T. Suzuki, S. Yokota, and K. Edamura, "Tube-type micropump by using electro-conjugated fluid (ECF)," Sens. Act. A, 174, 155-161.

233. S. Yokota, F. Yajima, K. Takemura, and K. Edamura, "Electro-Conjugate Fluid Jet-Driven Micro Artificial Antagonistic Muscle Actuators and their Integration," Adv. Rob., 24 (14), 1929-1943.

234. S. Yokota, A. Sadamoto, Y. Kondoh, Y. Otsubo, and K. Edamura, "A micro motor using electroconjugate fluids (ECFs)," JSME Int J C-Mech Sy, 44 (3), 756-762 (2001).

235. D. Han, J. W. Kim, S. Yokota, K. Edamura, "ECF micropump fabricated by electroforming with novel self-aligned micro-molding technology," JPCS, 660 (1), 012029: 012021-012025 (2015).

236. H.-J. r. Butt and M. Kappl, Surface and interfacial forces, (John Wiley & Sons, 2009).

237. K. Seibel, L. Schoeler, H. Schaefer, and M. Boehm, "A programmable planar electroosmotic micropump for lab-on-a-chip applications," J. Micromech. Microeng., 18 (2), 025008-025008 (2008).

238. C. Gu, Z. Jia, Z. Zhu, C. He, W. Wang, A. Morgan, J. J. Lu, and S. Liu, "Miniaturized electroosmotic pump capable of generating pressures of more than 1200 Bar," Anal. Chem., 84**,** 9609−9614 (2012).

239. L. M. Bellan, M. Pearsall, D. M. Cropek, and R. Langer, "A 3D Interconnected Microchannel Network Formed in Gelatin by Sacrificial Shellac Microfibers," Adv. Mater., 24 (38)**,** 5187-5191.

240. A. W. Martinez, S. T. Phillips, G. M. Whitesides, and E. Carrilho, "Diagnostics for the developing world: microfluidic paper-based analytical devices," Anal. Chem., 82 (1)**,** 3-10 (2009).

241. X. Li, D. R. Ballerini, and W. Shen, "A perspective on paper-based microfluidics: Current status and future trends," Biomicrofluidics, 6 (1)**,** 011301-011301-011313.

242. J. L. Engelke, H. H. Strain, and S. E. Wood, "Electroosmosis in Paper Electrochromatography with Electrode Vessels," Anal. Chem., 26 (12)**,** 1864-1868 (1954).

243. B. Balakrisnan, A. Nacev, J. M. Burke, A. Dasgupta, and E. Smela, "Design of compliant meanders for applications in MEMS, actuators, and flexible electronics," Smart Mater. Struct. , 21 (7)**,** 075033: 075031-075015 (2012).

244. A. P. Gerratt, B. Balakrisnan, I. Penskiy, and S. Bergbreiter, "Dielectric elastomer actuators fabricated using a micro-molding process," Smart Mater. Struct. , 23 (5)**,** 055004 (2014).

245. M. Brun, J.-F. Chateaux, A.-L. Deman, P. Pittet, and R. Ferrigno, "Nanocomposite Carbon-PDMS Material for Chip-Based Electrochemical Detection," Electroanalysis, 23 (2)**,** 321-324 (2010).

246. M. Kujawski, J. Pearse, and E. Smela, "PDMS/graphite stretchable electrodes for dielectric elastomer actuators" in SPIE EAPAD Vol. 7642 (SPIE Proceedings, San Diego, 2010), p. 76420R.

247. H. Yamada, I. Manas-Zloczower, and D. L. Feke, "Influence of matrix infiltration on the dispersion kinetics of carbon black agglomerates," Powd. Technol., 92 (2)**,** 163-169 (1997).

248. E. A. Van Nierop, B. Scheid, and H. A. Stone, "On the thickness of soap films: an alternative to Frankel's law," J. Fluid Mech., 602**,** 119-127 (2008).

249. Stratasys, "Digital Materials Data Sheet" (2015).

250. N. Binh-Khiem, K. Matsumoto, and I. Shimoyama, "Tensile Film Stress of Parylene Deposited on Liquid," Langmuir, 26 (24), 18771-18775 (2010).

251. Liquid encapsulation technology for microelectromechanical systems; *Vol.*, edited by N. Miki (InTech, 2013).

252. Á. G. Marín and D. Lohse, "Building water bridges in air: Electrohydrodynamics of the floating water bridge," Phys. Fluids, 22 (12), 122104.

253. A. D. Wexler, M. López Sáenz, O. Schreer, J. Woisetschläger, and F. E. C., "The Preparation of Electrohydrodynamic Bridges from Polar Dielectric Liquids," JoVE (91), 51819.

254. W. F. Pickard, "Experimental investigation of the sumoto effect," J. Appl. Phys 32 (10), 1888-1893 (1961).

255. H. Duan, Z. W. Hu, and Z. C. Fang, "Study on deformation characters of a large rubber circular plate," Model. Simul. Mater. Sci. Eng., 12 (2), 245 (2004).

256. A. Srivastava and C.-Y. Hui, "Large deformation contact mechanics of a pressurized long rectangular membrane. II. Adhesive contact," Proc. R. Soc. A, 469 (2160) (2013).

257. S. Xiao, J. F. Kolb, M. A. Malik, X. Lu, M. Laroussi, R. P. Joshi, E. Schamiloglu, and K. H. Schoenbach, "Electrical Breakdown and Dielectric Recovery of Propylene Carbonate," IEEE Trans. Plasma Sci., 34 (5), 1653-1661 (2006).

258. J. N. Lee, C. Park, and G. M. Whitesides, "Solvent compatibility of poly(dimethylsiloxane)-based microfluidic devices," Anal. Chem., 75 (23), 6544-6554 (2003).

259. L. Wågberg and R. Hägglund, "Kinetics of polyelectrolyte adsorption on cellulosic fibers," Langmuir, 17 (4), 1096-1103 (2001).

260. M. Abdelmouleh, S. Boufi, M. N. Belgacem, A. P. Duarte, A. B. Salah, and A. Gandini, "Modification of cellulosic fibres with functionalised silanes: development of surface properties," Int. J. Adhes. Adhes., 24 (1), 43-54 (2004).

261. N. Bowden, S. Brittain, A. G. Evans, J. W. Hutchinson, and G. M. Whitesides, "Spontaneous formation of ordered structures in thin films of metals supported on an elastomeric polymer," Nature, 393 (6681), 146-149 (1998).

262. Sigma-Aldrich, "MSDS for anhydrous propylene carbonate".

263. D. Armani, C. Liu, and N. Aluru, "Re-configurable fluid circuits by PDMS elastomer micromachining," IEEE MEMS, p. 222-227 (1999).

264. J.-B. Chossat, Y.-L. Park, R. J. Wood, and V. Duchaine, "A soft strain sensor based on ionic and metal liquids," IEEE Sensors Journal, 13 (9)**,** 3405-3414 (2013).

265. D. Therriault, S. R. White, and J. A. Lewis, "Chaotic mixing in three-dimensional microvascular networks fabricated by direct-write assembly," Nat. Mater., 2 (4)**,** 265-271 (2003).

266. A. K. Au, W. Lee, and A. Folch, "Mail-order microfluidics: evaluation of stereolithography for the production of microfluidic devices," Lab Chip, 14 (7)**,** 1294-1301 (2014).

267. J. H. Huang, J. Kim, N. Agrawal, A. P. Sudarsan, J. E. Maxim, A. Jayaraman, and V. M. Ugaz, "Rapid Fabrication of Bio-inspired 3D Microfluidic Vascular Networks," Adv. Mater., 21 (35)**,** 3567-3571 (2009).

268. H. Lim, Y. Wong, M. Rahman, and M. E. Lee, "A study on the machining of high-aspect ratio micro-structures using micro-EDM," Journal of Materials Processing Technology, 140 (1)**,** 318-325 (2003).

269. C. Lausted, T. Dahl, C. Warren, K. King, K. Smith, M. Johnson, R. Saleem, J. Aitchison, L. Hood, and S. R. Lasky, "POSaM: a fast, flexible, open-source, inkjet oligonucleotide synthesizer and microarrayer," Genome Biol., 5 (8)**,** R58 (2004).

270. J. Harden, D. Long, and A. Ajdari, "Influence of end-grafted polyelectrolytes on electro-osmosis along charged surfaces," Langmuir, 17 (3)**,** 705-715 (2001).

271. K. J. Quinn and J. M. Courtney, "Silicones as biomaterials," Polym. Int., 20 (1)**,** 25-32 (1988).

272. A. Colas and J. Curtis, "Silicone biomaterials: history and chemistry," Biomaterials science: an introduction to materials in medicine, 2**,** 80-85 (2004).

273. USFDA, "Code of Federal Regulations, Title 21"; Vol. 3 (U.S. Food and Drug Administration, 2016).

274. R. S. Kenneth, “Environmental Profile for Propylene Carbonate,” Report No. 68-C6-0027 (1998).

275. M. Maitz, "Applications of synthetic polymers in clinical medicine," Biosurf. Biotribol., 1 (3)**,** 161-176 (2015).

276. W. S. Wong and A. Salleo, Flexible electronics: materials and applications, Vol. 11 (Springer Science & Business Media, 2009).

277. E. Schwartz, "Roll to roll processing for flexible electronics," MSE Thesis, Cornell University (2006).

278. M.-W. Han and S.-H. Ahn, "Blooming Knit Flowers: Loop-Linked Soft Morphing Structures for Soft Robotics," Adv. Mater., 29 (13).

279. M. A. Unger, H.-P. Chou, T. Thorsen, A. Scherer, and S. R. Quake, "Monolithic microfabricated valves and pumps by multilayer soft lithography," Science, 288 (5463)**,** 113-116 (2000).

280. B. Shapiro and E. Smela, "Electrically driven microfluidic pumping for actuation " US patent application (number 20060056997) (2006).

281. E. Smela, "Challenges in realizing a self-contained hydraulically-driven contractile fiber actuator," Faraday Discussions (2017).

282. B. Arkles, "Silane coupling agents: connecting across boundaries" (Gelest Inc., 2003), p. 9-12.

283. B. Arkles, "Hydrophobicity, hydrophilicity and silane surface modification" (Gelest Inc., 2011).

284. G. Decher and J. Hong, "Buildup of ultrathin multilayer films by a self-assembly process: II. Consecutive adsorption of anionic and cationic bipolar amphiphiles and polyelectrolytes on charged surfaces," Ber. Bunsen-Ges. Phys. Chem., 95 (11)**,** 1430-1434 (1991).

285. T. Rohr, D. F. Ogletree, F. Svec, and J. M. J. Frechet, "Surface functionalization of thermoplastic polymers for the fabrication of microfluidic devices by photoinitiated grafting," Adv. Funct. Mater., 13 (4)**,** 264-270 (2003).

286. D. O. Carlsson, "Structural and electrochemical properties of functionalized nanocellulose materials and their biocompatibility," Acta Universitatis Upsaliensis (2014).

287. G. Chitnis, Z. Ding, C.-L. Chang, C. A. Savran, and B. Ziaie, "Laser-treated hydrophobic paper: an inexpensive microfluidic platform," Lab Chip, 11 (6)**,** 1161-1165.

288. W. Qu and D. Li, "A model for overlapped EDL fields," Journal of Colloid and Interface Science, 224 (2)**,** 397-407 (2000).

289. K.-D. Huang and R.-J. Yang, "Electrokinetic behaviour of overlapped electric double layers in nanofluidic channels," Nanotechnology, 18 (11)**,** 115701 (2007).

290. M. Deng, Q. Zhou, A. Du, J. van Kasteren, and Y. Wang, "Preparation of nanoporous cellulose foams from cellulose-ionic liquid solutions," Materials Letters, 63 (21)**,** 1851-1854 (2009).

291. M. Pääkkö, J. Vapaavuori, R. Silvennoinen, H. Kosonen, M. Ankerfors, T. Lindström, L. A. Berglund, and O. Ikkala, "Long and entangled native cellulose I nanofibers allow flexible aerogels and hierarchically porous templates for functionalities," Soft Matter, 4 (12)**,** 2492-2499 (2008).

292. S. W. Pattinson and A. J. Hart, "Additive manufacturing of cellulosic materials with robust mechanics and antimicrobial functionality," Adv. Mater. Technologies, 2 (4) (2017).

293. H. Jeffsol and A. Carbonates, "Polymer Solubility Data" in Houston, TX, edited by H. Corporation (2001).

294. N. A. Patankar and H. H. Hu, "Numerical simulation of electroosmotic flow," Anal. Chem., 70 (9)**,** 1870-1881 (1998).

295. P. Dutta, A. Beskok, and T. C. Warburton, "Electroosmotic flow control in complex microgeometries," J. Microelectromech. Syst., 11 (1)**,** 36-44 (2002).

296. H. Park, J. Lee, and T. Kim, "Comparison of the Nernst–Planck model and the Poisson–Boltzmann model for electroosmotic flows in microchannels," Journal of colloid and interface science, 315 (2)**,** 731-739 (2007).

297. T. Postler, Z. Slouka, M. Svoboda, M. Přibyl, and D. Šnita, "Parametrical studies of electroosmotic transport characteristics in submicrometer channels," Journal of colloid and interface science, 320 (1)**,** 321-332 (2008).

298. I. D. Joshipura, H. R. Ayers, C. Majidi, and M. D. Dickey, "Methods to pattern liquid metals," Journal of Materials Chemistry C, 3 (16)**,** 3834-3841 (2015).

299. T.-W. Chou, L. Gao, E. T. Thostenson, Z. Zhang, and J.-H. Byun, "An assessment of the science and technology of carbon nanotube-based fibers and composites," CSTE, 70 (1)**,** 1-19 (2010).

300. R. H. Baughman, A. A. Zakhidov, and W. A. De Heer, "Carbon nanotubes - the route toward applications," Science, 297 (5582)**,** 787-792 (2002).

301. D. Li, Electrokinetics in microfluidics, Vol. 2 (Academic Press, 2004).

302. H. Zhang and A. Cloud, "The permeability characteristics of silicone rubber," Global Advances in Materials and Process Engineering, Dallas, TX, (SAMPE), p. 1-10 (2006).

303. J. B. Fortin and T.-M. Lu, Chemical vapor deposition polymerization: the growth and properties of parylene thin films, (Springer Science & Business Media, 2003).

304. Z. Fu, Z. Wei, X. Lin, T. Huang, and A. Yu, "Polyaniline membranes as waterproof barriers for lithium air batteries," Electrochim. Acta, 78**,** 195-199 (2012).

305. B. Henry, F. Dinelli, K.-Y. Zhao, C. Grovenor, O. Kolosov, G. A. D. Briggs, A. Roberts, R. Kumar, and R. Howson, "A microstructural study of transparent metal oxide gas barrier films," Thin Solid Films, 355**,** 500-505 (1999).

306. B. G. Hawkins and B. J. Kirby, "Electrothermal flow effects in insulating (electrodeless) dielectrophoresis systems," Electrophoresis, 31 (22)**,** 3622-3633 (2010).

307. D. S. Reichmuth, G. S. Chirica, and B. J. Kirby, "Increasing the performance of high-pressure, high-efficiency electrokinetic micropumps using zwitterionic solute additives," Sens. Act. B, 92 (1)**,** 37-43 (2003).

308. C.-H. Lin, G. S. Ferguson, and M. K. Chaudhury, "Electrokinetics of Polar Liquids in Contact with Nonpolar Surfaces," Langmuir, 29 (25)**,** 7793-7801 (2013).

309. M. H. Dickinson, C. T. Farley, R. J. Full, M. Koehl, R. Kram, and S. Lehman, "How animals move: an integrative view," Science, 288 (5463)**,** 100-106 (2000).

310. N. Xydas and I. Kao, "Modeling of contact mechanics and friction limit surfaces for soft fingers in robotics, with experimental results," Int. J. Robot. Res. , 18 (9)**,** 941-950 (1999).

311. K. Autumn, M. Sitti, Y. A. Liang, A. M. Peattie, W. R. Hansen, S. Sponberg, T. W. Kenny, R. Fearing, J. N. Israelachvili, and R. J. Full, "Evidence for van der Waals adhesion in gecko setae," Proc. Natl. Acad. Sci. U.S.A., 99 (19)**,** 12252-12256 (2002).

312. K. Johnson, K. Kendall, and A. Roberts, "Surface energy and the contact of elastic solids," Proc. R. Soc. A, (The Royal Society), vol. 324, p. 301-313 (1971).

313. W. J. Lyman, W. F. Reehl, and D. H. Rosenblatt, "Environmental behavior of organic compounds " in Handbook of Chemical Property Estimation Methods, Vol. 110, p. 61 (American Chemical Society, Washington DC, 1990).

314. S. Zadeh, S. R. Swanson, and S. L. Anna, "Highly uniform micro-cavity arrays in flexible elastomer film," Soft Matter, 5**,** 743-746 (2009).

315. A. P. Gerratt and S. Bergbreiter, "Microfabrication of compliant all-polymer MEMS thermal actuators," Sens. Act. A, 177**,** 16-22 (2012).

316. R. Pelrine, R. Kornbluh, Q. B. Pei, and J. Joseph, "High-speed electrically actuated elastomers with strain greater than 100%," Science, 287 (5454)**,** 836-839 (2000).

317. S. M. Lee, D. J. Oh, I. D. Jung, P. G. Jung, K. H. Chung, W. I. Jang, and J. S. Ko, "Evaluation of the waterproof ability of a hydrophobic nickel micromesh with array-type microholes," J. Micromech. Microeng., 19 (12)**,** 125024 (2009).

318. M. Hamedi, E. Karabulut, A. Marais, A. Herland, G. Nyström, and L. Wågberg, "Nanocellulose Aerogels Functionalized by Rapid Layer-by-Layer Assembly for High Charge Storage and Beyond," Angew. Chem. Int. Ed., 52 (46)**,** 12038-12042 (2013).

319. B. T. Ginn and O. Steinbock, "Polymer surface modification using microwave-oven-generated plasma," Langmuir, 19 (19)**,** 8117-8118 (2003).

320. L. Shen, W. Wang, H. Ding, and Q. Guo, "Flame soot stably deposited on silicone coatings possess superhydrophobic surface," Appl. Surf. Sci., 284**,** 651-656.

321. A. Vilfan and F. Jülicher, "Hydrodynamic flow patterns and synchronization of beating cilia," Phys. Rev. Lett., 96 (5)**,** 058102 (2006).

322. J. Lighthill, "Flagellar hydrodynamics," SIAM review, 18 (2)**,** 161-230 (1976).

323. D. R. Soll, E. Voss, B. Varnum-Finney, and D. Wessels, "“Dynamic Morphology System”: a method for quantitating changes in shape, pseudopod formation, and motion in normal and mutant amoebae of Dictyostelium discoideum," Journal of cellular biochemistry, 37 (2)**,** 177-192 (1988).

324. D. R. Soll, E. Voss, O. Johnson, and D. Wessels, "Three-dimensional reconstruction and motion analysis of living, crawling cells," Scanning, 22 (4)**,** 249-257 (2000).

325. S. L. Tamm, "Ciliary motion in Paramecium: a scanning electron microscope study," The Journal of cell biology, 55 (1)**,** 250 (1972).

326. S.-H. Cheon, S. R. Kim, H.-O. Song, M.-H. Ahn, and J.-S. Ryu, "The dimension of Trichomonas vaginalis as measured by scanning electron microscopy," The Korean journal of parasitology, 51 (2)**,** 243 (2013).

327. K. Liolos, B. Abt, C. Scheuner, H. Teshima, B. Held, A. Lapidus, M. Nolan, S. Lucas, S. Deshpande, and J.-F. Cheng, "Complete genome sequence of the halophilic bacterium Spirochaeta africana type strain (Z-7692 T) from the alkaline Lake Magadi in the East African Rift," Standards in genomic sciences, 8 (2)**,** 165 (2013).

328. A. I. Teixeira, G. A. Abrams, P. J. Bertics, C. J. Murphy, and P. F. Nealey, "Epithelial contact guidance on well-defined micro-and nanostructured substrates," Journal of cell science, 116 (10)**,** 1881-1892 (2003).

329. W. M. Kier, "The diversity of hydrostatic skeletons," J. Exp. Biol., 215**,** 1247-1257 (2012).

330. N. Uehlein, B. Otto, D. T. Hanson, M. Fischer, N. McDowell, and R. Kaldenhoff, "Function of Nicotiana tabacum aquaporins as chloroplast gas pores challenges the concept of membrane CO2 permeability," Plant Cell, 20 (3)**,** 648-657 (2008).

331. I. Burgert and P. Fratzl, "Actuation systems in plants as prototypes for bioinspired devices," Philosophical Transactions of the Royal Society of London A: Mathematical, Physical and Engineering Sciences, 367 (1893)**,** 1541-1557 (2009).

332. B. S. Hill and G. P. Findlay, "The power of movement in plants: the role of osmotic machines," Q. Rev. Biophys., 14 (2)**,** 173-222 (1981).

333. E. Steudle and C. A. Peterson, "How does water get through roots?," Journal of experimental Botany, 49 (322)**,** 775-788 (1998).

334. P. T. Martone, M. Boller, I. Burgert, J. Dumais, J. Edwards, K. Mach, N. Rowe, M. Rueggeberg, R. Seidel, and T. Speck, "Mechanics without muscle: biomechanical inspiration from the plant world," ICB, 50 (5)**,** 888-907 (2010).

335. L. J. Gibson, "The hierarchical structure and mechanics of plant materials," Journal of the Royal Society Interface**,** rsif20120341 (2012).

336. L. Taiz and E. Zeiger, Plant Physiology, 3rd ed. (Sinauer Associates, 2002).

337. J. Fromm and S. Lautner, "Electrical signals and their physiological significance in plants," Plant Cell Environ., 30 (3)**,** 249-257 (2007).

338. A. Fahn and E. Werker, "Anatomical mechanisms of seed dispersal," in Seed Biology: Importance, Development, and Germination, edited by T. T. Kozlowski, p. 151-221 (Academic Press, New York, 1972).

339. E. Reyssat and L. Mahadevan, "Hygromorphs: from pine cones to biomimetic bilayers," Journal of the Royal Society Interface, 6 (39), 951-957 (2009).